Engineering of Materials for Hole Transport Applications in Perovskite Solar Cells

Thesis

Engineering of materials for hole transport applications in perovskite solar cells

Thesis submitted in partial fulfilment for the award of the degree of Doctor of Philosophy

Paheli Ghosh

School of Engineering and Innovation, Faculty of STEM

The Open University

Milton Keynes, United Kingdom

Supervisors

Prof Satheesh Krishnamurthy

Dr Tony Nixon

December 2019

Abstract

Immense interest has been generated in organic-inorganic perovskite solar cells (PSCs) due to their favourable attributes. PSCs show promise to overcome the trade-off between high efficiency and low-cost device fabrication. Perovskites, being ambipolar in nature, can conduct both electrons and holes. But since holes are present in low concentration, a hole transport material/layer (HTM/HTL) becomes essential for enhanced device performance, resilience and reproducibility.

This thesis explores different hole transport materials, namely spiro-OMeTAD, SFX-OMeTAD, SFX-TAD and graphene oxide. In this thesis chemical and plasma doping of HTMs have been studied. Doping with Li-TFSI is commonly undertaken to improve the hole conductivity and mobility in spiro-OMeTAD. Atmospheric pressure plasma jet (APPJ) based functionalization techniques have been proposed as inexpensive and environmentally friendly alternative to chemical p-type doping for improving the hole conductivity of spiro-OMeTAD and graphene oxide hole conductors. X-ray spectroscopic techniques have been extensively used for understanding the chemical structure and electronic properties of the HTMs.

The understanding of structural variation and its correlation with electronic properties is limited in Li-TFSI doped spiro-OMeTAD. Near edge X-ray absorption fine structure (NEXAFS) spectroscopy and X-ray photoelectron spectroscopy (XPS) have been demonstrated as effective techniques for probing the surface chemistry and electronic properties of spiro-OMeTAD. The findings provide insight into the electronic properties as a result of oxidation of spiro-OMeTAD and provide guidelines for the optimised doping levels suitable for enhanced device performance. The understanding gained from spiro-OMeTAD using NEXAFS has been extended to probe the electronic properties of two novel HTMs, SFX-OMeTAD and SFX-TAD.

P-type dopant, Li-TFSI being hygroscopic in nature, affects the stability of PSCs. A novel alternative in the form of functionalization with low-power (10 W) APPJ has been proposed. The conductivity after 5 minutes of plasma treatment was comparable to spiro-OMeTAD doped with 10-25% Li-TFSI. XPS shows the variation in chemical structure and electronic properties. KPFM measurements demonstrate an increase in work function which is indicative of p-type doping using helium and oxygen plasma jet.

Graphene oxide (GO) has found applications as charge transport layer and electrode due to the fact that it's work function can be tailored to device specification. A low power (3 W) APPJ was used to functionalize GO sheets with nitrogen, hydrogen and oxygen with helium as carrier gas. The variation in surface chemistry and electronic properties was probed using XPS. Ultraviolet photoelectron spectroscopy (UPS) was used to determine the tuning of work function of the plasma-functionalized GO films for targeted applications as HTL in PSCs.

A novel aerosol-based APPJ deposition technique has been developed for dopant-free spiro-OMeTAD with *in situ* modification of electronic properties. XPS gave insight into the variation in structural chemistry and electronic properties. Plasma-deposited spiro-OMeTAD showed x4.5 higher conductivity compared to aerosolized films. UPS reported increase in density of states at the top of the valence band, indicating the change in conductivity and the tuning of work function of the functionalized spiro-OMeTAD films.

Acknowledgement

I would like to express sincere thanks to my supervisors Prof Satheesh Krishnamurthy and Dr Tony Nixon for their guidance, advice, encouragement and for challenging me during my PhD which has helped me develop as an independent researcher. Special thanks to Prof Nicholas Braithwaite for his help and advice during commissioning of the plasma-printing equipment and Dr James Bowen for his help in setting up the spin coater and the Ellipsometry measurements.

Heartfelt gratitude to my examiners, Prof Peter Taylor and Dr Sagar Jain for their time and efforts in providing insightful feedback for shaping the final version of this thesis.

Special thanks to Dr Aruna Ivaturi (University of Strathclyde) and Prof Neil Robertson (University of Edinburgh) for preparation of bunch of high-quality hole transport samples for spectroscopic studies. I gratefully acknowledge the valuable collaborations with Dr Dennis Nordlund (Staff scientist at SLAC for his help during X-ray spectroscopy measurements), Prof Dermot Brabazon (DCU), Prof Yimin Chao (University of East Anglia), Dr Sanjayan Sathasivam (UCL), Dr Debabrata Bhattacharya (Cranfield University) and Dr Amit K. Chakraborty (NIT Durgapur, India).

I would take this opportunity to thank Heather Davies, Jill Clarke, Gordon Imlach, Stan Hiller and Dr Matt Kershaw for their support, help and patience during laboratory sessions and Thomas Webley for his help in setting up laboratory equipment.

This thesis probably would not have been possible without the help, advice, encouragement and incessant efforts of Dr Avishek Dey, not to mention the long hours of discussions. Dr Fatima Yusuf needs special mention for being such a great friend. Special thanks to my colleagues and friends, Dr George Matthew, Dr Danson Kimani, Dr José Rodolpho de Oliveira Leo, Dr Safaa Lebjioui, Dr Yadunandan Das, Rahul, Vibha, Telma, Mai, Erika, Gauthaman, Beverly, Anas, Nicola, Michela, Maxim, Lois, Nibedita, Ishita and Pritha for their help, friendship and encouragement.

Finally, I would like to express my sincere thankfulness and heartfelt gratitude to God for helping me through this journey safely and to my parents, Mr Paresh Ghosh and Mrs Purnima Ghosh, and other family members for their unconditional love, constant inspiration, encouragement and support. This thesis is dedicated to God and my family.

I may have missed some names here, but everyone whom I have crossed paths with during this journey, deserves a ‘Thank you’.

Table of contents

List of figures

List of tables

List of acronyms

AFM: atomic force microscopy

APPJ: atmospheric pressure plasma jet

CdTe: cadmium telluride

CIGS: copper indium (di) selenide

CNT: carbon nanotube

CV: cyclic voltammetry

DBD: dielectric barrier discharge

DOS: density of states

DSSC: dye-sensitized solar cell

EDS: electron dispersive spectroscopy

EFM: electron force microscopy

ETA: extremely thin absorber

ETL: electron transporting layer

eV: electron volt

FESEM: field emission scanning electron microscopy

FF: fill factor

FTO: fluorine doped tin oxide

FWHM: full width at half maxima

GaAs: gallium arsenide

GO: graphene oxide

GIXS: grazing incidence X-ray scattering

GW: gigawatt

HOMO: highest occupied molecular orbital

HOPG: highly oriented pyrolytic graphite

HTL: hole transport layer

HTM: hole transport material

EFM: electron force microscopy

I_{SC}: short-circuit current

ITO: indium tin oxide

KPFM: Kelvin probe force microscopy

Li-TFSI: lithium bis (trifluoromethane) sulfonimide

LUMO: lowest unoccupied molecular orbital

NEXAFS: near edge X-ray absorption fine structure

P3HT: poly-3-hexyl thiophene

PCE: power conversion efficiency

PEDOT/PSS: poly-(2, 3-dihydrothieno-1, 4-dioxin)-poly (styrene sulfonate)

PHJ: planar heterojunction

PL: photoluminescence

PSC: perovskite solar cell

PV: photovoltaic

PTAA: poly-triaryl amine

QDSSC: quantum dot-sensitized solar cell

RF: radio frequency

RGO: reduced graphene oxide

SAED: selected area electron diffraction

SBF: spiro bifluorene

sccm: standard cubic centimetre per minute

Spiro-OMeTAD: 2, 2', 7, 7'-tetrakis-(N, N-di-4-methoxyphenylamino)-9,9'-spirobiflourene

tBP: 4-tertiary-butyl pyridine

TPA: triphenyl amine

WAXS: wide angle X-ray scattering

XPS: X-ray photoelectron spectroscopy

UPS: ultraviolet photoelectron spectroscopy

List of publications

Publications associated with this thesis:

1. Book chapter titled 'Influence of Nanostructures in Perovskite solar Cells' for Reference Module in Materials Science and Materials Engineering for Elsevier. **Ghosh, P**.; Sundaram, S.; Nixon, T. and Krishnamurthy, S (2016).
2. Avishek Dey, **Paheli Ghosh**, James Bowen and Satheesh Krishnamurthy, Engineering the work function of graphene oxide from p to n type using a low power atmospheric pressure plasma jet, (manuscript under review at PCCP).

3. **Paheli Ghosh**, Aruna Ivaturi, Debabrata Bhattacharya, James Bowen, Tony Nixon, N.S. Braithwaite and Satheesh Krishnamurthy, Dopant-free atmospheric pressure plasma functionalized spiro-OMeTAD- An efficient hole transport material for perovskite solar cells, (manuscript under review at ACS Applied Electronic Materials).
4. **Paheli Ghosh**, Avishek Dey, Tony Nixon, N. S. Braithwaite and Satheesh Krishnamurthy, *In situ* functionalization and deposition of dopant-free spiro-OMeTAD hole transport material with atmospheric pressure plasma jet, (manuscript in preparation).

5. **Paheli Ghosh** *et al*. Spectroscopic investigation of the role of dopants in electronic properties of hole transporter materials for perovskite solar cells, (manuscript in preparation).

Other publications:

1. Behray, Mehrnaz; Webster, Carl; Pereira, Sara; **Ghosh, Paheli**; Krishnamurthy, Satheesh; Al-Jamal, Wafa; Chao, Yimin, Synthesis of novel diagnostic silicon nanoparticles for targeted delivery of thiourea to EGFR-expressing cancer cells, *ACS Appl. Mater. Interfaces*, 2016, 8 (14), pp 8908–8917.
2. K. Bagga, R. McCann, F. O'Sullivan, **P. Ghosh**, S. Krishnamurthy, A. Stalcup, M. Vázquez and D. Brabazon, Nanoparticle functionalized laser patterned substrate: an innovative route towards low cost biomimetic platforms, *RSC Adv*. 2017, 7, 8060.

3. Avishek Dey, **Paheli Ghosh**, N. S. Braithwaite and Satheesh Krishnamurthy, Low temperature synthesis of copper oxide nanowires using atmospheric pressure plasma jet, (manuscript in preparation).

Chapter 1

Introduction and Motivation

1.1 Solar energy

The ever-increasing demand for energy and increasing threat of global warming due to CO_2 emissions are the future challenges for mankind. Harvesting solar energy is a key approach for clean and sustainable energy production. Solar energy is by far the most abundant source of energy and life on earth is sustained by energy from the sun. Direct conversion of sun's energy to electricity by photovoltaic (PV) cells is one of the most potent routes to harness solar power. Renewable energy technology, in particular solar photovoltaics, is a promising alternative to fossil fuels and carbon-free energy production. Almost two-thirds of the new global electricity installations has seen the usage of renewable energy technology, mounting to almost 165 gigawatts (GW) in 2016 [1]. The new solar PV installations around the world increased by 50%, reaching over 74 GW around the same time [1]. Forecast suggests that the total solar PV capacity would reach 740 GW globally by 2022 [1]. The International Energy Agency roadmap envisions this trend to increase to 5% of global contribution in 2030, rising to 16% (4500 Tera Watt hour per year) by 2050 [2]. Solar PV is classified into three generations as discussed below (Figure 1.1).

First generation: The first-generation cells, made of crystalline silicon are the commercially dominant PV technology. Since the first silicon solar cells were reported in 1941 with power conversion efficiency (PCE) less than 1%,[3] there has been substantial improvement, culminating in ~26% at present [4]. But the efficiency has barely improved over the past decade as compared to the second and third generation technologies. Several inherent challenges limit the predicted theoretical efficiency of silicon PV to 33% [5] and impart on the carbon footprint such as: (1) material properties

like absorption coefficient, thus increasing the typical wafer thickness to ~200 μm; (2) fabrication being an energy-intensive process and (3) installation of silicon modules. Development of second-generation thin film PV has been undertaken to overcome these challenges.

Second generation: Second generation cells are thin film devices which include amorphous silicon, gallium arsenide (GaAs), cadmium telluride (CdTe) and copper indium gallium selenide (CIGS). These are direct band gap materials which absorb sunlight more efficiently than crystalline silicon and have film thicknesses around few microns. Low material consumption and less energy-intensive production lowers cost and energy payback time [6,7].Thin film solar cells being semi-transparent in nature find applications for building integrated photovoltaics (BIPV) [7] and also have a niche market in the electronics industry. However,

(i) complex materials processing,

(ii) high temperature treatments for device fabrication,

(iii) availability of rare-earth materials and hence the associated costs, make them less attractive for large-scale production purposes. Hence, research has been directed towards low-cost, efficient third generation devices with promise for scaling up.

Third generation: The need to overcome the theoretical efficiency limit, optimise charge collection and energy harvesting has led immense research on dye-sensitized solar cells (DSSCs), organic PV and the organic-inorganic hybrid perovskite solar cells (PSCs) (hybrid is a combination of organic and inorganic materials). These represent the most promising and fast-evolving third generation PV technologies with the possibility of printing and large-scale fabrication even on flexible substrates. One of the prime candidates with a near-vertical increase in efficiency is the recently explored perovskite solar cells which are advantageous due to their facile fabrication techniques, materials diversity and high absorption coefficient.

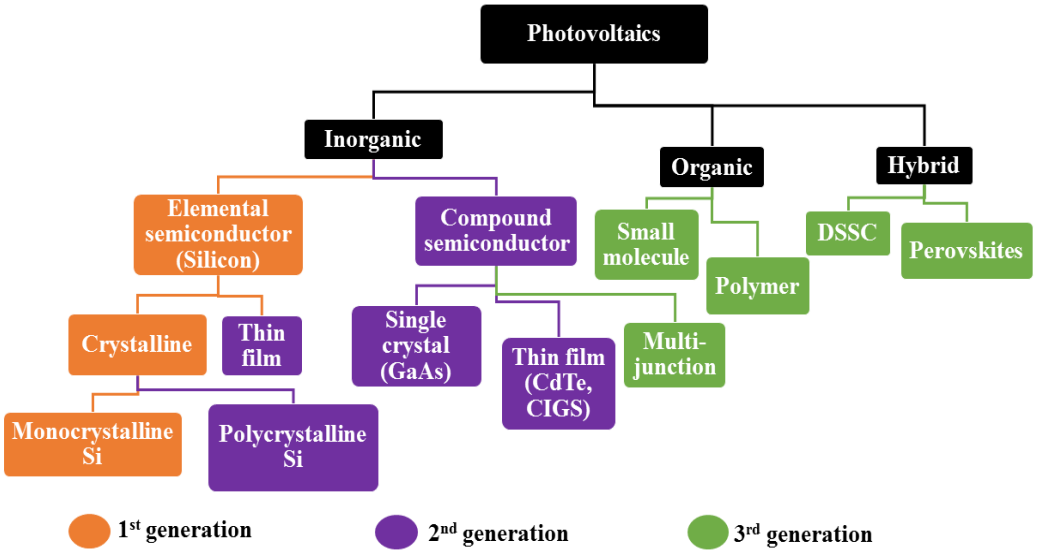

Figure 1.1 Hierarchy of PV technologies.

Inorganic-organic hybrid halide perovskite materials with excellent attributes such as ambipolar (i.e. both p- and n- conductive) charge transport [8], high charge carrier mobility, long diffusion length [9], high open circuit voltage (V_{OC}) [10] and low-cost processes of fabrication from earth-abundant materials are suitable alternatives to first and second generation solar cells. These favourable properties of perovskite materials have spurred intense research in this field. As a consequence, a stupendous increase in device efficiency from 9.7% in 2012 to >24.0% in 2019 [11] has been achieved in comparison to first and second generation technologies which have been in existence for several decades but struggle to keep pace with the PCE improvement of PSCs as shown in Figure 1.2. Despite the impressive performance, the major challenge which has hindered their commercial adoption is

1. Device stability which arise from (i) degradation of the perovskite absorber due to moisture ingress; (ii) poor interfacial contact and (iii) instability of individual conducting layers, primarily the hole transport material/layer (HTM/HTL). Stability may be enhanced by optimising different constituents such as crystal structure, film quality,

conducting layers, interfaces and device encapsulation. Hence, one of the key challenges in PSC research lies in making the HTLs efficient and cost-effective. This thesis aims to address the key challenge in the form of selection of suitable hole transport materials and engineering them to optimise the properties that are comparable to conventional methods.

Toxicity issue with the commonly used lead (Pb) in devices and reproducibility of device performance during upscaling from lab-scale to modules are two other challenges which need addressing but are beyond the scope of this thesis.

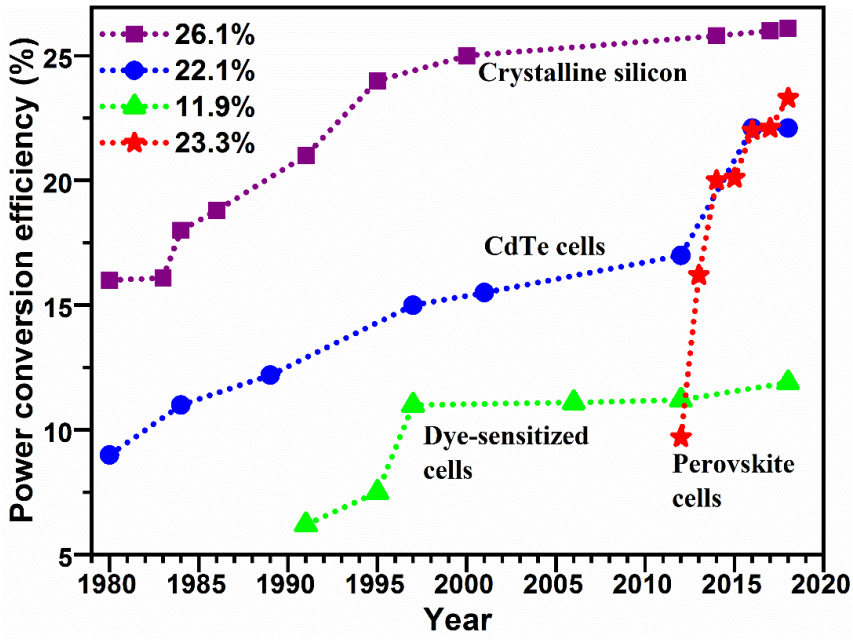

Figure 1.2 Comparison of the rate of efficiency increase in perovskite solar cells (red lines and markers) with DSSCs, CdTe (second generation) and crystalline silicon (first generation) solar cells along with the highest reported efficiency values.

1.2 Thesis structure

The key issues this thesis addresses are based on the selection of hole transport materials, the systematic understanding of their morphology, electronic and optical properties after functionalization as described in seven chapters. In the present chapter (Introduction and motivation), a brief introduction of PSCs and HTMs has been

presented. The motivation for using spiro-OMeTAD, graphene oxide and atmospheric pressure plasma functionalization and deposition has also been described.

Chapter 2 (Experimental techniques) introduces the experimental techniques employed in the thesis for synthesis, functionalization, comparison and probing different hole transport materials. Synchrotron-based element-specific spectroscopic techniques (at Stanford Synchrotron Radiation Light Source) have been used to get deeper understanding of the properties of hole transport materials.

Chapter 3 (Probing the electronic properties of different hole transport materials) provides a thorough investigation of the structural and electronic properties of spiro-OMeTAD doped with different concentration of Li-TFSI. A mechanism for the variation of electronic properties as a function of dopant concentration has been proposed. The understanding acquired for spiro-OMeTAD has been extended to two new molecules with spiro[fluorine-9,9'-xanthene] (SFX) core structure, namely, SFX-OMeTAD and SFX-TAD. SFX-OMeTAD and SFX-TAD have been introduced as low-cost alternatives to spiro-OMeTAD and have found only limited application in PSC fabrication [12,13].

In Chapter 4 (Dopant-free atmospheric pressure plasma functionalized spiro-OMeTAD-efficient hole transport material for perovskite solar cells), atmospheric pressure plasma jet (APPJ) has been demonstrated for the first time as an alternative to chemical doping with hygroscopic Li-TFSI and tBP as additive. Results show an enhancement in conductivity after 3 minutes of plasma treatment. Conductivity after 5 minutes of plasma functionalization is comparable to spiro-OMeTAD doped with 10-25% Li-TFSI.

Graphene oxide has found applications as charge transport layer and electrode material due to the fact that its work function can be tailored to device specifications. A

low power (3 W) APPJ using admixtures of helium, hydrogen, nitrogen and oxygen has been used for functionalization of GO in Chapter 5 (Tuning the work function of graphene oxide hole transport material using atmospheric pressure plasma jet). The variation in surface chemistry and electronic properties along with the tuning of work function of the functionalized films were investigated spectroscopically. GO films showed $x10^3$ times better conductivity after treatment with $He+H_2$ plasma.

Chapter 6 (*In situ* functionalization and deposition of dopant-free spiro-OMeTAD hole transport material with atmospheric pressure plasma jet) describes the deposition and *in situ* modification of the electronic and electrical properties of dopant-free spiro-OMeTAD using an aerosol-assisted APPJ technique. The understanding gained from plasma functionalization of spiro-OMeTAD (Chapter 4) was extended to bulk plasma processing and variation in structural chemistry and electronic properties were studied with Raman spectroscopy, XPS and UPS.

Chapter 7 discusses the summary of the thesis and the future prospects of the findings of this thesis.

1.3 Background and motivation

Ever since their discovery, inorganic perovskites have seen widespread applications as superconductors [14], pyroelectric [15] and electro-optic devices. But it took over 170 years to realise their potential in solar cells. The concept of incorporation of perovskites as a sensitizer (sensitizer is absorber or active material for sunlight harvesting) has emerged from the field of DSSCs [16,17] where a light-absorbing dye adsorbed on the surface of a mesoporous n-type conductor and filled-up with a redox electrolyte, functions efficiently as a solar cell. Methylammonium lead trihalide ($CH_3NH_3PbX_3$, X = I, Br, Cl) is one of the most widely used perovskite absorber material in PSCs which has come to the forefront of research following the seminal work by

Miyasaka *et al.*, proposing a new direction for DSSC fabrication [18]. However, the device's long-term stability remained an issue due to the dissolution of the perovskite in the electrolyte. This challenge was largely overcome by the fabrication of solid-state DSSCs by replacing the liquid electrolyte with solid hole transporting material, spiro-OMeTAD (2,2',7,7'-tetrakis (N,N-di-p-methoxyphenylamine)-9,9'-spirobifluorene) in 2012 by Park, Grätzel *et al*. with a reported PCE of 9.7% [19]. Research in PSCs was pioneered by Snaith *et al.*[20] by introducing some novelties for improved device performance in terms of (i) the usage of mixed halide perovskite $CH_3NH_3PbI_{3-x}Cl_x$ as active absorber, (ii) coating nanoporous titania (TiO_2) surfaces with a thin perovskite layer, forming extremely thin absorber (ETA) cells, (iii) replacing conducting nanoporous TiO_2 by a non-conducting alumina (Al_2O_3) scaffolding and (iv) deployment of planar cells without the scaffolding. The tunable properties of PSCs with promise for low-cost, efficient, large-scale devices have encouraged intense research with the device performance soaring up to ~24% [11] in a short span of time.

1.4 Charge generation and recombination in perovskite solar cells

Given the challenges associated with PSCs, the mechanism of generation and transfer of charge carriers in PSCs will be discussed in this section. An archetypal perovskite solar cells comprises an n-type compact layer, a mesoporous oxide layer for electron transport (ETL), a light-harvesting perovskite layer, a HTM/HTL and two electrodes as shown in Figure 1.3 (a). Various steps and mechanism involved in electron-hole generation and charge transfer and working of PSCs (Figure 1.3 b) are shown below.

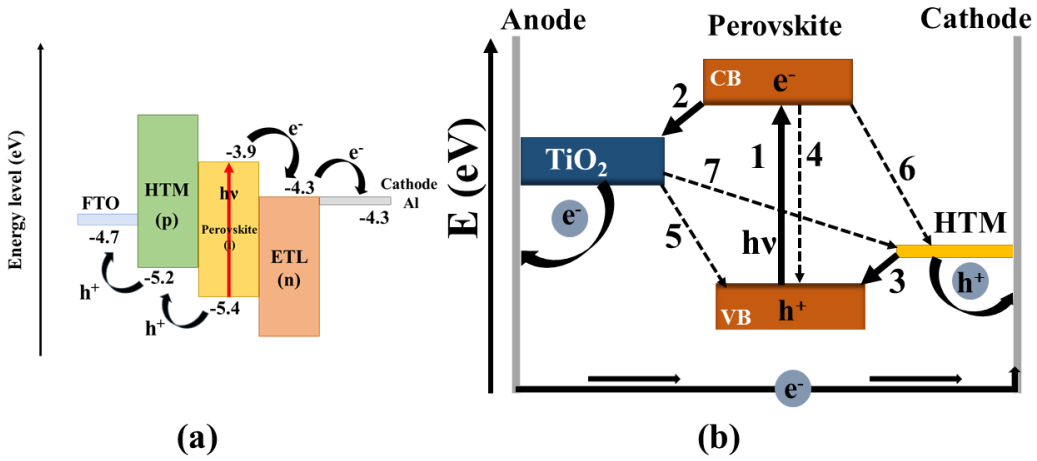

Figure 1.3 Schematic representation of (a) the generic structure of PSCs (in p-i-n inverted architecture) with the different layers deposited on FTO (Fluorine doped tin oxide)/ITO (Indium tin oxide) glass substrate upwards and (b) the steps involved during charge transfer processes in a TiO_2 (ETL)/Perovskite/HTM solar cell [21].

Step (1): Perovskite active material absorbs light (hv) resulting in creation of electron-hole pairs. Step (2): Photo-generated electrons in the perovskite conduction band (CB) transfer to the TiO_2 conduction band as primary charge separation step, leaving behind a hole (h^+) in the perovskite absorber (equation 1).

$$(e^- \ldots h^+)_{perovskite} \rightarrow e_{CB}{}^-(TiO_2) + h^+(perovskite) \qquad \ldots\ldots\ldots\ldots\ldots 1$$

This hole is eventually transferred to the HTL. Step (3): Injection of these holes into the HTM as the primary charge separation step (equation 2)

$$(e^- \ldots h^+)_{perovskite} \rightarrow h^+(HTM) + e^-(perovskite) \qquad \ldots\ldots\ldots\ldots\ldots 2$$

Where e^- denotes electrons, h^+ are the holes, $(e^- \ldots h^+)_{perovskite}$ denotes electron-hole pair formed in the perovskite absorber, $e_{CB}{}^-$ (TiO_2) stand for electrons in the conduction band of TiO_2 and h^+ (perovskite) are holes formed in the perovskite absorber layer.

Finally, both electrons and holes are collected at the respective front and back electrodes to generate photocurrent.

Undesirable processes such as exciton annihilation can occur leading to photoluminescence (hv') (equation 3) or non-radiative recombination (denoted by ∇) (equation 4); as well as recombination of charge carriers at the interfaces e.g. back electron transfer at the TiO_2/perovskite interface (equation 5) as well as back hole transfer at the HTM/perovskite interface (equation 6) and charge recombination at the TiO_2/HTM interface (equation 7), which occurs only during incomplete coverage of the perovskite layer.

Exciton annihilation:

$$(e^- \ldots h^+)_{perovskite} \rightarrow hv' \qquad \ldots\ldots\ldots\ldots\ldots\ldots 3$$

$$(e^- \ldots h^+)_{perovskite} \rightarrow \nabla \qquad \ldots\ldots\ldots\ldots\ldots\ldots 4$$

Back electron transfer at the TiO_2/perovskite interface:

$$e_{CB}^- (TiO_2) + h^+(perovskite) \rightarrow \nabla \qquad \ldots\ldots\ldots\ldots\ldots\ldots 5$$

Back hole transfer at the HTM/perovskite interface:

$$h^+(HTM) + e^- (perovskite) \rightarrow \nabla \qquad \ldots\ldots\ldots\ldots\ldots\ldots 6$$

Charge recombination at the TiO_2/HTM interface (in case of incomplete coverage of perovskite layer):

$$e_{CB}^- (TiO_2) + h^+(HTM) \rightarrow \nabla \qquad \ldots\ldots\ldots\ldots\ldots\ldots 7$$

For a PSC to yield high PCE, the charge recombination processes (4-7) should occur at slower time scale compared to charge generation, separation and extraction processes (1-2).

1.5 Importance of hole transport layer in perovskite solar cells

As can be observed from Figure 1.3, each intermediate layer (HTL and ETL) plays an important role in the functioning of PSCs. First, they selectively extract one type of charge carriers (hole or electron) and transport them to the respective electrodes. Second, an intermediate layer can be used to bridge a mismatch of energy levels between the active layer and the electrode to avoid charge recombination. An intermediate layer can also compensate for roughness and remove shunts resulting from non-uniformity of the electrode films. Perovskites, being ambipolar in nature, can conduct holes. But since holes are present in low levels, an HTL becomes a prerequisite during PSC fabrication. Moreover, in an inverted architecture (p-i-n) (Figure 1.3 a), the surface properties of the HTL strongly influence the morphology, crystallization and conditions of crystal boundaries of the perovskite layer deposited over the HTL. Additionally, tuning the electronic and electrical properties of the HTL/perovskite interface is important to facilitate charge extraction and collection whilst minimizing recombination [22]. Several other factors such as reliability, chemical compatibility of the HTM, hydrophobic properties, UV light cut off, cost of raw materials and fabrication must be considered to minimize the energy mismatch in a HTL/perovskite interface and for long-term device stability [23–25]. As PSCs are the new generation solar cells which have shown considerable progress within a short time span, research is focussed on both the active layer as well as hole transporting layer. In the following section, a brief review of the organic small molecules explored as HTMs in PSCs is summarised. Figure 1.4 shows a schematic energy level diagram with the most efficient perovskite light absorbers $MAPbI_3$, $MAPbI_{3-x}Cl_x$, $(FAPbI_3)_{0.85}(MAPbBr_3)_{0.15}$, with the highest occupied molecular orbital (HOMO) and lowest unoccupied molecular orbital (LUMO) positions. Different HTMs employed have also been shown with respective HOMO edges and TiO_2 as ETL. The

energy levels of $MAPbI_{3-x}Cl_x$, $MAPbI_3$, $(FAPbI_3)_{0.85}(MAPbBr_3)_{0.15}$ were taken from references [20,26,27] (MA: methylammonium; FA: formamidinium).

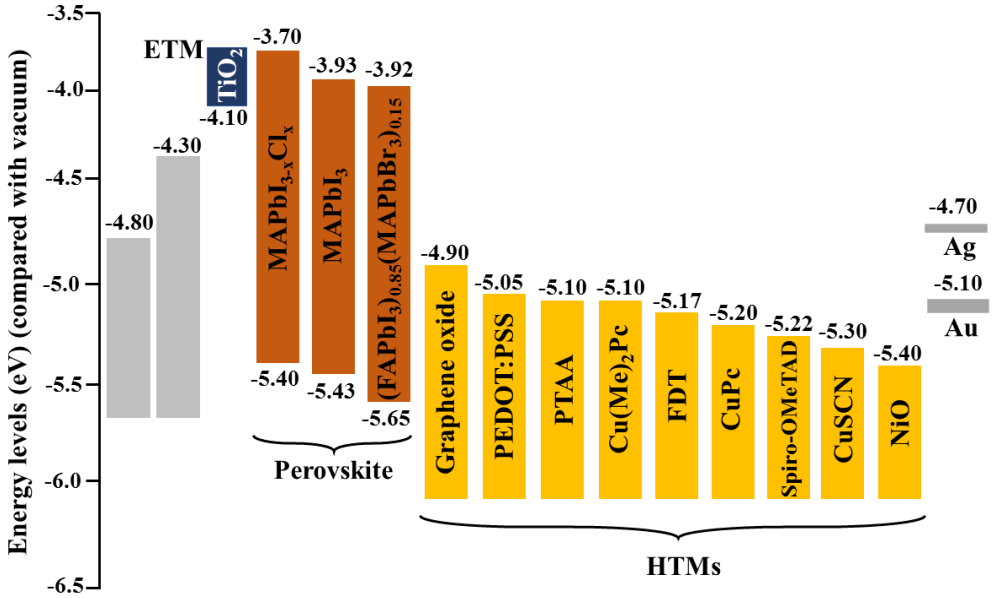

Figure 1.4 Schematic energy level diagram of the components of perovskite solar cells including the most efficient perovskite light absorbers $MAPbI_3$, $MAPbI_{3-x}Cl_x$, $(FAPbI_3)_{0.85}(MAPbBr_3)_{0.15}$, HTM and TiO_2 as ETL.

1.5.1 Organic HTMs

The desirable attributes of an HTM can be summarised as

(i) Transparency in the visible region of the spectrum with no interference with absorption of the absorber material.

(ii) The HOMO level should be located above the ground state of the absorber such that a shift of the HOMO level towards the perovskite will result in increased V_{OC}.

(iii) Optimum hole mobility (possibly > 10^{-3} $cm^2V^{-1}s^{-1}$) in order to conduct holes and impede charge recombination.

(iv) Amorphous in nature with glass transition temperature over 100 °C to avoid crystallization.

(v) Good thermal, photochemical, air and moisture stability, adequate pore filling ability to infiltrate perovskite absorber in mesoscopic configuration, and low molecular weight and high solubility.

Though, polymeric HTM [28,29] such as poly triaryl amine (PTAA) have shown the best device efficiency in PSCs, it suffers from drawbacks such as indistinct molar mass due to poly-dispersity, reproducibility, complex purification process, low solubility, poor infiltration into absorber layer and lack of stability under low vacuum conditions which limit their technological applications [29,30]. These drawbacks have led to the designing of small organic molecules as hole conductors discussed in detail in the following section.

1.5.2 Small molecule organic hole conductor

Triphenyl amine (TPA)-based HTMs exhibit good thermal and morphological stability, charge transport and suitable Ionization potential. TPA is an electron donating unit [31] which possesses two favourable properties: easy oxidation of the amine nitrogen atoms and the ability to transport positive charge effectively [32]. Several aromatic amines are hole conductors where the electron-donating amine nitrogen is responsible for hole transporting behaviour [32]. TPA-based compounds, both as small molecules and oligomers, find widespread applications in PSCs especially due to their propeller conformation which impedes the charge recombination by preventing close contact between perovskite and HTL [33]. Spiro-based TPA molecules are structurally most stable and one of the most adapted forms of molecular glasses and several molecules have been designed containing spiro-bifluorene (SBF) as the central core [34,35]. Crosslinking two molecular π systems with a sp^3 hybridized atom is the concept behind formation of HTMs with spiro centre (as shown in Figure 1.5). The sp^3 hybridized atom at the junction of the two halves of the biflourene molecule, results in a perpendicular arrangement and

a sterically demanding structure. The aforementioned molecular arrangement induces structural rigidity and impedes crystallization below the glass transition temperature (T_g) and enhances stability of the amorphous state which is desirable in HTMs. As a result of the perpendicular arrangement of both units, the intermolecular π-π interactions are suppressed leading to an increased solubility of Spiro compounds. The added advantage of such molecules is that they can be substituted at each position which gives immense scope for synthesizing novel molecules with tailored properties [36]. All these desirable attributes make Spiro-based small organic molecules exceptionally suited for HTL application.

1.5.3 Importance of Spiro-OMeTAD:

The twisted SBF-based molecule, spiro-OMeTAD is the most widely investigated small organic molecule hole conductor and has been responsible for consistently good device performance since its inception in 1998 by Bach and Grätzel [37].

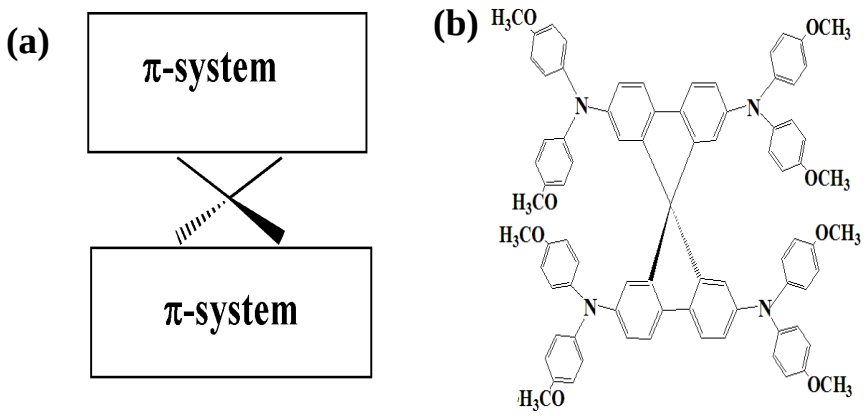

Figure 1.5 Molecular structure of (a) spiro-linked systems and (b) spiro-OMeTAD (adapted from reference [38]).

From the crystal structure of spiro-OMeTAD it is observed that the phenylenes in the methoxyphenyl-amine substituents have a relatively anisotropic arrangement in the crystals. The amine nitrogen is planar in nature with the methoxy groups (-OCH_3) on the

side chains being oriented in a propeller configuration. Such an arrangement favours delocalization of charge and packing of spiro-OMeTAD occurs as a result of sharing of electrons between the p-orbitals of nitrogen and the electron-donating methoxy groups. The anisotropically arranged phenylene groups further contribute to the packing of the molecules. The crystal structure of spiro-OMeTAD reveals π-π stacking between the fluorene units and random alignments with respect to the fluorene backbone. Molecular dynamic calculations performed by Shi *et al* [39]. and Yavuz *et al* [40]. demonstrated several possible interfluorene packing configurations. The π-π stacking between molecular pairs may have contribution from interflourene spiral packing motifs as well as slipped π-π stacking between neighbouring phenylene units. During intermolecular π-π stacking two fluorene rings are separated by a vertical plane-to-plane distance of ~3.8 Å. The amine nitrogen being the active site for reaction during Li-TFSI doping of spiro-OMeTAD, may become positively charged during the doping procedure. The methoxy groups were introduced into spiro-OMeTAD to control the oxidation potential and thus help in adjusting the electronic properties of the hole conductor. The methoxy groups being electron-donating in nature help in stabilising the positive charge on the nitrogen atom of the tertiary amine by resonance stabilization and the extension of π-electron delocalization over the whole molecule. The methoxy groups also play an important role in aligning the HOMO level of the molecule apart from anchoring the spiro-OMeTAD molecule to the perovskite absorber layer in n-i-p configuration.

This cross-linked structure results in improved morphological stability of low molar mass materials while retaining their electronic properties. They have several advantages such as

1. The orthogonally interconnected flourene rings leads to high steric hindrance which suppresses intermolecular interactions between the π systems.

2. This arrangement leads to better solubility of the Spiro compounds compared to the non-Spiro-linked molecules.

3. Doubling of the molecular weight along with the crosslinking structure imparts certain rigidity to the Spiro compounds which causes entanglement in the amorphous state and hinders recrystallization. Glass transition temperature of spiro-OMeTAD is 120° C.

4. Spiro-OMeTAD is compatible with solution-processed techniques such as spin coating, dip coating, slot-die coating etc.

5. The methoxy groups in spiro-OMeTAD structure are not only responsible for adjusting the HOMO level of the material but also help in anchoring the film onto the underlying perovskite layer in n-i-p architecture.

Although spiro-OMeTAD has a lot of advantages but it suffers from low hole conductivity. The following sections will describe the methods to increase conductivity.

Objective 1: Doping and oxidation of spiro-OMeTAD

Though widely explored as HTM in PSCs, spiro-OMeTAD suffers from low hole mobility ($\sim 10^{-5} cm^2 V^{-1} s^{-1}$) [35,41] and conductivity ($\sim 10^{-8}\ S\ cm^{-1}$) in its pristine form [37,42,43]. The low conductivity and hole mobility of spiro-OMeTAD stems from the sp^3 hybridized N atom with pyramidal structures which leads to large intermolecular distances. Thus, charges have to move along longer paths and hence the conductivity is lowered [44]. The lower hole mobility can also be explained in terms of the two types of steric hindrances which exist in unit cells of spiro-OMeTAD and affect the π-π stacking of the molecules. The steric hindrance between two molecules in a single crystal unit cell prevents the formation of close π-π stacking upon crystallization whereas the hindrance between the outer fragments of each cell prohibits the formation of continuous π-π stacking. The second mechanism is possibly due to the twisted nature of the central

Spiro carbon [39]. This discontinuity inhibits delocalization of charge carriers and charge transport occurs primarily by hopping from one spiro-OMeTAD molecule to another [39].

Electronic doping is a suitable technique to tune the type and density of charge carriers as well as bring about controllability and reproducibility for efficient device performance [41,45–50]. Doping of organic semiconductors relies on the charge transfer mechanism between the organic host and the dopant. The latter maybe either a donor (n-type doping) or acceptor (p-type doping) moiety that leaves part of the host molecules in a reduced or oxidized state. The ionization potential or electron affinity of the dopant with respect to the energy level of the host plays a significant role in understanding the feasibility of the doping procedure. Controlled doping with molecular-dopants are expected to be applicable for the controllability and reproducibility of PV performance. Addition of dopants not only generates additional charge carriers but also tunes the electronic properties and different dopants such as Li-TFSI [45], Na-TFSI [51], Ag-TFSI [52], Co (III) complexes [42,53,54], WO_3 [55], Cu(II) salts [56,57] have been utilised to dope spiro-OMeTAD [45,55,58–62].

(a) Lithium bis (trifluoromethyl-sulfonyl)imide (Li-TFSI) for doping spiro-OMeTAD:

Spiro-OMeTAD was originally synthesized for hole transport application in solid-state DSSCs and in pristine form achieved a PCE of 0.74% which increased to 2.56% with additives 4-tert-butylpyridine (t-BP) and lithium bis(trifluoromethane-sulfonyl)imide (Li-TFSI) [63]. Li-TFSI improves the conductivity of spiro-OMeTAD by shifting the Fermi level towards the HOMO, which implies p-type doping [45,59]. Addition of Li-TFSI leads to improvement of the solar cell efficiency, and reduces recombination losses at interfaces which might be due to alteration of the TiO_2 band edge position for higher potentials [37,64]. Lithium and antimony-based salts and $N(PhBr)_3SbCl_6$, were the first additives employed for doping spiro-OMeTAD in solid state DSSCs [37]. The antimony

salt was proposed to act as dopant by introducing free charge carriers by the oxidation of spiro-OMeTAD. The lithium salt was used to control the surface electrochemical properties of TiO_2 by adsorption and intercalation of Li^+ ions [37,64]. Addition of 12% Li-TFSI was reported to have increased hole mobility of spiro-OMeTAD by two orders of magnitude. This increase in mobility was explained on the basis of increased disorder and broadening of the density of states as well as screening of deep Coulomb traps to reduce the potential barrier for charge transfer [41].

(b) Role of tert-butyl pyridine (tBP) additive in doping spiro-OMeTAD: The concept of 4-tert-butyl pyridine as additive has stemmed from the usage of tBP-dipped TiO_2 electrode in DSSCs which was reported to substantially enhance the V_{OC} and fill factor (FF). Defects such as oxygen vacancies originating from TiO_2 upon heating has a negative impact on the solar cell performance [65]. tBP is used to passivate the under-coordinated titanium atoms within the lattice, thus minimising charge recombination. Kruger *et al*. proposed the improvement in photovoltaic performance when tBP was blended with spiro-OMeTAD and Li-TFSI solution due to reduction in interfacial charge recombination [63]. More recently, Juarez-Perez *et al*. [66] and Wang *et al*. [67] reported that tBP improves miscibility of spiro-OMeTAD with Li-TFSI and impedes phase segregation in solution, resulting in uniform distribution of Li-TFSI during film deposition. Molecular structure of Li-TFSI and tBP additives used for doping spiro-OMeTAD are shown in Figure 1.6. In this thesis both LiTFSI and tBP have been used for doping hole conductors and studied using synchrotron spectroscopic techniques to understand the influence of the dopants on the materials properties.

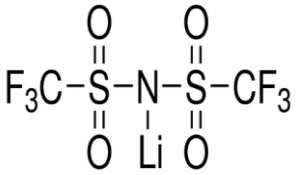

(a) Li-TFSI

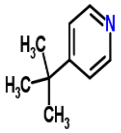

(b) tBP

Figure 1.6 Li-TFI and tBP as p-type additives used for doping spiro-OMeTAD hole conductor for perovskite solar cells.

1.5.4 Hole transport materials beyond spiro-OMeTAD

The complexity of synthesis of the spiro biflourene core and requirement of Pd-catalyst coupling, limits the applications of spiro-OMeTAD in large-scale device fabrication. To overcome the cost and complexity associated with synthesis, SFX core based small molecules were synthesized [68]. Two SFX-based molecules have been studied in Chapter 3 of this thesis, SFX-OMeTAD and SFX-TAD (Figure 1.7). These molecules are amorphous in nature, have high solubility, high glass transition temperature and HOMO level alignment identical to spiro-OMeTAD, but have been mostly employed as organic semiconductors in organic light emitting diodes (OLEDs) [69–71].

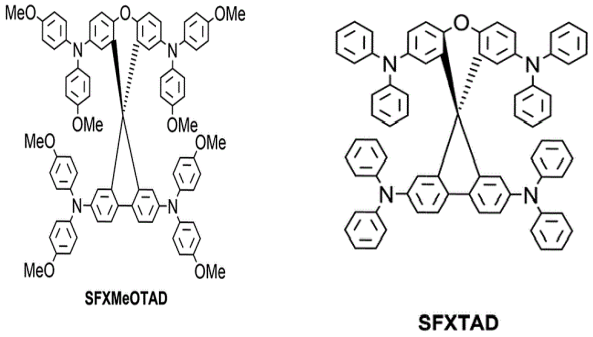

Figure 1.7 Chemical structure of SFX-based hole conductor molecules [12].

Objective 1: The first objective of this thesis is to investigate the variation in electronic properties due to differential doping of spiro-OMeTAD, SFX-OMeTAD and SFX-TAD with Li-TFSI and tBP as additive and will be described in Chapter 3.

The conductivity of spiro-OMeTAD, Li-TFSI and tBP blend is influenced by dopant concentration and is subject to the additional protocol of exposure to atmospheric conditions, light soaking etc. to achieve the desired device performance [45,47,72–74]. The exposure to ambient condition adversely affects the stability of solar cells as a result of formation of pin-holes and degradation of the perovskite absorber layer [45,67,75,76]. This is primarily due to the low boiling point and volatility of tBP [67,77] which leaves behind accumulation of hygroscopic Li-TFSI. Other dopants such as Co(III)-based complexes [53,78–82], Cu(II) pyridine complex [57], F4-TCNQ [83], CuSCN or CuI [56], find applications in PSCs. But they have certain disadvantages being quite expensive due to complex synthesis techniques and requirements of high purity raw materials, exhibit poor solubility in organic solvents, high volatility, and/or intensive and complicated synthesis procedure, display vibrant colours [84–87]. Hence, the quest to develop efficient and stable p-type dopants for HTMs seems challenging. Using a hydrophobic dopant or modifying the chemical structure for improved π-π stacking and charge transport are solutions to the problem.

A non-thermal atmospheric pressure plasma jet as a facile means to increase the hole conductivity by functionalizing spiro-OMeTAD films has been demonstrated in this thesis to address the issues with chemical dopants.

1.6 Atmospheric pressure plasma

Plasma is often considered as the fourth state of matter. It is a plume of charged particles, neutral molecules, metastables and radiation and is generated by heating a gas or applying strong electromagnetic fields. The applied energy results in ionization of the gas by breaking the molecular bonds with the ionized gas being neutral since it has equal densities of oppositely charged particles (electrons and ions). The presence of charged particles renders the plasma conductive. Plasmas generated under atmospheric

conditions are named as atmospheric pressure plasmas. The sources are categorized according to their operating frequencies into three groups: direct current (DC) and low frequency discharges, radio frequency (RF) discharge (13.56 MHz) and microwave (MW) discharge (2.45 GHz). Different types of sources with varied frequencies can be used to generate plasmas under atmospheric conditions. Frequency of the excitation source plays a crucial role since it strongly influences the characteristics of electrons and ions in the plasma. Plasmas generated using DC sources are less expensive but have been reported to be least efficient in material processing, surface cleaning and activation. It is easy to create glow discharge with an applied DC voltage and the plasma is sustained as a result of secondary electron emission upon impact at the cathode. But with increasing pressure, the discharge becomes unstable and confined within the electrodes, thus making the sustenance difficult. Comparatively, the RF and MW sources are more popular in plasma research because they generate more electrically charged species compared to low frequency sources. Plasmas generated using RF sources are reported to be more homogenous, a characteristic crucial for treating irregularly-shaped or 3D objects. Plasma ignited with MW sources are inhomogeneous compared to RF sources and are suited for soft materials as they generate low energy ions. A major disadvantage of MW sources which limits their application is the design requirements of microwave cavity.

Atmospheric pressure plasmas are mostly non-thermal in nature where the applied energy is primarily utilized to generate high energy electrons which have enough energy to ionize molecules and atoms creating excited species and free radicals. The energised electrons with temperatures of a few electron volts (eV) are capable of initiating chemical reactions and thus, non-thermal plasmas can enhance the efficiency of various physical and chemical processes related to material processing/manufacturing and most

importantly will have appreciable lower impact on the environment than conventional techniques.

Plasma has replaced conventional methods to develop various nanostructured materials with complex morphology and advanced properties, with the possibility for scaling up and fast, multi-scale production. Moreover, the benefit of plasma technology is wet-free doping of semiconducting nanomaterials with heteroatoms to tune the bandgap energy and conductivity for many promising applications. The two primary reasons for which plasmas have attracted interest are the associated high power and energy density and the presence of active species with sufficient energies to initiate reactions. Low-temperature, non-thermal plasmas are non-destructive in nature and find applications where the high temperature associated with thermal plasmas are undesirable and should be particularly avoided. In these plasmas, the high electron temperatures enhance the plasma chemistry processes which lead to generation of highly reactive species. Of late, the interest in atmospheric pressure plasmas in materials processing has surged since they do not require the high-maintenance, sophisticated vacuum equipment, can be easily incorporated into production lines, hence, reducing processing cost. APPJs with lower gas temperature are suitable for treating temperature-sensitive materials and are also found to be easily adapted to complex geometries and conventional processes. APPJs have evolved as a tool of significant practical importance because the plasma jets are not restricted to being within the dimensions of the electrodes. APPJs comprise charged particles, neutral metastable species, radicals and radiation in UV and visible region [88]. Non-thermal plasmas have proven their feasibility in a variety of applications such as sterilization [89,90], surface modification of polymers [91–93], environmental and industrial applications [94] and in medicine [95]. Polymeric molecules usually show poor adhesion to surfaces due to their low surface energies. Applications of plasma jets are not limited to the modification of polymer surfaces including surface activation for better

adherence [96–98], surface cleaning [99], surface wettability [100,101], and etching [102,103]. The applications of atmospheric pressure plasma for surface and bulk functionalization are summarized in Figure 1.8.

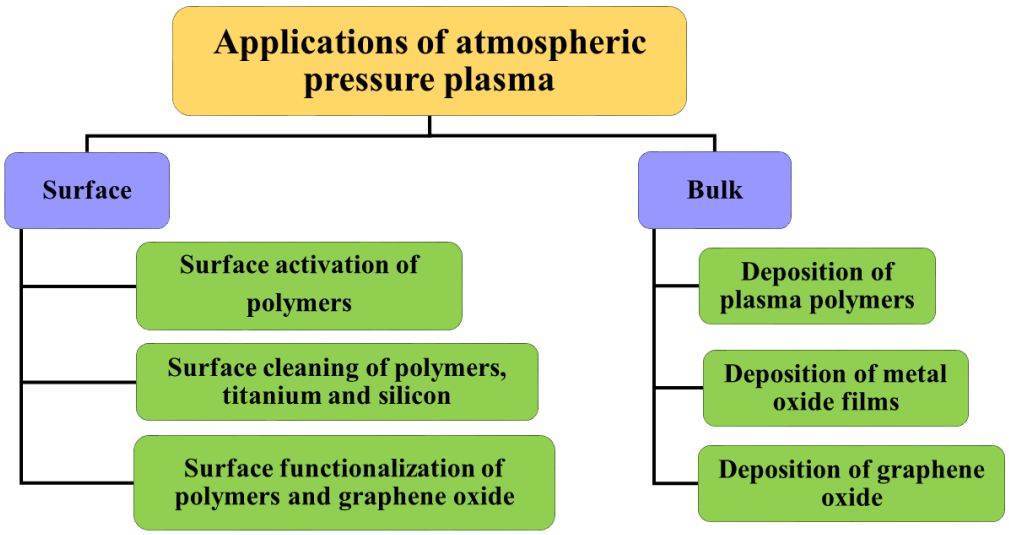

Figure 1.8 Applications of atmospheric pressure plasma in surface modification of polymers [96,103] and graphene oxide [104] and deposition of plasma polymers [105], metal oxides [106–108] and graphene oxide films [109].

Applications of plasma in PSCs

In the field of PSCs, the applications of plasma are limited to surface cleaning and removal of impurities from FTO/ITO substrates which result in improvement in photovoltaic performance [110,111]. Very recently the application of plasma in PSCs have been widened to encompass

(i) encapsulation with plasma polymers [112],

(ii) improvement in stability using submicron organosilicate barrier film by scalable cold plasma spray process [113],

(iii) argon plasma treatment to modify the surface composition of perovskite absorber by tuning the ratio of organic and inorganic components and defects [114],

(iv) a scalable atmospheric pressure plasma post-deposition technique to rapidly form efficient and mechanically robust $CH_3NH_3PbI_3$ perovskite layer without the need of a hot plate for curing the active material [115],

(v) oxygen plasma treatment on NiO_x layer as HTL for PSCs in p-i-n architecture was reported by Nishihara *et al* [116].

But mostly, all the processes rely on high vacuum low-pressure plasmas which involve high maintenance, vacuum-based systems. In this work, APPJ has been proposed as a benign, cost-effective and scalable technique for surface and bulk functionalization.

The two objectives of using APPJ in this thesis are as follows:

Objective 2(a): Plasma functionalization of spiro-OMeTAD with helium and oxygen plasma jet. The application of atmospheric pressure plasma generated using an RF source, for functionalizing films of spiro-OMeTAD and graphene oxide as hole transport materials in PSCs has been described in Chapter 4 and Chapter 5.

(b): Plasma jet printing-Deposition and *in situ* functionalization of spiro-OMeTAD with helium and oxygen plasma jet has been discussed in Chapter 6.

1.7 Graphene oxide as hole transport material in perovskite solar cells

Graphene is a sp^2 hybridized monolayer consisting of a two-dimensional honeycomb lattice. Incorporation of carbon-based nanostructures such as graphene [117,118], graphene oxide [119–126], reduced graphene oxide [127,128] and carbon nanotubes [76,129,130] have been undertaken to replace conventional HTMs and metallic counter electrodes in PSCs. The nanocarbons help to increase the area of contact between interfaces, thus aiding efficient charge accumulation and separation in PSCs. The electrical properties of GO have been reported to vary depending on the number of sp^2 (π states) and sp^3 (σ states) carbon sites with π states being conductive whereas σ states

have large band gap. Graphene/2D materials have excellent mechanical, electronic and optical properties and hence can be used in a wide variety of applications [117,118,131–134]. Graphene oxide has attracted attention due to its reliability, low-cost large-scale production capability and good dispersibility in many solvents [135–137]. GO consists of a two-dimensional carbon-carbon network decorated with various oxygen-containing functional groups in the form of carboxyl, carbonyl, phenol, lactone and quinone at the basal planes and sheet edges [138,139]. This structure favours modification of GO sheets by covalent functionalization[137]. The oxygen functionalities create structural inhomogeneities, including reduced electron mobility which make it suitable for retarding electron recombination in PSCs [140,141].

Seminal work by Wu *et al*. demonstrated graphene oxide as an alternative HTM in inverted planar heterojunction (PHJ) architecture reporting an efficiency in excess of 12% [119]. GO was used as hole conductor because of its suitable work function (~4.9 eV). The perovskite film grown on graphene oxide exhibited improved crystallization with large textured domains, high surface coverage and large-scale roughness which positively influenced the light harvesting capability due to enhanced light scattering. Li *et al*. designed PSCs with graphene oxide as an interfacial buffer layer between $CH_3NH_3PbI_3$ perovskite and spiro-OMeTAD HTL [120]. The GO layer was reported to have improved interfacial contact/wettability at the absorber/HTL junction by forming Pb-O bonds with the perovskite on the one hand, and π-π interaction with spiro-OMeTAD on the other side. Consequently, highly efficient PSCs with 14.5% PCE were reported. A composite formed with graphene oxide and PEDOT:PSS has been employed as HTL for PHJ PSCs exhibiting good device performance and stability [142] compared to devices based only on PEDOT:PSS [121–123,126]. The matched work function between GO (4.9 eV) and PEDOT: PSS (5.1 eV) was proposed to be the reason for better charge

transport and reduced series resistance. Moreover, it was reported that decomposition of the $CH_3NH_3PbI_3$ perovskite to PbI_2 was restricted upon using GO/PEDOT: PSS HTM which is possibly because GO prevents direct contact between ITO and the highly acidic PEDOT: PSS. In 2017, Yang *et al*. demonstrated that the work function and conductivity could be tuned by controlling the thickness of solution-processed GO [125]. The GO layer with optimised thickness was then employed as HTL in PSC to yield PCE of 16.5%. The devices reported encouraging stability by retaining >80% of initial PCE after 2000 h operation. The higher work function of GO (5.2 eV) and larger perovskite crystals were thought to be responsible for proper alignment of interfacial energy level between HTL (GO) and $CH_3NH_3PbI_3$ perovskite (Work function = 5.4 eV). Besides, comparison of steady-state photoluminescence (PL) and transient photocurrent studies for GO-based and PEDOT: PSS-based devices showed better hole extraction ability of the GO/perovskite interface compared to PEDOT: PSS/perovskite interface.

Objective 3: Tuning the work function of graphene oxide using APPJ

Work function is defined as the energy difference between the Fermi level and the vacuum level. The work function of the charge transport layers and electrodes is of paramount importance for the choice of material in solar cells. The high degree of oxygen content on graphene oxide sheets results in high work function but corresponds to lower conductivity which limit their application as HTL [143]. Balancing work function and conductivity is a pre-requisite for achieving optimal photovoltaic performance. The ability of graphene oxide to be the ideal candidate for electrodes [132] and HTL [144] stems from the fact that its work function can be tuned from 4.35 (n-type) to 5.28 (p-type) [125,145]. Theoretical studies have shown that doping GO with substitutional impurities result in tuning of work function and electronic properties [146–148]. Thus, tuning the

bandgap shows immense prospect for widespread applications in semiconductor devices [149], sensors [150], batteries [151], ultracapacitors [152] and solar cells [119–126,153].

Various strategies of plasma-assisted doping protocol have been adopted, of which APPJ presents a rapid and non-invasive technique for functionalizing graphene oxide. Plasma doping of GO is an energy-saving and wet-free alternative to the conventional chemical processes which mostly rely on toxic reducing agents [127,128,154–156].

Nitrogen plasma: Nitrogen, with its comparable atomic radii and five valence electrons, is the most appropriate candidate for doping GO. Doping with nitrogen results in different bonding configurations in the graphene lattice which results in distortion of the π electron density and variation in the hybridization of orbitals [157]. This influences the charge distribution around the carbon atom in the lattice and helps in tuning the charge transport properties. Akada *et al*. reported tuning the work function of graphene by doping with nitrogen plasma [158]. The work function of graphene showed strong dependence on the doping configuration and amount of doped nitrogen with graphitic N lowering the work function unlike pyridinic or pyrollic N. The work function was tuned from 4.3 eV to 5.4 eV by controlling the plasma treatment time and amount of initial defects in graphene sheets which shows promise for numerous industrial applications. Zeng *et al*. reported work function variation from 4.91 to 4.37 eV using nitrogen plasma for applications in electronic and optoelectronic devices [159].

Hydrogen plasma: Reduced graphene oxide is a promising material for widespread application as an alternative to graphene. RGO possesses inherent passivation ability against oxygen and moisture, which decreases the recombination probability between interfaces and makes it suitable as hole conductor in PSCs. Several chemically-driven reduction processes have been designed to lower oxygen content in GO which provide encouraging results [127,128,154,160]. But chemical reduction protocols complicate device fabrication and are mostly toxic [127,128,154–156], making them ill-suited for scalable

production. Research has been focussed on the influence of hydrogen plasma on graphene oxide for different applications ranging from flexible conductors and gas sensors [161] to electrodes [162] in solar cells [163] and supercapacitors. However, most of the reported works were undertaken in low-pressure conditions which entails high-maintenance vacuum equipment and are incompatible with fast, inline, roll-to-roll processes for large-scale fabrication of flexible electronics or high temperature conditions which are unsuitable for flexible substrates. Since, reduction by hydrogen plasma has not been extensively studied compared to other reduction techniques such as chemical and thermal reduction processes, many points to investigate include reduction mechanism and optoelectronic properties of reduced graphene oxide. By controlling the plasma parameters and exposure time, tailored structures of graphene oxide can be achieved.

Oxygen plasma: Oxygen plasma presents a benign and feasible technique for p-type doping of graphene oxide. Oxygen plasma treatment has been reported for band gap opening of graphene [164], electrochemical actuator [165], surface functionalization and cleaning [166], molecular sensing [167] and patterning transparent graphene electrodes on large-scale flexible substrates [168]. But the reports are either based on low-pressure or high-power plasma based systems which have limitations for large-scale cost-effective applications.

Extensive research has been undertaken regarding functionalization of graphene oxide but are mostly based on low-pressure conditions with expensive vacuum-based equipment and are incompatible with in-line processing (summarized in Table 1.1). However, a systematic report on time-dependent controlled doping of graphene oxide is lacking. Atmospheric pressure oxygen plasma jet presents a low-cost alternative with the ability to tailor the properties of GO. Chapter 5 explores a systematic treatment and functionalization of graphene oxide using different admixtures of nitrogen, hydrogen

and oxygen using an atmospheric pressure plasma microjet. A thorough investigation of the electronic structure and work function of plasma-functionalized GO has been undertaken using X-ray spectroscopy.

Table 1.1 Overview of recent progress in plasma doping of graphene and graphene oxide.

Plasma parameters				Characteristic changes	Applications	Ref
Element/ species	**Source**	**Time**	**Generation parameters**			
Hydrogen (H_2) and NH_3 plasma	Microwave generator	1 hr	500 W, 50 sccm each of H_2 and NH_3 at 1 Torr	Simultaneous reduction and nitrogen doping of GO	Electrochemical energy devices and oxygen reduction reaction	[169]
Nitrogen plasma	RF power		10 W, N_2 gas flow rate 0.2 sccm, N_2 gas pressure 0.1 Pa	Tuning the work function from 4.3 to 5.4 eV	Industrial applications	[158]
N_2 plasma	RF power	5 mins	70 W, Base pressure $2.4x10^{-4}$ Pa, working pressure 0.7 Pa	Work function tuned from 4.91 to 4.37 eV	Electronics	[159]
N_2 plasma	DC plasma chamber	20, 40 secs	300 – 350 V bias, 460 Pa	Increase in number of active sites post plasma treatment	Counter electrodes in bifacial DSSCs	[153]
N_2 plasma	RF plasma	Varied	100 – 300 W, base pressure 10^{-3} mbar, working pressure 0.15-0.3 mbar, flow rate up to 100 sccm	Functionalization for GO by nitrogen		[170]
N_2 plasma	APPJ	1-30 secs	15 kV, 25 kHz	Tuning of hydrophobic to hydrophilic character, N doping with less structural damage	Electronics	[171]

Argon and H_2 plasma	High voltage DC	30 mins	2 kV	Deoxygenation and reduction of GO	Deposition on PET substrates to obtain highly conductive films	[172]
H_2 plasma	RF power	20 and 40 secs	10 W, 13.56 MHz, 50 sccm (set 1) and 20 sccm (Set 2)	Removal of oxygen moieties and reduction of GO	Carbon dioxide sensor	[161]
H_2 plasma	Microwave discharge	30 secs	1 kW, 2.45 GHz and chamber pressure 1 mbar.	Formation of highly hydrogenated graphene	Electrochemical transducers, electrodes, batteries, supercapacitors and sensors	[173]
H_2/Ar plasma	RF power	5 mins	Varied between 20 and 100 W, chamber pressure 10^{-3} Pa	Reduction of GO	Electrodes	[162]
H_2 plasma	Dense coplanar DBD	8 and 16 secs	Power density 70 W cm^{-3}	Hydrogenation and reduction of graphene oxide with improved conductivity	Electrodes, flexible electronics	[174]
H_2 plasma	RF power			Treatment and reduction of GO	Sterilization against bacteria	[175]
Helium and H_2 plasma	High voltage AC			Removal of oxygen functional groups and reaction intermediates in GO	Plasma jet printing and *in situ* reduction of GO	[109]
Oxygen plasma	Parallel plate RF plasma	3 secs	15 W, chamber pressure 20 mTorr	Tuning of the bandgap and transition from semimetallic to semiconducting	Electronics	[164]

O_2 plasma	RF power generator	10 secs	200 W, chamber pressure of 100 Pa with hexane or O_2 flow	Increased response towards electrochemical activity	Electrochemical actuator	[165]
O_2 plasma	Microwave plasma	2 mins	1000 W, 1 Torr, 1000 sccm O_2	Cleaning of polymer residue	Electronics	[166]
O_2 plasma	Parallel plate RF plasma	5 secs - 2 mins	2-5 W, 0.15 mbar chamber pressure	Enhanced Raman intensity of adsorbed Rhodamine B molecules, downward shift of Fermi level	Molecular sensing	[167]
O_2 plasma	Capacitively coupled plasma	1-5 mins	25-200 W, 120 mTorr chamber pressure	Patterning	Transparent flexible electrodes	[168]

1.8 Research methodology

Schematic representation of the research methodology adopted in this thesis is as shown in Figure 1.9.

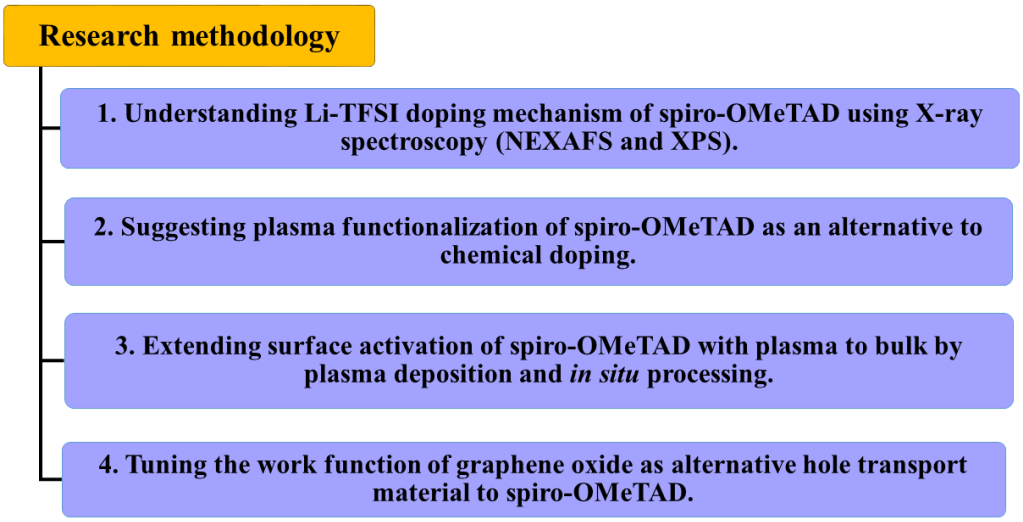

Figure 1.9 Schematic representation of the research methodology adopted in this thesis.

1.9 Soft X-ray spectroscopy for surface analysis

X-rays typically with energy in the range 0-1500 eV are termed as soft X-rays. This energy is sufficient for spectroscopic investigation of most of the elements in the periodic table. Soft X-ray spectroscopy provides a finger print of the chemical bonds and nearest neighbour interaction in molecules. Soft-ray spectroscopy techniques involve the excitation of the electrons in an element using X-ray photons and monitoring their decay process occurring either via radiative or non-radiative processes. X-ray photons can excite a core level electron to an unoccupied bound state or eject it into the continuum. The first process forms the basis of X-ray absorption spectroscopy (XAS) while the latter is probed in XPS. A schematic representation is shown in Figure 1.10. Thus, XPS probes the total density of states whereas XAS probes the partial density of states.

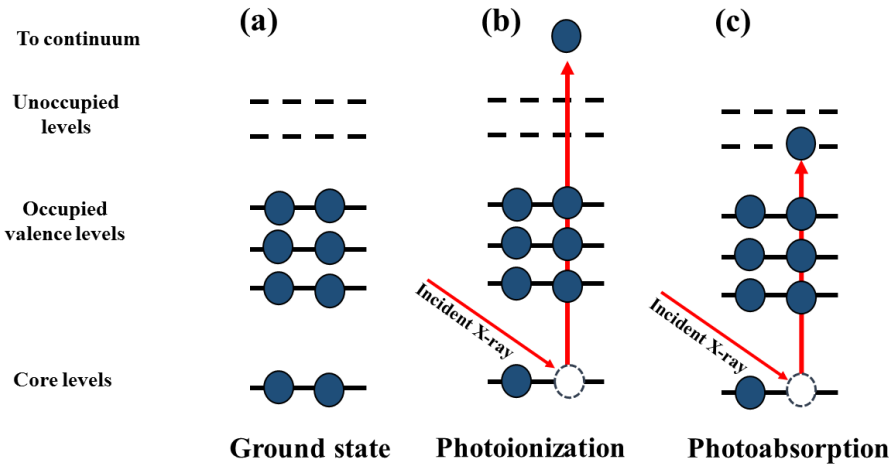

Figure 1.10 Schematic representation of soft X-ray induced excitation process (a) ground state electronic configuration, (b) photoionization (XPS) where the incident photon excites the core electron to continuum and (c) photoabsorption (XAS) when a core electron is excited to the unoccupied density of states of the conduction band.

Soft X-ray spectroscopy has emerged as a powerful technique to study the surface and interfacial properties of materials. Both XAS and XPS are highly element-specific and site-selective techniques and help in probing the subtle variation in local chemical environment due to nearest neighbour interaction. Due to the selection rules involved, chemically non-equivalent sites of the same atomic species can be resolved in NEXAFS spectroscopy, unlike XPS. C1*s* XPS spectra of pristine and Li-TFSI doped spiro-OMeTAD have same line shape with overlapped features (Figure 1.11 a), whereas the carbon *K*-edge NEXAFS spectra for the samples show variation in the features (Figure 1.11 b). Resonance features in NEXAFS spectra arise from the variation in chemical environment of carbon. In this thesis, soft X-ray spectroscopy has been used to analyse the electronic and structural properties of Li-TFSI-doped spiro-OMeTAD, SFX-OMeTAD and SFX-TAD (Chapter 3), plasma-functionalized spiro-OMeTAD (Chapter 4) and graphene oxide (Chapter 5) and plasma-deposited spiro-OMeTAD (Chapter 6)

for applications as hole conductors. The basic principles of XPS and XAS are described in details in Chapter 2.

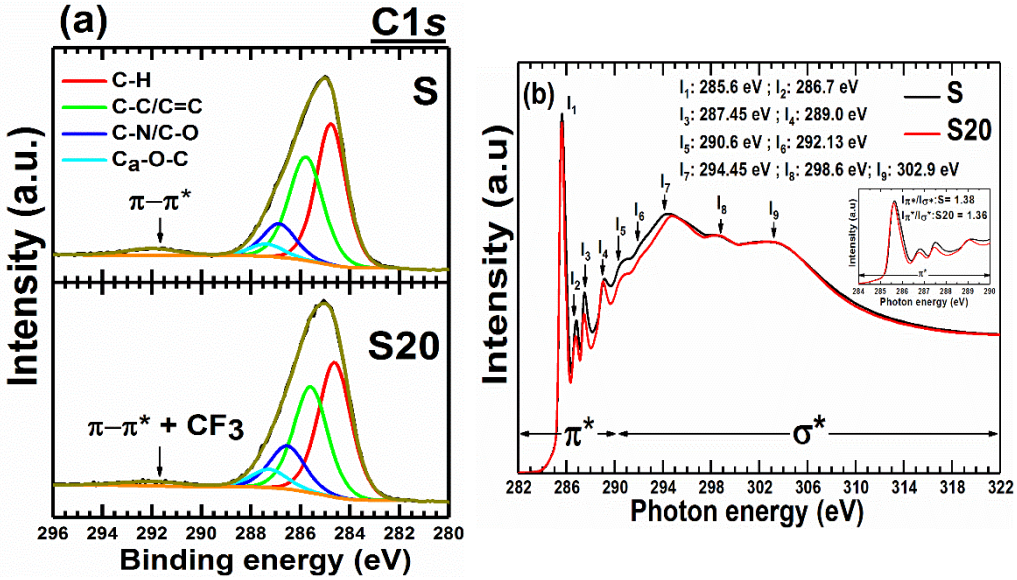

Figure 1.11 Comparison spectra of pristine (S) and 20% Li-TFSI doped spiro-OMeTAD (S20) (a) C1*s* XPS and (b) C *K*-edge XAS. Inset of (b) shows the first resonance at absorption edge along with $\frac{I_{\pi*}}{I_{\sigma*}}$ratio.

1.10 Thesis summary

This thesis contributes towards understanding and addressing the key challenges in hole transport materials. There is limited understanding regarding the overall story of surface and interfacial properties of HTMs which are crucial for deeper insight into the photophysics involved. In this thesis different hole transport materials have been studied, namely, spiro-OMeTAD, SFX-OMeTAD, SFX-TAD and graphene oxide. This thesis aims to develop atmospheric pressure plasma jet-based functionalization technique as environmentally friendly and cost-effective alternative to conventional chemical routes. This thesis is based on getting a deeper understanding of the variation in electronic and optical properties of HTMs after plasma functionalization. The understanding has then

been extended to bulk functionalization in the form of deposition and *in situ* processing of spiro-OMeTAD. Characterization techniques such as X-ray spectroscopy (NEXAFS and XPS), UPS, EFM, KPFM, sheet resistivity, SEM and optical microscopy has been used for understanding the variation in electronic properties, conductivity and morphology of different HTMs. Basic working principles of the different characterization techniques employed in this thesis have been described in Chapter 2.

In summary all the challenges are represented schematically in Figure 1.12.

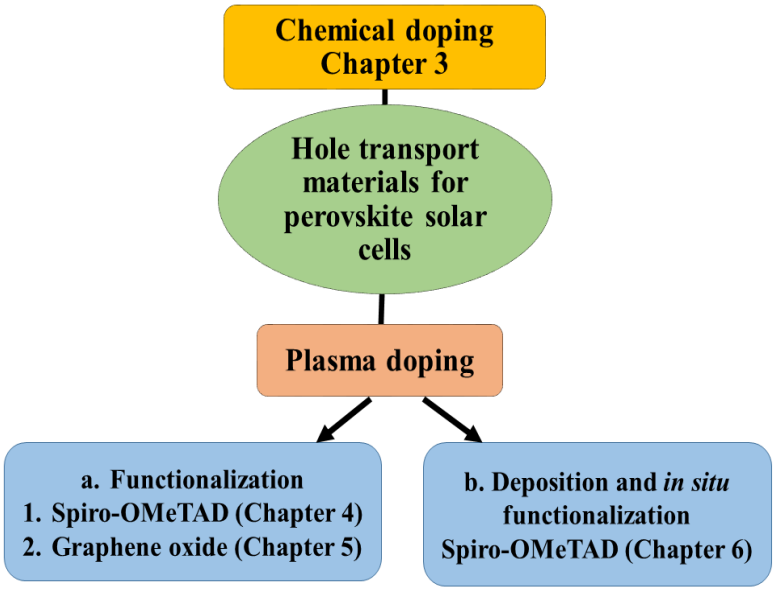

Figure 1.12 Schematic representation of the structure of this thesis.

Chapter 2

Experimental techniques

This chapter will give an overview of synthesis, functionalization using plasma and different characterization techniques to understand the properties of materials for hole transport applications in perovskite solar cells. This chapter also describes the in-house set up of atmospheric pressure plasma for functionalization and plasma jet deposition and in situ processing. Surface-sensitive techniques such as XPS, UPS and X-ray absorption spectroscopy (XAS) were extensively used to understand the electronic properties of materials. Electrical properties were studied using Electrostatic force microscopy (EFM), Kelvin probe force microscopy (KPFM) and four-point probe method.

2.1 Experimental methods

2.1.1 Deposition of hole transport materials

Spiro-OMeTAD: The primary hole transport material used in this work is the organic small molecule spiro-OMeTAD. Thin films of spiro-OMeTAD were deposited following the usual procedure as reported elsewhere in literature without Li-TFSI and tBP [66,176]. In brief, 72 mg spiro-OMeTAD was dissolved in 1 mL chlorobenzene. 100 μL of the solution was spin coated onto silicon substrates at 2000 rpm for 30 secs. Prior to the deposition of thin films, the silicon wafers of dimensions 1.5 cm x 1.5 cm were cleaned thoroughly by sequential ultrasonication in acetone, deionized water and ethanol for 10 minutes each.

Two SFX core-based hole conductor molecules are introduced in Chapter 3. For synthesis of doped HTMs, Li-TFSI dopant and tBP (10 μL) additive were dissolved in 10 and 20 mol. % in acetonitrile, (all concentrations in mol% were calculated relative to spiro-OMeTAD; mole % is the percentage of moles of a particular component relative to the total number of moles in the mixture). 100 μL of the solution was spin coated at 2000 rpm for 30 secs for preparation of thin films [12]. The project was undertaken in collaboration with the University of Edinburgh.

Graphene oxide: Graphene oxide was synthesized in the laboratory using modified Hummer's method. The technique is as follows: To produce a certain quantity of GO, 0.003 kg of powdered natural graphite flakes and 0.0015 kg of sodium nitrate is stirred together into 0.1 L 98% sulphuric acid (H_2SO_4). The reactants are mixed in a 1 L beaker that has been cooled to 0ºC in an ice bath as a precautionary measure. The suspension is continuously stirred and to it 0.009 kg of potassium permanganate ($KMnO_4$) is added slowly. The rate of addition of $KMnO_4$ is controlled carefully to prevent the temperature of the suspension from exceeding 20ºC. The ice bath is then removed, and the temperature of the suspension brought to around 27 ± 3 ºC. The temperature was maintained for 30 minutes with constant stirring. With the progress of the reaction, the mixture is found to thicken gradually with diminishing effervescence. After 30 minutes, the mixture is found to have turned into a thick brownish grey slurry with the evolution of only a small amount of gas. After 30 minutes, 0.138 L of distilled water is added slowly into the paste accompanied by continuous stirring. Violent effervescence and a sudden increase in temperature to 98 ºC is observed. The diluted brown colour suspension is maintained at this temperature for 15 minutes. The suspension is then further diluted with approximately 0.02 L of warm distilled water and treated with 30% hydrogen peroxide (H_2O_2) to oxidise the residual permanganate and manganese dioxide to colourless soluble manganese sulphate. The suspension turns golden brownish on treatment with peroxide. The suspension is allowed to settle overnight. The supernatant solution is discarded carefully so as not to disturb the GO settled at the bottom of the beaker. The GO solution is then washed thoroughly for several times till the pH of the solution becomes ~7. The supernatant solution is taken in a beaker and centrifuged at 8000 RPM for 10 minutes to extract GO. The GO paste is dried in a vacuum oven overnight (temperature 80° C), ground and stored in a desiccator.

The thin films of spiro-OMeTAD, SFX-OMeTAD and SFX-TAD samples studied in Chapter 3 were deposited in the University of Edinburgh by Prof Neil Robertson and Dr Aruna Ivaturi. The sheet resistance measurements of the plasma-functionalized and plasma-deposited spiro-OMeTAD thin films were undertaken by Dr Debabrata Bhattacharya at the University of Cranfield. The UPS measurements of the plasma-functionalized and plasma-deposited spiro-OMeTAD thin films were undertaken by Dr Sanjay Sathasivam at University College London. All NEXAFS measurements (sample loading and characterization) was undertaken at SLAC during a beam time extending over 5 days were carried out by myself including the XPS measurements at the Open University. All other samples studied in this thesis, plasma-functionalized, plasma-deposited spiro-OMeTAD and plasma-functionalized graphene oxide, were fabricated at The Open University by me. All the results from different characterization techniques undertaken in the thesis, were analysed by me.

2.1.2 Atmospheric pressure plasma jet (APPJ) for surface functionalization

The in-house atmospheric pressure plasma jet used for functionalization of the spiro-OMeTAD films is as shown in Figure 2.1. The plasma discharge is ignited by applying radio frequency power through a series LC circuit between two stainless steel electrodes covered with quartz which function as a dielectric barrier discharge. The frequency used to drive the LC circuit has been chosen to be 13.56 MHz. The LC circuit consists of a tunable capacitor (C_{ext} = 2-22 pF) and an inductor (L = 16.5 μH, Micrometals T68-6 core) [177]. When the applied frequency matches that of the LC circuit, the voltage drop across the electrodes gets amplified (resonance) to initiate a plasma discharge. At resonance, the voltage between the electrodes is measured to be 100 times that of the input voltage. In practise, when the plasma is ignited, the discharge gap also needs to be considered and added to the series LC circuit and has been optimised in the

set-up. To account for any shift in the resonance frequency, the drive frequency of the signal generator is tuned accordingly to achieve the desired resonance.

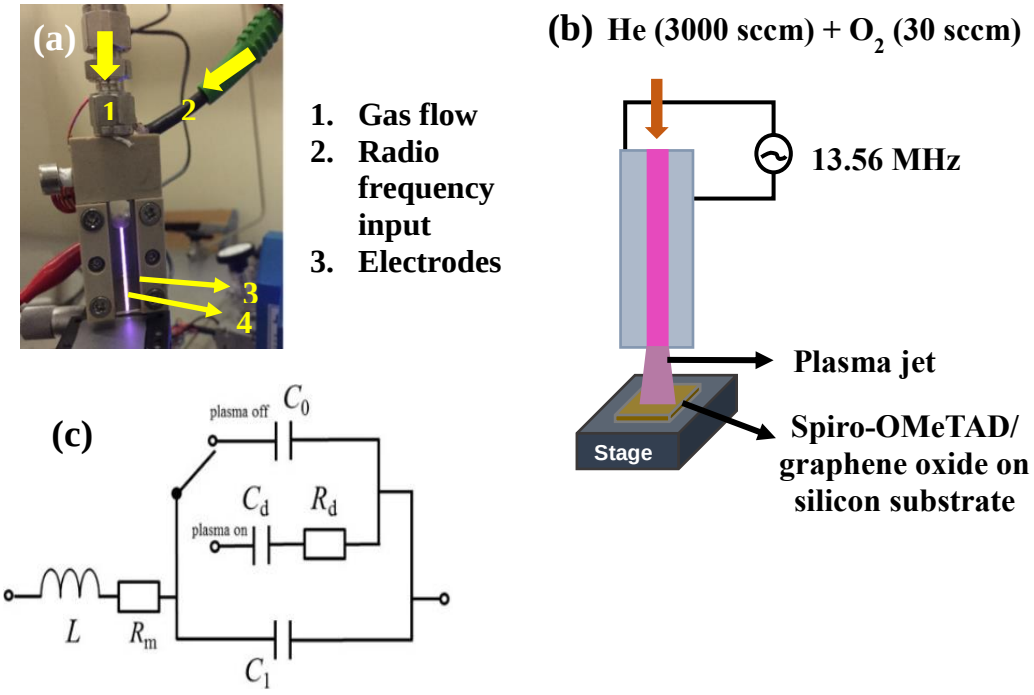

Figure 2.1 The picture of in-house atmospheric pressure plasma jet, (b) Schematic of the He/O_2 plasma jet and (c) the LC circuit with plasma ON condition.

2.1.3 Plasma jet deposition and *in situ* processing of spiro-OMeTAD

Basic principle of Dielectric barrier discharge atmospheric pressure plasma jets

A wide spectrum of plasma sources can operate at atmospheric pressure. Plasma excitation can be classified into different regimes depending on the source of plasma generator as RF excited plasma discharges, microwave excited discharges, low frequency AC discharges and DC discharges.

Dielectric barrier discharge (DBD): Dielectric barrier discharge systems consist of two electrodes, which are separated by a gap of a few millimetres with at least one of the two electrodes being covered by a dielectric material. Preferred materials for the dielectric barrier are glass, ceramic or thin polymer layers. The electrical parameters for DBDs operated at atmospheric pressure depend on the discharge geometry, but ignition

voltages are typically a few kilovolts and driving frequencies are in the range of tens of hertz to a few hundred kilohertz. The dielectric barrier is intended to restrict and rapidly terminate the arcs that form in the potential field between the two electrodes. This is achieved by accumulating the charge that suppresses the electric field in the gap until the voltage reverses, whereby the charge enhances the field, reigniting the discharge. In DBD configuration the generated plasma is predominantly non-thermal in nature. Due to the high pressure, there are no high-energy ions (>1 eV), so this plasma is extremely useful for surface treatment and functionalization as it does not cause substrate sputtering.

This section briefly discusses the mechanism behind generation of a dielectric barrier discharge, mainly focussing on the phenomenon of plasma generation. When a sufficiently high voltage is applied between two metal electrodes at atmospheric pressure, a highly conductive plasma channel will be formed rapidly. This spark-like discharge, sometimes called a single filament, may turn into an arc discharge as a result of significant heating of the electrodes leading to thermionic emission. Adopting a dielectric barrier discharge configuration is a plausible solution to prevent undesirable arcing. DBD designs can have a single bare metal electrode while others have dielectrics covering both electrode surfaces. The dielectric barrier can be made from glass, quartz, ceramic or other materials of low dielectric loss and high breakdown strength. If, however, one of the electrodes is covered with a dielectric material, the single filament plasma channel may soon extinguish leading to the formation of multiples of plasma channels in the discharge gap. This phenomenon is known as dielectric barrier discharge. During the first cycle of operation of the discharge, charge is accumulated on the dielectric surface in front of the metal electrode. This accumulated charge induces an electric field opposite in direction to the external field, thereby reducing the electric field in the discharge gap, unless the current flow diminishes and extinguishes eventually.

This process takes place in nanoseconds [178]. In order to have a sustained discharge of plasma, the polarity of the external field needs to be altered continuously, such that the direction of applied electric field changes, and the charge accumulated on the dielectric surface is pushed back to the discharge gap. During the second cycle of operation, when the polarity of the external field is reversed, charge that had accumulated on the dielectric surface will be deposited on the opposite electrode. If this electrode is also covered with dielectric material, the charge will accumulate on the surface while for the case of uncovered electrode, the charge will be conducted away. The generated plasma is predominantly non-thermal in nature and is extremely useful for surface treatment and functionalization without causing unwanted surface abrasion or sputtering. The current-voltage characteristics of DBD depend on its operating conditions, including frequency, gas type, electrode gap and applied voltage. Depending on these conditions, dielectric barrier discharges can operate in two linked regimes-the filamentary mode and the glow mode.

Construction of the DBD atmospheric pressure plasma jet

The dielectric barrier APPJ used for printing in this thesis was commissioned at the Open University. It consists of a dielectric tube having concentric nozzles with two ring electrodes located on the outside surface of the tube. The tube with concentric nozzles is made of Pyrex glass with a tapering end to form a convergent plasma jet. The broad end of the nozzle has an outer diameter of 15 mm whereas the tapering end is 6.2 mm. Brass was used as the electrode material due to its electrical and thermal properties and the electrodes were covered with Teflon for insulation. Substrates were attached to a unidirectional translational stage to bring about simultaneous deposition and translation over larger areas. This method shows great promise for scaling up of the technology if multiple and broader dimension nozzles can be used for deposition. The

high voltage (HV) transformer was connected to the electrodes with a matching box for reliable electrical coupling. High voltage wires were used to connect the electrodes to the matching box, and a HV coaxial cable was used to connect the matching box to the transformer. The flow of helium and oxygen gas through the dielectric nozzle was controlled by calibrated mass flow controllers from Alicat. Helium was used as the carrier gas and oxygen was used to generate additional excited species in the plasma jet. The purity of helium and oxygen gases used was 99.999%.

Power supply unit: The power supply unit used to generate the discharge consisted of an Agilent pulse generator connected to a low frequency high voltage amplifier, which was in turn connected to a HV transformer. The low frequency HV amplifier was a model BK MF1000 made by BK electronics, and could amplify signals in the range 1-100 kHz. The upper limit of the HV amplifier-HV transformer was only 10 kHz due to the homebuilt HV transformer.

The primary parameters of the homebuilt HV transformer are

i. Specific frequency - 10 kHz, with working range 5 -15 kHz
ii. Maximum input voltage - 42 V rms
iii. Maximum output voltage - 7.5 kV rms

The transformer was placed into a suitable box and the power cables were connected to the sides of the box.

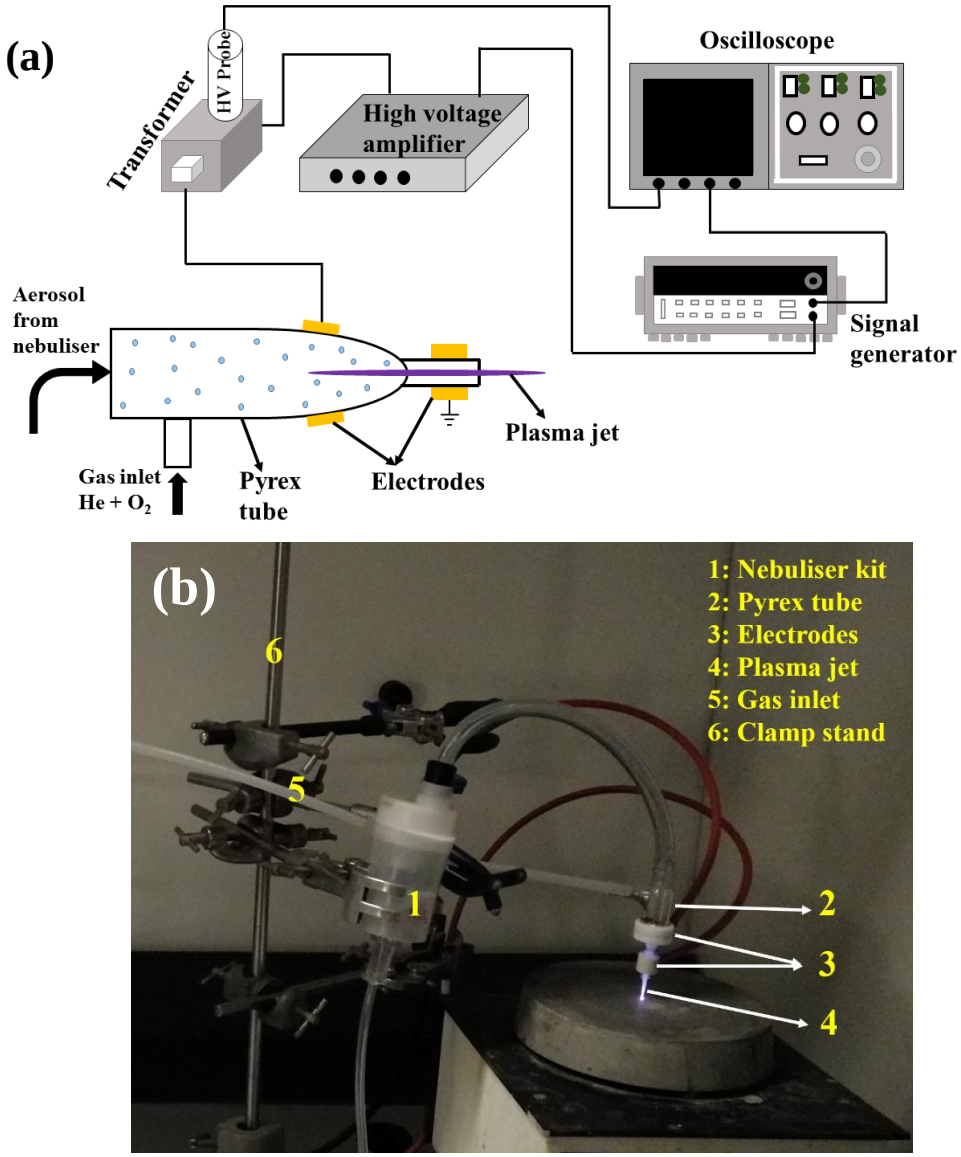

Figure 2.2 (a) Schematic of the plasma jet used. The experimental set up for plasma jet printing system comprises (1) nebuliser kit, (2) Pyrex glass nozzle, (3) circular electrodes, (5) inlet for the gas and (6) clamp stand for holding the components in place and (b) the plasma jet in operation. The spiro-OMeTAD solution was aerosolized using a commercial nebuliser and carried through to the plasma by compressed air. A mixture of He or He + O_2 gas was fed though other inlet to ignite the plasma jet.

Schematic of the complete experimental arrangement for deposition of spiro-OMeTAD and (b) the plasma jet in operation, are presented in Figure 2.2. The plasma

jet was mounted stably with electrical and gas connections. The ring electrodes around the dielectric tube were powered by a radio frequency power supply system, consisting of a pulse generator connected to a low-frequency high-voltage amplifier with an external home-built high-voltage transformer. In this plasma jet apparatus, helium and helium + oxygen plasma is generated inside the tube in the region between the electrodes when a 10 kV voltage signal (peak to peak) in the frequency range of 1-8 kHz is applied. In addition to the discharge inside the tube, a transient plasma jet is also observed outside the tube when the front electrode is active and the rear one is grounded. The size of the jet varies according to the discharge conditions and usually consists of rapidly propagating plasma 'blob' or 'bullet' [179]. The plasma jet was used to deposit spiro-OMeTAD films using chlorobenzene and DMF as solvents and is described in Chapter 6.

2.2 Characterization techniques

2.2.1 X-ray photoelectron spectroscopy (XPS)

Lab-based X-ray sources

The primary source of radiation in laboratory-based X-ray instruments are the X-ray tubes. In an X-ray tube, electrons are generated by thermionic emission upon applying a high voltage to a filament or cathode. These rapidly accelerated electrons are focussed onto a metal target known as the anode. On collision with the anode, the electrons undergo deceleration, thus giving rise to a continuous source of X-rays or *bremsstrahlung*. The incident photons, having sufficiently high energy are capable of ionizing atoms by knocking off electrons from their inner shell, a phenomenon known as photoelectric effect. A free electron from a valence shell may fill up the vacant position radiatively, thus giving rise to an X-ray photon feature on top of the continuous

spectrum of radiation e.g. Mg K_α or Al K_α. The K_α is the most intense radiation associated with these elements and correspond to $2p \rightarrow 1s$ transitions.

X-ray photoelectron spectroscopy is based on Einstein's photoelectric effect. In a typical photo-ionization process, a sample is irradiated with a flux of photons and the emitted photoelectrons are monitored. Considering the principle of conservation of energy, the energy of the emitted electron in a photo-ionization process can be presented as $E_i^n + h\nu - E_f^{n-1} = E_k$ …….2.1

Where $E_i^n \; and \; E_f^{n-1}$ are the energies of the initial and final states of the system with n and n-1 electrons, respectively, and E_k is the kinetic energy of the emitted photoelectron from the Fermi level of the system. According to Koopman's theorem [180], the binding energy of the photoelectron can be expressed in terms of these initial and final state configurations, as

$E_i^n - E_f^{n-1} = E_B$ …….2.2

Where E_B is the binding energy of the emitted photoelectron. Thus, for the photon energy, $h\nu$, the binding energy of the photoelectron can be represented as

$E_B = h\nu - E_k$ ……..2.3

Figure 2.3 represents the fundamental principle of the photoemission process. The spectrometer counts the number of electrons as a function of kinetic energy or binding energy and an experimental spectrum is obtained. Electrons with binding energy, E_B, can be excited above the vacuum level, E_{vac}, by photons with energy $h\nu > E_B + \Phi_0$, where Φ_0 is the work function of the material under consideration [181]. The photoelectron distribution I (E_{kin}) can be measured by the analyser and is in essence an image of the occupied density of electronic states N (E_B) in the sample. While passing through to the

vacuum level, the core electrons lose energy via inelastic scattering, which gives rise to the secondary electron background.

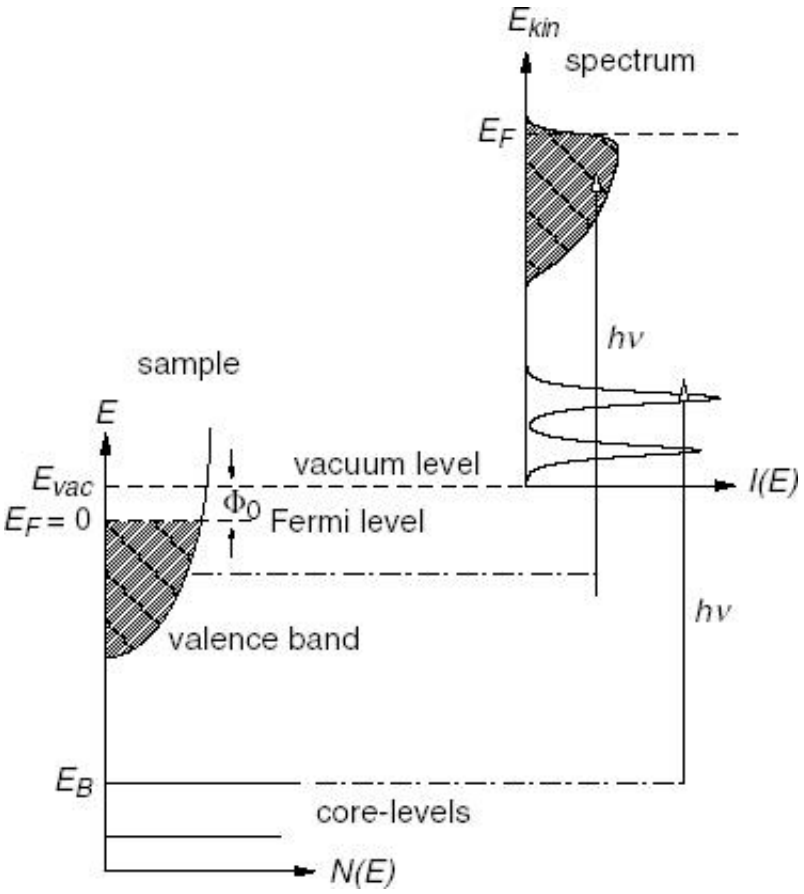

Figure 2.3 Schematic of the photoemission process in the single-particle picture [181].

During the photoemission process, the photocurrent can be calculated from the first order perturbation theory and Fermi's golden rule. The photocurrent, J, results from the excitation of electron from the ground state $|\psi_i>$ to the final state $|\psi_f>$ by the incident photon flux. Considering H_0 as the ground state Hamiltonian of the solid, which gets perturbed by the electromagnetic field E

$$H_0 = \frac{p^2}{2m_e} + eV(r) \qquad \text{.....2.4}$$

where p is the momentum operator given by$-i\hbar\nabla$. The electromagnetic field, E, transforms the momentum operator p to $p - eE/c$. Thus, the perturbed Hamiltonian can be written as

$$H = \frac{1}{2m_e}[p - eE/c]^2 + eV(r) \quad \text{.....2.5}$$

$$= \frac{p^2}{2m_e} + \frac{e}{2m_e c}(E.p + p.E) + \frac{e^2}{2m_e c^2} E^2 + e\,V(r) \quad \text{.....2.6}$$

$$= H_0 + H_{PE} \quad \text{.....2.7}$$

where $H_{PE}$is the perturbation operator.

$$H_{PE} = \frac{e}{2m_e c}(E.p + p.E) + \frac{e^2}{2m_e c^2} E^2 \quad \text{.....2.8}$$

For low photon intensities, the quadratic term in E can be neglected and the perturbation operator written as

$$H_{PE} = \frac{e}{m_e c} E.p \quad \text{.....2.9}$$

Considering the perturbation operator, the photoelectron current density can be written as $J(h\nu) = \frac{2\pi}{\hbar}\Sigma_s| < \psi_i|E.p|\psi_f > |^2 \delta(\epsilon_f - \epsilon_i - h\nu)$ 2.10

In the dipole approximation, the perturbation operator can be written as

$$H_{PE} = E.D \quad \text{.....2.11}$$

Where D is the dipole moment.

XPS is a highly surface-sensitive versatile surface analysis technique used to gain insight into the electronic state, chemical state and atomic concentrations of elements. For a multielectron system, the electronic states are generally classified as core level states and valence states where core level electrons are tightly bound to the nucleus and hence possess higher binding energies while valence electrons have low binding energies. Valence electrons actively take part in chemical bond formation unlike the core electrons. Even though core electrons are not involved in chemical bonding they are highly sensitive to the local chemical environment i.e. neighbouring atoms, molecules or surfaces.

Chemical shifts: The binding energy of a core electron is the work needed to remove the inner shell electron and is affected by any changes in the potential of the valence

shell. The binding energy of a core electron can be presented in terms of charge potential model as $E_i = E_i^0 + kq_i + V_i$ where $V_i = \Sigma_{j \neq i} \frac{q_i}{r_{ij}}$ …….2.12

Here E_i is the binding energy of a core electron, E_i^0 is the energy reference, q_i is the charge of an atom with the concerned core electron, k is a constant and V_i is the total electrostatic potential felt by this atom due to the surrounding atoms. Changes in the valence electron cloud will lead to redistribution of the surface charge as well as potential felt by the core electron. Hence, from equation 2.12, the shift in binding energy due to a change in valence electron can be expressed as

$$\Delta E_i = k\Delta q_i + \Delta V_i \quad \text{……..2.13}$$

Formation of a chemical bond involving the valence electrons leads to perturbation of the electron density in an atom resulting in a change in the core level binding energies (chemical shifts) as mentioned in equation 2.13. These shifts are of the order of a few eV, ranging from ~1-10 eV. Bonds formed between heterogeneous atoms (one having higher electronegativity compared to the other), shifts the electron density towards the higher electronegative atom, thus, resulting in higher binding energy features. Hence, chemical shifts can be used as a fingerprint to identify an atom in a molecule or the local chemical environment. Figure 2.4 represents an example of the aforementioned chemical shift in the C1*s* core level spectra of graphene oxide. Here the binding energy of carbon has shifted to higher binding energy values due to the presence of the highly electronegative oxygen atom bonded to carbon.

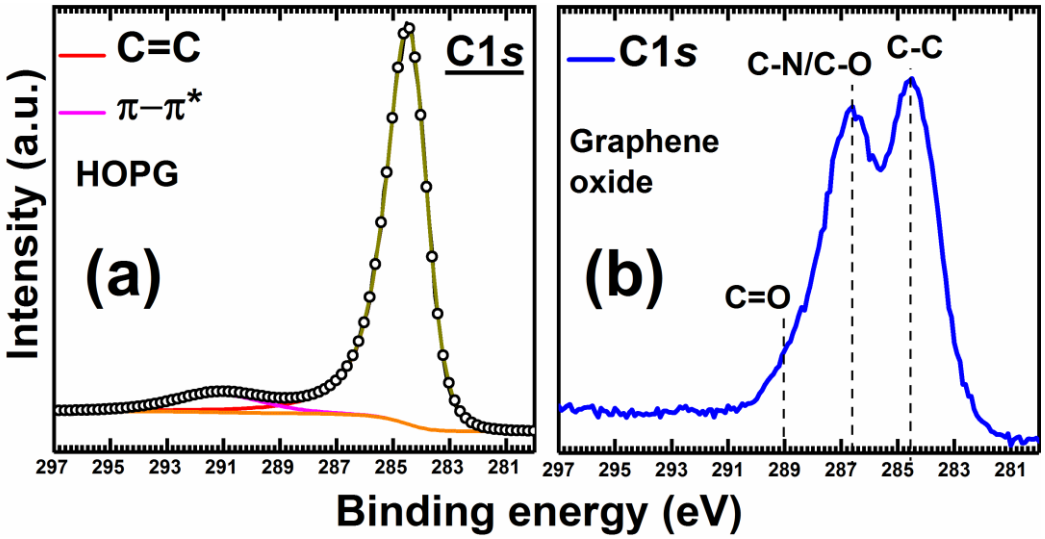

Figure 2.4 High resolution C1*s* core level XPS spectrum of (a) freshly-cleaved highly oriented pyrolytic graphite (HOPG) used as reference XPS spectrum in this thesis and (b) graphene oxide shows shift in binding energy due to difference in chemical environments of carbon atoms (detailed description in chapter 5). Here C-C denotes carbon bonded to carbon (sp^3), C-N/C-O denotes carbon bonded to nitrogen/oxygen which are difficult to resolve using the in-house XPS and C=O denotes carbon atom doubly bonded to oxygen (sp^2).

The intensity of photoemission peaks is related to the amount of each element present in the sample. The ionization cross-section (σ) and attenuation length (λ) are two very important parameters which need to be considered for accurate analysis. The photoemission cross-section is defined as a measure of the probability that a photoelectron will be created by the incident X-ray photon and is dependent on the energy and polarization of the incident photons. On the other hand, the attenuation length can be considered as the inelastic mean free path of a photoelectron i.e. the average depth through which an electron can move without undergoing energy loss due to inelastic scattering and is directly proportional to the kinetic energy of the photoelectrons. The sharp peaks in the XPS spectra denote the electrons which have escaped from the surface

without any loss of energy whereas, the background signal has contribution from electrons which are scattered and have suffered losses whilst escaping. Thus, the photoelectric current detected by the spectrometer can be expressed as

$$I = \sigma j K \int n(x) \exp\left(\frac{-x}{\lambda \cos\theta}\right) dx \qquad \text{……..2.14}$$

Where I, σ , j, K, $n(x)$, λ and θ denote the peak intensity, photoionization cross-section for a particular transition, flux of incident X-ray photons, instrument factor, concentration of the element of interest at a depth 'x' below the sample surface, the attenuation depth and the angle between the normal and ejected electrons, respectively[180].

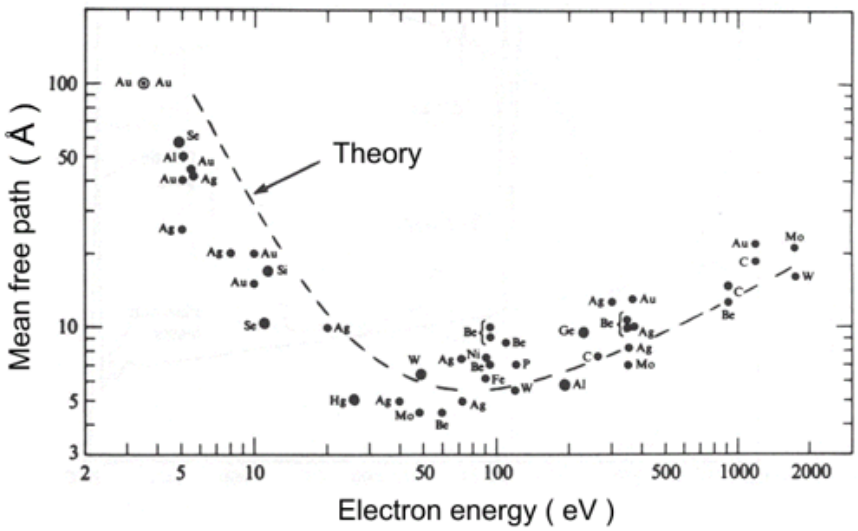

Figure 2.5 Universal curve for the inelastic mean free path [182].

The universal curve for inelastic mean free path of an electron is shown in Figure 2.5. As is clearly discernible from the figure, at very low and very high kinetic energies, the photoelectron has a long mean free path because in the former case it does not possess enough energy for excitation whereas in the latter it passes swiftly without suffering much energy loss. The high surface sensitivity of the XPS stems from the fact that electrons have very short escape depth and even with a high kinetic energy (1-2 keV),

the escape depth is not more than a couple of nanometres. XPS is not only used for identifying elements but also to quantify the chemical composition. Atomic concentration can be determined as

$$C_i = \frac{{}^{I_i}/_{S_i}}{\Sigma_i {}^{I_i}/_{S_i}} \qquad \text{……..2.15}$$

Where I_i is the intensity of the element and S_i is the sensitivity factor of the peak i.

Final state effects: The electronic structure of an atom excited by the incident X-ray photon suffers from significant perturbation as an aftermath of the escape of a core electron which results in reorganisation of the remaining electrons to screen the core hole. Intermolecular and intramolecular relaxation are the two dominant mechanisms which come into play to screen the created core hole and can lead to shifting of the binding energy in the XPS spectra. Intermolecular relaxation is caused by the electronic polarization of the surrounding molecules and can cause measured binding energy shift of about 1-2 eV. On the other hand, during intramolecular relaxation, the outer shell electrons undergo rearrangement within 10-100 femtoseconds. Intermolecular relaxations can result in additional features in the spectrum which arise due to the decay processes occurring from the various excited states. Figure 2.6 shows some excitation events which occur during and after photoionization, namely, shake-up, shake-off and Auger emission [183]. A shake-up feature is formed when an outgoing photoelectron loses part of its kinetic energy to a valence electron and excites it to an unoccupied state, for example $\pi \rightarrow \pi^*$ transition in the C1*s* spectrum of graphite. If the transferred energy is sufficient to ionize the valence electron to the continuum, then a shake-off feature is visible. Furthermore, an Auger decay occurs when the energy released after filling the core electron excites another electron to the continuum. The abovementioned features

arise due to energy loss and hence are observed at higher binding energies or lower kinetic energies compared to the main spectral emission line.

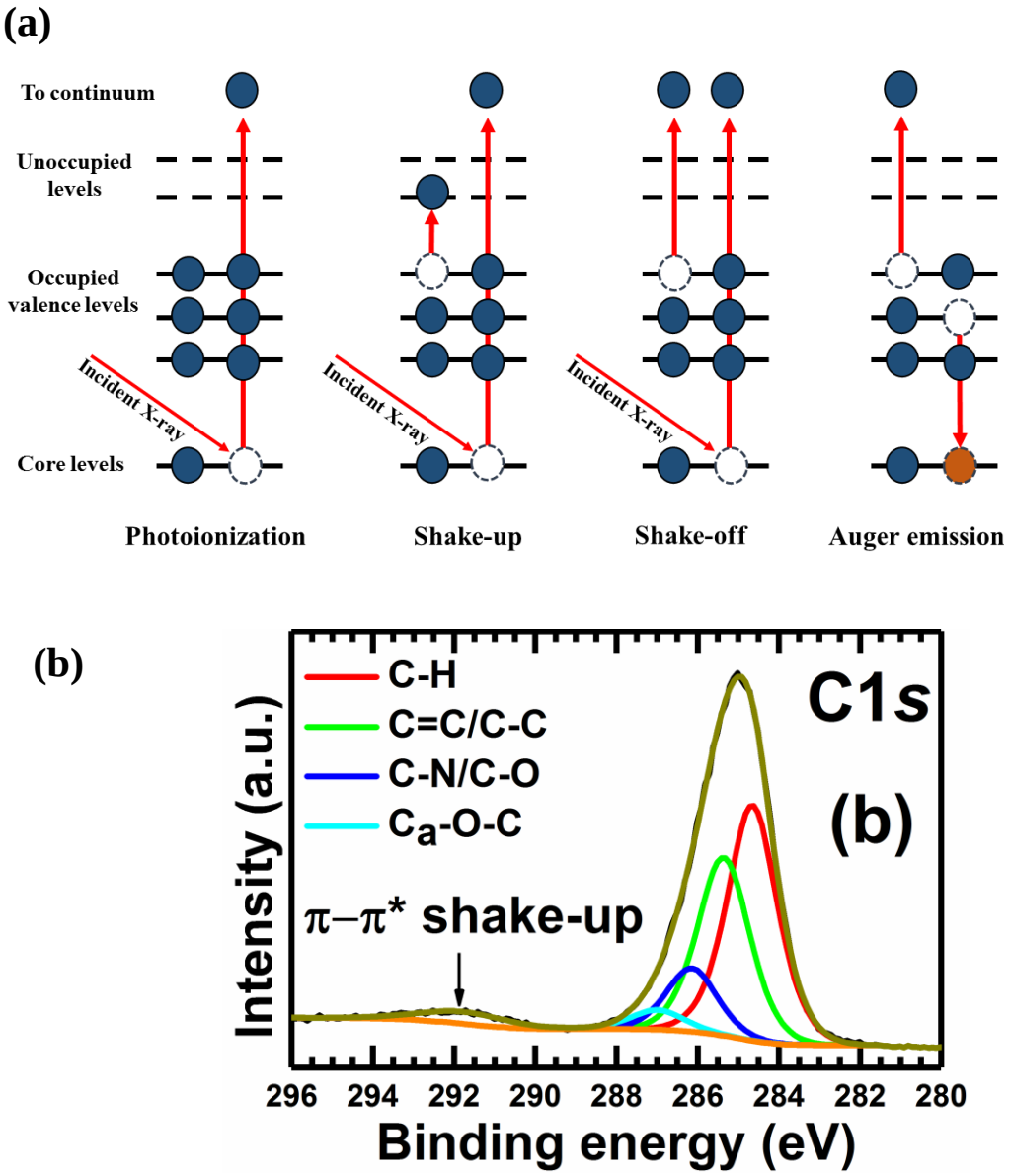

Figure 2.6 (a) Various excitation events that can occur during or after the photoionization process and (b) shake-up feature in C1*s* spectrum of SFX-OMeTAD hole conductor.

Instrumentation

The kinetic energy of the emitted photoelectron is measured with respect to the vacuum level of the sample but in actual practise the measurements are performed with

reference to the vacuum level of the spectrometer and the two levels are different from each other. Thus, a common reference between the sample and spectrometer is required to define the binding energies of the photoelectrons and this is achieved by grounding both the sample and the spectrometer. After grounding, the Fermi level (E_F) of both the systems are at the same energy level and can be considered as a reference.

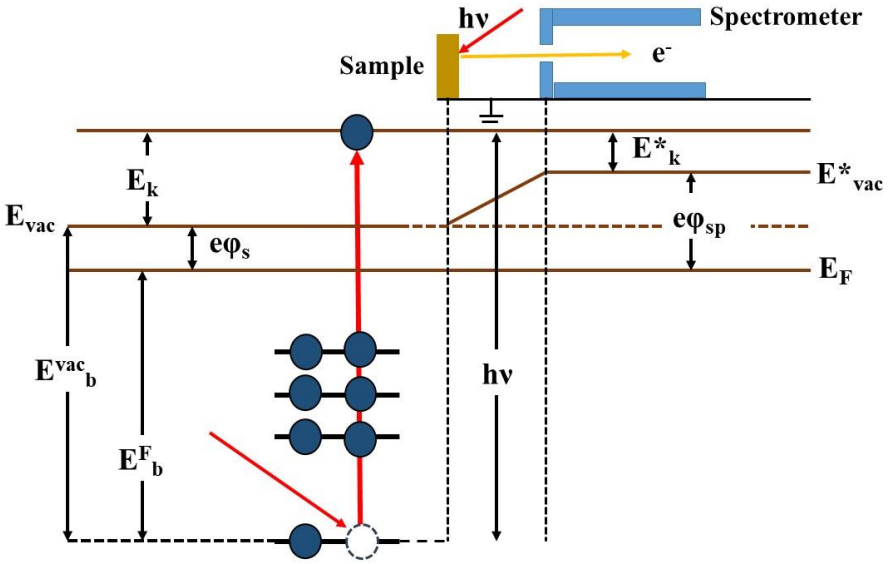

Figure 2.7 The energy level diagram showing band alignment between the sample and the spectrometer [183].

Whilst measurements are made, the work function difference between sample ($e\phi_s$) and spectrometer ($e\phi_{sp}$) should be considered for determining the energy of the emitted electron. Hence, the kinetic energy of the photoelectron at the spectrometer (E_k^*) can be related to the kinetic energy of the photoelectron at the sample (E_k) as

$$E_k^* = E_k - (e\phi_{sp} - e\phi_S) \qquad \text{.....2.16}$$

From Figure 2.7, the kinetic energy of the photoelectron at the sample can be related to the binding energy E_b^F (with respect to the Fermi level) and the incident photon energy as $E_k = h\nu - e\phi_s - E_b^F$ 2.17

Replacing equation 2.16 in 2.17, we get

$$E_b^F = h\nu - E_k^* - e\phi_{sp} \quad \text{…….2.18}$$

Hence, E_b^F can be determined by measuring E_k^* and $e\phi_{sp}$ values for a known incident photon energy. Using a sample with well-known binding energy, for example, Au, Ag or Pt, the work function of the spectrometer can be calculated. The XPS is mostly calibrated using a clean gold surface with respect to Au $4f_{7/2}$ core line at 84 eV.

Electron energy analyser: The electron energy analyser is crucial for the working of photoelectron spectroscopy. KRATOS systems use a concentric hemispherical analyser, also known as hemispherical sector analyser (HAS). As the name suggests, the hemispherical analyser consists of two concentric hemispheres of radii R_1 (inner) and R_2 (outer) ($R_2 > R_1$). The outer and inner hemispheres are biased with negative voltages, V_2 and V_1 where $V_2 > V_1$. The applied bias directs the photoelectrons between the two hemispheres in a circular path of radius R_0 such that ($R_2 > R_0 > R_1$). The energy of the electron entering the analyser is fixed to the pass energy (E_P) such that $E_P = eV_0$. V_0 is determined such that the electrons are attracted by the inner hemisphere and repelled by the outer one. Hence, an electron with kinetic energy greater than the pass energy will collide with the outer hemisphere and vice versa. The value of V_0 can be related to the applied bias voltage and radii of the hemispheres as [180]

$$V_2 - V_1 = V_0 \left(\frac{R_2}{R_1} - \frac{R_1}{R_2}\right) \quad \text{…….2.19}$$

A high-resolution analyser is required to define the complex chemical structure of molecules since higher resolution signifies narrower line width (full width at half maxima; FWHM) of the core level spectra. The instrument resolution is defined in terms of slit width 'w' and angular speed 'α' of the electron beam as

$$\frac{\Delta E}{E} = \frac{w + R_0\alpha^2}{2R_0} \qquad \text{.....2.20}$$

Thus, the resolution of the spectrometer can be effectively increased by either reducing the slit width or increasing R_0 i.e. larger spectrometer.

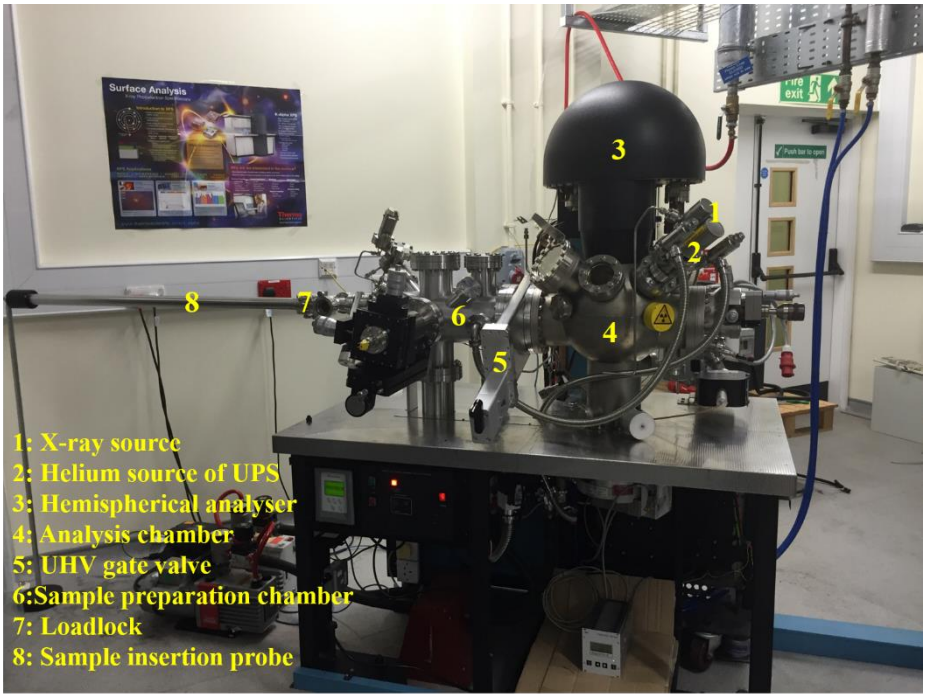

Figure 2.8 X-ray photoelectron spectroscopy (XPS) equipment at the Open University.

The in-house XPS system used for photoelectron measurements in this thesis is a Kratos XSAM 800 equipment consisting of a dual anode emitting Mg K_α (1254.6 eV) and Al K_α (1486 eV) X-rays (Figure 2.8). The corresponding line widths for these sources are 0.7 eV and 0.8 eV, respectively. The dual anode assembly uses a thoriated filament as the electron source and thin films of aluminium and magnesium are coated over the copper anode to generate the characteristic X-rays. De-ionized water is used to cool the anode. The HAS operates in two modes: Fixed analyser transmission (FAT) and fixed retarding ratio (FRR). All the experiments reported in this thesis were obtained in FAT mode. The pass energy of the analyser can be programmed to any of the three values, high pass (20 eV), medium pass (38 eV) and low pass (65 eV). There is also a Helium

discharge lamp to carry out ultraviolet photoelectron spectroscopy (UPS) measurements. The helium lamp produces characteristic He (I) (21.2 eV) and He (II) (40.8 eV) lines. These high intensity UV photons can be used to probe the valence band structure (total density of states).

2.2.2 X-ray absorption spectroscopy (XAS)

Synchrotron radiation

Laboratory based conventional X-ray sources suffer from several drawbacks, namely limited photon flux, unpolarised radiation and lack of tunability of the photon intensity/energy. So, experiments which require high intensity, tunable and polarized X-rays, turn to synchrotron radiation sources. In synchrotrons, electrons are accelerated in a circular path by bending magnets to produce radiation. Synchrotron sources produce photons having a continuum of energy spanning from infrared to X-rays. For electrons moving with velocities close to that of light, the radiation is directed in the direction of the electron's travel and the relativistic effect results in a collimated beam. The angular distribution ($\Delta\phi$) of the emitted radiation is related to the Lorentz factor as

$$\Delta\phi \approx \gamma - 1 \qquad \text{…….2.21}$$

And

$$\gamma = 1 \Big/ \sqrt{1 - \frac{v^2}{c^2}} \qquad \text{…….2.22}$$

Where ν is the speed of electrons and 'c' is the speed of light in vacuum.

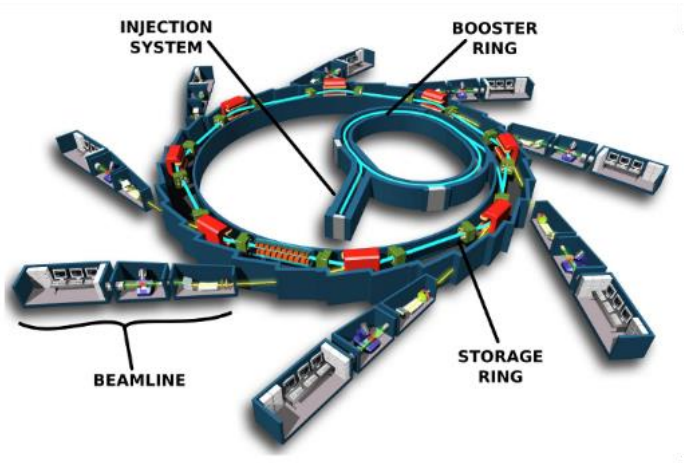

Figure 2.9 Schematic of a typical synchrotron facility with different components: electron gun, Linac, Booster ring, Storage ring, beamline and experimental station.

The primary components of a synchrotron radiation facility, namely the electron gun, linear accelerator (Linac), booster ring, storage ring, beamlines and experimental/end stations are shown in Figure 2.9. Electrons are emitted by a cathode and accelerated to energies ~120 MeV by the linear accelerator and injected into the booster ring in discrete bunches. The electromagnets in the booster ring accelerate the electrons and force them to travel around the ring. Variable magnetic fields guide the electron in a circular trajectory of constant radius while RF system boosts the energy of the electron beam. Electrons rotate in the booster ring until they achieve sufficient energy (2.3 GeV) to be injected into the storage ring. The booster ring feeds electrons into the storage ring, a many-sided donut shaped structure. The storage ring further ramps up the energy of the particles to 3 GeV and is maintained under vacuum to prevent deflection of electrons. Synchrotron radiation is produced when the bending magnets in the storage ring deflect the electron beam with each set of bending magnets being connected to a beamline. Precise focussing of the beam is undertaken with the help of the computer-controlled quadrupole and sextupole magnets. Undulators, wigglers and monochromators filter, intensify and modulate the beam to correspond to the various experimental requirements [184,185]. Synchrotron-based studies (Chapter 3) in this project

were undertaken at Stanford Synchrotron Radiation Lightsource, California. The storage ring at SLAC is named as SPEAR (Stanford Positron Electron Accumulator Ring) and was originally built for high energy physics research. Under normal conditions, the SPEAR stores up to 100 mA of current in its 234-meter circumference vacuum chamber.

XPS, though being highly surface-sensitive, provides information about the total density of states whereas NEXAFS is element-specific and probes the partial density of states of the concerned element. Near edge X-ray absorption fine structure (NEXAFS) was mainly developed in 1980s to study the structure of molecules bonded to the surface [186]. Primarily it was aimed for low-Z molecules (where Z signifies the atomic number), but has ever since been used to understand the transitions during X-ray absorption and probe the nearest neighbour interactions, chemical structure, orientation of molecules and molecular fragments. Moreover, NEXAFS demonstrates channel selectivity when probing total and partial fluorescence yield.

X-rays incident on matter lose their intensity during transmission due to the interaction with matter. In addition to being transmitted and absorbed, some part of the incident X-ray also gets elastically, or inelasticity scattered. As a result, the incident intensity (I_0) is observed to reduce exponentially. The transmitted intensity is also affected by properties such as mass density (ρ) and absorption coefficient (μ). X-ray absorption spectrum is a plot of the variation in absorption coefficient with incident photon energy. Sharp features known as absorption edges, corresponding to the transition of a core electron to the unoccupied density of states, are observed in a typical absorption spectrum and have energy values corresponding to the binding energy of the core electron. Figure 2.10 shows a typical C *K*-edge XAS spectrum demonstrating the pre-edge, absorption edge, NEXAFS and EXAFS regions.

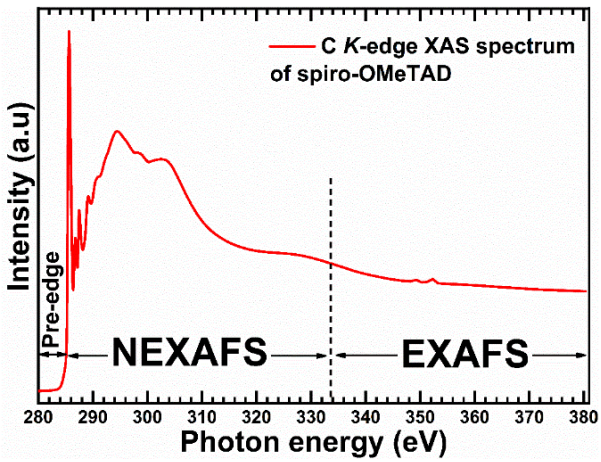

Figure 2.10 Typical C *K*-edge XAS spectrum showing the pre-edge, NEXAFS and EXAFS regions.

A NEXAFS spectrum is usually characterized by sharp resonance features in the energy region just below and up to ~50 eV [187] above the core level ionization threshold (absorption edge), arising due to transitions from the *K*-edge (the deepest core shell) of an atomic species into unoccupied bound or continuum levels. These transitions are governed by dipole selection rules (i.e. $\Delta l = \pm 1$) and are sensitive to the local electronic structure, chemical configuration, oxidation state, molecular orientation and symmetry [186,188].

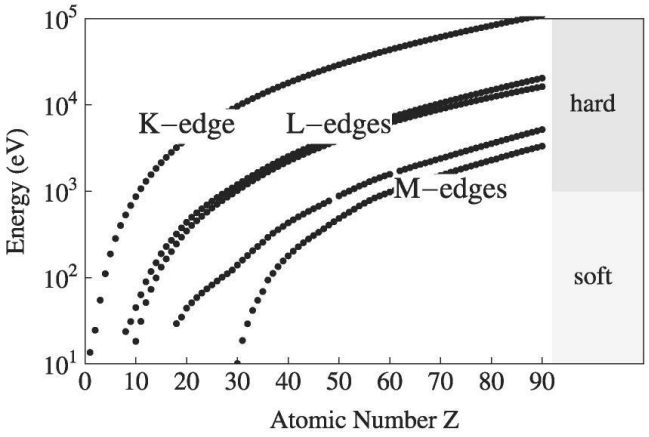

Figure 2.11 Energy of K, L and M absorption edges as a function of atomic number Z. X-ray energies below 1 keV are referred to as soft X-rays and those above, as hard X-rays [189].

Figure 2.11 presents the X-ray energies required to obtain excitation features at different absorption edges (*K*, *L*, and *M* edge). In this thesis, NEXAFS spectroscopy has been used extensively to reveal the electronic structure and bonding environment of different doped hole transport materials. Chapter 3 provides insight into the carbon and nitrogen *K*-edge NEXAFS corresponding to the transitions from 1*s*→2*p* unoccupied states for differentially doped hole transport materials spiro-OMeTAD, SFX-OMeTAD and SFX-TAD.

Theory of NEXAFS

Figure 2.12 shows the origin of the absorption features in NEXAFS spectra. In the figure, the potential distribution of a diatomic molecule is depicted along the X-axis with the corresponding *K*-shell absorption features. The anti-bonding π* and σ* levels are unoccupied states corresponding to the orbitals with π and σ symmetry, respectively. For a neutral molecule, the σ* orbitals have energy distribution above the ionization potential while the strong coulombic interaction between the excitons (electron-hole pairs) pulls down the π* orbitals below the vacuum level. The transitions from the core levels to the unoccupied π* and σ* levels give rise to the corresponding transitions wherein π* show sharper features and are easy to resolve and identify. In contrast, transitions to σ* orbitals are significantly broader due to life time broadening and vibrionic features. In addition to π* and σ* states, Rydberg resonances are often found just below the IP [188]. The absorption cross section describes the probability of interaction of an electron with a photon. The X-ray absorption cross section (σ_x) is defined as the number of electrons excited per unit time divided by the number of photons incident per unit time per unit area. A detailed quantum mechanical description about the absorption cross section has been presented by Stöhr in his book "NEXAFS Spectroscopy" [188].

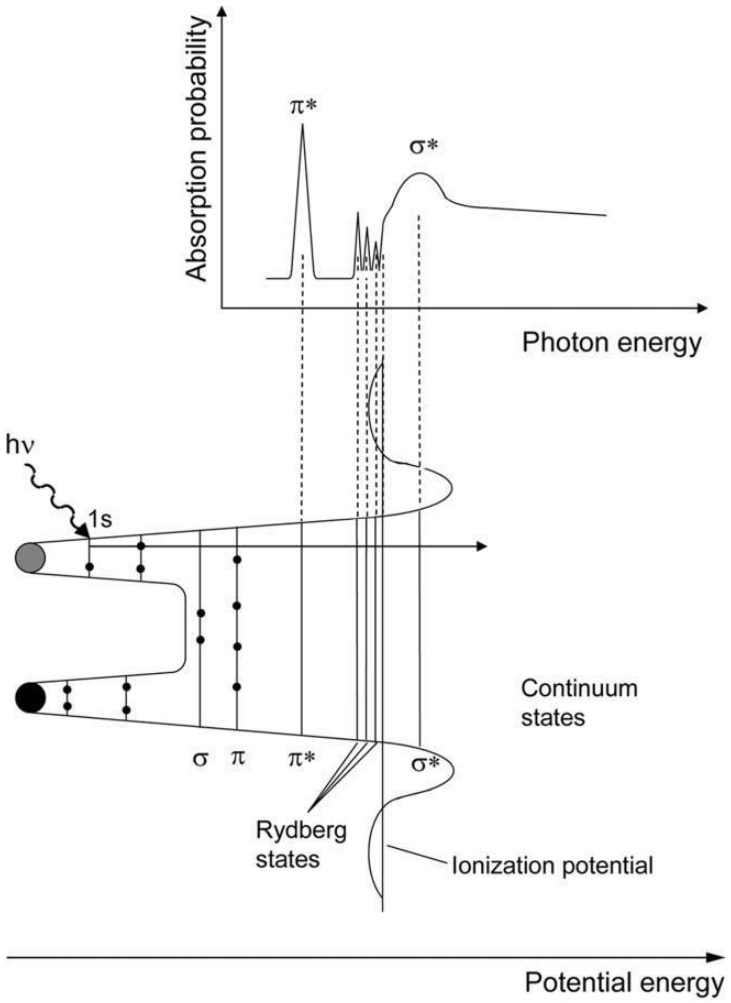

Figure 2.12 Schematic potential (bottom) and corresponding NEXAFS *K*-shell spectrum (top) of a diatomic molecular (sub) group. In addition to Rydberg states and a continuum of empty states similar to those expected for atoms, unfilled molecular orbitals are present, which is reflected in the absorption spectrum [186].

According to Fermi's Golden rule for initial and final state transitions, the probability of transition from an initial state $|\mathrm{i}\rangle$ to a final state $|\mathrm{f}\rangle$ driven by a harmonic time dependent perturbation $V(t) = Ve^{-i\omega t}$ is given by

$$P_{ij} = \frac{2\pi}{\hbar} |<f|V|i>|^2 \rho_f(E) \qquad \text{.....2.23}$$

With the dipole approximation, the X-ray absorption coefficient can be expressed as

$$\sigma_x = \frac{4\pi^2\hbar^2}{m^2}\frac{e^2}{\hbar c}\frac{1}{\hbar\omega}|<f|e.p|i>|^2\rho_f(E) \quad \text{.....2.24}$$

where $\hbar\omega$ is the incident photon energy, 'e' is the electronic charge and 'm' is mass of electron, $\rho_f(E)$ represents the density of final states and $<f|e.p|i>$ is the dipole matrix showing the interaction between the linear momentum operator 'p' with unit vector of the electric field 'e' of a polarized incident light. This dipole matrix reveals the polarization dependence of the NEXAFS spectra. The transitions which involve change in angular momentum quantum number by $\Delta l = \pm 1$ are only allowed and this is reflected in the NEXAFS spectra. The transitions between the molecular orbitals are governed by the dipole selection rules. For linearly polarized light, the dipole matrix can be written as $<f|p|i>$. The direction of this matrix element will be same as that of orientation of the orbital i.e. the vector *O*. The resonant features are most intense when the electric field vector has the same direction as that of the orbital orientation. On the other hand, if the electric field vector is perpendicular to the molecular orbital then the corresponding resonance features will be absent from the spectra.

Detection schemes

A tunable monochromatic soft X-ray source having photon energy less than 2000 eV is used for photoabsorption during NEXAFS measurements. The core hole thus created can be filled up by an electron either radiatively or non-radiatively. The radiative process results in the emission of florescence photon whereas the non-radiative process results in the emission of an Auger electron. There are two detection schemes for acquiring NEXAFS spectra. First is by measuring the secondary electrons, known as electron yield (EY) and second is by counting the florescence photons, known as fluorescence yield (FY). Total electron yield (TEY), Partial electron yield (PEY) or Auger electron yield (AEY) are the different ways in which electron yield measurements can be carried out. Electrons of all energies are collected in the TEY mode. The TEY

signal usually has a strong intensity and low signal-to-noise ratio due to the dominance of secondary electrons. In TEY mode, spectra are recorded by measuring the current to the sample such that the sample remains electrically neutral after the photoionization process. The mean free path of the released electrons limits the sampling depth for the TEY detection scheme to about 10 nm of the surface. During the actual spectrum acquisition process, spectra for TEY is acquired by measuring the sample drain current (I_0). The PEY signal is acquired by placing a retarding voltage in front of the electron detector such that only electrons with low kinetic energies are allowed through to the detector known rendering this technique highly surface-sensitive. However, the electron yield methods are limited only to conducting samples. Auger electrons are measured by tuning the energy of the electron analyser to specific Auger transitions whereas fluorescence yield detection is carried out using a photodiode placed close to the sample. FY, on the other hand, is independent of the sample conductivity. The sampling length for FY mode depends on the attenuation length of the incident X-ray and the composition of the material under study and longer mean free path of photons reduce the surface sensitivity. In general, the sampling depth in FY mode being of the order of 100 nm for soft X-rays. The advantage for FY mode is the ease of sample preparation as the presence of surface oxides and contaminants can effectively be ignored. Both electron yield and florescence yield are normalized by dividing the signal by the incident photon flux measured at a gold grid placed upstream of the beam path (between the main chamber and the beamline optics).

2.2.3 Ultraviolet photoelectron spectroscopy (UPS)

UPS is a powerful and versatile technique for studying the valence electronic structures of materials in atoms, solids and molecules. The common ionization sources for UV radiation range from 16.6 to 40.8 eV namely Ne I (16.6 eV), Ne II (26.8 eV), He I (21.2 eV) and He II (40.8 eV). The emission lines are produced by cold capillary

discharge and represent fluorescence produced upon decay of the excited gas molecules in the discharge. Inelastically scattered electrons can be detected as secondary electrons to form the background. The photoionization process to produce state 'I' of the positive ion M^+ can be described by the following equation

$$I_i = h\nu + K_i \qquad \text{.....2.25}$$

Where I is the Ionization energy.

UPS can be used to determine the work function by measuring the width of the emitted electrons (W) from the secondary threshold to the Fermi edge and subtracting W from the incident UV light energy, $h\nu$. The work function (φ) can then be described as $\Phi = h\nu - W$ 2.26

Figure 2.13 shows a typical UPS spectrum of Ag foil which has been used as reference for measuring UPS spectra of plasma jet deposited spiro-OMeTAD and plasma-doped graphene oxide.

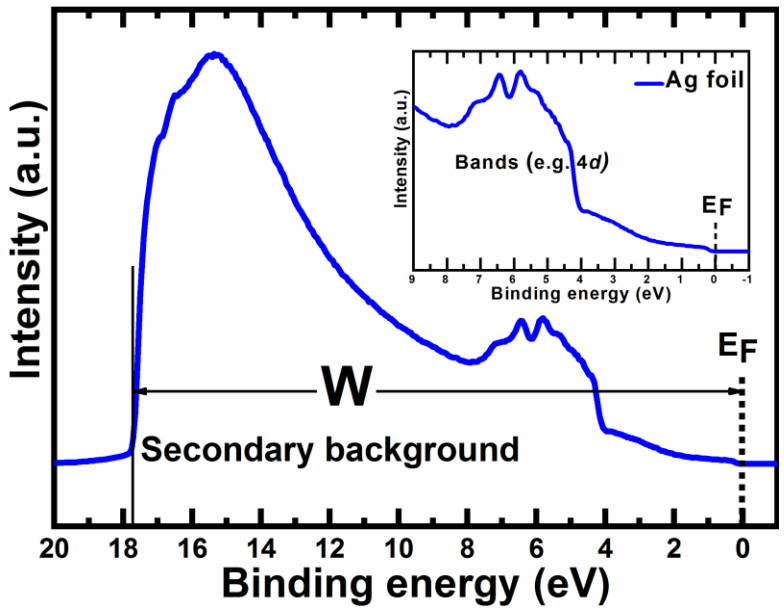

Figure 2.13 A typical UPS spectrum of Ag foil (used as reference in this thesis in Chapters 5 and 6).

In this thesis, UPS was used to investigate the variation in valence band during plasma functionalization and deposition using a Thermo Theta Probe spectrometer with a base pressure of 5x10^-10 mbar using He(I) UV light with photon energy 21.2 eV at University College London. Photoelectron kinetic energy was measured using a hemispherical analyser with angular acceptance over a solid angle of 60 °. Samples were biased at - 9V relative to the spectrometer electron optics. The high and low energy photoemission onsets were determined by taking the differential of the spectrum. Samples were mounted on the stage using carbon tape and copper clips to secure them in place and to provide electrical contacts.

2.2.4 Raman spectroscopy

Light gets scattered in various ways upon interaction with matter. Rayleigh scattering occurs when the scattering process is elastic in nature and the scattered wave possesses the same frequency as that of the incident light. On the other hand, inelastic scattering process results in a discrete shift of the frequency value and is referred to as Raman scattering. For Raman scattering, the frequency shifts are independent of the exciting frequency and have characteristic footprint of the scattering molecule. Essentially these frequencies resemble the vibrational frequencies of the molecule and hence Raman spectroscopy can be used to probe the vibrational energy levels of molecules. In a typical Raman spectrum, the intensity of the scattered photon is plotted as a function of the energy difference between incident and scattered photon. This frequency shift is referred to as the Raman shift and can be represented in terms of wavenumber (ν) as

$$\Delta\nu\ (cm^{-1}) = \left(\frac{1}{\lambda_{incident}} - \frac{1}{\lambda_{sattered}}\right) \qquad \text{……2.27}$$

And

$$\nu\ (wavenumber) = \frac{\nu}{c/n} = \frac{1}{\lambda} \qquad \text{……2.28}$$

Where, Δν is the Raman shift, is the wavelength of the excitation source and is the corresponding scattered wavelength, 'c' is the speed of light in vacuum (2.997925 x 1010 cm sec^{-1}), and ($^{c}/_{n}$) is the velocity of light in a medium whose refractive index is n, for which the wavenumber is measured.

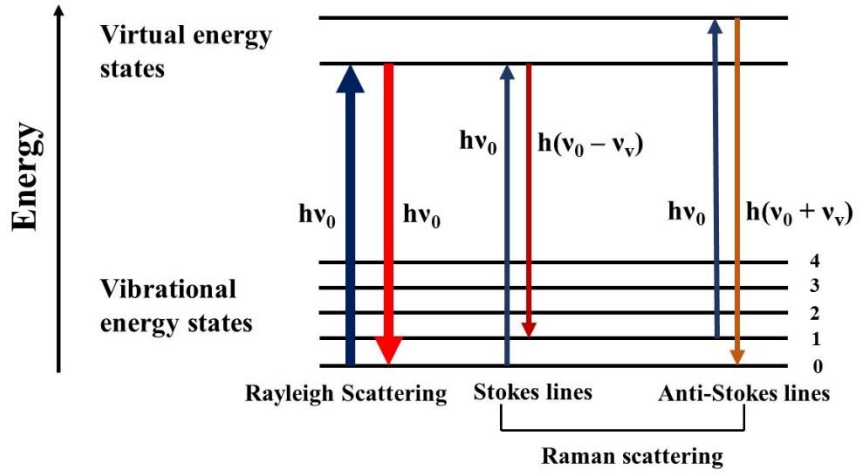

Figure 2.14 Jablonski diagram for Rayleigh and Raman scattering.

The elastic and inelastic scattering process can be presented schematically using the Jablonski diagram as shown in Figure 2.14. Raman scattering is typically a very weak process, about 10^{-9} to 10^{-6} times that of Rayleigh scattering. Hence an intense monochromatic light source, typically lasers, is essential to observe this phenomenon. It is worth mentioning that in Raman scattering process there is no inherent absorption of photon by the molecule but only the ground state of the molecule gets disturbed, resulting in vibrational and rotational transitions. These transitions are ultrafast occurring at a timescale of nanoseconds [190,191].

In this thesis, a Horiba Jobin-Yvon Labram HR laser Raman microprobe with Ar^{+} laser (514.5 nm line) as the excitation source was employed to determine the chemical and structural variation due to plasma jet deposition of spiro-OMeTAD films. The laser power was kept <0.5 mW to minimise the heating effect.

2.2.5 Atomic force microscopy (AFM)

Atomic force microscopy is a highly versatile surface analytical tool to image structural morphology of the surface at a resolution down to atomic or molecular level. In AFM, a sharp probe having dimensions of tens of nanometre attached to a cantilever is used to raster the surface of samples. A 3D image of the surface can be created by monitoring the displacement of the probe. The intermolecular force between the tip and the sample can be used to acquire information about the mechanical, electrical, chemical and magnetic properties of the sample at nanoscale resolution. The basic operational principle is described in the following section [192,193].

Operation:

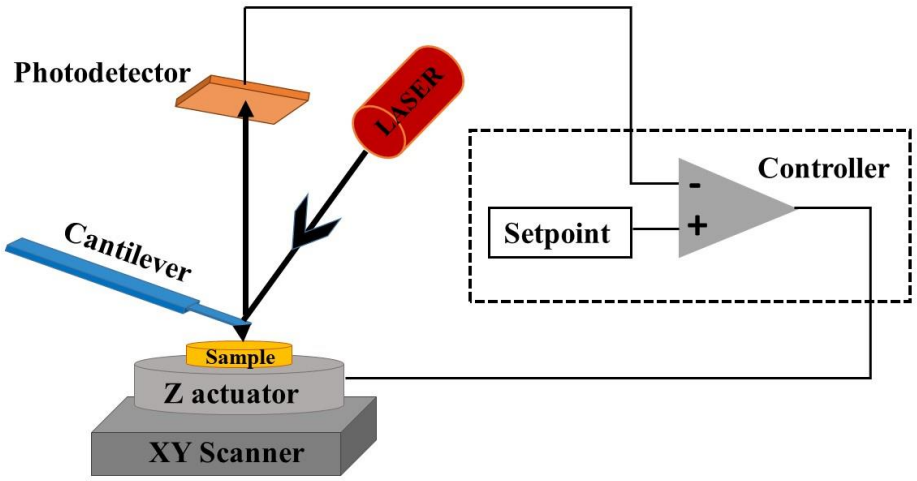

Figure 2.15 Schematic of basic working principle of an AFM.

Schematic of the basic working principle of an AFM is as shown in Figure 2.15. An atomically sharp Si/Si_3N_4 tip is mounted on a single beam cantilever. The tip is placed in close proximity to the sample surface and the force between the tip and the sample is measured by the deflection of the cantilever while scanning the surface. The cantilever deflection is monitored by a laser beam reflected off the back of the cantilever to a position-sensitive photodetector. As the laser is reflected to the detector, any

deflection of the cantilever doubles the deflection of the laser beam. The tip taps over the surface during scanning providing information about chemical and physical properties of the surface, in addition to topography [194].

AFM can be operated in contact, non-contact and tapping modes. In contact mode of operation, the tip is brought into physical contact with the sample surface due to which the tip apex faces repulsive forces whereas the rest of the tip experiences attractive forces. The cantilever experiences constant deflection as the tip scans over the surface. High resolution topographic images can be obtained in contact mode due to the sensitivity of the short-range forces. However, the resolution is determined by the contact area of the tip apex. In non-contact mode of operation, the tip oscillates at its resonant frequency above the sample surface without being in actual contact. The attractive forces at the tip result in shifting of the frequency of oscillation between the tip and the sample. But the major disadvantage of this technique is its inability for measurements in liquid environment. The intermittent contact (tapping) mode is useful for this purpose where the cantilever oscillates in such a way that the tip touches the surface first and then retracts to avoid damage. The intermittent contact on the surface reduces the free oscillation amplitude of the cantilever which can then be used to measure and identify the topography. The feedback loop is used to maintain a constant frequency of oscillation and the force applied by the tip on the sample is maintained at the lowest value. Tapping mode is especially beneficial for studying soft samples such as polymers and biomaterials to avoid damage to the sample. Any change in material properties namely, composition, adhesion, friction and viscoelasticity, results in a phase lag between the piezoelectric drive frequency and cantilever oscillation frequency. Thus, a flat surface with variation in composition would exhibit negligible spatial change in the height profile but appreciable change in the phase profile.

In this thesis, AFM has been used in tapping mode to study the topography of plasma-functionalized spiro-OMeTAD (described in Chapter 4). Data analysis has been performed with the Gwyddion software.

2.2.6 Scanning Kelvin probe microscopy (SKPM)

Kelvin Probe Force Microscopy (KPFM), also called Scanning Kelvin Probe Microscopy, is one of the most widely used nanoscale electrical characterization techniques with broad applications ranging from corrosion studies of alloys, photovoltaic effects of solar cells and surface analysis. The background for this technique dates back to the gold-leaf electroscope experiment by Lord Kelvin in 1898 who observed that plate of copper and zinc mounted on insulating shafts created charge when they were brought into electrical proximity and then moved apart. This discovery can be explained in terms of difference in work function. Electrical contact between two conductors results in the flow of electrons from the one with lower work function to the one with higher, thus aligning the Fermi level. If the conductors were placed such as a parallel plate capacitor, opposite charges will be induced between the two surfaces and the potential difference between them is known as contact potential difference (CPD) or surface potential (SP), which equals the difference in work function of the two materials. In KPFM, the biased conducting tip and the sample surface behave as a parallel plate capacitor and the KPFM works on this mechanism of measuring the CPD by applying an external potential (in the form of a feedback loop) until the induced surface charges disappear. At this instance, the external potential equals the CPD.

KPFM is dual-pass technique, where the topography is mapped first similar to the tapping mode AFM, which is again traced at a fixed delta height above the surface for measurement of the phase profile using a conducting tip which is biased with AC voltage. The phase and amplitude of vibration of the cantilever tip are affected when a

voltage bias is applied between the tip and the sample surface. The modulated electric force, by the application of an AC bias between the tip and sample, can be measured using the oscillation of the cantilever. The applied DC bias is modulated by the feedback loop to match the surface potential difference between the tip and the sample surface [195]. The KPFM feedback, adjusts a DC bias until the oscillation amplitude drops to 0, when V_{DC} equals CPD or the surface potential. The measured surface potential difference from KPFM, though accurate have multiple contributions which renders this technique pseudo-quantitative. The work function measured is not an absolute value, but the values are measured with respect to the tip. Schematic of the principle of Kelvin probe force microscopy as performed with an Asylum research MFP3D equipment is as shown in Figure 2.16.

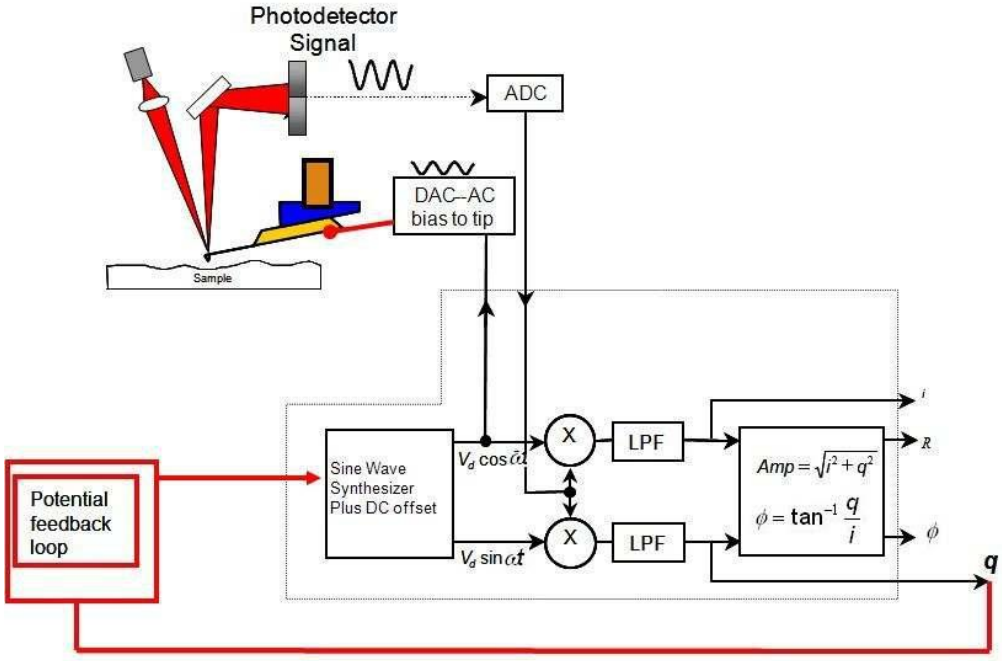

Figure 2.16 Schematic of the principle of Kelvin probe force microscopy as performed with an Asylum research MFP3D equipment. The probe is driven electrically with an AC bias. The potential difference between the tip and the sample causes the probe to oscillate. These oscillations are then cancelled by a potential feedback loop. The voltage

required to match the probe to the sample is captured as the surface potential channel in the software (from instrument brochure) [195].

In this thesis, KPFM measurements were performed using Pt-Ir coated tips to observe the variation in work function of the spiro-OMeTAD samples, before and after plasma processing (Chapter 4).

2.2.7 Electrostatic force microscopy (EFM)

Electrostatic force microscopy is a useful technique to investigate the electrical properties of nanomaterials and has extensively been used to study the distribution of electrical potential and charge at the nanoscale for graphene and graphene oxide [196–199]. EFM primarily allows qualitative mapping of the surface potential. EFM is a dual-pass technique, similar in operation to the SKPM technique, only that there is no active feedback loop in this case. The oscillation of the cantilever tip is shifted due to the force gradient when a voltage bias is applied between the tip and the sample. This frequency shift introduces a phase lag between the drive frequency and that of the cantilever. Areas of the sample with varying electrical properties can be identified by tracking these phase shifts. This type of imaging can be used to measure the relative change in the local electrostatic force between the tip and the sample surface. If the DC bias on the conducting tip is kept constant along with the distance between the tip and the sample, then the measured variation in electrostatic force corresponds to the changes in surface potential distribution. In EFM, the capacitive force between a biased tip and the grounded sample surface induces phase shifts of the tip oscillations as [200,201]

$$\Delta\varphi = \frac{Q}{2k}\frac{d^2C}{dz^2}(V_t - \varphi)^2 \qquad \text{.....2.29}$$

In equation 2.29, $\Delta\varphi$ is the phase shift, Q and k are the quality factor and spring constant of the cantilever, C is the capacitance of the system, V_t is the voltage of the tip, and ϕ is the surface potential.

EFM was performed using an Asylum research MFP3D equipment using Pt-Ir coated conducting tips to map the variation in conductivity of plasma-functionalized spiro-OMeTAD films (Chapter 4). The ability of EFM to differentiate between conductive and non-conductive domains was exploited to reflect the variation in conductivity. Schematic of the working principle of an EFM is shown in Figure 2.17.

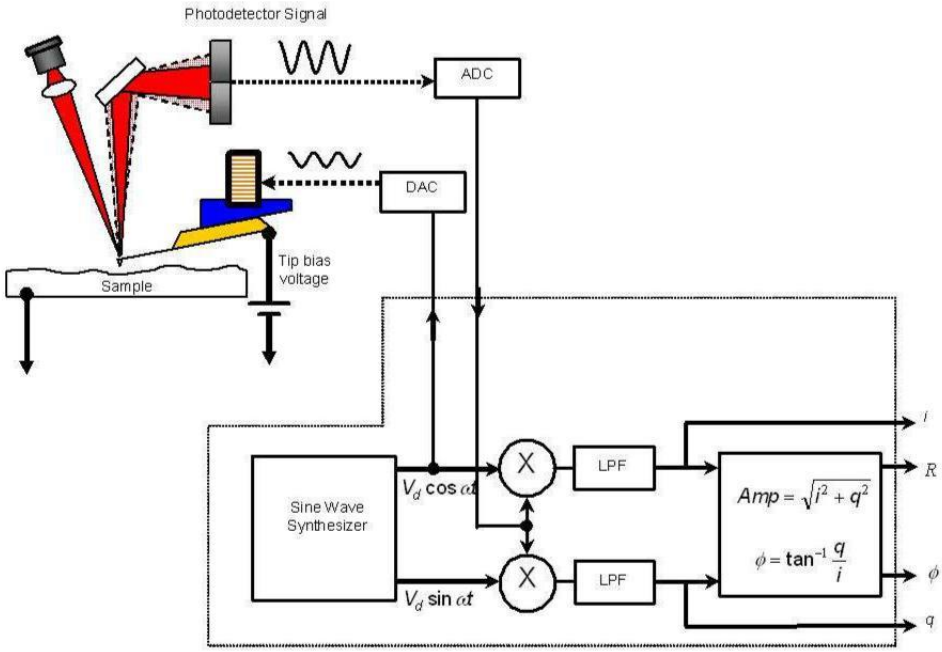

Figure 2.17 Schematic of the working principle of Electrostatic force microscopy with an Asylum research MFP3D equipment. The Probe is oscillated both during the main scan and during the nap scan. During the nap scan, the probe is lifted off of the surface, and a bias applied between the tip and sample to show the location of areas that are conductive or strongly charged (instrument brochure) [195].

2.2.8 Four-point probe measurement

Sheet resistivity, also known as surface resistivity, is a measure of the lateral resistance through a thin square of material i.e. the opposite sides of a square and is a common electrical property used to characterise thin films of conducting and semiconducting materials. Four-probe apparatus is one of the commonly used

techniques for measuring sheet resistivity mostly employed when the sample is in the form of a thin wafer. A four-point probe comprises four electrical probes in a line, with equal spacing. A constant current is passed through two probes and the potential drop, V, across the other two probes, are measured.

The resistance of a regular 3D conductor is measured as

$$R = \rho \frac{L}{A} = \rho \frac{L}{Wt} \quad \text{.....2.30}$$

where ρ is the resistivity (Ω m), A is the cross-sectional area, and L is the length. For A in terms of W and t,

$$R = \frac{\rho}{t}\frac{L}{W} = R_S \frac{L}{W} \quad \text{.....2.31}$$

where R_s is the sheet resistance. Unit is Ω but can also be expressed as Ω sq^{-1}.

For a thin film sample (thickness t<<s), we have the case of current rings, so that area A = 2πxt

$$\int_{x_1}^{x_2} \rho \frac{dx}{2\pi xt} = \int_{s}^{2s} \rho \frac{dx}{2\pi xt} = \frac{\rho}{2\pi xt} (\ln x)_s{}^{2s} = \frac{\rho}{2\pi t} \ln 2 \quad \text{.....2.32}$$

Superposition of current at outer two tips leads to $R = {}^{V}/_{2I}$, so that the sheet resistance of a thin film sample is $\rho = \frac{\pi t}{\ln 2}\left(\frac{V}{I}\right)$ 2.33

The expression proves that the sheet resistance is independent of s, spacing between the probes. Thus, sheet resistivity is defined as

$$R_s = \frac{\rho}{y} = k\left(\frac{V}{I}\right) \quad \text{.....2.34}$$

Where k is a geometric factor which for a semi-infinite thin film is ${}^{\pi}/_{\ln 2}$ = 4.53.

In this thesis, sheet resistivity of plasma-functionalized spiro-OMeTAD was measured using a four-point probe equipment with a Keithley SourceMeter (Model

2400), set to lower current range in pico Amps (pA). The current range was set up between 50-100 pA and compliance was at 210 V. Further attention was given to minimise the noise level due to charging effect in recording the data for each set and the final value was averaged for a range of current values in pA. The four-point probe apparatus used for the measurement of sheet resistivity is as shown in Figure 2.18.

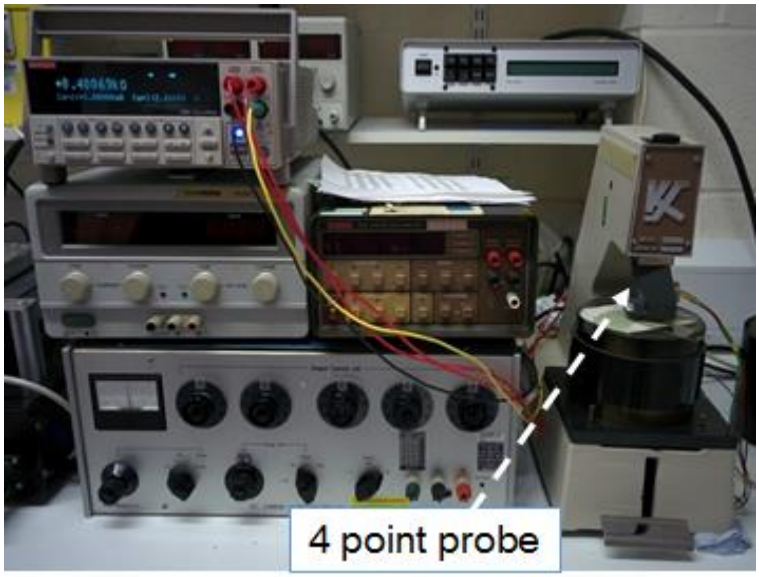

Figure 2.18 The four-point probe at Cranfield University used for the measurement of sheet resistivity along with the Keithley Sourcemeter Model 2400.

2.2.9 Ultraviolet and visible absorption (UV-Vis) spectroscopy

Ultraviolet-visible spectroscopy is one of the more ubiquitous analytical and characterization techniques in science. Ultraviolet and visible photons are energetic enough to promote electrons to higher energy states in molecules and materials and is useful for probing the electronic properties of materials. UV-Vis absorption spectroscopy is the measurement of the attenuation of a beam of light after it passes through a sample or after reflection from a sample surface. It includes a variety of absorption, transmittance, and reflectance measurements in the ultraviolet (UV), visible, and near-infrared (NIR) spectral regions which can be acquired at a single wavelength or over an extended spectral range. According to Beer-Lambert law

$$A = \xi cd \quad \text{.....2.35}$$

Where ξ is the molar extinction coefficient, c is the concentration and d is the thickness of the illuminated material. In terms of incident (I_0) and transmitted intensity (I), the absorbance can also be written as

$$A = \log {}^{I_0}/_{I} \quad \text{.....2.36}$$

In this thesis, UV-vis spectroscopy has been used to understand the variation in absorption of plasma-functionalized spiro-OMeTAD as a function of plasma treatment time using a JASCO UV-Vis equipment. The results have been analysed in Chapter 4.

2.3 Summary:

This chapter provides details of all the equipment that have been used to the understand the appropriate hole transport materials by optimising their electronic and surface properties. APPJ was used not only for functionalization but also deposition and *in situ* processing of spiro-OMeTAD. A novel aerosol-based plasma deposition and *in situ* processing technique for spiro-OMeTAD has been explored which can be extended to fabrication of perovskite devices. APPJ was also used for functionalizing graphene oxide as alternative cost-effective hole transport molecule using different gases, nitrogen hydrogen and oxygen.

This thesis aims to get a deeper understanding of the variation in electronic and optical properties of Li-TFSI-doped spiro-OMeTAD, plasma-functionalized spiro-OMeTAD, graphene oxide and plasma-deposited spiro-OMeTAD using different characterization techniques. Morphology of the functionalized and doped HTMs was studied using SEM, optical microscopy and AFM. NEXAFS is one of the best techniques for correlating structural variation and electronic properties. Variation in electronic properties of Li-TFSI doped spiro-OMeTAD, SFX-OMeTAD, SFX-TAD

was probed using NEXAFS for the first time. Electronic properties of plasma-functionalized spiro-OMeTAD, plasma-functionalized graphene oxide and plasma-deposited spiro-OMeTAD were studied using XPS and UPS. Variation in surface conductivity and work function upon plasma treatment of spiro-OMeTAD was probed using EFM and KPFM. The results will be discussed in the following chapters.

Chapter 3

Probing the electronic properties of different hole transport materials

Hole transport molecules are an integral part of perovskite solar cells. Spiro-OMeTAD has been used as a hole transport molecule with consistent efficient device performance. But pristine spiro-OMeTAD suffers from low hole mobility and conductivity and chemical doping with Li-TFSI is commonly undertaken to improve the charge transport properties. X-ray spectroscopy has proven to be the best technique for correlating the variation in electronic properties with the structural changes in molecules. In the present work, NEXAFS has been used to probe, the carbon and nitrogen K-edge spectra of doped spiro-OMeTAD. NEXAFS spectroscopy and XPS have been demonstrated as effective techniques for probing the surface chemistry and electronic properties of doped spiro-OMeTAD. A pathway for the interaction of Li-TFSI with spiro-OMeTAD has been suggested. The findings provide insight into the photochemical reactions which might occur in PSCs as a result of oxidation of spiro-OMeTAD and provide guidelines for the optimised doping levels suitable for enhanced device performance. The understanding gained for spiro-OMeTAD has been extended to the studies of SFX-OMeTAD and SFX-TAD hole conductor molecules. NEXAFS has been used to map the variation in structure and electronic properties in the newly synthesized molecules as a function of differential Li-TFSI doping.

3.1 Introduction

The hole transport layer is indispensable for better and reproducible device performance in PSCs since they not only help in extraction of holes but also aligning the energy level at the HTL/absorber layer interface. Spiro-OMeTAD is the most widely explored small molecule organic hole conductor in PSCs. But spiro-OMeTAD, in its pristine form, suffers from low hole mobility and conductivity and hence dopants such as Li-TFSI (bis(trifluoromethane) sulfonimide lithium salt) is required to improve the charge transport properties. Li-TFSI has found widespread use as p-type dopant [45,67] to improve the low hole mobility and conductivity of spiro-OMeTAD [45–48]. Li^+ ions reduce recombination losses at interfaces by tuning the TiO_2 band edge position for higher potentials and promotes p-type doping of spiro-OMeTAD by shifting the Fermi level towards the HOMO resulting in the oxidation and improving the conductivity of HTL for devices [37,45,59,63,64,202]. Although reasons for increased conductivity and oxidation of

spiro-OMeTAD has been reported in literature [45,203], how the Li^+ ions influence the oxidation of spiro-OMeTAD, is still an enigma. There is lack of fundamental understanding of the role of doped spiro-OMeTAD in charge transport mechanism at the interface of active perovskite material and HTL.

Soft X-ray absorption spectroscopy (XAS) is a powerful tool to probe the surface chemistry and electronic properties by providing information about the specific bonding configuration of molecules. XAS has two regimes: near edge X-ray absorption fine structure (NEXAFS) [188] spectroscopy and extended X-ray absorption fine structure (EXAFS) spectroscopy. NEXAFS is an element-specific and site-selective technique which allows for atomic-level characterization of molecules. The high sensitivity of NEXAFS towards the chemical nature of intramolecular bonds makes it advantageous for investigating organic molecules. For example, an unambiguous distinction between singly and doubly bonded carbon atoms is a challenge in XPS. Whereas, NEXAFS can clearly differentiate between transitions to the π* (antibonding π orbital) and σ*-orbitals (antibonding σ orbital) due to its sensitivity to the position of the final state of an atomic species. This simplifies the detection of single and double bonds. Moreover, the ground state electrons are perturbed by the creation of a core hole due to photoexcitation in XPS, whilst in NEXAFS the pronounced screening effect results in negligible influence on the ground state electron cloud. Unlike XPS, NEXAFS is not quantitative in nature and hence these techniques are complimentary in nature.

XPS provides information about the occupied density of states whereas NEXAFS probes the unoccupied density of states (DOS), local chemistry and nearest neighbour interactions. NEXAFS and XPS are complimentary in nature and due to the dipole selection rules involved, chemically non-equivalent sites of the same atomic species can be separated in NEXAFS spectroscopy, unlike XPS. C *K*-edge NEXAFS spectra

correspond to excitations of C1*s* core electrons to the unoccupied or partially filled levels in the conduction band of molecules. NEXAFS has been widely exploited to probe the unoccupied DOS of various inorganic and organic molecules such as benzene, naphthalene, anthracene, tetracene, perylene, coronene, pyridine and pyrazine [204–212]. NEXAFS has been used to correlate the electronic properties of these systems with their local chemical environment. C *K*-shell excitation spectra of benzene and aniline in gas phase, solid and monolayers chemisorbed on Pt(111) were investigated by Stöhr *et al* [213]. This study demonstrated that a change in length of carbon-carbon bond may result in a shift in the σ* resonances. Solomon *et al*. used NEXAFS to determine the orientation of benzene, aniline and phenol adsorbed on Ag (110) [207]. This study showed the presence of -NH_2, -OCH_3 and -OH nearest neighbours to aromatic ring resulted in splitting of the π* molecular orbitals by lifting the degeneracy of the π* e_{2u} molecular orbital and increased the probability of C1*s*→π* transitions. NEXAFS was used to study the influence of bonding, orientation and reactions of aniline, nitro-substituted benzene and aniline adsorbed on substrates by Huang *et al.* [214] and Turci *et al* [208]. NEXAFS has also been used to investigate the chemical structure of organically-bound nitrogen in fossil fuels such as petroleum asphaltenes (Mitra-Kirtley *et al.* [215]) and organic carbon moieties in soil (Solomon *et al.* [216]). Johansson *et al*. have combined theoretical studies based on density functional theory (DFT) and NEXAFS to study the molecular and electronic surface structure of a triarylamine-based hole conductor evaporated on rutile TiO_2(110) [217]. Study performed on hydrothermal carbon (HTCs) structures by NEXAFS revealed the presence of C=C, C-O-C (furan), C=O and C-OH functionalities. Nitrogen-doped HTCs showed the presence of C=N and C-N moieties [218]. The efficacy of different reducing agents in defunctionalizing graphene oxide was investigated using NEXAFS at carbon and oxygen *K*- edges by Lee *et al* [219]. The relative intensities of the π* and σ* resonances at the C *K*-edge spectra indicated the high extent of recovery of π-

conjugation upon reduction with phenyl hydrazine. Polarized NEXAFS measurements allowed for the evaluation of the extent of planarity induced upon reduction of graphene oxide. In the above-mentioned studies on complex carbon-based systems, NEXAFS provided crucial information correlating structural variation and electronic properties of materials. Hence, in this chapter X-ray spectroscopy (NEXAFS and XPS) have been used to understand the structural variation and electronic properties as a result of chemical doping. This technique will help to get a deeper understanding of the changes in chemical dopant concentration and its influence on the electronic properties of organic hole conductor molecules, spiro-OMeTAD, SFX-OMeTAD and SFX-TAD. Synthesis of the spiro bifluorene core (SBF) and Pd-catalyst coupling for spiro-OMeTAD enhances its cost, thus limiting applications in large-scale device production. Hence, two new SFX-core based molecules, SFX-OMeTAD and SFX-TAD, have been introduced in this chapter as cost-effective HTMs. The SFX core was synthesized using a mixture of fluorenone, phenol and methanesulfonic acid following procedure reported previously [12]. Unlike synthesis of the SBF core which involves multistep protocols and complex drying processes, the SFX core can be synthesized using a simple one-pot technique [13] beginning with reagents phenol and methanesulfonic acid which are comparatively cheaper than 2-bromobiphenyl or 2-iodobiphenyl required for SBF synthesis. Introduction of the SFX core not only reduces the final price of the materials by about five times (from $92-$108 for spiro-OMeTAD to $17 for SFX-OMeTAD) but also the number of synthesis steps are halved [12]. SFX-based molecules have found applications in OLEDs but their implementation in PSCs have been rather limited [12,13].

3.2 Experimental section

3.2.1 Deposition of spiro-OMeTAD films

This chapter is based on collaborative work and the samples S, M1 and M3 were studied as-received from the University of Edinburgh. SFX-OMeTAD and SFX-TAD were synthesized as novel low-cost alternative HTMs to spiro-OMeTAD [12]. The details of the samples studied are summarized in Table 3.1. The molecular structures of the different hole transport materials and the dopants studied in this chapter are shown in Figure 1.5, Figure 1.6 and Figure 1.7.

Table 3.1 Details of the samples (S, M1 and M3) and dopants studied in the chapter.

Samples		**Samples**	
S	Spiro-OMeTAD	M10	SFX-OMeTAD + 10 μL tBP + 10 mol% Li-TFSI
S0	Spiro-OMeTAD + 10 μL tBP	M110	SFX-OMeTAD + 10 μL tBP + 20 mol% Li-TFSI
S10	Spiro-OMeTAD + 10 μL tBP + 10 mol% Li-TFSI	M3	SFX-TAD
S20	Spiro-OMeTAD + 10 μL tBP + 20 mol% Li-TFSI	M3N	SFX-TAD + 10 μL tBP
M1	SFX-OMeTAD	M3D	SFX-TAD + 10 μL tBP + 20 mol% Li-TFSI

3.2.2 Characterization techniques

NEXAFS experiments were performed at the beam-line 8-2 of the Stanford Synchrotron Radiation Lightsource of SLAC National Accelerator Laboratory [220] (discussed in details in chapter 2). The samples were mounted on an aluminium stick with a conductive carbon tape and measurements were performed under ultra-high vacuum conditions ($< 1 \times 10^{-9}$ Torr). The energy of the incident beam was calibrated at the carbon dip (284.7 eV) arising from the contaminations in the beamline optics. Beamline slits and the pass energy of the analyser was set to achieve a total energy resolution of 0.3 eV. Spectra at the C and N *K*-edge spectra were acquired from 280 to

330 eV and 380 to 440 eV, respectively, in total electron yield mode at 54.7° (magic angle) incidence of the soft X-ray beam to eliminate effects of sample orientation on the intensities of the resonances (refer to section 2.2.2). For normalisation, the incoming flux (I_0) was measured using a gold mesh in the beamline and the signal was divided by the incident flux. The spectra were normalised to a linear background following the protocol developed by Wang *et al.* [221,222] Pre- and post-edge normalization were carried out from 275-285 eV and 320-330 eV for the C *K*-edge and the edge jump was normalised to unity. C and N *K*-edge NEXAFS spectra of the pristine and doped molecules were probed individually to understand the variation in electronic properties as a function of dopant concentrations.

3.3 Results and discussions

Extensive studies have been undertaken showing the improvement in conductivity and oxidation of spiro-OMeTAD doped with Li-TFSI and tBP, which provides an evidence for the formation of a spiro-OMeTAD$^+$ (TFSI)$^-$ complex [45,62,203], however, there exists no proof of the structural variation in spiro-OMeTAD due to Li-TFSI doping. Furthermore, structural insights into pristine and doped spiro-OMeTAD are crucial for understanding the charge transport mechanism. For this reason, synchrotron-based NEXAFS constitutes a complementary and important spectroscopic technique to investigate the electronic properties of doped spiro-OMeTAD. Probing the unoccupied DOS is essential to understand the nearest neighbour influence as a function of dopants and oxidation. Understanding the dynamics of excitation and decay of a core electron is a key point for the spectroscopic investigation of doped HTMs. The photoionization process of a core electron in doped spiro-OMeTAD is accompanied by vibrational or electronic excitations, charge transfer and internal charge rearrangement. This process leaves the molecule in a variety of possible excited states immediately after ionization.

The lifetime of these excited states determines the nature of radiationless decay channels. It is possible to probe the various lifetimes involved in the excitation and decay processes by using the tunability of the synchrotron radiation. As the NEXAFS transitions occur at discreet photon energies depending on the nearest neighbour interactions, it is possible to infer the chemical functionalities/bonding environment contained in complex molecular systems [209,210,223].

3.3.1 X-ray photoelectron spectroscopy (XPS) of doped Spiro-OMeTAD

High resolution XPS spectra were acquired to probe the variation in the electronic properties by observing the local chemistry around carbon, nitrogen and oxygen atoms as a function of Li-TFSI dopant percentage for spiro-OMeTAD (details of samples studied is provided in Table 3.1). XPS and NEXAFS are complementary spectroscopic techniques. Since, the doped films have contribution from three chemical compounds (Figure 1.5 and Figure 1.6), the deconvolution of the C1*s* spectra becomes cumbersome due to the inherent overlapping of the C-C, C-N and C-H bonds.

XPS measurements on spiro-OMeTAD with tBP additive showed no difference in the C1*s* spectra from the pristine film which may be due to the high vapour pressure of tBP such that it desorbs in vacuum, thus leaving behind no spectroscopic signature [47].

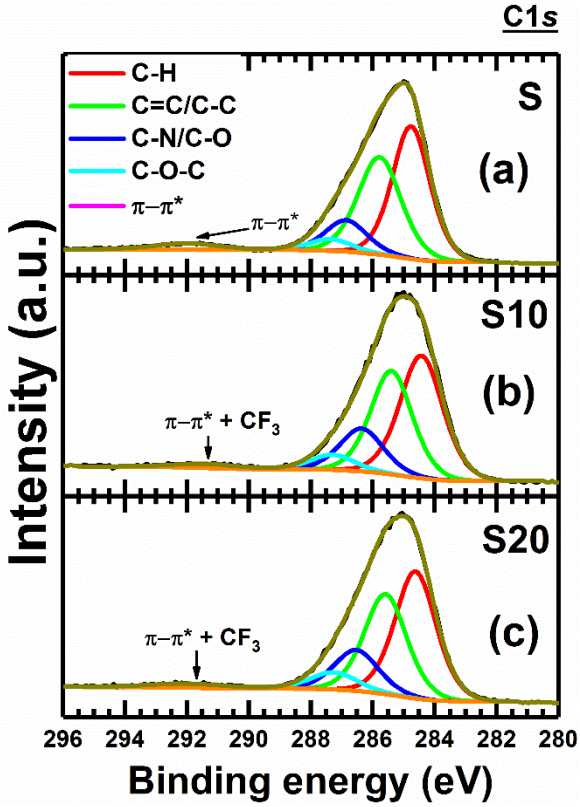

Figure 3.1 C1*s* core level XPS spectra corresponding to (a) Spiro-OMeTAD (S), (b) Spiro-OMeTAD doped with tBP and 10% Li-TFSI (S10), and (c) Spiro-OMeTAD doped with tBP and 20% Li-TFSI (S20).

The C1*s* core level XPS spectra of spiro-OMeTAD, (a) pristine and (b and c) doped with Li-TFSI and tBP, are shown in Figure 3.1. Pristine spiro-OMeTAD is deconvoluted into five components, namely, C-H, C=C/C-C, C-N/C-O, C_a-O-C and π-π* at 284.7 ± 0.2 eV, 285.7 ± 0.2 eV, 286.8 ± 0.2 eV, 287.8 eV and 291.5 eV, respectively [46,47,55,74]. The disorder-induced peak (sp^3) occurs 0.5 eV above the graphitic (sp^2) peak [224] but cannot be resolved using the in-house XPS due to the 0.9 eV resolution. Hence, the peak at 285.7 eV is expected to have contribution from both sp^2 and sp^3 hybridized carbon. The peak at 286.8 eV may have contribution from both C-N and C-O bonds. The π-π* plasmon feature originates from the delocalized electron density over the carbon atom and is a signature of the aromatic nature of the molecule. The fitting

parameters extracted from C1*s* core level XPS spectra of pristine and doped spiro-OMeTAD is summarized in Table 3.2.

The appearance of a new peak at ~688.0 eV corresponding to F1*s* of the -CF_3 groups in TFSI (Figure 3.2) and broadening of the peak at ~291.5 eV are clear signatures of doped spiro-OMeTAD films. The signature from the -CF_3 moieties is not appreciable but the broadening of the peak at ~291.5 eV from pristine to doped spiro-OMeTAD samples signifies contribution from both π-π* and CF_3 components. Unlike doped films, pristine S showed no F1*s* signal. This observation corroborates the diffusion of Li-TFSI from the bottom to the top of the doped spiro-OMeTAD films over time. The monotonic decrease in atomic percentage of C-H bonds in spiro-OMeTAD (43% for pristine sample to 35% in S10) as a function of doping can be correlated with the decrease in intensity of the C-H resonance of the C *K*-edge spectra from pristine to doped S molecules due to the air exposure of the samples prior to measurements [47]. The increase in C-N/C-O component can be corroborated with the variation in local chemistry due to additional nitrogen environment from the dopants. The broadening of the C_a-O-C component upon doping could be an indication that some molecules are oxidised [202].

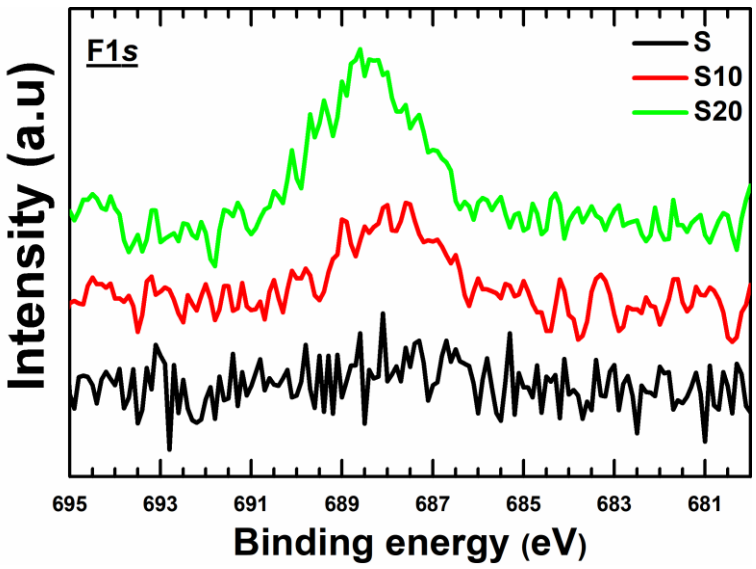

Figure 3.2 Comparison F1*s* spectra of pristine and 10% and 20% Li-TFSI doped spiro-OMeTAD (S, S10 and S20, respectively).

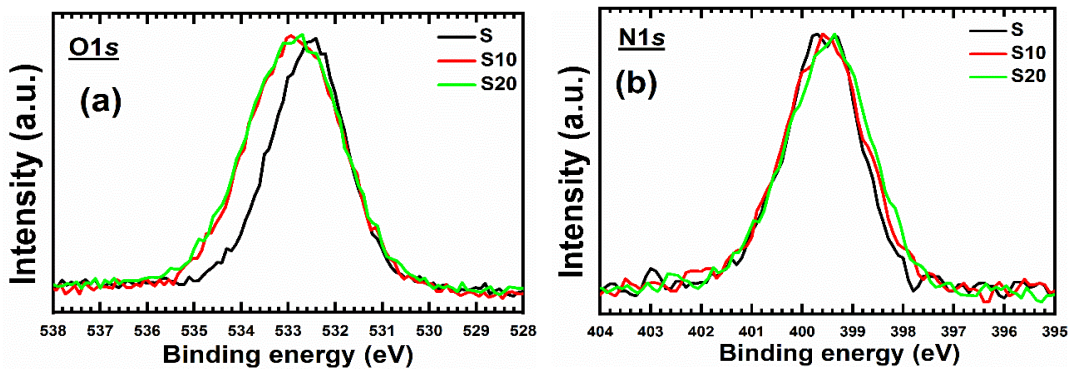

Figure 3.3 Comparison (a) O1*s* and (b) N1*s* spectra of pristine and 10% and 20% Li-TFSI doped spiro-OMeTAD.

Figure 3.3 (a) compares the O1*s* spectra of S, S10 and S20. The O1*s* spectra is fitted with a single peak at ~532.4 eV corresponding to the C_a-O species in pristine and doped spiro-OMeTAD. A 0.6 eV increase in FWHM on doping with 10% Li-TFSI can be interpreted as oxidation upon exposure to atmosphere. There is no increase in FWHM beyond 10% Li-TFSI as 20% dopant does not show any broadening. A similar trend has been previously been observed for the conductivity of spiro-OMeTAD doped with Li-TFSI where the conductivity values have become saturated after 15% dopant concentration [45]. Figure 3.3 (b) shows the overlaid N1*s* spectra of S, S10 an S20. The peak was calibrated to the amine peak, C-N of spiro-OMeTAD at 399.5 eV [47]. FWHM of the N1*s* spectra increases by 0.2 eV from S to S10 and by 0.4 eV from S10 to S20. The broadening of N1*s* spectra from pristine to doped samples is related to increase in area in the N *K*-edge NEXAFS spectra due to addition of nitrogen from tBP and Li-TFSI and will be discussed later (Figure 3.10).

Table 3.2 Fitting parameters extracted from C1*s* core level XPS spectra of pristine and doped spiro-OMeTAD.

Sample	Region	Component	FWHM ± 0.1 eV	Atomic % ± 0.2
S	C1*s*	C-H	1.4	43.6
		C-C	1.6	36.6
		C-O	1.5	11.4
		C_a-O-C	1.6	4.3
		π-π*	2.6	3.8
S10		C-H	1.5	35.0
		C-C	1.3	28.4
		C-O	1.5	23.6
		C_a-O-C	1.7	9.0
		π-π*	2.5	2.0
S20		C-H	1.5	41.3
		C-C	1.4	33.7
		C-O	1.4	15.8
		C_a-O-C	1.5	6.9
		π-π*	2.7	2.2

The results show that doping with Li-TFSI not only results in oxidation of spiro-OMeTAD but also variation in the local chemistry around N which possibly influences the conductivity of the doped films. It is not possible to find any conclusive answers regarding the structural variation in spiro-OMeTAD and to propose a mechanism as a function of Li-TFSI doping. Hence, the studies have been extended to NEXAFS to understand the variation in electronic properties and structural variation as a result of Li-TFSI doping.

3.3.2 C *K*-edge spectra of doped spiro-OMeTAD (S)

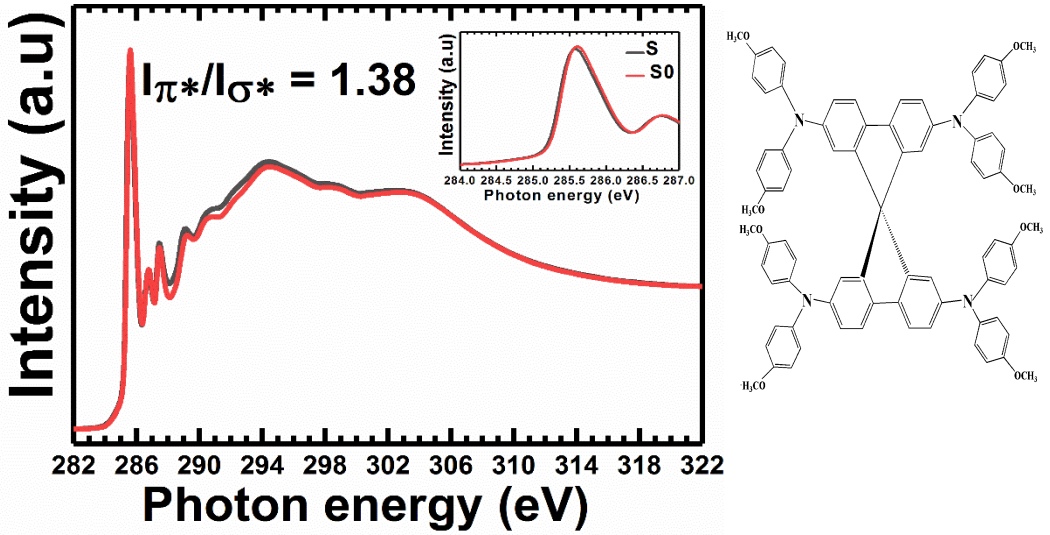

Figure 3.4 C *K*-edge NEXAFS spectra corresponding to spiro-OMeTAD, pristine (S) and tBP-doped (S0). Inset shows the absorption edge of pristine and tBP-doped S.

In Figure 3.4, C *K*-edge comparison spectra of pristine and tBP-doped S has been presented. Spectra for all pristine molecules indicate sharp π* and σ* resonances around 285.0 eV and 292.0 eV, respectively [207,213,225–228]. Five π* resonances at 285.6, 286.7, 287.4, 289.0 and 290.6 eV and four σ* resonances at 292.1, 294.4, 298.6 and a broad band at 303.0 eV are observed. From the molecular orbital picture, π* resonances occur due to transitions from the core level to the unoccupied antibonding π molecular states (1*s*→2*p*) whereas the σ shape resonances occur because of transition of core electrons to different antibonding σ molecular states. Excitations into Rydberg or multi-electron states are also possible [188]. The π* orbital is the lowest unoccupied molecular orbital of a π-bonded diatomic molecule, while σ* orbitals are found at higher energies, often above the vacuum level for the neutral molecule. However, the π* state is pulled below the ionization potential by the electron-hole Coulomb interaction [188]. The 1*s*→π* transition is a signature of molecules with π-bonding, i.e. double and triple bonds or aromatic systems, and are not observed in case of saturated molecules [207]. The positions and assignments of the C *K*-edge NEXAFS resonances of S, M1 and M3 are summarized

in Table 3.3 and their origin have been discussed in the following sections. The resonances for the tBP-doped samples are observed within ± 0.1 eV of the pristine molecules. From the inset of Figure 3.4, no shift in the absorption edges of spiro-OMeTAD is observed as a result of tBP doping. This is possibly because tBP improves miscibility of spiro-OMeTAD and Li-TFSI, preventing phase segregation in solution and has no role in influencing the local chemistry around the carbon atoms.

Table 3.3 Peak positions and assignments of the C *K*-edge resonances of S, M1 and M3 (pristine and doped).

Peak position ± 0.2 eV	**Assignment**	**Reference**
285.6	$1s\rightarrow\pi_1^*(C_{2,3}) + 1s\rightarrow\pi_2^*(C_{2,3,4})$	[207,213,214,229]
286.7	$1s\rightarrow\pi_2^*$ (C_1) + $1s\rightarrow\pi^*$ transition of aryl-O + π* C-N	[207,209,210,213,230–233]
287.5	$C1s\rightarrow\pi^*$ (C-H) + $C1s\rightarrow\sigma^*$ C-H/3p Rydberg-like excitations	[207,210,213,216,234–236]
289.0	$C1s\rightarrow\pi_3^*(C_{2,3,4})$ + σ* (C-H)	[207,213,214]
290.6	$C1s\rightarrow\pi_3^*$ (C_1)	[207,213,214]
292.2	$C1s\rightarrow\sigma^*$ (C-C + C-O + C-N)	[209,218,234–236]
294.2	$C1s\rightarrow\sigma_1^*$ (C-C) + $C1s\rightarrow\sigma^*(e_{2g} + a_{2g})$ + π* shake-up feature	[207,213,214,229,237]
298.6	$C1s\rightarrow\sigma^*$ (C-O)	[238]
303.2	$C1s\rightarrow\sigma_2^*$ (C=C)	[207,213,214,236]

Where $C_{2,3}$ and C_1 signify the position of the carbon atoms on the benzene ring as shown in Figure 3.7.

For aromatic molecules, there is a strong interaction between the localized π* and σ* states producing delocalized orbitals which are significantly separated in energy as shown in Figure 3.5 and Figure 3.7. The simplest aromatic molecule, benzene, possesses three unoccupied π* molecular orbitals, two of which are degenerate and hence C *K*-edge spectrum of benzene shows two π* resonances corresponding to transitions to unoccupied e_{2u} and b_{2g} π* orbitals (Figure 3.5) [237]. Schematic of the π* molecular orbitals

of benzene and the possible C1*s*→π* transitions are shown in Figure 3.5. The C1*s*→π* (e_{2u}) transition in benzene is highly asymmetric due to the vibrational broadening and can be fitted with a main line and vibrational structures owing to C-H bending, C-C and C-H stretching modes as reported by Ma *et al* [239]. For the HTMs reported in this chapter, having cross-linked aromatic backbones, the C *K*-edge NEXAFS spectra show multiple resonances which may result from interaction between localized molecular states as in the case of benzene [188]. Conjugate π bonds in the aromatic backbone of aforementioned molecules interact to produce two or more degenerate energy levels resulting in splitting of the π* antibonding orbitals.

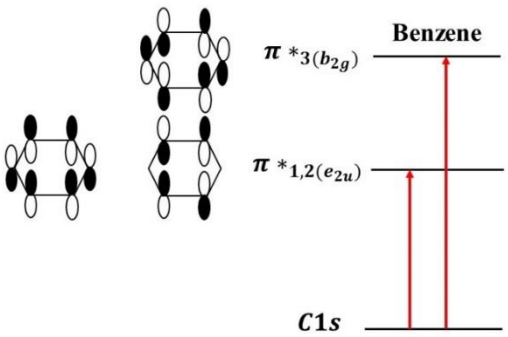

Figure 3.5 Schematic of the π* molecular orbitals of benzene and the possible C1*s*→π* transitions are shown (adapted from reference [236]).

Since, there is no appreciable difference in the C *K*-edge spectra of pristine and tBP-doped molecules, the discussion has been confined to Li-TFSI doped samples.

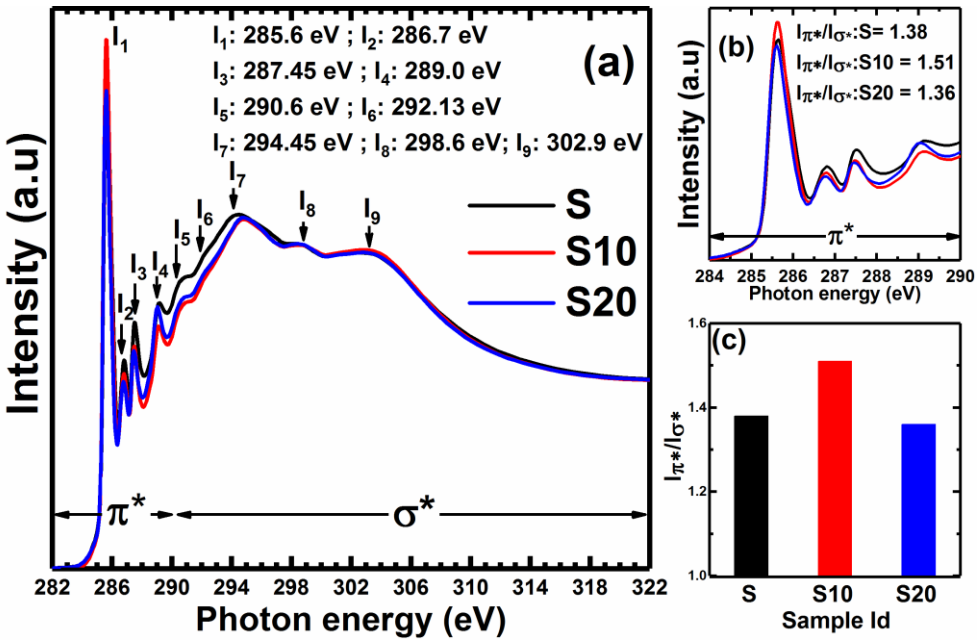

Figure 3.6 (a) Comparison of C *K*-edge NEXAFS corresponding to spiro-OMeTAD (S), pristine and doped with tBP and 10% Li-TFSI (S10), and S doped with tBP and 20% Li-TFSI (S20), (b) π* resonances at the absorption edge and (c) variation in $\frac{I_{\pi*}}{I_{\sigma*}}$ ratio as a function of dopant concentration.

The π* resonances I_1, I_2, I_4 and I_5 have been assigned to transitions from $C_{2,3}\rightarrow\pi_1$* (a_2) and $C_{2,3,4}\rightarrow\pi_2$* ($b_1$), C_1 to the π_2* (b_1), $C_{2,3,4}$ to π_3* and $C_1\rightarrow\pi_3$* (b_1) orbitals, respectively. Resonance I_3 at 287.5 eV has contribution from C1*s*→π* (C-H) with some σ* C-H/3p Rydberg-like excitations (details of the assignments provided in Table 3.3). There are contradictory views regarding assignment of resonances to different nearest neighbour interactions. The resonance between 286-287.4 eV maybe because of N-substituted aromatic C whereas the feature at 287-288.5 eV maybe due to aliphatic C-H [240]. The resonances related to C-N bonding overlap with oxygen moieties at 286.8 eV and 288.8 eV. Dennis *et al.* observed that the π* resonances of C-N bonds are at 286.8 eV and 288.6 eV in the C *K*-edge NEXAFS of imidazole [231–233]. Due to the significant broadening of the π* resonances, the low atomic concentration of nitrogen and the overlap with the C-O features, the clear signature of C-N at the C *K*-edge is quite difficult

to obtain. In the case of doped spiro-OMeTAD samples, resonance at 285.6 eV may also have contribution from C=N from tBP [235] whereas, the resonance at 287.4 eV may be due to both σ* C-S bond in Li-TFSI [241] and from pyridine nitrogen group in tBP.

C *K*-edge spectra of pristine S and doped S consist of same number of absorption bands which have close energy positions, except for variation in intensities (Figure 3.6). This proves that doping with Li-TFSI influences the density of π* and σ* states in spiro-OMeTAD. Even though the spectra of S10 and S20 resemble that of benzene, they contain resonances which reflect the presence of nearest neighbours -OCH_3 and -NR_3 (where R is a benzene ring). The presence of -OCH_3 and -NR_3 is known to lift the degeneracy of the π* e_{2u} molecular orbital of benzene and hence, there are more possible C1*s*→π* transitions in spiro-OMeTAD than for benzene [207]. Schematic of the possible transitions between different energy levels for benzene, aniline and phenol are compared in Figure 3.7. Transitions in spiro-OMeTAD have been assigned in analogy to those of aniline and phenol [207,213], where the splitting between the π* resonances is not only due to splitting of the C1*s* levels, but also results from transitions to different π* states.

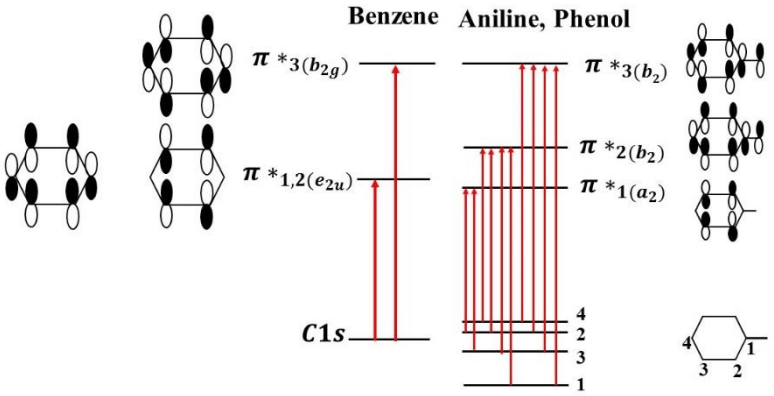

Figure 3.7 Schematic representation of the π* molecular orbitals of benzene, aniline and phenol. The possible C1*s*→π* transitions are shown (adapted from reference [207]).

The variation in $\frac{I_{\pi*}}{I_{\sigma*}}$ ratio as a function of Li-TFSI concentration is shown in Figure 3.6 (c). An increase in intensity of I_1 is observed from S to S10 before reducing for S20 (Figure 3.6 b). The ratio $\frac{I_{\pi*}}{I_{\sigma*}}$ is an important parameter to understand the influence of Li-TFSI dopant on the unoccupied DOS of S where an improvement in the ratio signifies enhanced aromatic character and vice versa. The increase in $\frac{I_{\pi*}}{I_{\sigma*}}$ from S to S10 means that 10% Li-TFSI contributes to improving the density of π* states of carbon which increases 1*s*→2*p* transition probability and may result in an enhancement in conductivity of S. Spiro-OMeTAD has eight methoxy (-OCH_3) groups attached to the triaryl amine side chains. Methoxy, being an electron-donating group, increases the charge density over the benzene ring and the electron cloud is stabilised by hopping through resonance donation (Figure 3.8). In doped S, $TFSI^-$ anion attaches with the N atom of the side chain to form spiro-$OMeTAD^+TFSI^-$ complex [45]. It is proposed that Li^+ ions exert an attractive pull on the charge cloud over methoxy groups because of their affinity for oxygen. This results in reduction in intensity of I_2 (C1*s*→C_a-O-C transition; C_a is aromatic carbon) because of perturbation of the charge density over -OCH_3. The charge on $TFSI^-$ compensates for the distortion in charge cloud over the benzene rings brought about by Li^+. It has been predicted that in the case of 10% dopant, the combined effect of charge withdrawal and donation results in increased π* states/transitions and hence the improvement in π* intensity is observed. But increasing the dopant concentration (20%) affects the molecule unfavourably since possibly the interplay between the electron-donating methoxy and Li^+ reduces the transition probability to the π* DOS of carbon in S. Reduction in intensity of I_3 is observed as a function of Li-TFSI dopant concentration. Hawash *et al*. have reported a decay in the intensity of C1*s* XPS peak in Li-TFSI-doped spiro-OMeTAD primarily induced due to air exposure [47]. The reduction in intensities of I_4 and I_5 can be explained with regards to the influence of $TFSI^-$ on the N atom of doped

S. As mentioned earlier, the presence of an electronegative nearest neighbour to carbon makes the π^* e_{2u} molecular orbital non-degenerate which may reduce the probability of transitions from C1$s \rightarrow \pi_3^*(C_{2,3,4})$ and $\pi_3^*(C_1)$. The mechanism suggested for doping of Li-TFSI into spiro-OMeTAD is schematically explained in Figure 3.9 (a). It can also be suggested that the Li-TFSI oxidation results in loss of the methyl groups and formation of quinoid structures with a positive charge on the amine nitrogen which in turn enhances the hole mobility of doped spiro-OMeTAD Figure 3.9 (b).

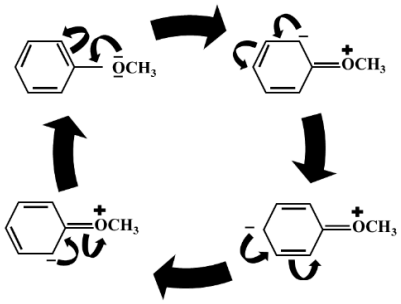

Figure 3.8 Mechanism of resonance donation on the benzene ring due to presence of electron-donating methoxy group.

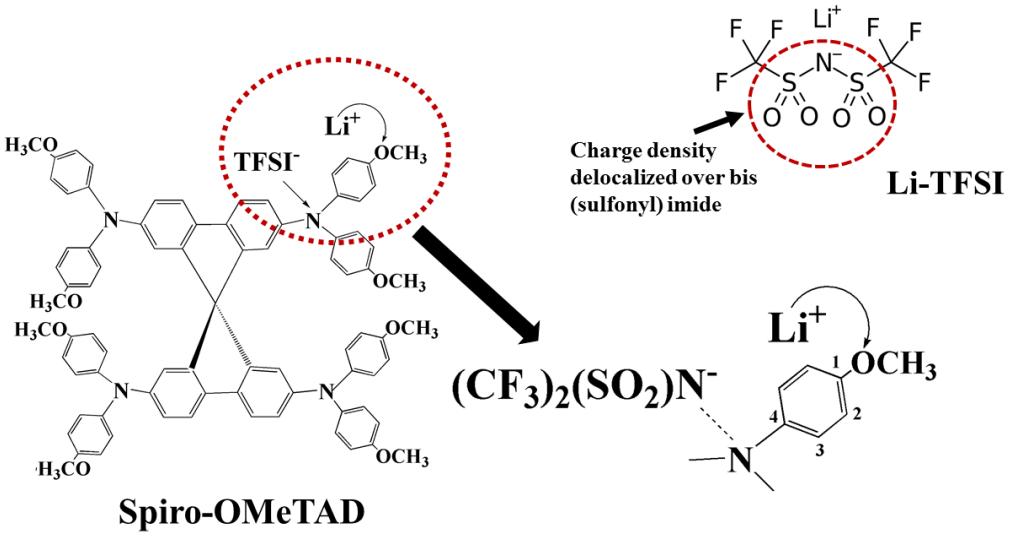

(a)

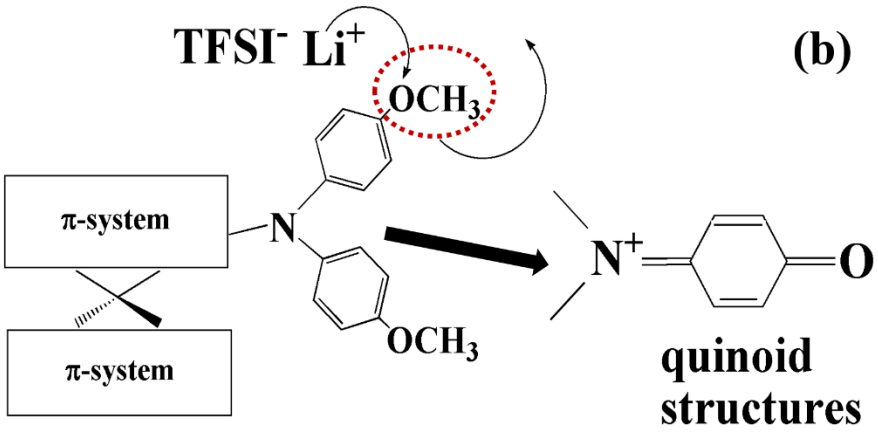

Figure 3.9 Suggested mechanism for (a) the interaction of Li-TFSI with spiro-OMeTAD and (b) formation of quinoid structures during spiro-OMeTAD oxidation due to loss of methoxy groups.

The resonances beyond 291.0 eV arise due to transitions from C1s→σ* molecular orbitals. The σ* resonances, I_6, I_7, I_8 and I_9 have been assigned to σ*C-C + σ*C-N [235,242,243], $\sigma_1 *$ with contribution from b_{2g} π* shake-up character, $\sigma_2 *$ and σ* C=C [207,210,213,237,244–248] transitions, respectively. The resonance at 292.0 eV might have a contribution from σ* C-F [249–252] in case of S10 and S20. The σ* shape resonances are usually broader since they involve multiple transitions or interaction of the in-plane carbon orbitals and hence the assignment of the transitions to the continuum states are quite ambiguous. An overall reduction in intensity of σ* resonances has been observed upon doping.

According to literature, doped spiro-OMeTAD shows the best conductivity with ~10% Li-TFSI [45]. C *K*-edge NEXAFS results reported in this chapter can be used to corroborate the conductivity results. It has been predicted here that 10% Li-TFSI is the optimum for best performance of spiro-OMeTAD since beyond that the aromaticity of the molecule is detrimentally affected which may result in reduced π-π stacking and possibly reduced hole conductivity.

N *K*-edge NEXAFS spectra

NEXAFS studies have been undertaken around the N *K*-edge to understand the effect of Li-TFSI doping on spiro-OMeTAD. The positions and assignments of the N *K*-edge resonances of spiro-OMeTAD are summarized in Table 3.4 and their origin have been discussed in the following sections.

Table 3.4 Peak positions and assignments of the N *K*-edge NEXAFS resonances of hole conductor molecules (pristine and doped).

Peak position ± 0.2 eV	**Assignment**	**Reference**
402.5	N1*s*→π* (Pyrrole N) + π* (amine N)	218,253
403.2	N1*s*→π* (Pyrrole N)	218
407.3	N1*s*→σ* (N-C)	218,235,254
411.5	N1*s*→σ*(N=C, N-C)	233,235,236

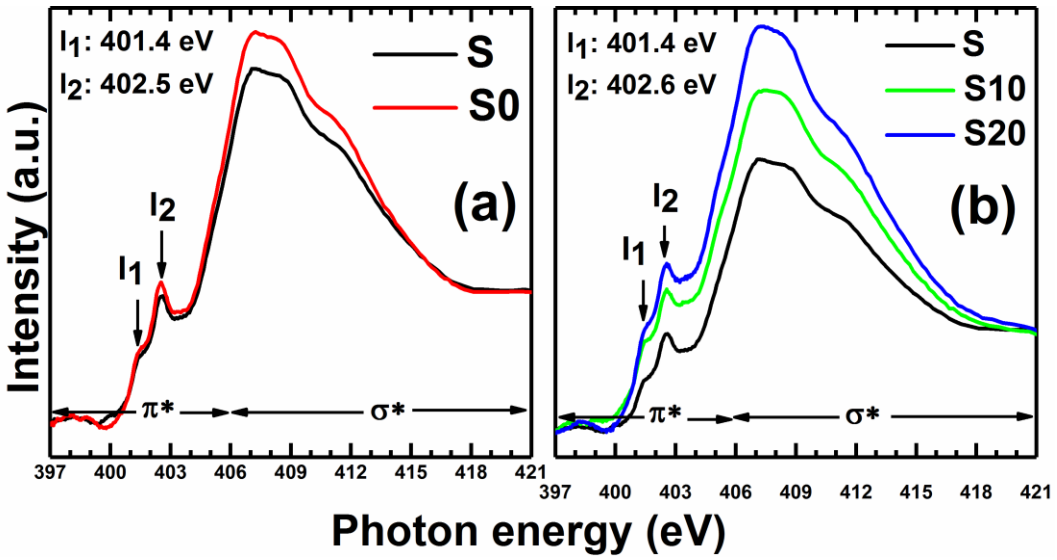

Figure 3.10 Comparison of N *K*-edge spectra of (a) pristine Spiro-OMeTAD (S) and tBP-doped (S0), (b) pristine S, doped with tBP, 10% and 20% Li-TFSI (S10, S20 respectively).

Figure 3.10 (a) compares the N *K*-edge spectra of pristine S and with tBP, S0. The spectra indicate clear signatures of π* and σ* states in the energy range 397-405 eV and

406-421 eV, respectively. The spectra are dominated by two π* resonances, denoted by I_1 and I_2, at 401.4 eV and 402.5 eV, respectively. The vast range of energy values and the assignments thereof make the absolute alignment of N *K*-edge features quite debatable. Schiros *et al.* [255] assigned the feature at ~401 eV to that of graphitic nitrogen whereas Gao *et al.* [256] and Schultz *et al.* [253] reported the same to be at 400.0 eV and 403.0 eV, respectively, in case of N-doped graphene and derivatives. According to Bhattacharya *et al.*, the peak at ~401 eV is a signature of pyrollic nitrogen [218,257]. Since, spiro-OMeTAD does not have nitrogen in any configuration other than amine structure, it is quite difficult to correctly assign the origin of the transitions. Hence, the resonance at 402.5 eV has been ascribed to transitions to antibonding orbitals localised on amine moieties [253]. Fantacci *et al.* performed density functional theory (DFT)/time-dependent DFT (TDDFT) calculations on the neutral and oxidised spiro-OMeTAD to understand the electronic and optical properties [62]. They reported a slight difference (0.006 Å) in bond length between the N-C bonds in the side chains of pristine spiro-OMeTAD. This difference in bond length is a plausible reason for splitting of the N1*s*→2*p* transitions in spiro-OMeTAD resulting in two π* features (Figure 3.10 a). Gutiérrez *et al.* have reported the splitting of C1*s*→π* transition resonance in graphene as a result of molecular orbitals formed between carbon atoms of different bond lengths [206]. The increase in edge jump intensity from S to S0 signifies an increase in nitrogen content in the molecule possibly due to the presence of pyridine N in tBP. But no separate signature is observed probably due to the high vapour pressure of tBP. It can be suggested that tBP which is used as an additive in the doping process is possibly only chemisorbed onto the doped film. The hybridization of the molecular orbitals of tBP and spiro-OMeTAD provides the additional decay channels for the excited core electrons of N1*s* and results in reduction of the lifetime of the final states.

Monotonic increase in the intensity of the π* resonances are observed with increasing Li-TFSI concentration (Figure 3.10 b). The splitting of the π* resonance in doped spiro-OMeTAD may be attributed to the difference in N-C bond length (0.022 Å) in doped spiro-OMeTAD [62]. Another possible reasoning may be the additional nitrogen environment from Li-TFSI. TFSI is a good nitrogen-based leaving group because the anionic charge is appreciably delocalized over the central bis(sufonyl) imide moiety. The inductive effect of the CF_3 groups further contributes to charge distribution (Figure 3.9) [258]. In the present study, the broadening of the π* and σ* resonances may also indicate the presence of additional decay channels available to the N atom in S10 and S20. During the oxidation of spiro-OMeTAD, formation of the spiro-$OMeTAD^{+}TFSI^{-}$ complex possibly leads to creation of additional DOS over the N atom. These unoccupied DOS provide additional decay channels for the transitions, thus resulting in increased π* intensity (Figure 3.9).

Thus, it was concluded that doping with Li-TFSI is instrumental in influencing the electronic properties of spiro-OMeTAD with both the carbon and nitrogen *K*-edges being affected. Further studies are required to understand the underlying mechanism regarding the influence of Li-TFSI dopant on the performance of spiro-OMeTAD.

3.3.3 Comparison of Spiro-OMeTAD (S), SFX-OMeTAD (M1) and SFX-TAD (M3)

(a) C *K*-edge NEXAFS

The understanding developed from the NEXAFS studies of spiro-OMeTAD doped with Li-TFSI has been extended to the case of two new hole conductor molecules SFX-OMeTAD and SFX-TAD (Figure 1.7) synthesized as low-cost alternatives to spiro-OMeTAD [12]. In this section, the C *K*-edge spectra of the pristine molecules S, M1 and M3 have been compared. The fundamental differences in molecular structure of the three

molecules are the presence of bridging oxygen in the SFX-based molecules and the absence of methoxy groups in M3. Comparison of C *K*-edge spectra of S, M1 and M3 is shown in Figure 3.11.

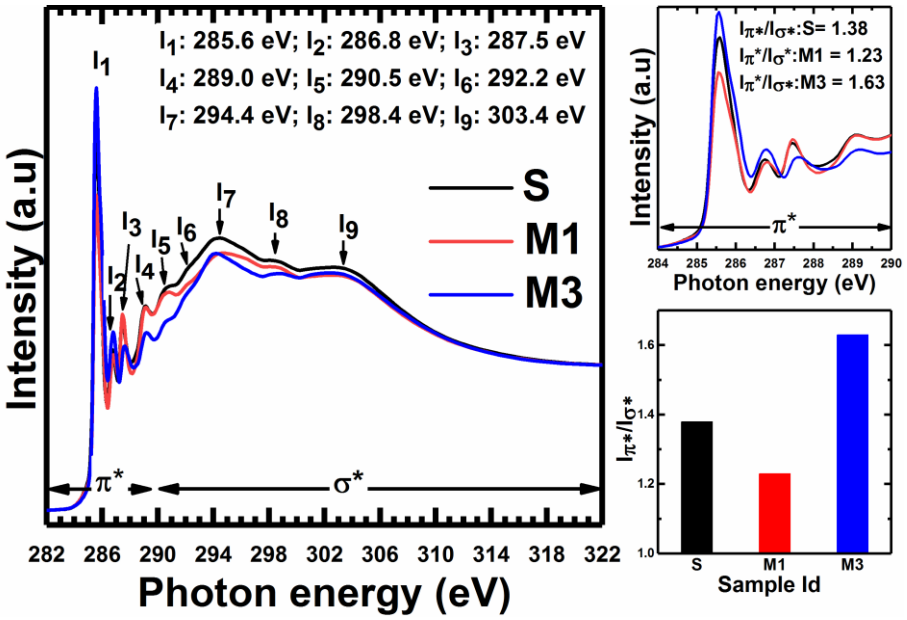

Figure 3.11 (a) Comparison of C *K*-edge NEXAFS spectra of S, M1 and M3, (b) π* resonances at the absorption edge and (c) variation in ratio of $\frac{I_{\pi*}}{I_{\sigma*}}$ for S, M1 and M3.

As can be observed from Figure 3.11 (b), I_1 reduces in intensity from S to M1 before increasing for M3. Spiro-OMeTAD molecule has a biflourene core structure with eight methoxy groups attached to the triaryl amine side chains. On the contrary, M1 and M3 have a xanthene core structure with a bridging oxygen which comprises a sp^3 hybridized carbon. Unlike M1, M3 lacks the eight methoxy groups. As explained earlier, the presence of methoxy groups has a role in influencing the intensity of the $1s \rightarrow \pi^*$ resonances. Presence of a methoxy group reduces the sp^2 or aromatic character of the benzene ring by making the carbon (of the $-OCH_3$) sp^3 hybridized as compared to the rest of the sp^2 carbon of the benzene backbone. The presence of the xanthene oxygen affects the π overlap depending upon the planarity of the system since the bridging oxygen can be either sp^2 or sp^3 hybridized depending on the planarity of the molecule.

This gives rise to more localisation of charge density on the aromatic rings compared to spiro-OMeTAD. The xanthene structure of M1 being sp^3 hybridized reduces the sp^2 character of the benzene rings and hence the reduction in π* intensity, whereas in M3 the lack of the electron donating methoxy groups leaves the charge cloud over carbon unperturbed which results in increased aromaticity. This is evident from the reduction in ratio of $\frac{I_{\pi^*}}{I_{\sigma^*}}$ from S to M1 but an enhancement for M3 (Figure 3.11 c). Broadening of the I_1 resonance, observed in case of M1 and M3 implies delocalization of π* orbitals [214]. Thus, it can be proposed that the presence of the bridging -O- in the xanthene core of M1 and M3 contributes to the origin of the higher energy shoulder. Change in lineshape may be due to difference in charge transfer. The reduced intensity of I_3 can be attributed to the absence of the methoxy groups in the molecular structure of M3 as compared to S and M1. The shift towards higher photon energy suggests that the electron-donating methoxy group alters the delocalization of the benzene rings in the molecule and brings about a change in the electronegativity around the C atom. An overall reduction in σ* resonances have been observed for M1 and M3 which his possibly due to the difference in charge transfer as a result of the variation in molecular structure.

Thus, it has been observed that SFX-TAD shows the best aromatic character when compared to spiro-OMeTAD and SFX-OMeTAD and has the possibility of functioning as the best hole conductor molecule.

(b) N *K*-edge NEXAFS

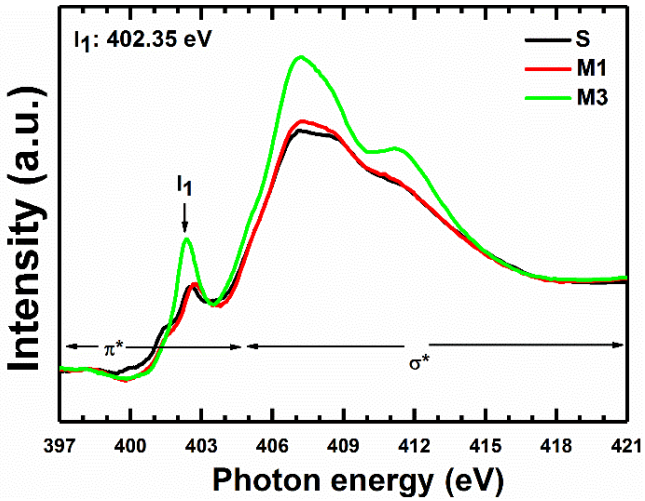

Figure 3.12 Comparison of N *K*-edge NEXAFS spectra of S, M1 and M3.

N *K*-edge spectra for S, M1 and M3 shows the presence of π* and σ* resonances (Figure 3.12). Unlike M3, clear splitting of the π* resonance is observed in case of S and M1. This has been attributed to either the inductive effect of the methoxy groups attached to the triphenyl side chains increasing the electron density over the amine nitrogen or as a result of the difference in bond length of the C-N bonds as proposed by Gutiérrez *et al*. in graphene [206]. The resonances are sharper in M3 compared to S and M1 indicating an enhanced aromatic character. Sharp resonances are observed when the orbitals over the benzene ring are delocalised, but the perturbation of the charge cloud by the presence of more functional substituents results in reduction in intensity of π* resonances. The broadness of the σ* resonances is due to superposition of contributions from a wide range of C-N bonds (delocalized pyridine-like and different N states in the fluorene aromatic backbone) [232,233].

Hence, C and N *K*-edge spectra indicate the better aromatic nature of SFX-TAD in comparison to spiro-OMeTAD and SFX-OMeTAD. This might suggest better π-π stacking and improved hole mobility in M3 compared to the other molecules.

3.3.4 NEXAFS of doped SFX-OMeTAD (M1) and SFX-TAD (M3)

In the following sections the variation in electronic properties as a result of doping with Li-TFSI of SFX-OMeTAD (M1) and SFX-TAD (M3) have been investigated with C and N *K*-edge NEXAFS.

(a) SFX-OMeTAD (M1)

C *K*-edge NEXAFS

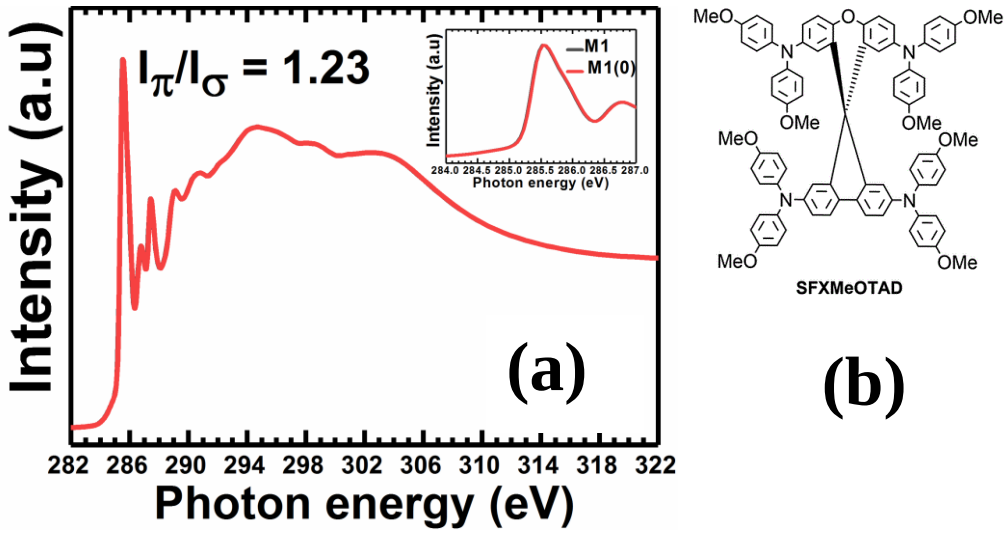

Figure 3.13 (a) Comparison of C *K*-edge NEXAFS spectra corresponding to SFX-OMeTAD, pristine (M1) and doped with tBP, M1(0) along with the $\frac{I_{\pi*}}{I_{\sigma*}}$ ratio. Inset shows the first π* resonance at the absorption edge and (b) Molecular structure of SFX-OMeTAD.

From Figure 3.13 (a) it can be observed that there is no appreciable variation in the C *K*-edge NEXAFS features corresponding to pristine (M1) and tBP-doped SFX-OMeTAD, M1(0). Hence, the discussion has been focussed on understanding the variation in electronic properties of SFX-OMeTAD due to Li-TFSI doping. The molecular structure of SFX-OMeTAD has been shown in Figure 3.13 (b).

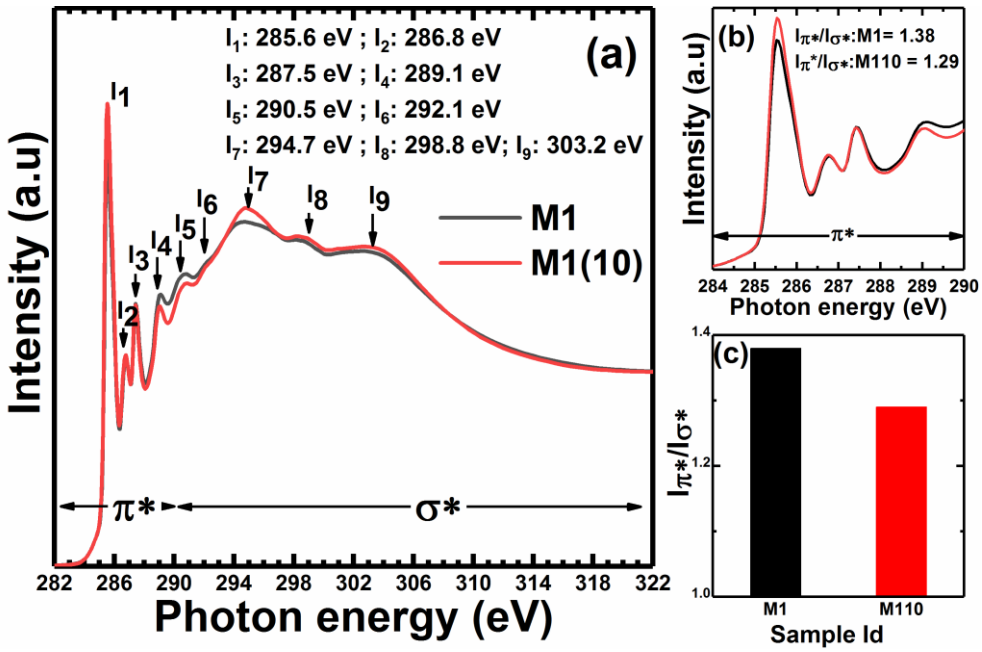

Figure 3.14 (a) Comparison of C *K*-edge NEXAFS spectra corresponding to pristine SFX-OMeTAD (M1) and doped with tBP and 10% Li-TFSI, M1(10), (b) π* resonances at the absorption edge and (c) variation in $\frac{I_{\pi*}}{I_{\sigma*}}$ ratio upon Li-TFSI doping.

C *K*-edge spectra of doped M1 samples have been compared in Figure 3.14 (refer to Table 3.1 for the list of samples samples). Five π* and four σ* resonances are observed for M1 and M1(10) which can be assigned as in the previous section (refer to Table 3.3). Unlike doped S samples, the aromaticity of M1 post-doping shows a different trend as is evident from the decrease in $\frac{I_{\pi*}}{I_{\sigma*}}$ from 1.38 to 1.29 upon addition of 10% Li-TFSI. In M1, the presence of the bridging oxygen in the xanthene structure introduces sp^3 bonds in the aromatic framework. It can be proposed here that Li^+ ions exert an attractive force towards the bridging oxygen due to their affinity for oxygen which results in a redistribution of charge density within the xanthene core. This redistribution might contribute towards reduction in π* transitions. Since, M1 has almost similar molecular structure to S, it has been considered that when Li-TFSI is added to M1, the SFX-$OMeTAD^+TFSI^-$ radical cation formed is weakly bound by the highly delocalized charge

on the TFSI anion and the Li^+ ion interacts with the -O- atom in the xanthene core of M1. Here it is proposed that the bridging -O- group is beneficial for the molecule since the π* aromatic character of the molecule is enhanced because of its presence. In xanthene structure, the Li complexes with Ar-O-Ar in preference to –OMe, thus affecting the π systems due to the sp^2/sp^3 nature of the bridging oxygen in xanthene. Slight reduction in intensities of I_4 and I_5 is observed due to the influence of Li^+ on the charge density over M1. When the Li^+ ions attack the bridging O site, there is slight redistribution of the electron density on the xanthene structure, without the disruption of any bond. This C_1 atom then pulls the charge cloud from $C_{2,3,4}$ to compensate for the charge density and hence the corresponding resonance I_4 decreases. Whereas the coupling of TFSI anion with the N site of SFX-OMeTAD does not drastically affect the charge density as to result in appreciable loss in intensity. But the C_1 is most affected since it is the site of attachment of the -O- bond. All the σ* resonances at 292.1 eV, 294.7 eV, 298.8 eV and 303.2 eV increase in intensity with increasing doping concentration due to increase in transitions from C=C, C-C, C-N, and C-O bonds. It can be proposed that Li^+ ions possibly have greater affinity for the bridging oxygen compared to oxygen in the methoxy group. Further studies must be undertaken to optimise the doping % for M1.

N *K*-edge spectra

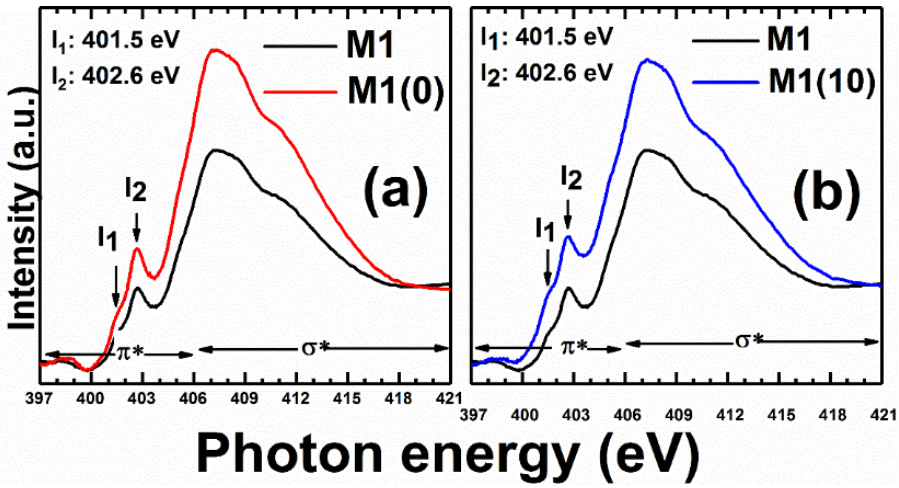

Figure 3.15 Comparison of N *K*-edge NEXAFS spectra corresponding to (a) SFX-OMeTAD, pristine (M1) and tBP-doped, M1(0) and (b) SFX-OMeTAD (M1), SFX-OMeTAD doped with tBP and 10% Li-TFSI, M1(10).

N *K*-edge spectra for M1 and M1(0) are shown in Figure 3.15 (a) and the edge-jump intensity which is proportional to the total nitrogen content shows an enhancement in M1(0) compared to M1. The substantial increase in area under the curve due to addition of tBP might mean that tBP has pronounced effect on SFX-OMETAD compared to spiro-OMeTAD. Steady increase in the nitrogen content of M1 after addition of Li-TSFI dopant is observed from Figure 3.15 (b) which points towards increase in π* and σ* DOS over nitrogen. Similar to the effect observed in doped spiro-OMeTAD films (Figure 3.10), splitting of N1*s*→π* resonance in SFX-OMeTAD may be due to the difference in bond length between N-C bonds in M1.

(b) SFX-TAD (M3)

C *K*-edge NEXAFS

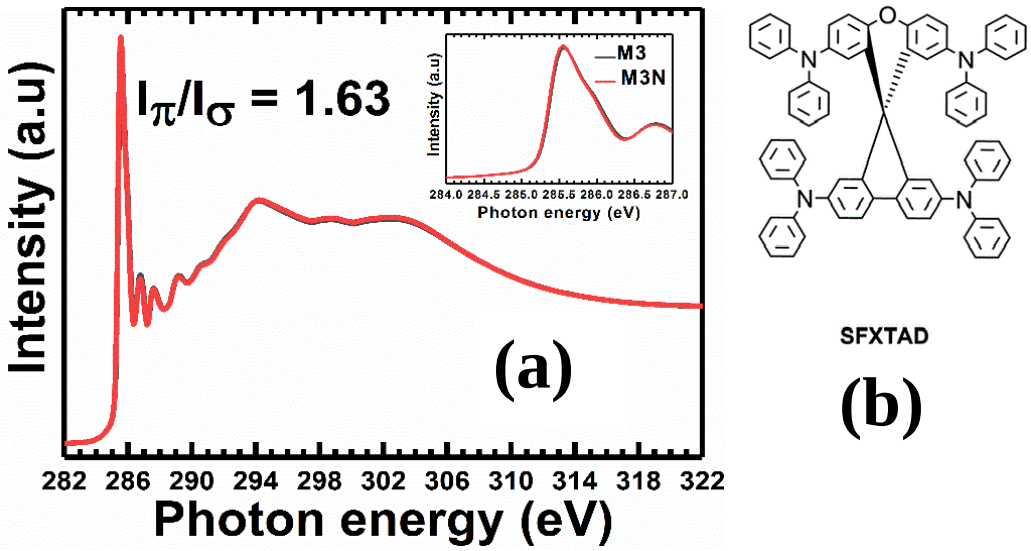

Figure 3.16 (a) Comparison of C *K*-edge NEXAFS spectra corresponding to pristine SFX-TAD (M3) and doped with tBP, M3D along with $\frac{I_{\pi*}}{I_{\sigma*}}$ ratio. Inset shows the first π* resonance at the absorption edge and (b) Molecular structure of SFX-TAD.

Figure 3.16 (a) shows the C *K*-edge NEXAFS spectra of pristine SFX-TAD (M3) and doped with tBP (M3N). There is no observable difference in the spectra possibly due to the high vapour pressure of tBP which leaves behind no spectroscopic signature. Molecular structure of SFX-TAD has been shown in Figure 3.16 (b).

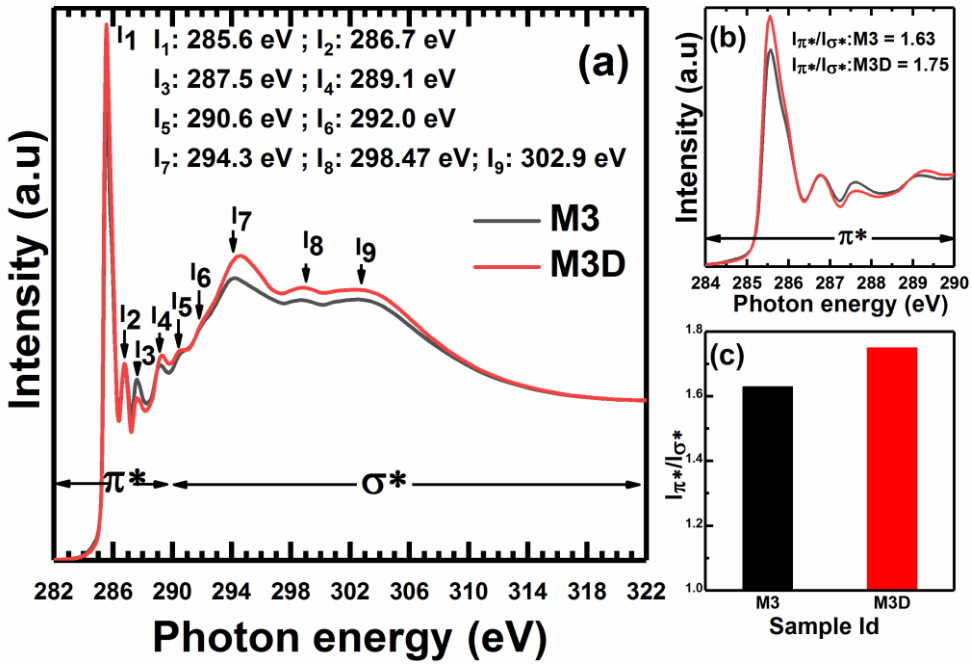

Figure 3.17 Comparison of C *K*-edge NEXAFS spectra corresponding to SFX-TAD (M3) and SFX-OMeTAD doped with tBP and 10% Li-TFSI (M3D), (b) π* resonances at the absorption edge and (c) variation in ratio of $\frac{I_{\pi*}}{I_{\sigma*}}$ upon Li-TFSI doping.

The C *K*-edge NEXAFS spectra of M3 and M3D are shown in Figure 3.17. Though the number of resonances is the same as those of doped S and M1 (described in sections 3.3.1 and 3.3.5), the line shapes show distinct variations. To begin with, $\frac{I_{\pi*}}{I_{\sigma*}}$ value increases from 1.63 for pristine to 1.75 for M3D signifying an enhancement in π* states. Resonance I_3 decreases substantially from M3 to M3D presumably due to exposure to ambient conditions prior to measurements being undertaken. There is very slight enhancement of I_4 and I_5 resonances with doping which suggests that Li-TFSI results in enhancement of π* states around carbon. The σ* shape resonances become sharper possibly due to increased aromatic nature of SFX-TAD.

Thus, it can be concluded that Li-TFSI doped M3 would possibly show improved hole conductivity as a result of enhanced aromatic character and better π-stacking of molecules.

N *K*-edge NEXAFS

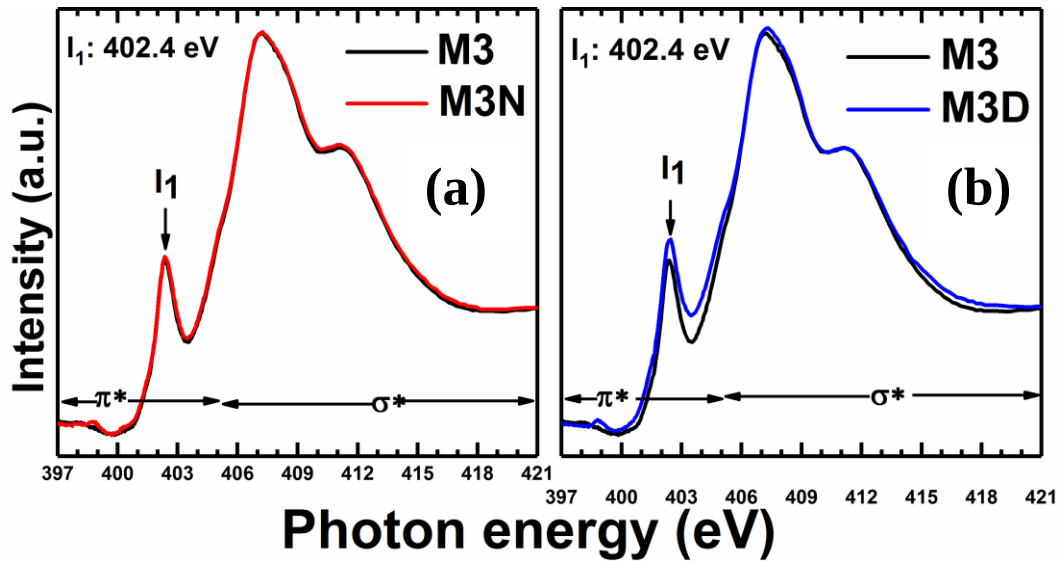

Figure 3.18 Comparison of N *K*-edge NEXAFS spectra of (a) SFX-TAD, pristine (M3) and tBP-doped (M3N) and (b) SFX-TAD, pristine (M3) and doped with tBP and 10% Li-TFSI (M3D).

Figure 3.18 (a) shows the comparison N *K*-edge spectra of M3 and M3N which shows negligible increase in nitrogen after addition of tBP. In contrary to the spectra acquired from doped S and M1 molecules (refer to Figure 3.10 and Figure 3.15, respectively), the N *K*-edge spectra of M3 shows no splitting of the N1*s*→π* resonance which implies that the bond length of N-C bonds in M3 are identical. Thus, it can be suggested that the presence of electron-donating methoxy group is responsible for the variation in the bond length of N-C groups as is the case with S and M1. Doping with Li-TFSI and tBP results in improved π* resonance which is suggestive of variation in local nitrogen environment in M3 and a similar mechanism (to doped S and M1 molecules) for the formation of SFX-TAD^{+}TFSI^{-} complex may be proposed (Figure 3.18 b). But the effect of doping on M3 is not as pronounced as in S and M1 molecules, which might possibly suggest that the presence of methoxy affects the charge density over the

molecules differently and has a crucial role in influencing the charge transfer in the molecules.

3.4 Conclusions

The Li-TFSI and tBP doping has been undertaken for three different hole transport molecules, spiro-OMeTAD, SFX-OMeTAD and SFX-TAD. SFX-OMeTAD and SFX-TAD have been synthesized as low-cost alternative HTMs to spiro-OMeTAD and differ from the same in having a bridging oxygen in the form of a xanthene core. X-ray spectroscopy (NEXAFS and XPS) have been undertaken to understand the variation in electronic properties of the molecules as function of doping with Li-TFSI. The major conclusions drawn from this work are (i) Both C and N *K*-edge spectra show the formation of additional unoccupied states after the doping procedure as is evident from the broadening of the resonances. (ii) Splitting of π* resonances have been observed in the C *K*-edge NEXAFS spectra of S, M1 and M3 molecules which were assigned to the transitions from the two C1*s* core levels to the three π* molecular orbitals. The strong interaction between localized π* and σ* orbitals produces widely separated delocalized states are thought to be the reason for the break in degeneracy. The splitting of resonances is not only due to splitting of the C1*s* levels but also as a result of transitions into different π* non-degenerate orbitals. (iii) It has been proposed that the bridging oxygen group in the xanthene core is beneficial for M1 and M3 molecules since it contributes towards enhancement of their aromaticity. But the methoxy groups in S and M1 affect the molecules unfavourably by disrupting the π* resonances and hence the aromatic nature of the molecules is reduced. (iv)The electron-donating -OMe group also has an important role in influencing the chemistry of doped S, M1 and M3. It has been suggested that the affinity of Li^+ ions towards oxygen results in perturbation of electron density over the doped molecules. This leads to variation in resonance intensities as a

result of combined effects of electron-donating methoxy groups, $TFSI^-$ anion and attractive pull of the Li^+ ions. (v) When compared within the differently doped spiro-OMeTAD molecules i.e. S, S10 and S20, spiro-OMeTAD doped with 10% Li-TFSI (S10) showed the best aromatic character and improvement in conductivity reported in literature can be correlated from the enhancement in π* density of states. (vi) In M1 and M3 molecules, Li^+ is proposed to distort the bridging oxygen site thereby influencing the intensity and probability of C1*s*→2*p* transitions. From the ratio of $\frac{I_{\pi*}}{I_{\sigma*}}$ it can be concluded that M3 demonstrated the best aromaticity between S, M1 and M3 molecules. (vii) Binding of the benzene rings with the N atom in the triaryl amine structure of S, M1 and M3 results in splitting of the N1*s*→π* resonance due to the extended π-π* system where more than one π* molecular orbital is available for the electrons excited from N1*s* core level. XPS results reveal that doping with Li-TFSI not only results in oxidation of spiro-OMeTAD but also variation in the local chemistry around N which possibly influences the conductivity of the doped films. A steady reduction in intensity of C-H component is also observed and the formation of the F1*s* peak with increasing dopant concentration. (viii) Incorporation of gas molecules into the doped films of S, M1 and M3 is confirmed from the observed increase in FWHM of XPS core level spectra. Thus, it can be concluded that doping of spiro-OMeTAD, SFX-OMeTAD and SFX-TAD improves their electronic properties. These results provide deeper understanding of the doping and electronic properties in spiro-OMeTAD, SFX-OMeTAD and SFX-TAD films and their application as HTL in PSCs.

Chapter 4

Dopant-free atmospheric pressure plasma functionalized spiro-OMeTAD-efficient hole transport material for perovskite solar cells

A dopant-free technique for functionalization of spiro-OMeTAD to increase the conductivity using atmospheric pressure plasma jet has been investigated in this chapter. Systematic investigation of plasma functionalization for 3, 4 and 5 minutes was carried out. An enhancement in conductivity from 9.4 x 10^{-7} S cm^{-1} for the pristine film to 6.35 x 10^-6 (3 minutes), 7.83 x 10^-6 (4 minutes) and 1.15 x 10^{-5} S cm^{-1} (5 minutes) of plasma treatment was observed. Conductivity values after 5 minutes of plasma functionalization was comparable to that of reported values for spiro-OMeTAD doped with 10-25% of Li-TFSI. A plausible reason can be an increase in the charge density in the molecule due to the presence of energetic species in the plasma jet. Plasma functionalization may also improve π-π stacking, thus improving the conductivity. The increase in conductivity was correlated to reduction in phase value from EFM. Oxidation of spiro-OMeTAD was also confirmed by the formation of the 500 nm absorption peak from UV-vis spectroscopy. An increase in work function after plasma exposure as measured by KPFM proved the p-type nature of the doping procedure. Plasma treatment did not induce much damage to the morphology of the films with the surface roughness values increasing slightly from 0.8 nm to 1.2 nm post plasma treatment. No pinholes were observed in the films even after several days of exposure to atmospheric conditions. Spectroscopic investigation with XPS showed surface oxidation of plasma functionalized films and variation in nitrogen chemistry. This work opens up the possibility of using atmospheric pressure plasma jet as a facile and effective means of doping and surface functionalization of spiro-OMeTAD thin films to circumvent the detrimental issues associated with different chemical dopants.

4.1 Introduction

Over the past few years organometal hybrid halide perovskite solar cells have attracted significant scientific and industrial attention due their rapid progression in device performance exceeding 23% [11]. The HTM serves a two-fold purpose in defining the efficiency/performance and the stability of PSCs

(i) extraction of positive charges (holes) and conduction to the top electrode.

(ii) prevention of direct contact between perovskite and metal electrode, which minimizes recombination and also stop moisture ingress into the perovskite layer

beneath in n-i-p architecture [259–261]. Hence, tailoring the properties of HTM is key for the development of PSCs.

Spiro-OMeTAD is one of the most common choice for HTL to date. However, pristine spiro-OMeTAD suffers from low hole mobility ($\sim 10^{-5} cm^2 V^{-1} s^{-1}$) [35,41] and conductivity (~10^{-7} S cm^{-1}) [37,42,43]. Electronic doping is a suitable technique to tune the type and density of charge carriers as well as bring about controllability and reproducibility of efficient device performance [41,45–49]. Addition of dopants not only generates additional charge carriers but also tunes the electronic properties and different dopants such as Na-TFSI [51], Ag-TFSI [52], Co (III) complexes [42,53,54], WO_3 [55], Cu(II) salts [56,57] have been utilised to dope spiro-OMeTAD [45,55,58–62]. Some of the p-type dopants exhibit poor solubility in organic solvents, high volatility, and/or involve intensive and complicated synthesis procedure, thus limiting their application in solution-processed PSCs. Moreover, a few display vibrant colours which might interfere with the light absorption of the photosensitizer in the visible region of the spectrum. Li-TFSI is the most widely used p-type dopant and has been demonstrated to improve the conductivity of spiro-OMeTAD by shifting the Fermi level towards the HOMO [45,59]. Addition of Li-TFSI leads to improvement of the solar cell efficiency, and reduces recombination losses at interfaces which might be due to alteration of the TiO_2 band edge position for higher potentials [37,64]. However, being hygroscopic in nature is a major drawback for Li-TFSI since it may result in pin-holes and degradation of the perovskite absorber [45,67,75,76]. tBP improves miscibility of spiro-OMeTAD and Li-TFSI and impedes phase segregation in solution resulting in uniform distribution of Li-TFSI during thin film deposition but due to the relatively low boiling point and volatile nature of tBP, it gets evaporated easily, leaving behind an accumulation of hygroscopic Li-TFSI [67,77]. To address these key challenges, a dopant-free facile technique for functionalization of spiro-OMeTAD films

using non-thermal atmospheric pressure plasma jet to increase the hole conductivity has been proposed in this chapter.

Non-thermal atmospheric pressure plasma jets find widespread applications in sterilization [89,90],modification of polymers for improved surface wettability and cleaning [91–93],environmental and industrial applications [94] and in medicine [95]. The benefit of plasma technology is wet free doping of semiconducting nanomaterials with heteroatoms to tune the band gap energy and conductivity for many promising applications. Atmospheric pressure plasma jets comprise charged particles, neutral metastable species, radicals and radiation in UV and visible region [88]. APPJs with lower gas temperature are suitable for treating temperature sensitive materials and are also found to be easily adapted to complex geometries and conventional processes. Oxygen plasma has been used extensively for surface functionalization of graphene and its oxide as electrodes for LEDs, field effect transistors (FETs), molecular sensors and many more [133,167,262]. The application of plasma jets is confined to surface cleaning and removal of impurities from FTO and ITO in DSSCs and PSC, resulting in improved device performance [110,111]. Idígoras *et al*. have used plasma polymer for encapsulation of PSCs and observed no change in the absorbance of the encapsulated perovskite films 30 days in ambient conditions with relative humidity of 35-60% [112]. Rolston *et al*. demonstrated the improvement in efficiency and stability of PSCs using a submicron organosilicate barrier film by scalable cold plasma spray process [113]. Oxidizing species and heat from the plasma is thought to be responsible for the enhancement in device performance by improving interfacial contact and conductivity of the hole transporting layer. In early 2018, Xiao *et al*. used argon plasma treatment to modify the surface composition of perovskite absorber by tuning the ratio of organic and inorganic components and defects [114]. This protocol resulted in enhancement of charge collection at the perovskite-electrode interface by impeding charge recombination with 20.4% device efficiency.

Hilt *et al*. demonstrated a scalable atmospheric pressure plasma post-deposition technique to rapidly form efficient and mechanically robust $CH_3NH_3PbI_3$ perovskite layer without the need of hot plate for curing the active material [115]. Air plasma arc discharge was used for 250 ms exposure to obtain defect-free films showing ultrafast crystallization and a very good PCE of 15.7%. The presence of reactive oxygen and nitrogen species in the plasma was proposed to be the reason for the rapid nucleation and growth of perovskite crystals monitored by *in situ* wide angle X-ray scattering. The influence of oxygen plasma treatment on NiO_x layer as HTL for PSCs in p-i-n architecture was reported by Nishihara *et al* [116]. They demonstrated the improvement in wettability and a consequent enhancement in efficiency to 12.3% after the plasma treatment process.

A systematic time-dependent oxygen atmospheric plasma treatment to functionalise spiro-OMeTAD films resulted in defect-free films with enhanced conductivity. Detailed investigation of electronic, optical properties and surface morphology was carried out. As PSCs are the new generation solar cells which have shown incredible progress within a short span, rigorous research is focussed on both the active layer as well as hole transporting material and tailoring the properties of the HTM is of great importance.

4.2 Experimental section

4.2.1 Deposition of spiro-OMeTAD films

Thin films of spiro-OMeTAD were deposited as described in Section 2.1.1 of Chapter 2.

4.2.2 Atmospheric pressure plasma jet (APPJ) for surface functionalization

The in-house atmospheric pressure plasma jet used for the functionalization of the spiro-OMeTAD films is as shown in Figure 2.1. The plasma was ignited with helium (as

the carrier gas) and oxygen having flow rates of 3000 and 30 standard cubic centimetre per minute (sccm), respectively, with an input power of 10 W. The thin films of spiro-OMeTAD on silicon were kept at 5 mm from the plasma jet source to prevent arcing between the sample and electrodes and rastered with oxygen plasma jet for 3, 4 and 5 minutes to obtain uniform functionalized thin films.

4.2.3 Characterization

The characteristics of the plasma jet was studied with the help of optical emission spectroscopy using a S2000+ Ocean Optics spectrometer and the signals were collected through an optical fibre for the plasma jet. UV-Vis spectroscopy was performed with a JASCO UV-Vis equipment. The electronic properties were investigated using X-ay photoelectron spectroscopy with a load-locked KRATOS XSAM-800 instrument equipped with a dual anode X-ray source using Mg Kα (1253.6 eV) excitation source. The high magnification analyser mode was chosen to collect electrons from the smallest possible area on the specimen for C1*s*, O1*s* and N1*s* core levels. Analysis of the XPS data was performed with CasaXPS version 2.3.16 software. The spectra were fitted with combined Gaussian and Lorentzian line. The morphology of the spiro-OMeTAD films, before and after plasma treatment, was studied with a ZEISS Supra 55 Variable Pressure Field Emission Scanning Electron Microscopy (SEM). Spectroscopic Ellipsometry was performed to calculate the thickness of thin films using a Jobin-Yvon/Horiba equipment operating a DeltaPsi2 v.2.0.8 software using a linearly polarized light at 45° incidence at three different positions on the thin films. The experimental wavelength range was chosen to be 250-800 nm (1.5-5.5 eV) and all measurements were made under ambient temperature, pressure and humidity conditions. The results were modelled using the Tauc-Lorentz oscillator model. A Leica optical microscope was used to acquire the optical images. An Asylum research MFP3D AFM equipped with a vibration isolation stage was used to study the surface and map the surface conductivity and surface

potential of the samples using Pt-Ir coated silicon probes (PPP-EFM-10, Nanosensors) with force constant of 2.8 N/m. The tip was biased at +5 V with a drive amplitude of 300 mV. The image parameters were set at scan size of 10 μm x 10 μm, scan rate 0.5 Hz, 512 points and lines. EFM and KPFM measurements were performed in the 'tapping' mode and the 'Nap' mode at delta height of 30 nm to obtain the height and potential profiles. The Gwyddion program was used to obtain the height profile and normalized nap phase images from the EFM and KPFM data. Sheet resistivity measurements were carried out with 4-point probe equipment using a Keithley Pico ammeter.

4.3 Results and Discussion

4.3.1 Optical Emission spectroscopy (OES) of the helium and oxygen plasma jet

Optical emission spectroscopy provides a non-invasive probe to investigate atoms, ions and molecules within a plasma to gain insights into the plasma chemical processes. In this work, OES was used to study the different species present in the atmospheric pressure helium-oxygen plasma jet. Figure 4.1 represents the optical emission spectra of the effluent from the helium-oxygen discharge. The nature of the plasma depends on the gas phase composition i.e. the excited atoms, ions and molecules. The emission spectra consist of atomic and molecular oxygen, as well as helium and nitrogen species emission peaks within the wavelength range of 200 nm to 880 nm. Since oxygen is an electronegative element, addition of oxygen to the plasma produces O^- and O^{2-} ions. Atomic and molecular lines of the selected reactive species are clearly observed in the spectra such as OH- transitions at 308 nm, N_2(C-B) second positive system with electronic transitions $C^3\prod_u \rightarrow B^3\prod_g$ in the range 300-450 nm, He I transition $3s^3S^1 \rightarrow 2p^3P^0$ at 706.8 nm, O I transitions $3p^5P \rightarrow 4d^5D^0$ at 615.8 nm, $3p^5P \rightarrow 3s^5S^0$ at 777.4 nm and $3p^3P \rightarrow 3s^5S^0$ at 844.8 nm and the A-band of molecular oxygen

corresponding to the transition $b^1\Sigma_g^+ \rightarrow X^3\Sigma_g^-$ at 760 nm [263–265]. The spectral emission of molecular oxygen is generally very weak and hence are not readily discernible in the emission spectra and in this work only the A-band at 760 nm has been recorded. Additional emission lines for helium discharge are observed at 391.3 nm and 427 nm for N_2^+ first negative system with electronic transitions $B^2\Sigma_u^+ \rightarrow X^2\Sigma_g^+$ ($\Delta v=0$) [266–268]. Strong N_2 emission lines was observed in the spectrum from helium discharge which has been reported previously in atmospheric pressure discharges arising due to the electron impact as the plasma plume propagates in ambient air [94]. Interestingly, the emission line at 308 nm due to the OH- transition is very prominent in the Helium plasma but is suppressed in the helium-oxygen plasma possibly due to the collisional quenching with oxygen molecules resulting in excited oxygen species in the plasma. The increase in O777 emission might suggest the preference for dissociative excitation whereas O845 emission signifies dominance of atomic oxygen excitation[264]. An increase in intensity of both the O777 and O845 emission lines in the helium-oxygen plasma jet would suggest an interplay of both dissociative and direct excitations mechanisms. In the spectrum for pure helium discharge, a series of strong peaks in the region of 215 nm to 271 nm originating from NO (γ) $A^2\Sigma^+ \rightarrow X^2\Pi$ is representative of the presence of oxygen in the afterglow [94,269]. The identified reactive species in the plasma jet such as singlet oxygen, hydroxyl radicals, metastables and photons play a significant role in surface functionalization of spiro-OMeTAD as will be demonstrated in this chapter.

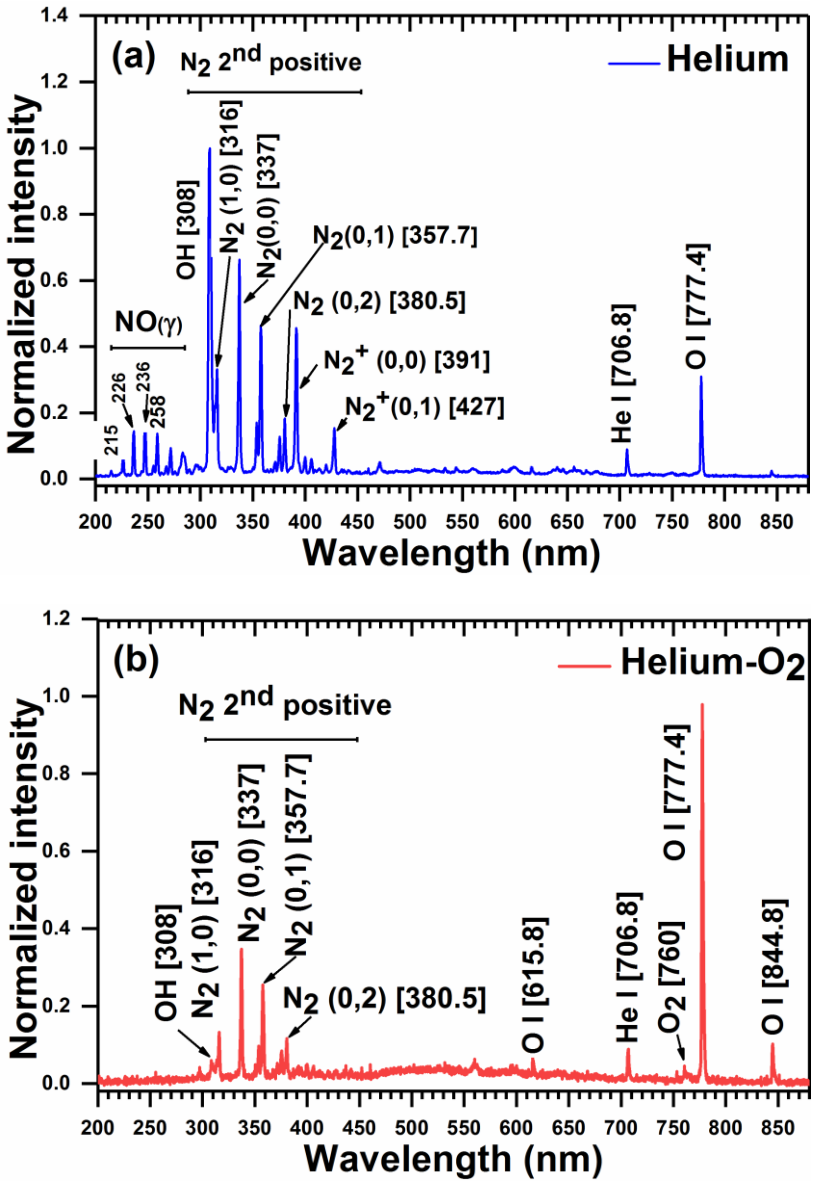

Figure 4.1 Optical emission spectra of the afterglow region of the APPJ (a) He discharge and (b) He (3000 sccm) + O_2 (30 sccm) discharge.

4.3.2 Electronic properties

X-ray photoelectron spectroscopy was used to probe the electronic properties and local chemical environment due to plasma functionalization of the spiro-OMeTAD films. C1*s*, N1*s* and O1*s* high resolution XPS spectra were energy calibrated with respect to the C1*s* of freshly-cleaved HOPG at 284.5 eV (Figure 2.4) and Au 4*f* peak at 84 eV as reference. Pristine spiro-OMeTAD molecule is composed of 81 C, 4 N and 8 O atoms (as shown in Figure 1.5). No X-ray induced damage was observed on the samples.

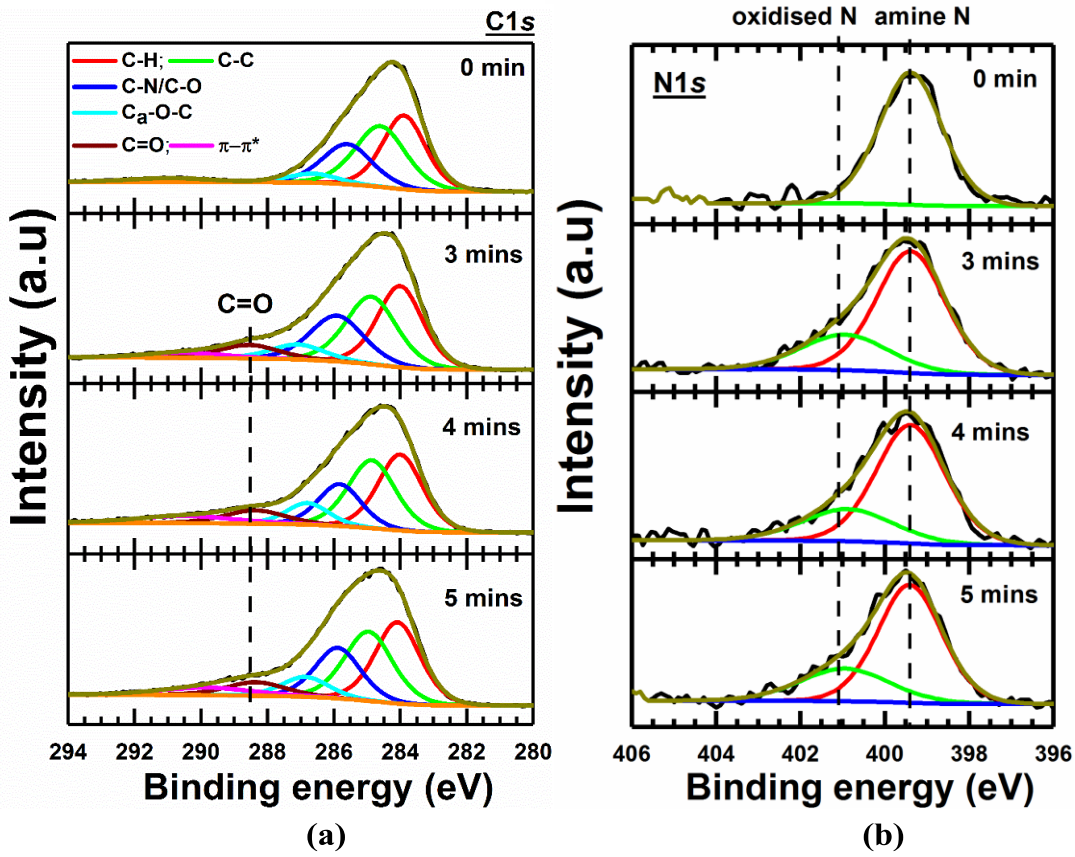

Figure 4.2 Variation of (a) C1*s* and (b) N1*s* XPS spectra of spiro-OMeTAD as a function of plasma treatment time.

C1*s*: Figure 4.2 (a) shows the C1*s* core level spectra as a function of plasma treatment time. The C1*s* spectra were fitted with an asymmetric Gaussian-Lorentzian line shape. Results of the fitting indicates untreated spiro-OMeTAD can be deconvoluted into C-H, C=C/C-C, C-N, C-O-C and π-π* components. The main peak at 283.9 ± 0.1 eV corresponds to C-H functionality, followed by the contribution at 284.8 ± 0.1 eV which is from a combined effect of C=C and C-C groups. The sp^3 bonded carbon occurs at 0.5 eV above the binding energy of sp^2 bonded configuration. The components at 285.8 ± 0.1 eV and 286.9 ± 0.2 eV have contributions from carbon singly bonded to nitrogen and C_a-O-C (C_a signifies the aromatic C), respectively [46,47,55,202]. The values agree quite well (within ± 0.5 eV) as reported in literature. The feature at ~291.0 eV is because of π-π* plasmon contribution.

In Figure 4.2 (a), the comparison of C1*s* line shape of untreated and plasma-treated spiro-OMeTAD shows a significant inhomogeneous broadening towards higher binding energy even with 3 mins treatment. This broadening can be attributed to the surface oxidation of spiro-OMeTAD films via the attachment of functional groups such as C-OH and C=O [270,271]. For the plasma-functionalized films, the C1*s* core level spectra were deconvoluted into C-H, C=C/C-C, C-N, C_a-O-C, C=O and π-π* components. The additional C=O component at 288.5 eV is as a result of the presence of different oxidised species in the plasma jet which bonded to carbon atoms of the spiro-OMeTAD film. The bombardment of the energetic ionic species present in the plasma jet may lead to the formation of defects which in turn form favourable sites for the attachment of oxygen moieties and hence contribute to surface functionalization. The fitting parameters extracted from the XPS spectra are summarized in Table 4.1.

A 0.2 eV decrease in the FWHM of the C bonded to C component from 1.8 (pristine) to 1.6 eV (4 mins) is observed from Figure 4.2 (a). The concentration of aromatic C bonded to O (C_a-O-C) component increases from 4.9% (pristine) to 7.0% upon 3 minutes of plasma functionalization. Further enhancement to 8.5% and 7.9% after 4 minutes and 5 minutes of plasma exposure, respectively, is observed. Monotonic increase in the C=O component is also observed from 0 to 7.0%. This signifies an enhancement in the carbon bonded to oxygen species to the aromatic structure of spiro-OMeTAD molecule. Figure 4.3 shows the trend of increasing (a) C_a-O-C and (b) C=O species from pristine to doped spiro-OMeTAD samples. The area of the π-π* plasmon peak shows a monotonic increase upon plasma functionalization from 3.6% (pristine) to 6.4% after 4 mins of plasma before settling at 6% for the 5 mins sample. The FWHM of the C-C/C=C component and the area of the plasmon feature can be used to describe the aromaticity of spiro-OMeTAD molecules. A larger π-π* peak signifies a polyaromatic system [272,273]. Hence, in the present study, the reduction in FWHM of the C-C

component and the increase in area of π-π* component can be attributed to an improvement in aromaticity of spiro-OMeTAD upon helium-oxygen functionalization. Increase in aromaticity might contribute to increase in conductivity as has been discussed in later sections.

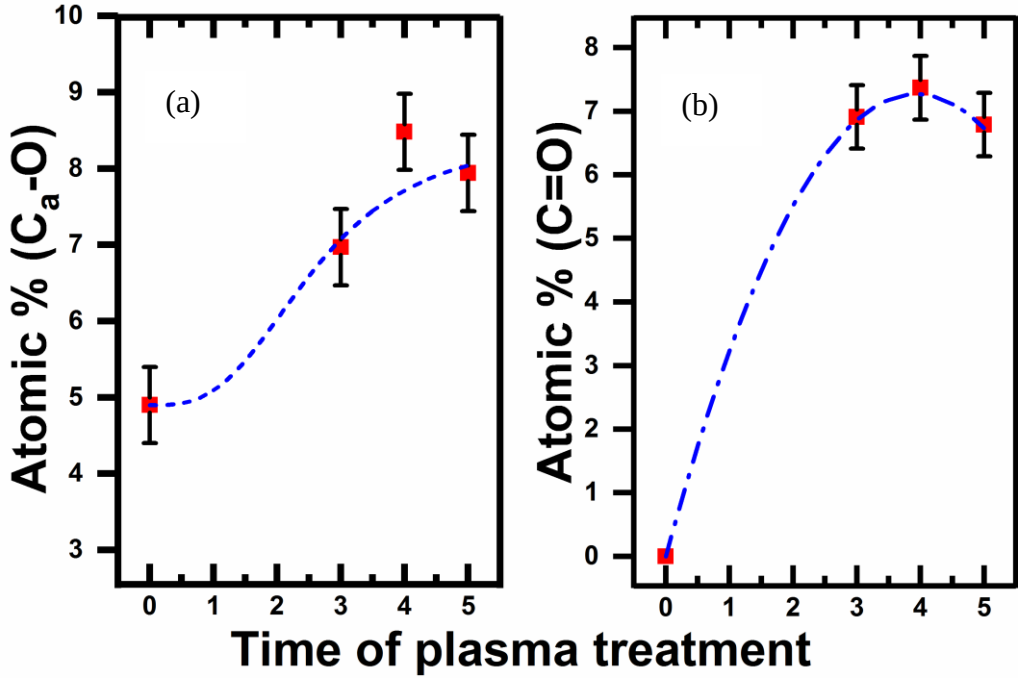

Figure 4.3 Variation of atomic percentage of (a) C_a-O-C and (b) C=O component with time of plasma functionalization.

N1*s*: Figure 4.2 (b) shows the comparison of high resolution N1*s* spectra of untreated and time-dependent plasma-treated spiro-OMeTAD. There is ambiguity in literature with regards to assignment of the exact position of the amine C-N in pristine spiro-OMeTAD with Scholin *et al.* having reported the N1*s* peak due to amine C-N from spiro-OMeTAD at 400.3 eV from XPS studies on a similar triphenyl amine hole conductor molecule [202,217]. However, in this study the spectrum for the untreated spiro-OMeTAD film was fitted with one component centred at ~399.5±0.15 eV corresponding to the amine N species of spiro-OMeTAD [46,274–277] which is ~0.8 eV shifted from other reports. The spectra for the plasma-treated films, irrespective of the time of plasma

functionalization, show a substantial broadening towards the higher binding energy and are fitted with an additional component centred at ~401.0 ± 0.2 eV. The higher binding energy component may have contribution from the oxidised N species [278–280].

With increased exposure to plasma, there is slight variation in the FWHM of the amine N component and has been fitted with a FWHM of 1.8 ± 0.15 eV. In Figure 4.4, the variation of FWHM of oxidised N component in fitted N1*s* spectra with respect to time of plasma treatment (0, 3, 4 and 5 minutes) is shown. A monotonic increase in FWHM of the oxidized N component upon plasma-exposure is observed from 0 eV (pristine) to 2.5 eV (5 mins). The amine N is thought to be the active site for the attachment of Li-TFSI dopants molecules in doped spiro-OMeTAD[32]. Here it can be proposed that plasma modifies the amine N site and the formation of the oxidised nitrogen species may result in improvement in conductivity of the films post treatment as discussed in section 4.5. Interaction of the plasma jet with spiro-OMeTAD may result in loss of methyl groups leading to the formation of quinoid structures with quaternary nitrogen +N=C which is predicted to contribute to the enhancement in positive charges in the molecule.

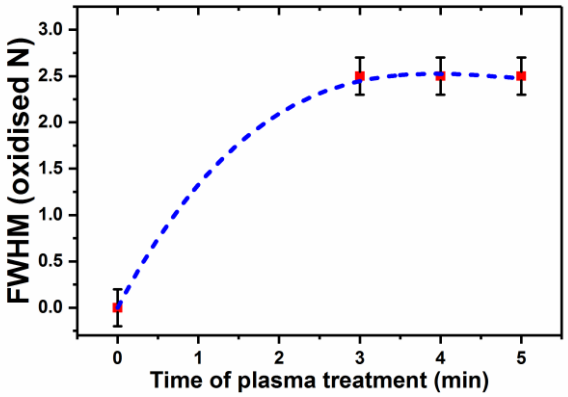

Figure 4.4 Variation of FWHM of oxidised N component in fitted N1*s* spectra with respect to time of plasma treatment (0, 3, 4 and 5 minutes).

Though a change in the nitrogen environment from the N1*s* spectra has been observed, no such variation is observed in the C-N component of the C1*s* spectra since it is overlapped with the contribution from the C-O component and cannot be deconvoluted due to the 0.9 eV resolution of the in-house XPS equipment.

O1*s*: The O1*s* core level spectrum of the as-deposited film was fitted with one component centred at ~533.3 ± 0.1 eV corresponding to the C_a-O as reported previously in literature [46,47]. As can be observed from Figure 4.5, the plasma treated films have FWHM 0.5 eV higher than the pristine spiro-OMeTAD sample. This 0.5 eV increase in the FWHM signifies an increased degree of oxidation of the spiro-OMeTAD films with time of plasma exposure. This broadening can be attributed to the formation of O doubly bonded to C, at ~531.1 ± 0.1 eV [227,271,281] which can be corroborated by the C=O signature from the C1*s* spectra of plasma-functionalized spiro-OMeTAD (Figure 4.2 a). The signature of C=O may result from the formation of quinoid structures with C=O moieties which in turn result in enhancement in hole conductivity as will be explained later. Figure 4.6 shows the variation of FWHM of the C_a-O component in fitted O1*s* spectra with respect to plasma treatment time (0 - 5 minutes). The FWHM is observed to have increased steadily with increase in time of plasma exposure.

Surface oxidation is consistent with the positive change in work function measured with KPFM which proves the incorporation of oxygen functional groups on the surface. Though chemical oxidation is the most common doping strategy for HTLs, other techniques have also been tried such as acidic dopants for conductive polymers, where the enhancement of conductivity is attributed to induction of positive charges that increase the carrier density in the systems [43]. The afore-mentioned quinoid structures may also be responsible for the increase in positive charge carriers. It can also be

proposed that oxygen plasma induces an increase in positive charges in spiro-OMeTAD that enhances the carrier density and hence the improvement in conductivity.

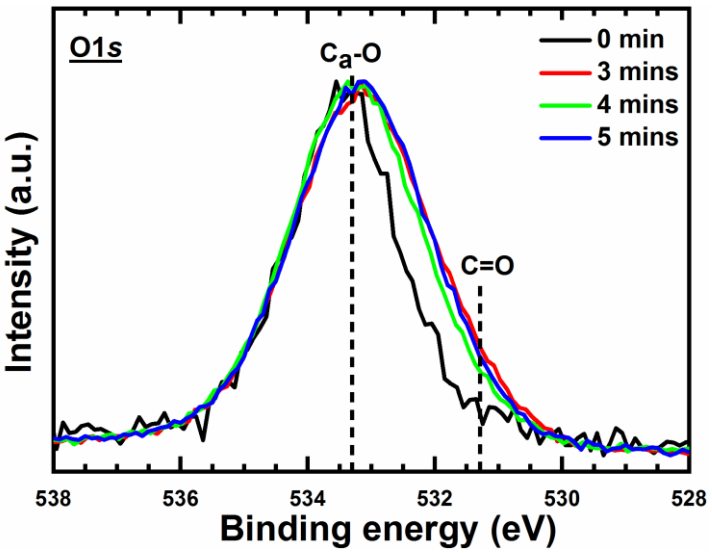

Figure 4.5 Variation of O1*s* XPS spectra of spiro-OMeTAD with respect to plasma treatment time (0, 3, 4 and 5 minutes).

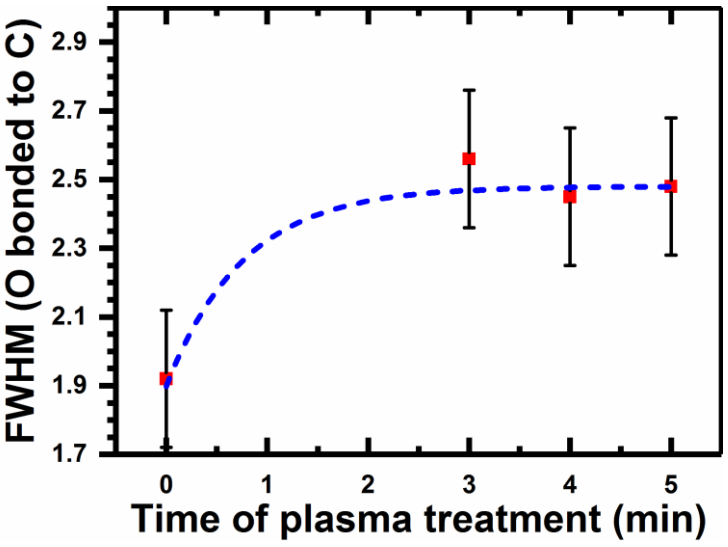

Figure 4.6 Variation of FWHM of the C bonded to O (C=O/C-O-C) in fitted O1*s* spectra with respect to plasma treatment time (0, 3, 4 and 5 minutes).

Table 4.1 Fitting parameters extracted from XPS spectra of pristine and He + O_2 plasma functionalized spiro-OMeTAD.

Sample	Region	Component	% conc. ± 0.2	FWHM ± 0.1 (eV)
Untreated Spiro-OMeTAD	C1*s*	C-H	35.0	1.5
		C=C/C-C	34.0	1.8
		C-N/C-O	22.2	1.7
		C_a-O-C	5.0	1.7
		C=O	0	0
		π-π*	3.6	2.8
	O1*s*	C_a-O-C	100.0	2.0
	N1*s*	amine N	100.0	1.7
		Oxidised N	0	0
3 mins plasma	C1*s*	C-H	31.6	1.6
		C=C/C-C	29.7	1.9
		C-N/C-O	21.0	1.9
		C_a-O-C	7.0	1.9
		C=O	6.9	2.1
		π-π*	3.6	2.9
	O1*s*	C_a-O-C	100.0	2.6
	N1*s*	amine N	72.6	1.9
		Oxidised N	27.3	2.5
4 mins plasma	C1*s*	C-H	31.3	1.6
		C=C/C-C	29.7	1.7
		C-N/C-O	16.6	1.5
		C_a-O-C	8.5	1.5
		C=O	7.4	2.1
		π-π*	6.4	3.5
	O1*s*	C_a-O-C	100.0	2.5
	N1*s*	amine N	73.6	1.9
		Oxidised N	26.4	2.5
5 mins plasma Spiro-OMeTAD	C1*s*	C-H	31.2	1.6
		C=C/C-C	28.4	1.7
		C-N/C-O	19.6	1.6
		C_a-O-C	8.0	1.6
		C=O	6.8	2.1
		π-π*	6.0	3.3
	O1*s*	C_a-O-C	100.0	2.5
	N1*s*	amine N	72.0	1.8
		Oxidised N	28.0	2.5

4.3.3 Morphology of spiro-OMeTAD films

Optical microscopy, scanning electron microscopy (SEM) and atomic force microscopy (AFM) were used to study the morphology of the spiro-OMeTAD films before and after time-dependent plasma treatment (Figure 4.7). No evidence of pinholes was observed in the optical, SEM and AFM images.

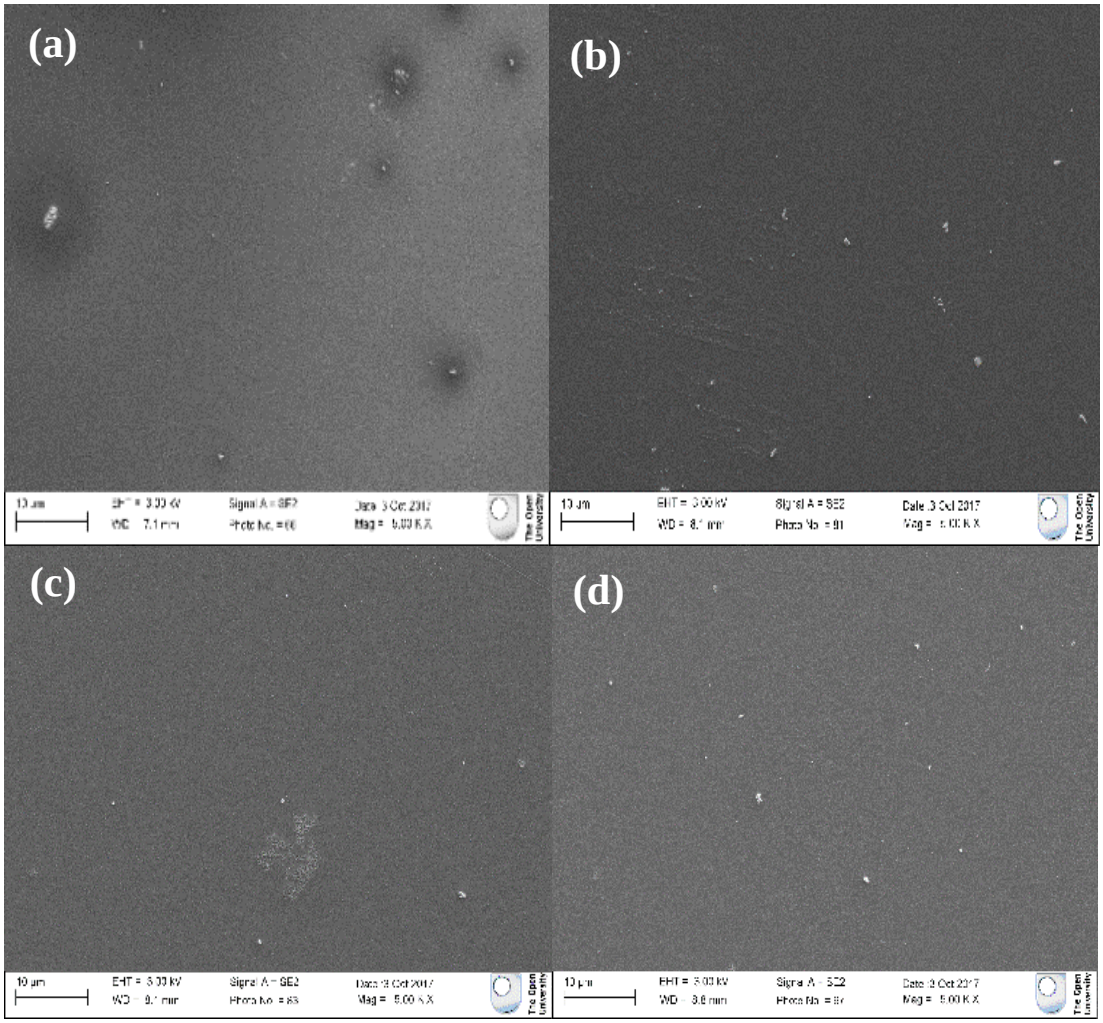

Figure 4.7 SEM images of untreated and plasma-treated spiro-OMeTAD (3, 4 and 5 mins - b, c and d, respectively).

No noticeable difference in film morphology was discernible with the SEM before and after plasma treatment (Figure 4.7). The films showed appreciable uniformity except for the presence of silicon dust on the surface (observed as small dots in the figure).

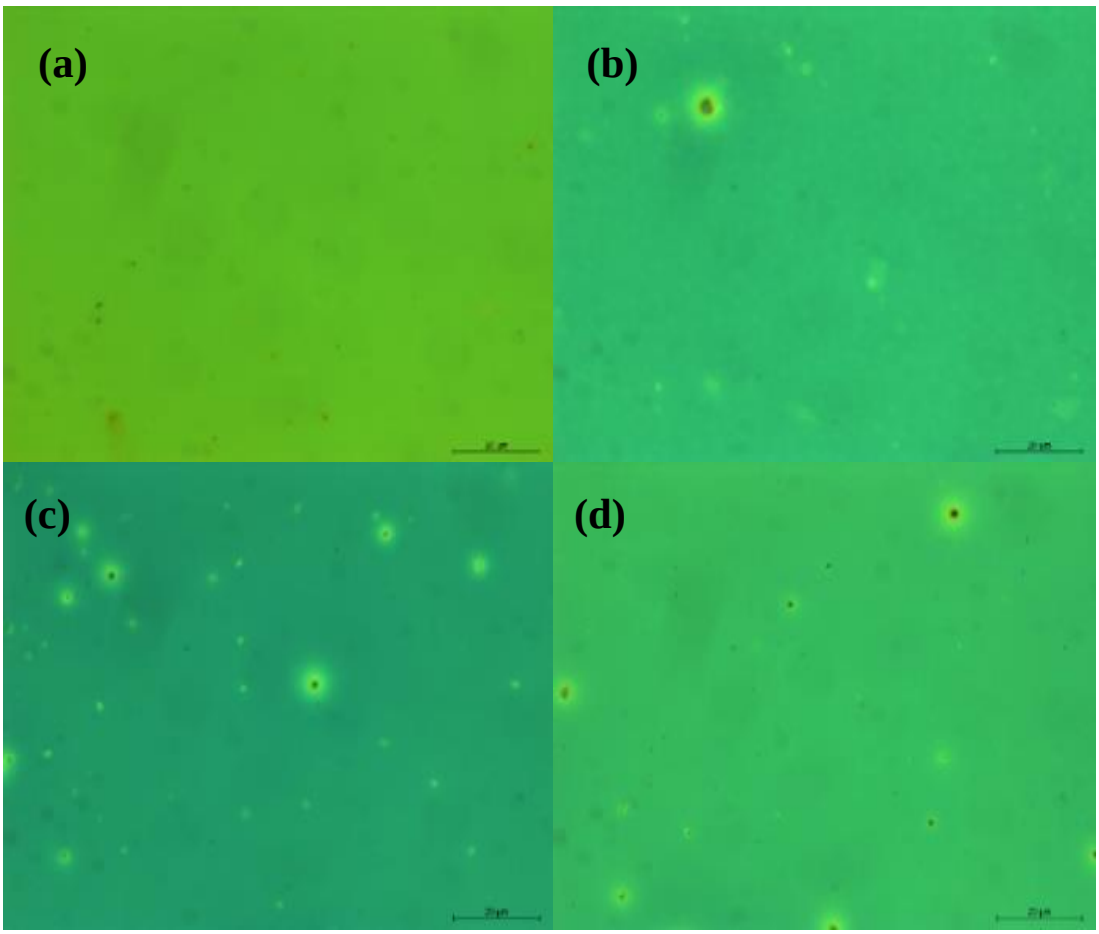

Figure 4.8 Optical images of untreated and plasma-treated spiro-OMeTAD (3, 4, 5 minutes of treatment time - b, c and d, respectively).

As was visible with the naked eye, the change in colour from the as-deposited film to the plasma-functionalized film, was proven with optical microscopy (Figure 4.8). The change in colour of the films post-treatment from greenish to bluish becomes appreciable as the time of plasma exposure increases to 3, 4 and 5 minutes.

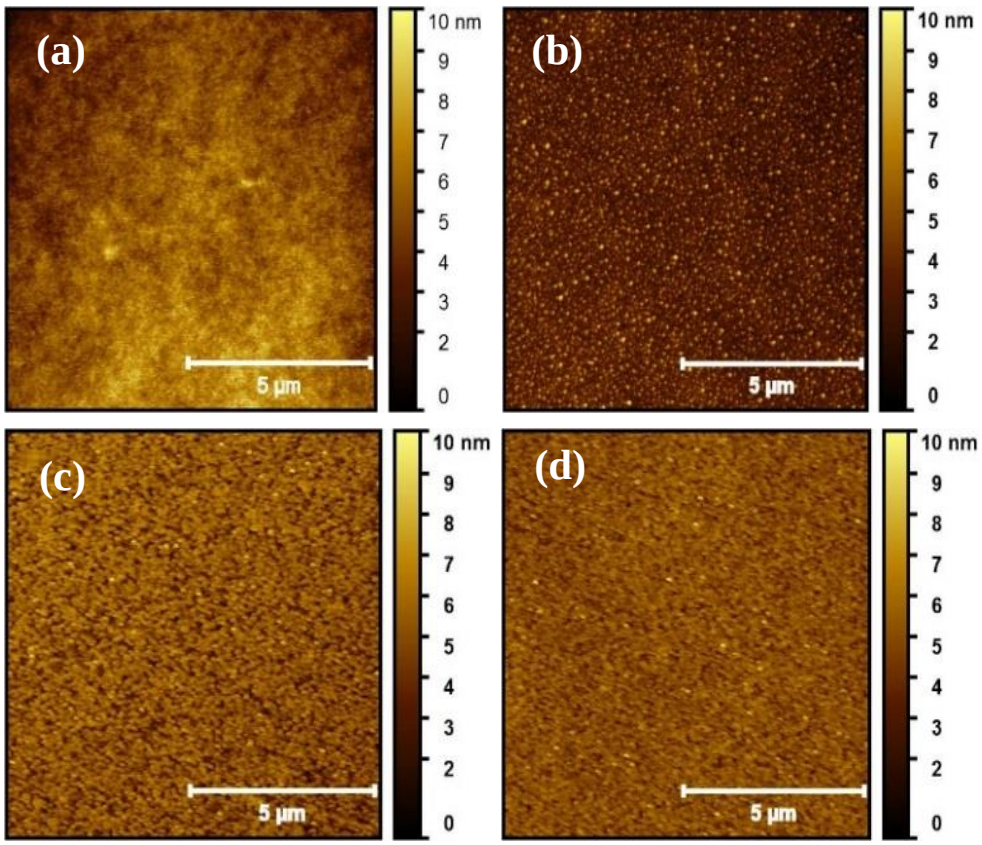

Figure 4.9 AFM images of (a) untreated and (b, c, d) plasma-treated spiro-OMeTAD with 3, 4 and 5 minutes of exposure time.

The AFM height profile of the pristine and plasma-treated spiro-OMeTAD films are shown in Figure 4.9. Variation in film roughness was noticeable with films post-treatment showing enhanced roughness values from 0.8 nm to 1.2 nm, though the values were not substantial. The accumulation of aggregates on the surface of the films is seen to increase with increased time of plasma exposure. This indicates that the low power plasma jet used in the current work does not induce noticeable surface damage to the spiro-OMeTAD films.

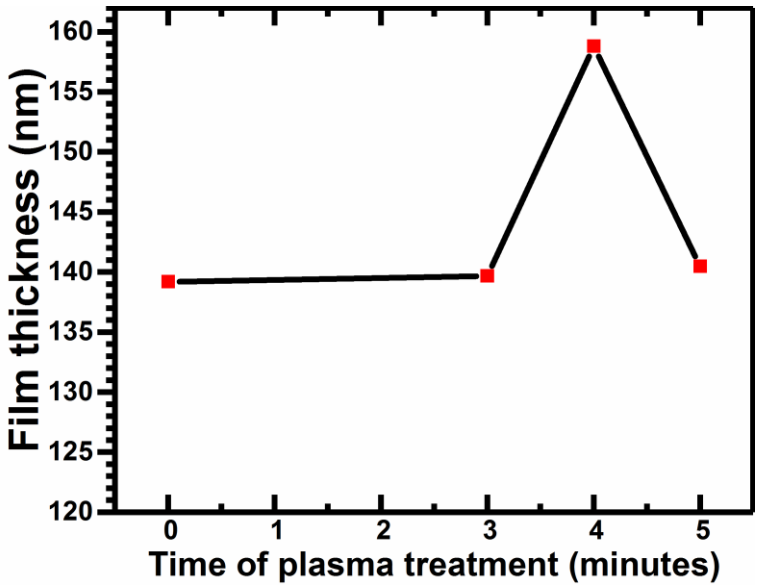

Figure 4.10 Variation in film thickness of spiro-OMeTAD with different time of plasma treatment (0, 3, 4 and 5 mins).

Figure 4.10 shows the variation in film thickness of spiro-OMeTAD with different time of plasma treatment (0, 3, 4 and 5 minutes). The thickness of the untreated spiro-OMeTAD film was 139.2 nm. There is not much variation in film thickness upon plasma treatment which indicates the non-abrasive nature of the APPJ. The thickness of the films after 4 minutes of plasma treatment were measured to be 158.8 nm. The thickness values were averaged after measurements at three different positions on the film. The maximum difference between the plasma-treated and untreated films was 19.6 nm which signifies that the plasma jet is not an abrasive technique and does not result in corrosion of the surface of spiro-OMeTAD.

4.3.4 Optical properties - UV-vis spectroscopy

The UV-vis absorption spectra of the pristine and plasma treated spiro-OMeTAD are shown in Figure 4.11. Spiro-OMeTAD has a sharp absorption peak in the UV region at around 395 eV [203]. But when oxidised, there is a broad peak at ~500 nm which is the signature of the spiro-OMeTAD^{+} radical [62]. From the figure, the difference in UV-vis spectrum of plasma treated films is clearly discernible from the untreated films. The

absorption peak at ~500 nm due to the presence of the oxidised spiro-OMeTAD radical in the plasma functionalized films is absent in the undoped film. This proves that the spiro-OMeTAD molecule has become oxidised after plasma exposure. The absorption peak at ~400 nm which is due to pristine spiro-OMeTAD slowly decreases in intensity with increase in time of plasma exposure whereas the peak at ~500 nm increases.

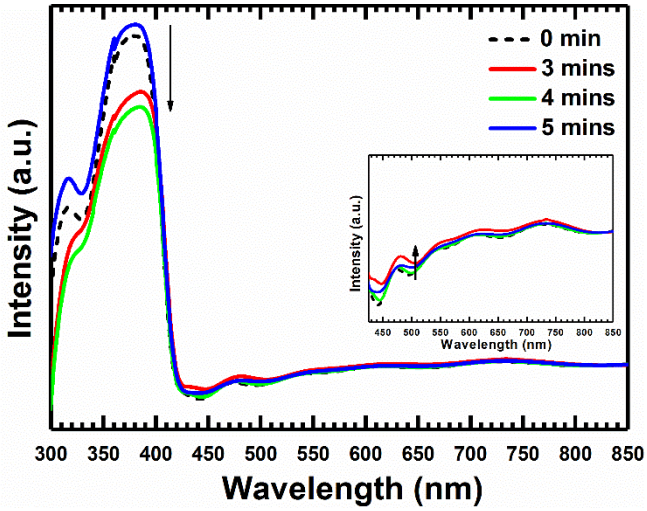

Figure 4.11 UV-vis spectra of pristine and plasma-functionalized spiro-OMeTAD.

4.5 Electrical properties

4.5.1 EFM and 4-point probe sheet resistance

Electrostatic force microscopy is a useful technique for investigating the electrical properties of nanomaterials. EFM primarily allows qualitative mapping of the surface potential. Though not much exploited in the field of organic-inorganic hybrid halide PSCs, this technique has been previously used by Emilio J. Juarez-Perez *et al*. to study the role of chemical dopants, Li-TFSI and tBP, on the morphological and transport properties of spiro-OMeTAD [66]. EFM was used to show the distribution of dopants on the spiro-OMeTAD film. It was shown that tBP acts as a homogeniser preventing phase separation of spiro-OMeTAD and Li-TFSI solution

In this chapter EFM has been used to evaluate the electrical properties of spiro-OMeTAD thin films at the nanometre scale before and after plasma treatment. EFM measurements were carried out around the same area of the sample before and after 3, 4 and 5 minutes of plasma exposure. A greater contrast in the pseudo colour image shows increased fluctuations in the phase value and signifies a less conducting region, whereas a darker colour means lower phase shift and hence more surface conducting nature of sample. The pseudo colour phase images before plasma treatment for all the samples show a uniform and high phase value (Figure 4.12 (a, c, e)). Whereas after 3 minutes of plasma exposure, the phase values reduce and the formation of small blob-like structures in the height profiles is observed (Figure 4.12 (b). Interestingly, these blobs or accumulations are the locations which report lower phase or higher conductivity on the films. These blobs are fairly uniformly distributed over the surface of the films. This signifies an improvement in the surface conductivity of the samples after plasma functionalization. After longer plasma exposure of 4 minutes and 5 minutes, no blob-like structures are visible in the height images, though the same trend of reduced phase values are clearly observed. For films treated with plasma for 4 and 5 minutes, the overall pseudo colour phase images show a trend towards lower phase values. The average value of the phase shift over the measured area is observed to have reduced by 0.2 °, 0.46 ° and 0.2 ° after plasma treatment for 3, 4 and 5 minutes, respectively, as summarised in Table 4.2. Thus, it can be concluded that the APPJ has resulted in improvement of the surface conductivity of the samples. The surface roughness of the films after plasma exposure has undergone slight increase as is evident from the R_{rms}(rms roughness values).

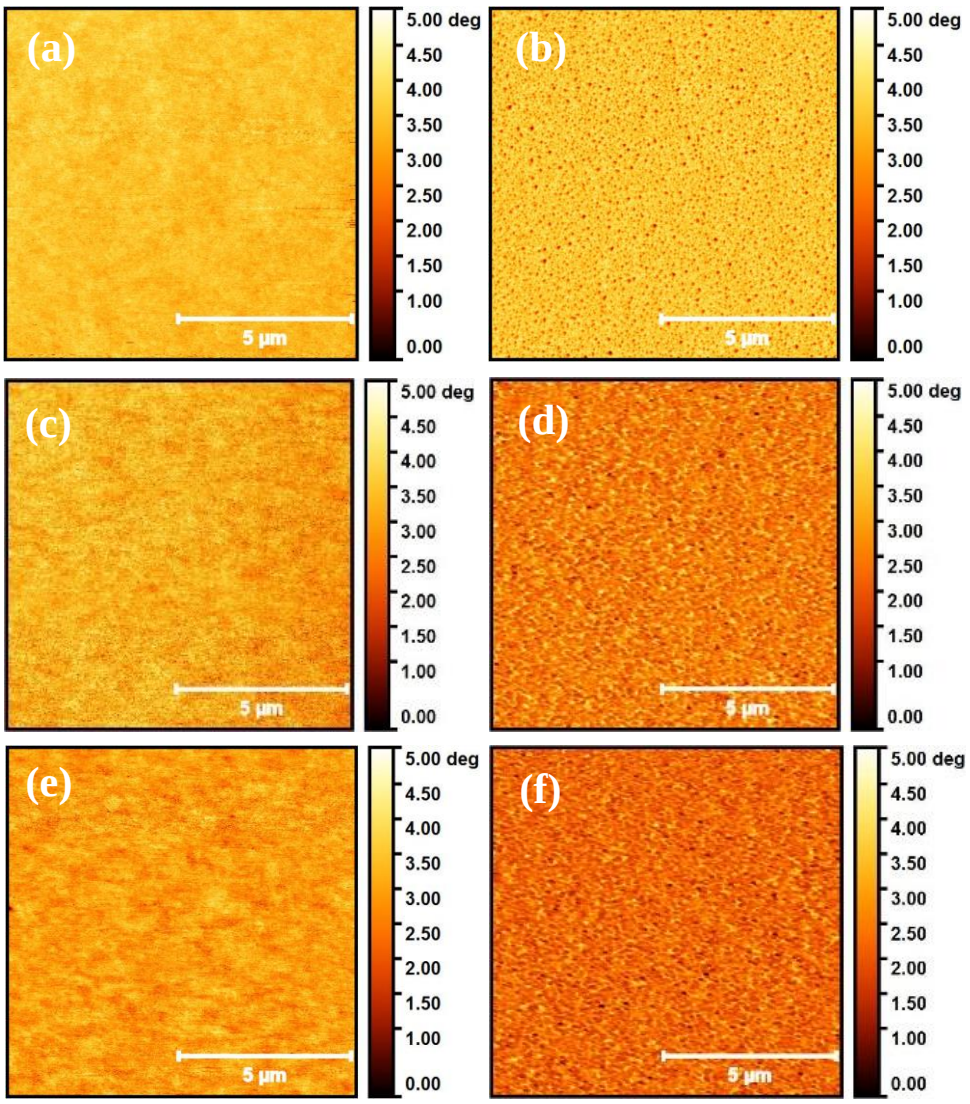

Figure 4.12 EFM phase images of pristine (a, c, e) and samples treated with plasma for 3, 4 and 5 mins, respectively (b, d, f). A greater contrast in the pseudo colour image shows increased fluctuations in the phase value and signifies a less conducting region, whereas a darker colour means lower phase shift and hence more surface conducting nature of sample.

Table 4.2 Variation of the average phase before and after plasma treatment of spiro-OMeTAD.

	Samples	**Avg. phase (Pre-treatment) (°)**	**Avg. phase (Post-treatment) (°)**	**Change in phase (°)**
1	3 mins	3.6	3.4	-0.2
2	4 mins	3.0	2.54	-0.46
3	5 mins	2.89	2.69	-0.2

Table 4.3 Variation of the sheet resistivity values and conductivity of pristine and plasma treated spiro-OMeTAD.

	Sample ID	**Period of plasma treatment (*mins*)**	**Sheet resistance *(G Ω sq^{-1})***	**Thickness (nm)**	**Conductivity (S cm^{-1})**
1	Untreated Spiro-OMeTAD	0	80.52	139.2	9.4×10^{-7}
2	Plasma-treated Spiro-OMeTAD	3	11.26	139.7	6.36×10^{-6}
3		4	8.041	158.8	7.8×10^{-6}
4		5	6.182	140.5	1.15×10^{-5}

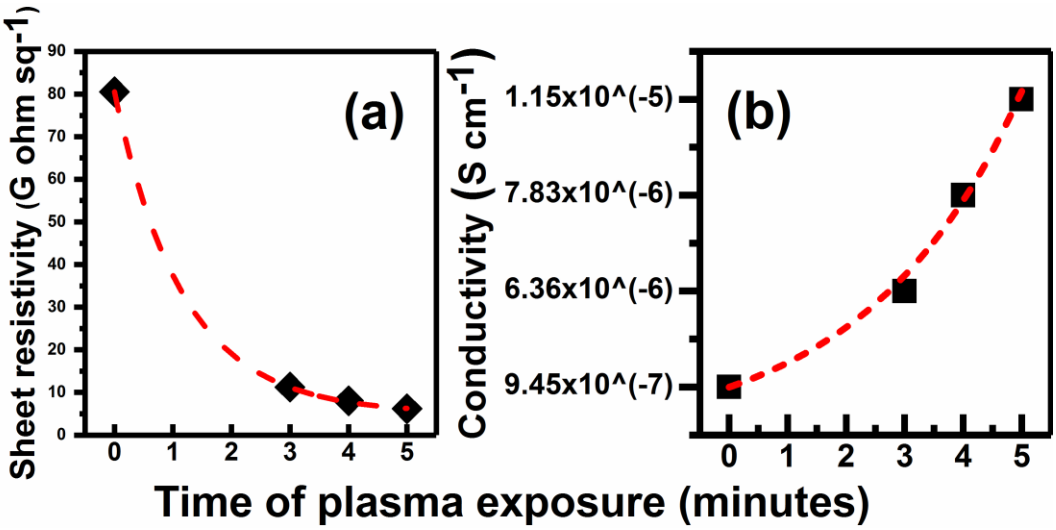

Figure 4.13 Variation of (a) sheet resistivity and (b) conductivity of spiro-OMeTAD with time of plasma functionalization.

Oxygen plasma is known to functionalize the surface of thin films by incorporation of polar functional groups such as C-O, C-OH [282,283] which may lead to enhancement of the conductivity of the films. This is also supported by the conductivity values of the samples calculated before and after the plasma functionalization as shown in Table 4.3. The conductivity of pristine spiro-OMeTAD thin films calculated from the measured sheet resistivity values was 9.4 x 10^{-7} S cm^{-1} which agrees well with reported values [41]. The conductivity increased to 6.36 x 10^{-6} S cm^{-1} after 3 minutes of plasma treatment which is comparable to reported values on doping spiro-OMeTAD with p-type dopant Li-TFSI [13,41,43,49]. The conductivity further increased to 7.8 x 10^{-6} and 1.15 x 10^{-5} S cm^{-1} after 4 and 5 minutes of plasma functionalization, respectively. The trend of exponential decrease in the sheet resistivity and the corresponding increase in the conductivity of the spiro-OMeTAD films post plasma exposure is shown in Figure 4.13.

3.5.2 Kelvin Probe Force Microscopy (KPFM)

Kelvin Probe Force Microscopy is a versatile technique which has been extensively used to probe the changes in cross-sectional surface potential, charge

separation, charge transport, map the local contact potential difference, and electronic structure at the interfaces of PSCs [284–287]. In this work KPFM was used to measure the work function change due to time dependent plasma exposure. To evaluate the work function of spiro-OMeTAD, before and after plasma-functionalization, initially the work function of the Pt/Ir coated tip was estimated by mapping the surface potential of freshly cleaved HOPG sample. The AM-KPFM maps revealed that the work function of the Pt/Ir tip is 5.21 eV. The contact potential difference is defined as:

$$\Delta V_{CPD} = \frac{\phi_{tip} - \phi_{sample}}{-e} \qquad \ldots\ldots\ldots\ldots\ldots\ldots 4.2$$

Where ϕ_{tip} is the work function of the KPFM tip, ϕ_{sample} is the work function of the sample, e is the elementary charge, and $\Delta V_{CPD}$is the measured contact potential difference.

Using this relation, the work function measurements were performed before and after plasma treatment. From the surface potential (SP) values it can be said that work function of the spiro-OMeTAD thin films increased after oxygen plasma treatment. This means that oxygen plasma induced p-type functionalization of the spiro-OMeTAD films. However, in practise, several factors affect the surface potential. Thus, the measured surface potential difference from KPFM, though accurate, have multiple contributions which renders this technique pseudo-quantitative. The work function measured is not an absolute value, but gives the value measured with respect to the tip.

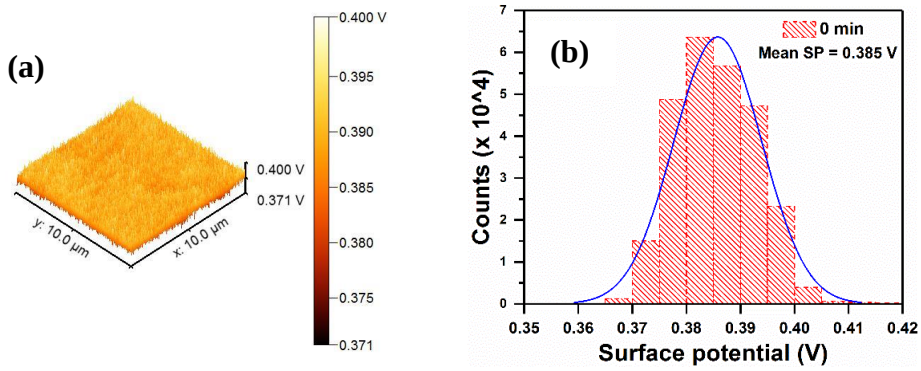

Figure 4.14 Representative image for the method of calculation of surface potential from KPFM data of pristine spiro-OMeTAD.

Figure 4.14 (a) shows the surface potential map of pristine the spiro-OMeTAD film and Figure 4.14 (b) shows the distribution of surface potential. The histogram plot of the surface potential has been fitted with a Gaussian distribution profile and the mean value of this distribution can be considered as the average potential difference between the KPFM tip and the spiro-OMeTAD film. The same technique was used for the calculation of the surface potential values for all the plasma-treated spiro-OMeTAD samples. KPFM measurements were performed on the same samples before and after plasma treatment and the change in surface potential due to plasma exposure was recorded as shown in Table 4.4. A wide variation in the surface potential values was observed. For the spiro-OMeTAD sample functionalized with plasma for 3 minutes, the change in surface potential was observed to be ~17 mV after plasma exposure. This change in surface potential increased to 49 mV after 4 minutes of plasma functionalization before finally reducing for 5 minutes to 14 mV. Thus, it can be concluded that the work function of the spiro-OMeTAD samples has increased after plasma treatment, albeit there is certain variation in the values with different time of functionalization which signifies p-type doping of spiro-OMeTAD with oxygen plasma.

Table 4.4 Variation of the surface potential of pristine and plasma treated spiro-OMeTAD as measured with Kelvin Probe Force Microscopy.

Time of plasma exposure	SP pre-treatment (V)	SP post-treatment (V)	Change in SP (mV)
3 mins	0.494	0.511	+ 17.0
4 mins	0.469	0.518	+ 49.0
5 mins	0.456	0.470	+ 14.0

Mechanism of increase in conductivity due to plasma treatment

The spiro-core with sp^3 hybridized N atom with pyramidal structure results in large intermolecular distances in spiro-OMeTAD. Thus, charges have to move longer paths and hence the conductivity is lowered [44]. The mechanism is explained in Chapter 1.

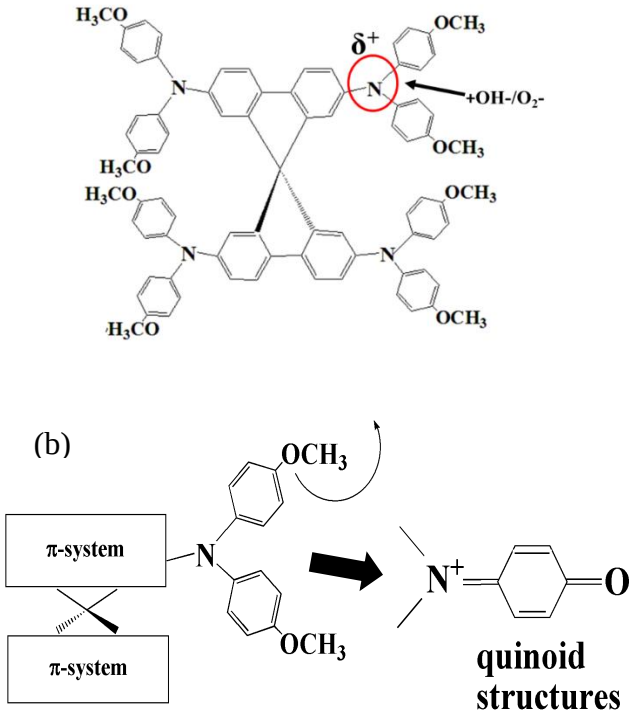

Figure 4.15 Proposed mechanism for the increase in conductivity due to plasma treatment (a) due to excess charge carrier centres from plasma jet and (b) due to

formation of quinoid structures after loss of methoxy groups from spiro-OMeTAD as a result of bombardment by excited species from plasma jet.

In this work, enhancement in conductivity of spiro-OMeTAD after plasma treatment has been observed. Here it has been proposed that the increase in conductivity occurs as a result of increase in number of charge carriers due to plasma doping/functionalization of the spiro-OMeTAD molecule. The spiro-OMeTAD$^{+\cdot}$ radical formed after oxidation of the molecule in presence of oxygen, has δ^+ charge on triaryl amine nitrogen which acts as a suitable site for attack by the numerous charged species such as radicals, ions, electrons present in the oxygen plasma. These charged species attack the δ^+ nitrogen of the triaryl amine nitrogen site provide additional charge carriers to the spiro-OMeTAD molecule and hence the conductivity is enhanced post plasma treatment (Figure 4.15).

This study reports functionalization of spiro-OMeTAD with an atmospheric pressure plasma jet for the first time and the role of plasma is still not clearly understood. The reason for increase in conductivity of spiro-OMeTAD post processing may also be as a result of an increase in π-π stacking possibly due to the suitability of formation of hydrogen bonding between OH^-/O_2^- species in plasma with the active centres of spiro-OMeTAD molecule. It is believed that the oxygen species in the discharge enhances the delocalization of charge carriers and hence contributes to an increase in conductivity post plasma exposure. Interaction of the plasma jet with spiro-OMeTAD may also result in loss of methyl groups leading to the formation of quinoid structures with quaternary nitrogen +N=C which is predicted to contribute to the enhancement in positive charge centres in the molecule. Since, the functionalization of spiro-OMeTAD has not been undertaken before, the mechanism for the interaction of the highly energetic species present in the plasma jet with the molecule remains elusive. Possibly plasma promotes

π-π or CH-π interactions in spiro-OMeTAD because of the presence of a multitude of different radicals/species in oxygen plasma which leads to increased conductivity, since it is well known that aromatic rings can form CH-π interactions with alcohols, amines, amides and different other molecules. Further research is being undertaken to understand the underlying mechanism of plasma interaction with the hole transport molecule.

4.6 Conclusion

A non-thermal atmospheric pressure plasma jet was used to functionalize and oxidise spiro-OMeTAD films. Time dependent plasma treatment was undertaken to understand the changes in conductivity, morphology, electronic and optical properties. The oxidation of spiro-OMeTAD and formation of spiro-OMeTAD^{+} radical was observed from UV-Vis spectroscopy. The enhancement in conductivity from 9.4 x 10^$^{-7}$ S cm^{-1} for the pristine film to 1.15 x 10^$^{-5}$ S cm^{-1} after 5 minutes of plasma treatment is comparable to that reported in literature when doped with 10-25% of p-type dopant Li-TFSI [43,45]. The surface conductivity mapping undertaken with EFM shows improvement in conductivity post plasma exposure as is evident from the reduction in average phase value. Oxidation of spiro-OMeTAD molecule and the change in electronic properties is evident from the carbon, nitrogen and oxygen chemistry of the molecule probed with XPS. The plasma treatment was also observed to have increased the work function of plasma functionalized spiro-OMeTAD compared to pristine film, thus leading to p-type doping of spiro-OMeTAD films. These observations demonstrate the suitability of atmospheric pressure plasma microjet as a scalable, facile and effective means of doping and surface functionalization of spiro-OMeTAD thin films. The enhancement in conductivity of the spiro-OMeTAD thin films after plasma treatment coupled with oxidation is expected to have positive implications on the hole transporting nature of spiro-OMeTAD thin films without causing detrimental problems to the

stability and resilience of the perovskite solar cells as is the case with chemical dopants. Thus, the experimental results show that treatment by positive ions and electrons in oxygen plasma is an effective technique for surface functionalization and modification of spiro-OMeTAD films which in turn may contribute to the enhancement of their hole transporting nature, promising efficient and stable perovskite solar cells. However, further work is needed to elucidate the mechanism behind functionalization with atmospheric pressure plasma and the confirmation of electronic properties and the suitability of using plasma-treated spiro-OMeTAD films as hole transport layer in perovskite solar cells.

Chapter 5

Tuning the work function of graphene oxide hole transport material using atmospheric pressure plasma jet

Ability to tune the work function of graphene oxide makes it suitable as hole conductor and electrode material in perovskite solar cells. The application of graphene oxide as hole conductor in PSCs has yielded device efficiency of 12% [119]*. In this chapter, a low-power (3 W) radio frequency atmospheric pressure plasma jet has been proposed for functionalization of graphene oxide. The plasma jet was ignited using helium as carrier gas and different admixtures (2 and 20 sccm) of nitrogen, hydrogen and oxygen. A systematic spectroscopic investigation was performed using XPS and UPS to observe the variation in the local chemical structure, bonding environment and electronic properties of plasma-functionalized GO. Different nitrogen-bonding species induced localised variation in the bonding configuration of GO. The reducing environment of the hydrogen plasma was found to be highly efficient in deoxygenation and recovering the electronic structure of graphene oxide which also resulted in an enhancement in conductivity. Variation in bonding environment resulted in work function changes as evident from UPS measurements.*

5.1 Introduction

Graphene has attracted immense interest since its discovery in 2004 due to the physical and chemical attributes [288]. Structurally, graphene oxide is a single layer of graphite oxide, consists of a honeycomb lattice of carbon atoms with oxygen-containing functional groups. Prepared by oxidative exfoliation of graphite, this material can be visualized as individual sheets of graphene decorated with >C=O, -C-OH groups at the basal planes and -OH and -COOH groups at the edges, hence making GO amphiphilic in nature, with a hydrophobic base and a hydrophilic edge [289,290]. The presence of different oxygen functional groups is crucial for determining the optical and electronic properties of GO [290].

Work function (φ) is defined as the minimum amount of energy required to remove an electron from the highest occupied level to the vacuum level just outside the solid.

$$\varphi = V_{vacuum} - E_{Fermi} \quad \text{.....5.1}$$

Work function is a fundamental property of a material and provides understanding of the relative position of the Fermi level [291]. Work function plays a crucial role in determining band alignment in a heterojunction device to facilitate selective electron and hole transport [292]. Nevertheless, several factors such as presence of defects, oxygen functionalities, and incorporation of water vapour and charge carrier concentrations influence the work function values [199]. Tuning the work function is the key factor for improved device performance of OLEDs, DSSCs and PSCs. HTMs with tunable work function are suitable for energy alignment at the interfaces in PSCs. The tunability of the work function of GO makes it a suitable candidate for charge transport applications [119]. Graphene oxide has been used as counter electrode as well as an interlayer between perovskite and HTL with reported PCE of ~12% [117] and 14.5% [120], respectively. The work function of graphene lies between 4.6 eV and 4.8 eV from scanning probe measurements, which also depends on the number of layers as well as charge carrier concentration [293,294]. Graphene and graphene oxide are propitious candidates for replacing the Au counter electrode in PSCs, because Au is known to diffuse into the adjacent HTLs and result in degradation of PV devices [295].

Thermal, chemical and electrochemical methods are most commonly employed for modification of work function of GO. However, plasma functionalization is a promising, environment-friendly and energy-saving alternative to existing chemical processes to circumvent the toxicity of chemical dopants such as hydrazine and sodium borohydride [227]. Atmospheric pressure plasma jets have been used treatment and functionalization of graphene oxide with nitrogen to improve the electrical conductivity of GO. APPJ plume consists of charged, neutral metastable species, radicals, electrons and ions which can bring about functionalization of GO by attachment of functional groups or formation of dangling bonds at edges of GO sheets. Liu *et al*. treated graphene counter electrodes with atmospheric pressure plasma at 700 W for application as

electrodes [296]. Other efforts include APPJ treatment of graphene to increase hydrophilicity [171], and introduction of band gap at 150 W [224]. For chemically reduced graphene oxide, a work function of 4.88 eV has been reported measured using photoelectron spectroscopy [297]. Kelvin probe force measurements of chemically reduced graphene oxide and mechanically exfoliated graphene reported values between 4.7 and 5.1 eV [298]. The ability to tune the work function of graphene is of paramount importance for its application as electrode material [299]. The objectives of this chapter are (i) functionalization of graphene oxide using nitrogen, hydrogen and oxygen plasma with helium as carrier gas and (ii) systematic investigation of the variation in electronic properties using spectroscopic techniques, XPS and UPS.

Nitrogen: Nitrogen doping in graphitic materials such as graphene, carbon nanotubes and graphene oxide has been reported to modify the physical, chemical and electronic properties, and has been extensively studied for numerous applications such as catalysts for oxygen reduction, biosensors, capacitors and electrodes in lithium ion batteries [104,131,300–307]. The suitability of nitrogen for substituting the carbon atoms in GO stems from the fact that it has similar atomic radius and five valence electrons. Doping with nitrogen influences the charge distribution around the carbon atom in the lattice and helps in tuning the electronic properties. The work function of graphene has strong dependence on the doping configuration and amount of doped nitrogen with graphitic N lowering the work function unlike pyridinic or pyrollic N.

Hydrogen: The role of hydrogen plasma in graphene oxide has been explored in flexible conductors, gas sensors [161,308], electrodes [162] in solar cells [163] and supercapacitors. Since, reduction by hydrogen plasma has not been extensively studied, several unanswered questions need investigation pertaining to reduction mechanism and optoelectronic properties of reduced graphene oxide.

Oxygen: Oxygen plasma presents a benign and feasible technique for p-type doping of graphene oxide and has been applied in electrochemical actuator [165], molecular sensing [167], electrodes [168] and for band gap opening [164]. Oxygen plasma functionalization of GO reportedly enhanced the hole injection property of OLEDs [309]. For details of the role of nitrogen, hydrogen and oxygen plasma in graphene oxide refer to Chapter 1.

5.2 Experimental details

5.2.1 Synthesis of graphene oxide

Hummers' method

Graphene oxide was synthesized using modified Hummer's method as described in Chapter 2. Hummers' method [138] is the easiest chemical process for the synthesis of graphene oxide (Figure 5.1).

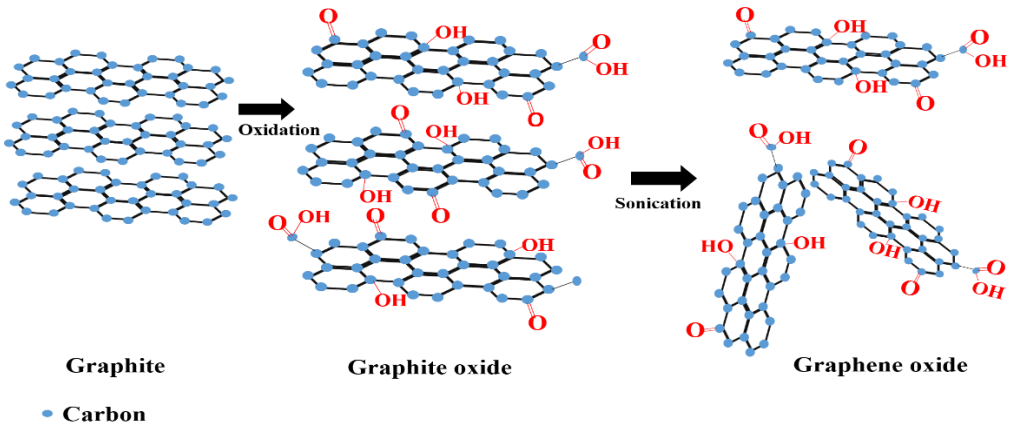

Figure 5.1 Schematic of graphene oxide synthesis using modified Hummers' method. Graphite flakes are oxidatively expanded to graphite oxide and then ultrasonicated to exfoliate graphene oxide.

5.2.2 Atmospheric pressure plasma jet for surface functionalization of graphene oxide

The GO solution extracted using Hummer's method was centrifuged at 8000 RPM for 10 minutes and the supernatant was drop cast on silicon substrate of dimension about 1cm × 1cm. Prior to film deposition, the substrates were thoroughly cleaned by ultra-

sonication in isopropanol. The in-house atmospheric pressure plasma jet used for functionalization of graphene oxide films is shown Figure 2.1. The details of the circuit is as described in Section 2.1.2 of Chapter 2. Low power APPJ (3 W) was used for functionalization of the graphene oxide sheets. Plasma functionalization of the GO sheets were carried out systematically in three different gaseous environments, helium-nitrogen, helium-hydrogen and helium-oxygen. Helium was used as the carrier gas in each case with a constant flowrate of 2000 sccm whereas the flowrates of the gases for the admixture were varied at 2 sccm and 20 sccm using mass flow controllers. The purity of the gases used was 99.999%. Time-dependent studies were performed at 1, 3 and 5 minutes of plasma treatment for each of the admixtures allowing for a stabilization time of 1 minute for the plasma jet between each sample. The list of samples studied in this chapter is given Table 5.1.

Table 5.1 List of atmospheric pressure plasma functionalized graphene oxide samples studied.

<table>
<tr><th></th><th>Sample</th><th>Gas admixture</th><th>Flowrate (sccm)</th><th>Time (mins)</th></tr>
<tr><td>1</td><td>Pristine graphene oxide</td><td colspan="2">No plasma</td><td>0</td></tr>
<tr><td>2</td><td rowspan="19">Plasma treated graphene oxide</td><td rowspan="6">He + N_2</td><td rowspan="3">2</td><td>1</td></tr>
<tr><td>3</td><td>3</td></tr>
<tr><td>4</td><td>5</td></tr>
<tr><td>5</td><td rowspan="3">20</td><td>1</td></tr>
<tr><td>6</td><td>3</td></tr>
<tr><td>7</td><td>5</td></tr>
<tr><td>8</td><td rowspan="6">He + H_2</td><td rowspan="3">2</td><td>1</td></tr>
<tr><td>9</td><td>3</td></tr>
<tr><td>10</td><td>5</td></tr>
<tr><td>11</td><td rowspan="3">20</td><td>1</td></tr>
<tr><td>12</td><td>3</td></tr>
<tr><td>13</td><td>5</td></tr>
<tr><td>14</td><td rowspan="6">He + O_2</td><td rowspan="3">2</td><td>1</td></tr>
<tr><td>15</td><td>3</td></tr>
<tr><td>16</td><td>5</td></tr>
<tr><td>17</td><td rowspan="3">20</td><td>1</td></tr>
<tr><td>18</td><td>3</td></tr>
<tr><td>19</td><td>5</td></tr>
</table>

5.2.3 Characterization of functionalized graphene oxide

The characteristics of the plasma jet was studied with the help of optical emission spectroscopy using a S2000+ Ocean Optics spectrometer and the signals were collected through an optical fibre. XPS measurements were undertaken with an in-house Kratos XSAM800 equipment using Mg *K*α (1253.6 eV) excitation source (detailed description in Chapter 2) to understand the variation in electronic and chemical structure of the GO films upon plasma functionalization. UPS (with He I excitation source at 21.22 eV) was undertaken to investigate the variation in valence band structure and work function of GO upon plasma functionalization.

5.3. Results and discussions

5.3.1 Optical Emission spectroscopy (OES)

Optical emission spectroscopy provides information on excited atomic or molecular species [94,310]. The nature of the plasma depends on the gas phase composition i.e. the excited atoms, ions and molecules. In the present work, OES was used to study the different species present in the atmospheric pressure helium-nitrogen, helium-hydrogen and helium-oxygen plasma jets.

He + N_2 plasma jet:

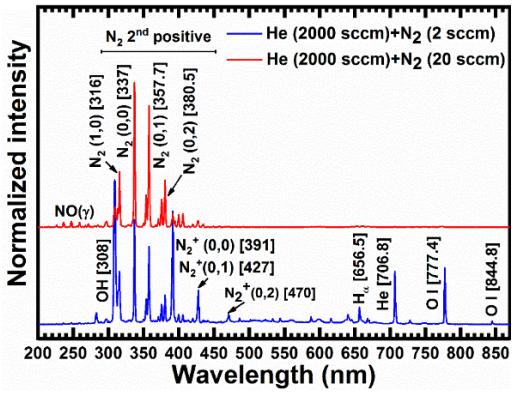

Figure 5.2 Optical emission spectra of the afterglow region of the APPJ with He (2000 sccm) and N_2 (2 sccm; blue and 20 sccm, red) discharge.

The emission spectra of helium-nitrogen plasma jet with 2 sccm (blue line) and 20 sccm (red line) nitrogen was measured within the range 200 to 870 nm and is shown in Figure 5.2. The OES spectrum of helium and 2 sccm nitrogen is rich in helium, nitrogen, hydrogen and atomic oxygen emission peaks. Atomic and molecular lines of reactive species are clearly observed in the spectra such as OH^- ($A^2\Sigma^+$ (v = 0, 1) → $X^2\prod$ (Δv=0)) at 308.9 nm, N_2(C-B) second positive system with electronic transitions $C^3\prod_u \rightarrow B^3\prod_g$ in the range 300-450 nm, He I transition $3s^3S^1 \rightarrow 2p^3P^0$ at 706.8 nm, O I transitions $3p^5P \rightarrow 3s^5S^0$ at 777.4 nm and $3p^3P \rightarrow 3s^5S^0$ at 844.8 nm [263–265]. Additional emission lines for H_α at 656.6 nm and N_2^+ ($B^2\Sigma_u^+ \rightarrow X^2\Sigma_g^+$) bands at 357.7 (1,0), 391.4 nm (0,0), 427.8 nm (0,1), and 470 nm (0,2) of the first negative system of nitrogen are also observed [266–268,311]. The electron collisions on H, OH or H_2O maybe considered responsible for the H and OH emissions [263]. On the other hand, the OES spectrum of helium and 20 sccm N_2 is dominated by transitions corresponding to the N_2 2nd positive system in the range 300-450 nm. Moreover, emission lines corresponding to OH^- and NO(γ) $A^2\Sigma^+ \rightarrow X^2\Pi$, which is the representative of the presence of oxygen in the afterglow, is also observed [94,269]. Oxygen incorporation is highly likely due to the nature of the plasma jet. Not only is the emission line corresponding to OH transition significantly suppressed in the spectrum from higher nitrogen content plasma jet, but also the H_α, He I and O I transitions are not visible. The lifetime of OH in air, at room temperature may be short which results in recombination reactions OH + OH → H_2O + O and OH + OH + M → H_2O + O + M, where M can be N_2, available for collision [312,313]. The reduction in intensity of He transitions is mainly due to the "*quenching*" of excited helium atoms on collision with nitrogen molecules resulting in excited nitrogen species in the plasma [264,311].

He + H_2 plasma jet:

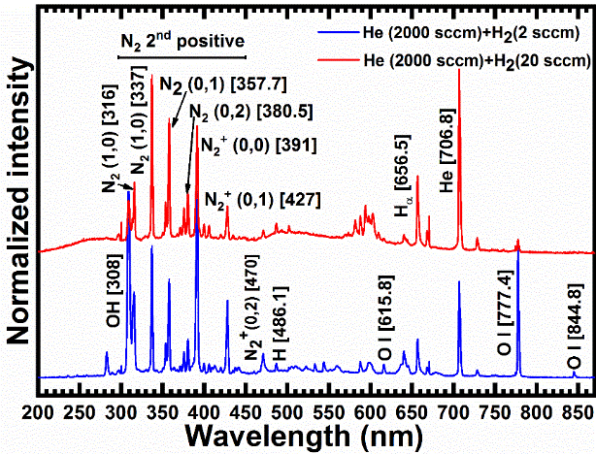

Figure 5.3 Optical emission spectra of the afterglow region of the APPJ with He (2000 sccm) and H_2 (2 sccm; blue and 20 sccm, red) discharge.

Figure 5.3 represents the optical emission spectra of the APPJ with admixture of He with 2 sccm (blue line) and 20 sccm (red line) hydrogen. The OES spectra with 2 sccm H_2 is dominated by the N_2 second positive system in the range 300-450 nm, along with strong emission lines from OH (λ = 308.9 nm), N_2^+ first negative system (λ = 357.7, 391, 427 and 470 nm), H (λ = 486.1 and 656.5 nm) and atomic O (λ = 615.8, 777.4 and 844.8 nm) transitions [266–268,311,314]. Excited H, OH and O spectral lines originate as a result of dissociation of H_2O, H_2 and O_2 contained in the helium carrier gas [315]. Increasing the hydrogen concentration to 20 sccm not only results in strong suppression of the OH emission line at 308.9 nm but also disappearance of the transitions corresponding to excited oxygen at 615 and 844.8 nm. The reduction in intensity of OH possibly results from the collisional recombination of OH with O_2 or N_2 in air as described in case of Helium-nitrogen spectra [312,313]. Hence, a simultaneous increase in O I emission is also observed. The H_α signature at 656.5 nm becomes intense and so does the He line at 706 nm. Presence of the hydrogen emission lines prove that a flow rate as low as 2 sccm can provide a reducing environment for the deoxygenation of graphene oxide samples as will be shown in following sections.

He + O_2 plasma jet:

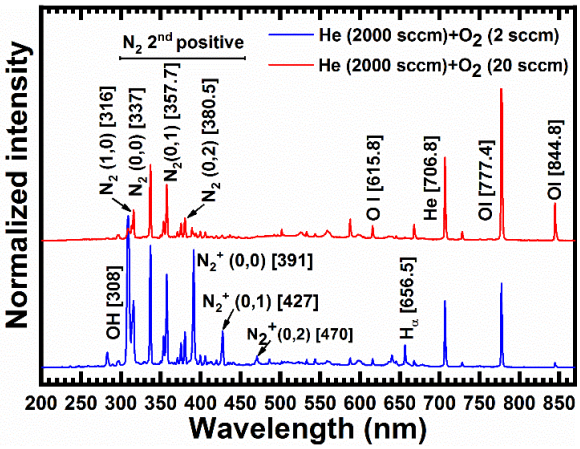

Figure 5.4 Optical emission spectra of the afterglow region of the APPJ with He (2000 sccm) and O_2 (2 sccm; blue and 20 sccm, red) discharge.

In a majority of atmospheric pressure plasma discharges, nitrogen dominates the ionic composition, and this has been corroborated in the present study. The OES spectra of the afterglow region of the APPJ with He (2000 sccm) and O_2 (2 and 20 sccm) plasma jet is shown in Figure 5.4. The strongest emission line for helium and 2 sccm O_2 plasma jet is observed to be the in the range 300-450 nm corresponding to N_2 second positive system. Being an electronegative gas, addition of O_2 to the plasma gives rise to O^- and O^{2-} ions by electron attachment [266]. O615 (O I; λ = 615.8 nm), O777 (O I; λ = 777.4 nm) and O845 (O I; λ = 844.8 nm) are also observed, either due to direct excitation from the ground state or O_2 dissociation [263–265]. A significant H_α signature (656.5 nm) is visible in the spectrum along with the emission lines corresponding to OH, and He transitions at 308.9 and 706.8 and N_2^+ first negative system at 357.7 391, 427 and 470 nm, respectively [266–268,311]. The presence of OH and N_2 emission lines which has been reported previously in atmospheric pressure discharges arising due to the electron impact as the plasma plume propagates in ambient air [94]. Increasing the oxygen content in the plasma jet to 20 sccm results in significant reduction in intensity of emission peaks of N_2 second positive system along with the enhancement of O615, O777 and O845 lines.

The increase in O777 emission might suggest the preference for dissociative excitation whereas O845 emission signifies dominance of atomic oxygen excitation when higher gas volumes are involved [264]. Thus, an interplay of both, dissociative and direct excitations mechanisms, has been observed in the present study. The drastic reduction in intensity of OH^- transition can be possibly attributed to "*quenching*" of excited helium atoms on collision with oxygen molecules resulting in excited oxygen species in the plasma. The emission lines at 391.3 nm and 427 nm for N_2^+ first negative system [266–268] are strongly suppressed when 20 sccm oxygen is used for ignition of plasma jet. The identified species in the plasma jet, molecular (OH, NO), atomic radicals (H, O, N), other reactive species such as N_2, N_2^+, metastables and photons play a significant role in surface functionalization of graphene oxide as will be demonstrated in the present study.

5.3.2 X-ray photoelectron spectroscopy (XPS)

XPS is a surface analysis technique and has been used to understand the variation in atomic concentration, local chemical environment and electronic structure of GO thin films after plasma functionalization by careful analysis of the core level (C1*s*, O1*s*, and N1*s*) spectra.

(i) <u>Nitrogen plasma</u>

Nitrogen can be doped into graphitic lattice in pyridinic, pyrollic and graphitic configurations, [104] as shown in Figure 5.5. Each of these configurations affect the electronic structure of GO differently. The nitrogen atoms at the edge of planes, each of which is bonded to two carbon atoms and donates one p-electron to the aromatic π system, constitute the pyridinic N. The nitrogen atoms bonded to the five-membered heterocyclic ring and which contribute two p-electrons to the π system are known as pyrrolic N. A third type, graphitic N, also referred to as quaternary N, is placed in the hexagonal lattice with three carbon neighbours. Graphitic and pyridinic N are sp^2

hybridized and pyrrolic N is sp^2 hybridized. In addition to these, N oxides of pyridinic N have also been reported [316,317]. These bonding environments cannot be resolved directly from the C1*s* spectra, but can be extracted by deconvoluting the nitrogen spectra, revealing the individual contributions.

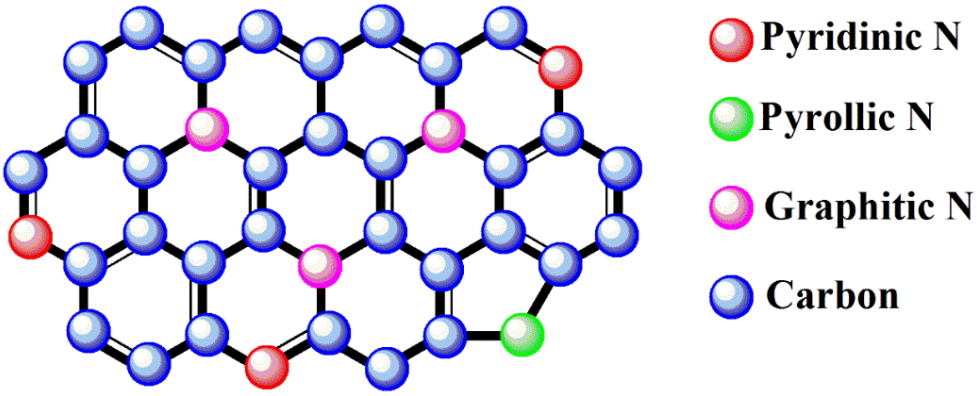

Figure 5.5 Different bonding configurations of nitrogen doped graphene oxide.

(a) Helium (2000 sccm) + nitrogen (2 sccm)

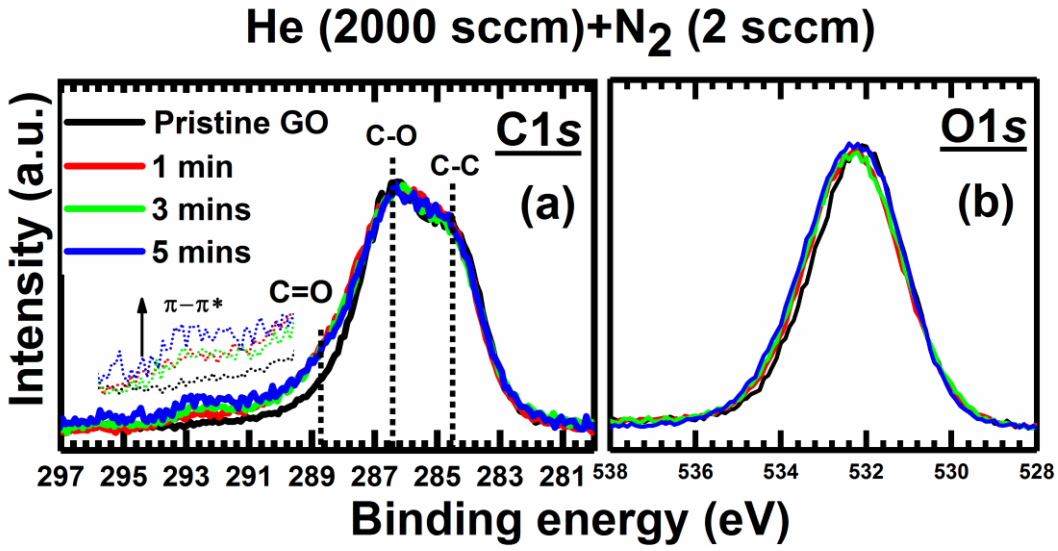

Figure 5.6 Comparison core level photoelectron spectra of (a) carbon (C1*s*) and (b) oxygen (O1*s*).

The core level spectra were referenced with the C1*s* line of freshly cleaved HOPG at 284.5 eV (Figure 2.4) and core level of gold at 84 eV (Au4$f_{7/2}$). The comparison

spectra of C1*s* and O1*s* are shown in Figure 5.6 (a) and (b), respectively. The spectra have been overlaid to understand the variation in line shape as a result of plasma treatment. The high resolution C1*s* spectra exhibited doublet peak which is a signature of graphene oxide. The significantly broad line shape of the C1*s* spectra indicates the spectral contributions from the oxygen moieties inherent in the chemical structure of GO. The peak at 284.5 eV can be attributed to C bonded to C, followed by a peak at 286.6 eV corresponding to contributions from hydroxyl (OH^-) and epoxide (C-O-C) groups [227,318]. The contribution from ketone (>C=O) component is visible between 288-290 eV. These observations are consistent with the Lerf-Klinowski model of GO [319] where it is postulated that the basal planes of GO is decorated with hydroxyl and epoxy groups whereas the edges have phenols, lactones and carboxylic acid (O-C=O) moieties [271,320]. The contrast between the pristine GO and nitrogen plasma-functionalized GO is clearly discernible from the comparison spectra of C1*s*. The spectra broaden with increased time of plasma functionalization along with the appearance of a prominent π-π* shake-up satellite centered at ~292 eV. FWHM of the O1*s* spectra increases by ~0.3 eV after plasma functionalization (from 2.5 eV for pristine GO to 2.8 eV after 5 minutes treatment) due to the change in bonding environment of oxygen.

The reference spectrum of freshly-cleaved HOPG was fitted with asymmetric Doniach-Sunjic line shape [321] to account for the semi-metallic nature of C1*s* of HOPG. The spectra of pristine and plasma-functionalized GO were fitted with Gaussian and Lorentzian line shape with 40% Gaussian and 60% Lorentzian after subtraction of a Shirley background. The contribution from nearest neighbour interaction of carbon is deconvoluted using peak fitting as shown in Figure 5.7. The main peak located at 284.5 ± 0.1 eV has contribution from both sp^2 and sp^3 bonded carbon. The disorder induced sp^3 peak occurs at a binding energy of 0.5 eV above the graphitic sp^2 carbon signature (284.5 eV) [224]. The carbonyl concentration was observed to progressively increase (from

7.5% for pristine to 11.8% to 5 mins treated GO), whereas C-C concentration showed a downward trend from 42% to 33% after 5 minutes. This may be ascribed to the formation of >C=O at the defect sites. Bagri *et al.* demonstrated that defects formed by breaking of C-C bonds in the basal plane of GO are always decorated by the >C=O groups [322]. As previously mentioned, in the Lerf-Klinowski model of GO, the carbonyl/carboxyl groups are found at the edges and defect sites. The dangling bonds formed as a result of breaking of C-C bonds are hence more susceptible to the formation of >C=O species. The C1*s* spectra (Figure 5.7) showed a consistent trail for both functionalities. The C-O component showed a 2% increase in concentration with 0.4 eV increase in FWHM. This increase in FWHM can be as a result of the presence of OH radicals in the plasma. The monotonic increase in FWHM and concentration of >C=O upon plasma exposure can also be due to the rearrangement of the C-O-C moieties into carbonyl groups as has been previously reported [271,318]. Epoxides are an unusually reactive type of cyclic ether with the C-O-C bond angle being 60°, a significant deviation from the tetrahedral bond angle of 109.5°, which introduces strain in the ring. Hence, they are readily susceptible to nucleophilic attack, resulting in breaking of the C-O-C bond and release of the strain energy in the ring. Both the carbon atoms in the moiety are strong electrophiles to the presence of oxygen and oxygen itself is a strong nucleophile with a tendency to protonate to an alcohol. The π-π* feature shows a steady increase following time dependent plasma doping [318,323–326] which might signify repairing of the sp^2 framework of the GO backbone since π-π* feature is a signature of polyaromatic systems. Table 5.2 summarizes the FWHM and percentage composition of the components which have been used to fit the C1*s* spectra of pristine and plasma functionalized GO with helium-N_2 jet.

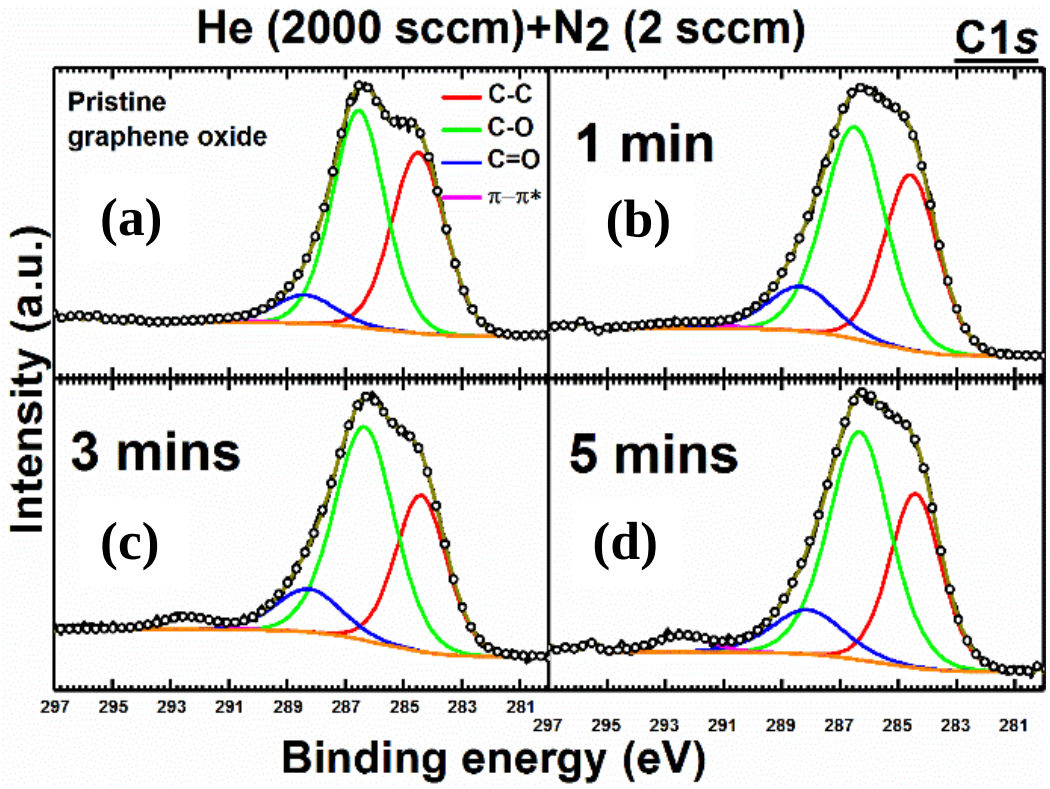

Figure 5.7 Fitted C1*s* core level photoelectron spectra of (a) pristine and (b – d) 1, 3 and 5 mins nitrogen plasma (2 sccm) functionalized GO.

O1*s*: The reorganization of the bonding environment around carbon and oxygen as an influence of plasma is also demonstrated in the O1*s* spectra. For pristine GO, the O1*s* spectrum shows a peak positioned at about 531.4 eV, along with an asymmetric tail at higher binding energy (Figure 5.8). Increasing time of plasma treatment results in significant broadening of the O1*s* spectra with a shift towards higher binding energy due to the bonding configuration of the electronegative oxygen atom. Plasma-treated GO shows contributions from three types of oxygen functionalities, namely, oxygen doubly bonded to carbon in aromatic structure as arising from single ketones, quinones and carbonyl groups (C_a=O) at ~531.3 ± 0.1 eV, oxygen singly bonded to aliphatic carbon (C-O) at ~532.4 ± 0.1 eV and oxygen singly bonded to aromatic carbon (C_a-O) at ~533.3 ± 0.1 eV (Figure 5.8 (b-d)) [227,327,328]. The increasing concentration of C-O and C_a-O at the expense of C_a=O is possibly due to the epoxide groups dissociating into phenols (C_a-

O) and hydroxyl groups upon plasma treatment. Another plausible reason might be the formation of oxygen-containing groups at the dangling bonds of GO sheets due to the presence of OH radicals in the APPJ [329].

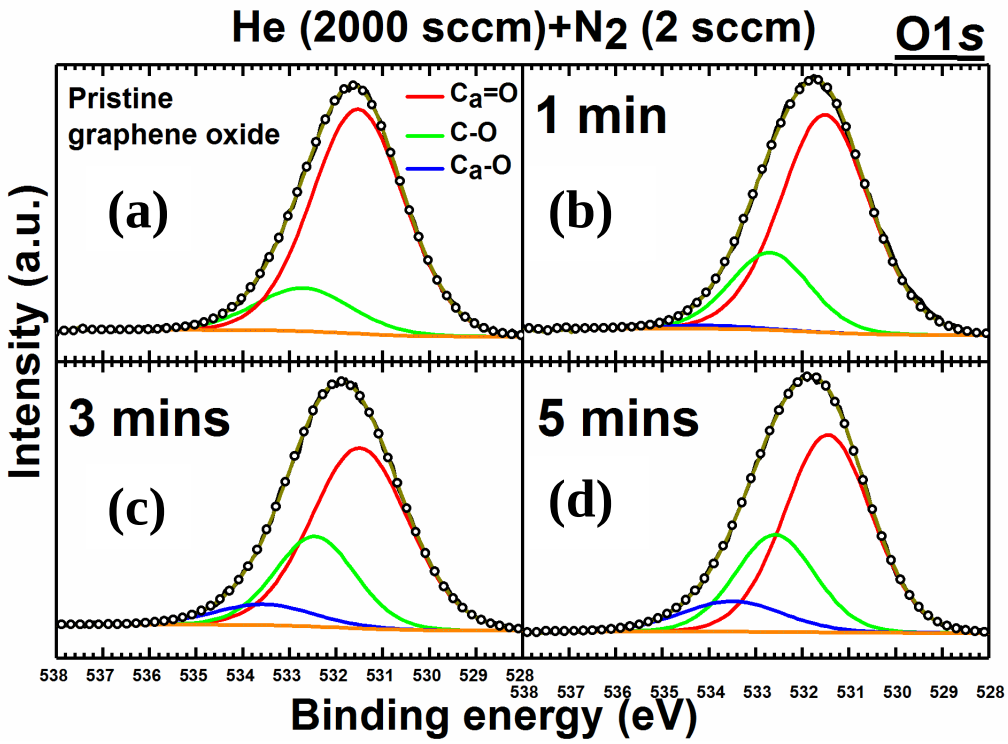

Figure 5.8 Fitted O1*s* core level photoelectron spectra of (a) pristine and (b – d) 1, 3 and 5 mins nitrogen plasma (2 sccm) functionalized GO.

N1*s*: The N1*s* spectra has been fitted with two components at 398.7 ± 0.2 eV and 401.2 ± 0.1 eV corresponding to the pyridinic and graphitic N configurations [104,330,331] as shown in Figure 5.9. As expected, pristine graphene oxide samples do not show the presence of any nitrogen. But all functionalized samples have a prominent graphitic N signature, along with a small feature corresponding to pyridinic N. The concentration of pyridinic nitrogen decreases slightly from 4.5% (1 minute) to 4.0% (5 minutes) with a small 0.5% increment in the graphitic N content from 95.5 (1 minute) to 96% (5 minute). Since, pyridinic N occupies the edge and existing defect sites of the graphene oxide backbone, it is easier to saturate the graphitic clusters with pyridinic nitrogen. However,

prolonged exposure to plasma would result in the energetic nitrogen species from the plasma jet replacing the C from the graphitic basal plane through defect formation which results in increased concentration of stable quaternary N as is evident from the strong signature of graphitic N.

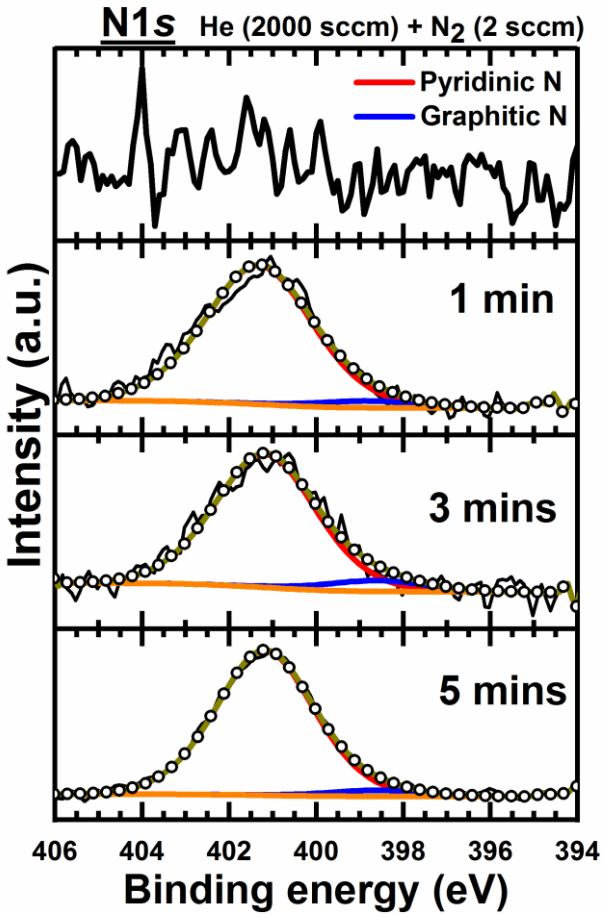

Figure 5.9 Fitted N1*s* core level photoelectron spectra of (a) pristine and (b – d) 1, 3 and 5 mins nitrogen plasma (2 sccm) functionalized GO.

(b) Helium (2000 sccm) + nitrogen (20 sccm)

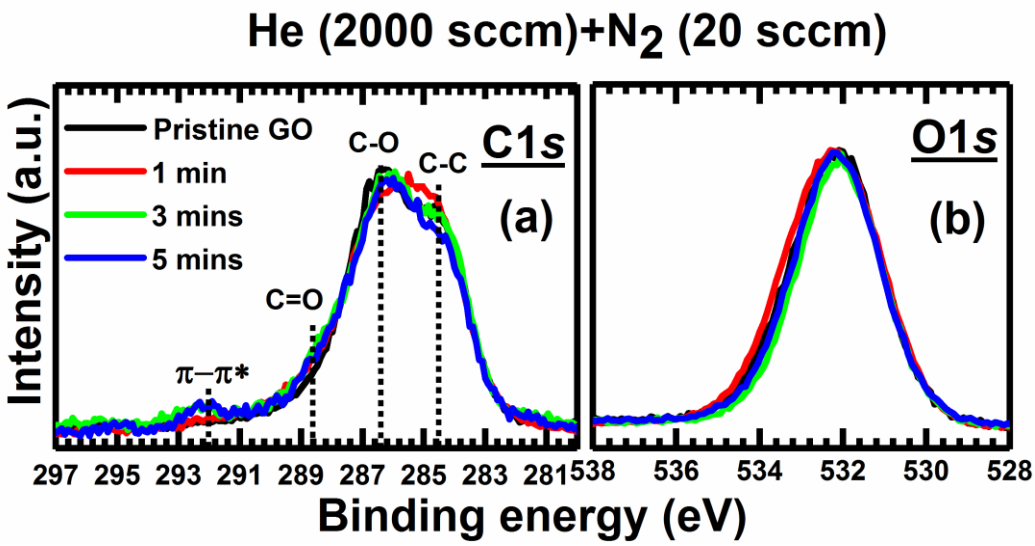

Figure 5.10 Comparison core level photoelectron spectra of (a) carbon (C1*s*) and (b) oxygen (O1*s*).

The C1*s* spectra of graphene oxide functionalized with He + N_2 (20 sccm) plasma exhibits three main peaks around 284.5 eV, 286.6 eV and 288.7 eV, tailing on the high energy side (~292 eV) due to π-bond shake-up satellite as shown in Figure 5.10 (a). Broadening of the spectra is observed especially for the >C=O component along with the appearance of a π-π* plasmon component upon plasma treatment. For the O1*s* spectra (Figure 5.10 b), the FWHM increases by 0.4 eV from the pristine to the sample after 1 minute of plasma exposure before reducing slightly for 3 and 5 minutes.

Figure 5.11 shows the deconvolved C1*s* spectra of graphene oxide and 20 sccm nitrogen plasma functionalized GO. The high resolution C1*s* peaks have been deconvoluted into three components at ~284.5 eV, 286.5 eV and 289 eV corresponding to the C=C/C-C, C-N/C-O and C=O components [318]. Intensity of peaks characteristic of C-O groups increased (50 to 54% from pristine to 5 minutes plasma functionalized GO), at the expense of C-C peaks (from 42%, pristine to 32%, after 5 minutes treatment) [316]. N_2 plasma creates structural defects with an increased amount of unsaturated carbon atoms at edge sites which are very active to reactions with oxygen, forming oxygen-containing

groups when exposed to air [329]. Steady increase in carbonyl component indicates the formation of strain-free >C=O at defect sites upon interaction with dangling bonds as a result of plasma treatment. The presence of additional nitrogen species in the plasma (20 sccm) possibly makes the defect sites in GO more susceptible to nucleophilic attack which results in increase in the concentration of both C-O and C=O moieties. The steady increase in percentage composition of π-π* peak might indicate restoration of aromatic carbon structure to some extent by the excited nitrogen species [318,323–326]. Table 5.2 summarizes the parameters of the fitted C1*s* spectra.

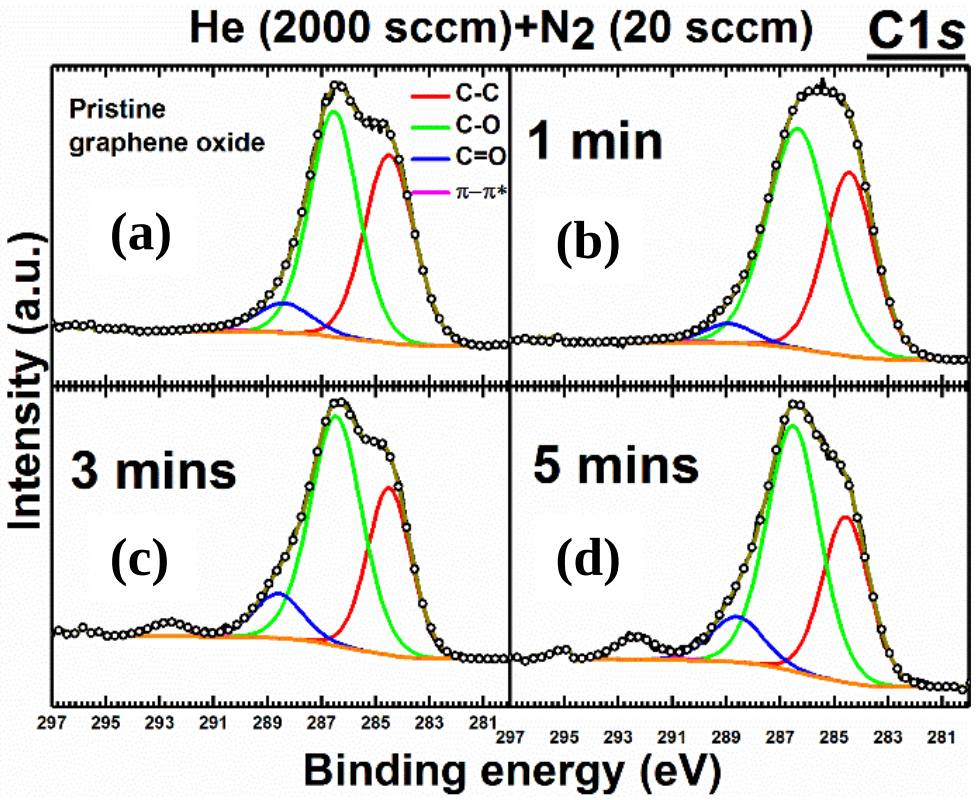

Figure 5.11 Fitted C1*s* core level photoelectron spectra of (a) pristine and (b – d) 1, 3 and 5 mins nitrogen plasma (20 sccm) functionalized GO.

O1s: Variation in bonding configuration in graphene oxide due to plasma treatment is also revealed from the O1*s* spectra. Untreated GO samples have been deconvoluted into C_a=O and C-O components (Figure 5.12 a). Similar to He + N_2 (2 sccm) plasma treated GO, samples functionalized with the He + N_2 (20 sccm) plasma jet shows contributions

from C_a=O, C-O and C_a-O at ~531.3 ± 0.1 eV, ~532.4 ± 0.1 eV and ~533.3 ± 0.1 eV, respectively, as observed from Figure 5.12 (b-d). The steady increase in concentration of C-O component with time of plasma exposure from 28% (1 min) to 34.7% (5 mins) along with the appearance of a C_a-O component possibly results from the dissociation of the strained epoxy groups into C-OH and phenol moieties as has been described previously. The monotonic increase in concentration of C-O and C_a-O components with plasma exposure time corroborates the fact that phenolic groups at basal plane of GO are the most stable species [227].

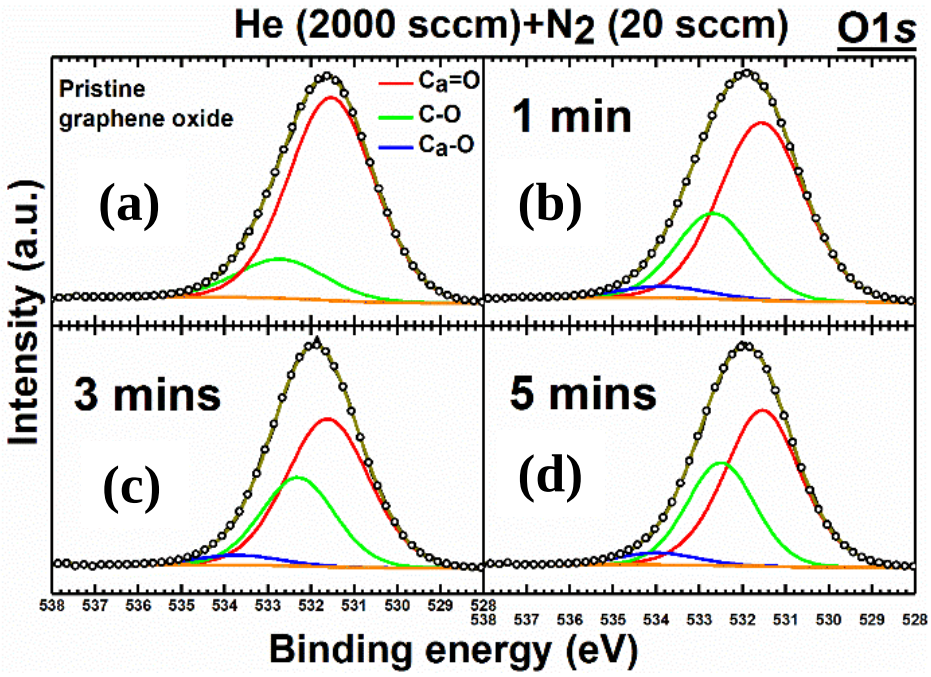

Figure 5.12 Fitted O1*s* core level photoelectron spectra of (a) pristine and (b-d) 1, 3 and 5 mins nitrogen plasma (20 sccm) functionalized GO.

N1*s*: The high resolution N1*s* spectra reveals two types of nitrogen species: pyridinic N and graphitic N, identified at a binding energy of about 398.7 ± 0.1 and 401.2 ± 0.2 eV [104,330,331], respectively (Figure 5.13). All functionalized samples show a significant graphitic nitrogen signature. The concentration of pyridinic N species is observed to have decreased from 10.6% (1 min) to 9% (5 mins), whereas the graphitic nitrogen

concentration increases progressively from 89 to 91% after 5 mins of treatment time. The FWHM of the pyridinic N component shows a 0.3 eV increase with that for the graphitic N increasing by 0.6 eV from 1 min to 5 mins of plasma exposure. A plausible reason for this broadening might be the formation of N-oxides of pyridinic N [104,316,317], though it has not been possible to deconvolute the aforementioned component. The presence of additional excited species corresponding to NO(γ) signature has been observed in the OES spectra corresponding to He and 20 sccm N_2 plasma jet which might be responsible for the broadening of the N1*s* spectra in GO samples treated for 3 and 5 minutes. Similar to the spectra treated with 2 sccm nitrogen plasma jet, 20 sccm nitrogen results in formation of both graphitic and pyridinic nitrogen at the pre-existing defect sites in the graphitic backbone of GO whereas prolonged exposure leads to substitutional effects leading to increased concentration of stable quaternary/graphitic nitrogen states as has been observed in the present case.

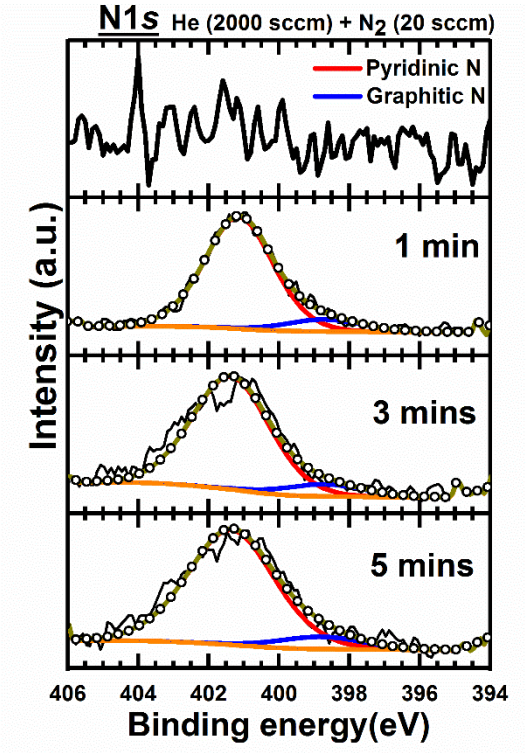

Figure 5.13 Fitted N1*s* core level photoelectron spectra of GO and nitrogen plasma (20 sccm) functionalized GO.

Table 5.2 Fitting parameters extracted from XPS spectra of pristine and He + nitrogen plasma functionalized graphene oxide.

Sample	Flow rate	Time (min)	Region	Component	% conc. ± 0.2	FWHM ±0.1 (eV)
Pristine GO			C1*s*	C-C	42.0	2.1
				C-O	50.0	2.1
				C=O	7.5	2.4
				π-π*	0.7	2.5
He + N_2 plasma treated GO	2 sccm	1		C-C	36.3	2.2
				C-O	50.6	2.5
				C=O	11.4	2.7
				π-π*	1.6	2.9
		3		C-C	33.0	2.1
				C-O	52.8	2.4
				C=O	11.5	2.6
				π-π*	2.6	2.1
		5		C-C	33.0	2.1
				C-O	52.1	2.5
				C=O	11.8	2.9
				π-π*	3.3	2.2
	20 sccm	1		C-C	38.4	2.2
				C-O	56.8	2.7
				C=O	4.1	2.2
				π-π*	0.6	2.5
		3		C-C	33.2	1.9
				C-O	54.4	2.2
				C=O	9.8	2.1
				π-π*	2.5	1.7
		5		C-C	32.0	2.0
				C-O	54.2	2.3
				C=O	9.9	2.3
				π-π*	3.9	1.7

Thus, plasma functionalization of graphene oxide with helium and nitrogen results in increase in >C=O concentration due to the formation of carbonyl groups at the defect sites. Increase in C_a-O but a decrease in the C_a=O occurs due to the rearrangement of epoxide groups to relieve the strain in the GO lattice (Figure 5.14). N1*s* spectra shows

the formation of graphitic nitrogen as a function of increased plasma treatment time because of substitution of C with N in the lattice.

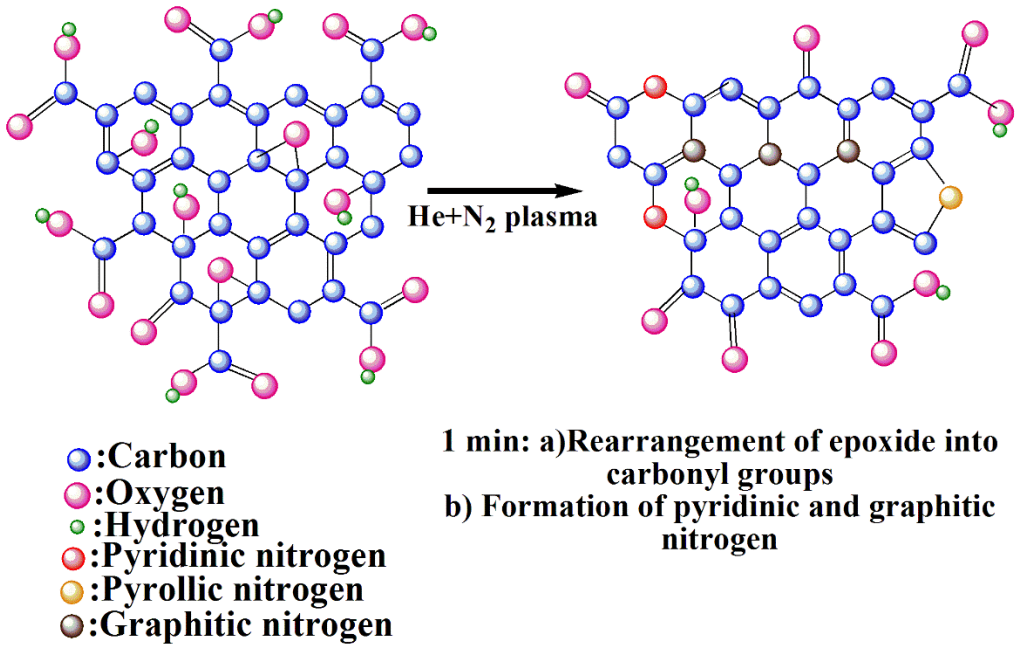

Figure 5.14 Schematic of evolution of graphene oxide after doping and functionalization with helium + nitrogen plasma.

(ii) <u>Hydrogen plasma</u>

The sp^2 network of honeycomb structure in graphene oxide is severely disrupted by the oxygen groups which affect the electrical properties of GO. Subsequent deoxygenation is required to recover the electrical conductivity for charge transport applications in PSCs. Conventional reduction techniques are limited by toxicity of the chemicals and rigorous experimental protocol. In this section, XPS will be used to study the deoxygenation of GO sheets induced by a non-conventional APPJ operated using helium and hydrogen gas mixture.

(a) Helium (2000 sccm) + hydrogen (2 sccm)

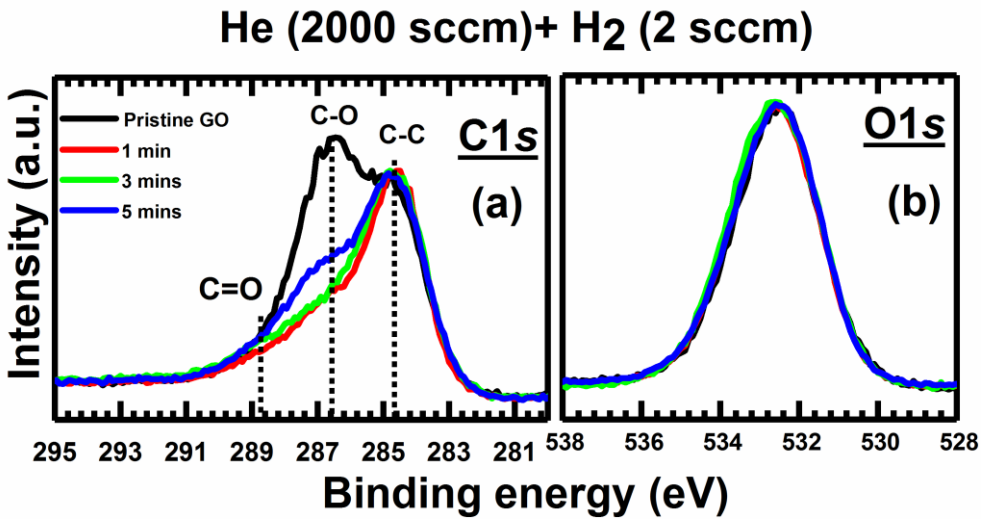

Figure 5.15 Comparison core level photoelectron spectra of (a) carbon (C1s) and (b) oxygen (O1*s*).

C1*s*: Figure 5.15 (a) shows the comparison spectra of pristine and hydrogen (2 sccm) plasma functionalized GO. The contrast between the pristine GO and hydrogen plasma functionalized GO after 1, 3 and 5 minutes is clearly visible from the comparison spectra of C1*s*. Upon hydrogen plasma functionalization, intensity of the C-O at ~286-288 eV [227,318] decreases markedly, signifying the deoxygenation of GO. But this component increases slightly after 3 and 5 mins of plasma treatment, possibly due to the presence of OH^- and atomic O in the plasma jet. The increase in amount of >C=O maybe due to formation of carbonyl groups at the defect sites in GO films because of the bombardment of highly energetic ions and electrons in the plasma. The increase in intensity of the π-π* plasmon feature around 292.0 eV can be correlated with the recovery of the sp^2 carbon domains in GO due to deoxygenation. The graphene oxide films are exposed to ions (He^+ and H^+), atomic hydrogen and neutral molecules (H_2 and He) in the helium and hydrogen plasma jet [163,172,332,333]. Except for He, all the other species are expected to contribute towards deoxygenation of the GO films. No appreciable change in the O1*s* spectra of plasma-functionalized GO samples is observed from the comparison spectra

(Figure 5.15 b). Hence, the spectra must be deconvoluted to understand the interplay between the different oxygen moieties.

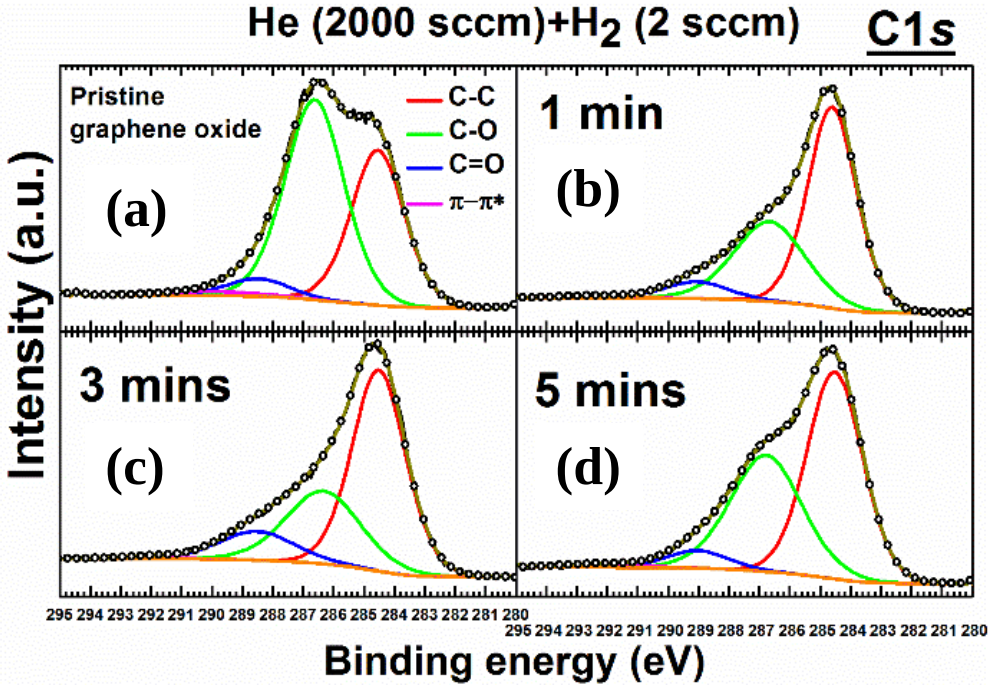

Figure 5.16 Fitted C1*s* core level photoelectron spectra of (a) pristine and (b-d) 1, 3 and 5 mins hydrogen (2 sccm) plasma functionalized GO.

The C1*s* signal of the pristine GO film can be deconvoluted into C=C/C−C (284.5 ± 0.2 eV), C-O (286.5 eV), C=O (289 ± 0.2 eV), and π−π* satellite peak (~292 eV) as shown in Figure 5.16. These assignments are consistent with previous reports of GO [172,281]. The concentration of C-C species showed a marked increase from 42% to 54% after 5 minutes of plasma treatment whereas the C-O component reduced substantially from 50% to 39.5%. This demonstrates the deoxygenation of GO. FWHM of C-C component reduces from 2.1 eV to 1.9 eV after 1 minute of plasma treatment suggesting restoration of the sp^2 bonded domains in graphene oxide as a result of healing of defects. Subsequent 0.2 eV increase in the FWHM for 3 and 5 minutes of plasma treatment possibly implies formation of defects (sp^3 carbon bonds) as a result of prolonged exposure. FWHM of C-O component increases from 2.1 to 2.9 eV after 3 minutes, whereas, the concentration

decreases from 57 to 29% after 3 minutes before subsequent increase to 39%. FWHM of >C=O component increases from 2.5 to 2.9 eV for 3 minutes functionalized samples with concentration increasing to 11.7% from 7.5%. The initial increase in C=O at the expense of C-O component may be interpreted as a result of the conversion of strained C-O-C component into strain-free C=O component as reported by Bagri *et al*. and Rani *et al* [271,318]. But the decrease in FWHM and concentration of C=O after 5 minutes of treatment possibly results from partial conversion of C=O to C-O [227]. Table 5.3 shows the FWHM and percentage composition of the components which have been used to fit the C1*s* spectra of GO and plasma functionalized GO with He and H_2.

O1*s*: Unlike untreated GO (Figure 5.17 a), He + H_2 (2 sccm) plasma-functionalized samples show contributions from an additional C_a-O component at ~533.5±0.1 eV (Figure 5.16 (b-d)). Formation of the phenolic (or aromatic diol) groups during deoxygenation of graphene oxide has been reported by Lerf *et al*. due to the proximity of C-O-C and C-OH on the basal planes [319]. The steady increase in concentration of C-O and C_a-O components with prolonged plasma functionalization possibly results from the transformation of C=O into C-O as reported earlier. The monotonic increase in concentration of C-O and C_a-O components with plasma exposure time corroborate the fact that the OH moieties on the basal plane of GO are the most stable species [227].

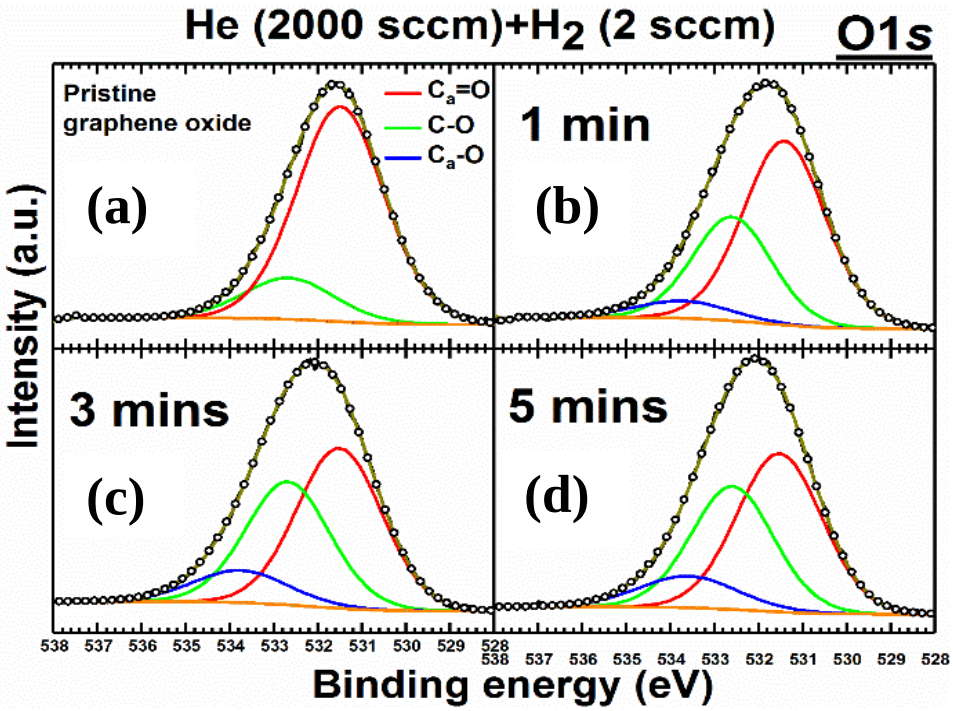

Figure 5.17 Fitted O1*s* core level photoelectron spectra (a) pristine and (b-d) 1, 3 and 5 mins hydrogen (2 sccm) plasma functionalized GO.

(b) Helium (2000 sccm) + hydrogen (20 sccm)

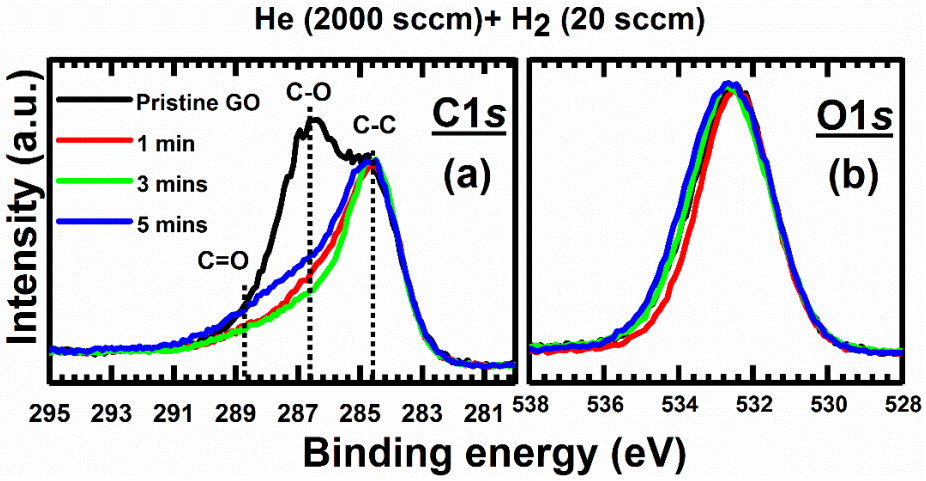

Figure 5.18 Comparison core level spectra of (a) carbon (C1*s*) and (b) oxygen (O1*s*) of pristine and plasma-functionalized graphene oxide with He + H_2 (20 sccm).

The contrast in the C1*s* spectra between the pristine and the hydrogen plasma functionalized GO with 20 sccm hydrogen is clearly discernible from Figure 5.18.

Similar to the 2 sccm H_2 plasma treated GO samples, the deoxygenation effect is pronounced when 20 sccm H_2 is used, showing clear transformation of a doublet to singlet peak. The signature from oxygen functionalities between 286-288 eV and 289 eV show significant reduction after 1 and 3 mins of plasma treatment, corroborating the reduction effect. But the C-O and C=O components increase in intensity after 5 minutes of treatment. Whilst the hydrogen plasma would be expected to provide a reducing environment for GO, the increase in C-O component after 5 minutes of plasma treatment may be as a result of the formation of C-OH species due to plasma exposure. The π-π^* plasmon feature shows a gradual increase after 1, 3 and 5 mins of plasma treatment, possibly signifying restoration of some aromatic character [318,323–326]. FWHM of the O1*s* spectrum for the GO sample treated with hydrogen plasma for 1 minute is reduced by 0.3 eV compared to the spectrum for pristine film as shown in Figure 5.18. But there is increase in the FWHM on increasing the time of exposure to 3 and 5 minutes possibly due to the presence of OH radicals in the APPJ.

Reduction/deoxygenation can occur due to several phenomena. Using high energy electrons or ions such as He^+ from the carrier gas plays a role in the deoxygenation process due to physical bombardment. But if admixtures of helium and hydrogen are used, the GO sheets are exposed to active species including hydrogen radicals, ions (He^+ and H^+) and neutral molecules (H_2 and He) which may lead to reduction [163,172].

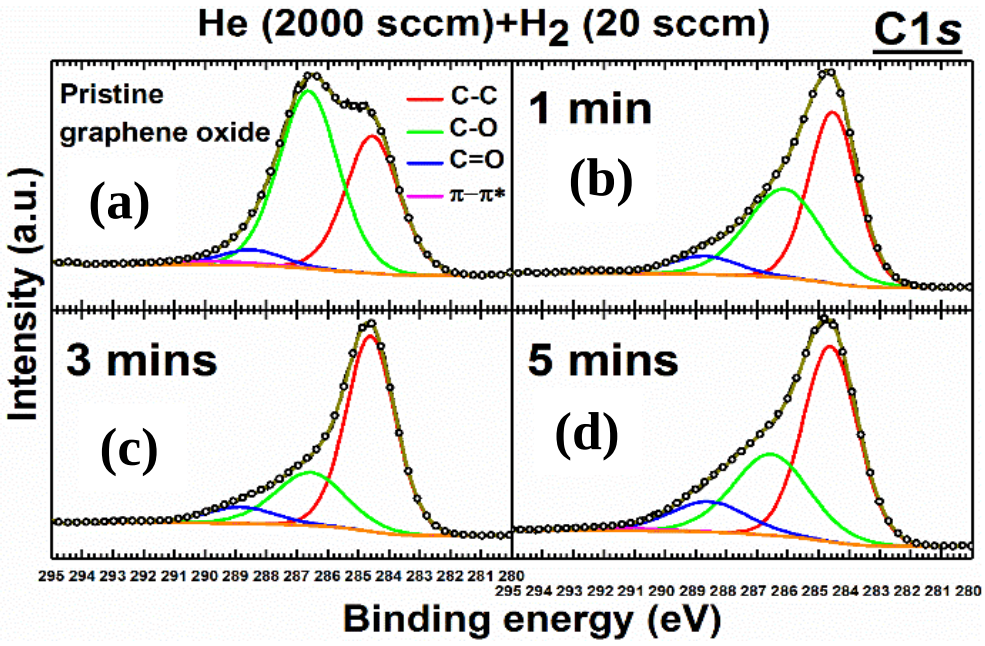

Figure 5.19 Fitted C1*s* core level photoelectron spectra of (a) pristine and (b – d) 1, 3 and 5 mins hydrogen (20 sccm) plasma functionalized GO.

Figure 5.19 shows the comparison spectra of pristine and plasma-functionalized graphene oxide samples with helium and hydrogen (20 sccm) jet with the deconvoluted components. Similar to the effect with 2 sccm hydrogen, the transformation of a double peak to a sharp single peak is indicative of a trend of restoration of the sp^2 bonding character. The significant increase in the concentration of C-C component from 42 to 54.8% after 5 minutes of hydrogen plasma treatment along with a decrease in the C-O component from 50% to 31.7% is observed due to deoxygenation of the GO films. The reduction in FWHM of C-C from 2.1 to 1.8 after 1 min of hydrogen plasma functionalization would suggest healing of the defect sites of GO. This trend is further supported by the intensity increase in π-π*shake-up satellite peak. The monotonic increase in >C=O concentration at the expense of C-O concentration is due to the conversion of epoxides into carbonyl groups [271,318].

O1*s*: O1*s* spectra of untreated and He + H_2 (20 sccm) plasma functionalized samples are shown in Figure 5.20. The increase in concentration of C-O and C_a-O components with

time of plasma exposure from 33% (1 min) to 37% (5 mins) and 8.2% (1 min) to 18.5% (5 mins), respectively, possibly results from the conversion of epoxide groups into carbonyl and phenol moieties [271,318] and prove the better stability of OH groups on the basal plane of GO [227].

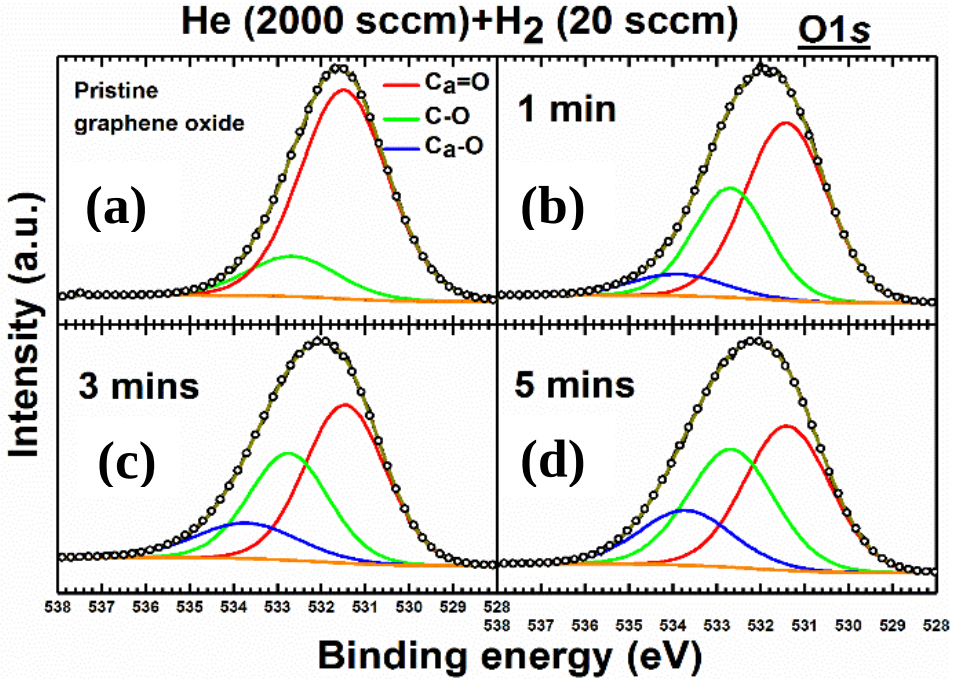

Figure 5.20 Fitted O1*s* core level photoelectron spectra of (a) pristine and (b-d) 1, 3 and 5 mins hydrogen (20 sccm) plasma functionalized GO.

Table 5.3 Fitting parameters extracted from XPS spectra of pristine and He + hydrogen plasma functionalized graphene oxide.

Sample	Flow rate	Time (min)	Region	Component	% conc. ± 0.2	FWHM ± 0.1 (eV)
Pristine GO			C1*s*	C-C	42.0	2.1
				C-O	50.0	2.1
				C=O	7.5	2.4
				π-π*	0.7	2.5
He + H_2 plasma treated GO	2 sccm	1		C-C	58.8	1.9
				C-O	34.0	2.7
				C=O	6.4	2.5
				π-π*	0.80	2.3
		3		C-C	58.3	2.1
				C-O	29.3	2.9
				C=O	11.7	2.9
				π-π*	0.71	2.0
		5		C-C	54.1	2.1
				C-O	39.5	2.8
				C=O	5.1	2.4
				π-π*	1.3	2.9
	20 sccm	1		C-C	50.6	1.8
				C-O	40.9	2.8
				C=O	7.6	2.6
				π-π*	0.9	1.8
		3		C-C	66.0	1.9
				C-O	25.6	2. 7
				C=O	7.8	2.6
				π-π*	0.5	1.8
		5		C-C	54.8	2.1
				C-O	31.7	2.9
				C=O	12.1	2.9
				π-π*	1.4	3.7

Hence, functionalization with helium and hydrogen plasma results in deoxygenation of graphene oxide as evident from the transformation of the C1*s* doublet into singlet feature. Initial treatment (1 and 3 minutes) results in rapid removal of edge plane >C=O along with restoration of the aromatic backbone. Prolonged exposure

results in additional phenolic groups. Increase in concentration of >C=O at the expense of C-O suggests the relaxation of the strained graphene oxide lattice. Formation of an additional C_a-O component in the O1*s* spectra indicates the conversion of C-O-C into phenolic groups upon deoxygenation (Figure 5.21).

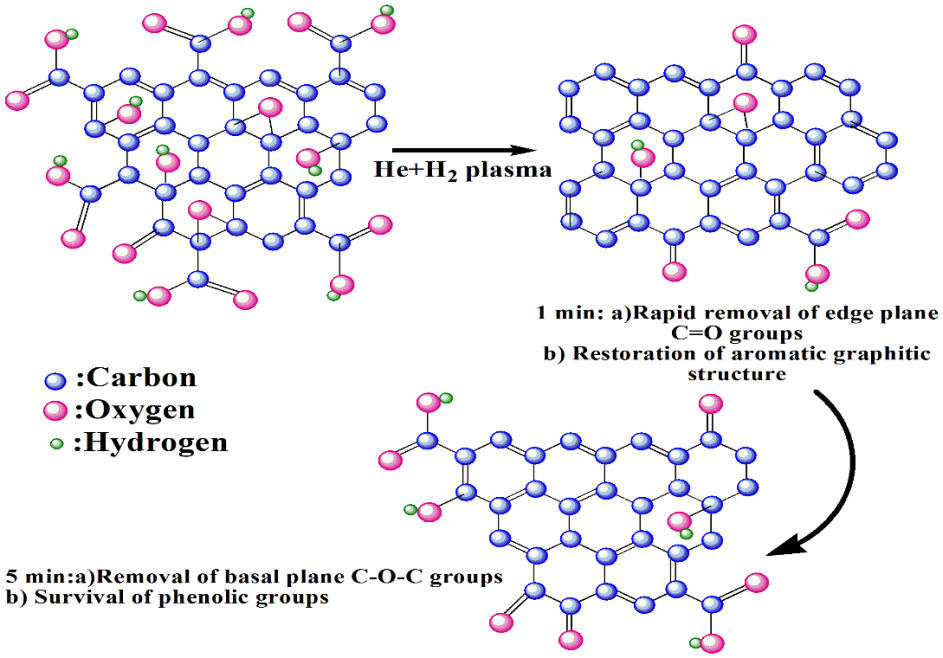

Figure 5.21 Schematic of evolution of graphene oxide after functionalization with helium + hydrogen plasma.

(iii) <u>Oxygen plasma</u>

(a) Helium (2000 sccm) + oxygen (2 sccm)

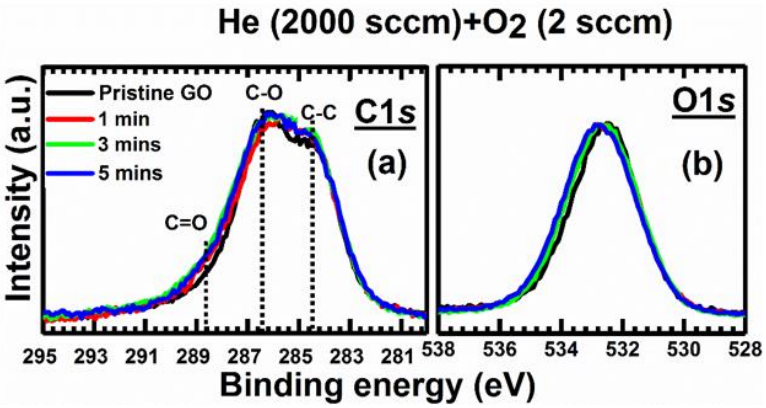

Figure 5.22 Comparison core level photoelectron spectra of (a) carbon (C1*s*) and (b) oxygen (O1*s*).

C1*s*: The C1*s* spectra of pristine and plasma functionalized GO with helium and 2 sccm oxygen is as shown in Figure 5.22 (a). Untreated and plasma treated GO show a clear contrast in the C1*s* spectra with 0.4 eV increase in FWHM after 1 minute of exposure. The effect of sequential oxidation is observable with broadening of FWHM with increased oxygen functionalization. The FWHM becomes saturated at 3 minutes. This increase signifies an enhancement in oxygen moieties such as C-O and C=O due to oxygen plasma functionalization. The comparison O1*s* spectra of the GO films treated with 2 sccm oxygen is as shown in Figure 5.22 (b). The FWHM of the spectra after 5 minutes of functionalization is 0.3 eV more than pristine sample suggesting an addition of different oxygen functionalities to the GO films as a result of plasma interaction.

C1*s* spectra of GO treated with He and 2 sccm oxygen plasma is as shown in Figure 5.23. The different C groups are characterized by the appearance of peaks at ~284.5 eV, 286.5 eV and 288.5 ± 0.2 eV corresponding to the C=C/C-C, C-N/C-O and C=O components [318]. Intensity of C-C component decreases monotonically upon plasma treatment, whereas, C-O and C=O components show a small increase from 50 to 53.7% and 7.5 to 8.0%, respectively. Measuring the FWHM is a good measure of the defects induced in the GO sheets due to bombardment with plasma. FWHM of C-C increases from 2.1 to 2.3 eV, with a 0.5 eV increase observed for the C-O component. This might indicate formation of defect sites and attachment of oxygen functional groups at the defect sites. Table 5.4 summarizes the parameters of the fitted C1*s* spectra.

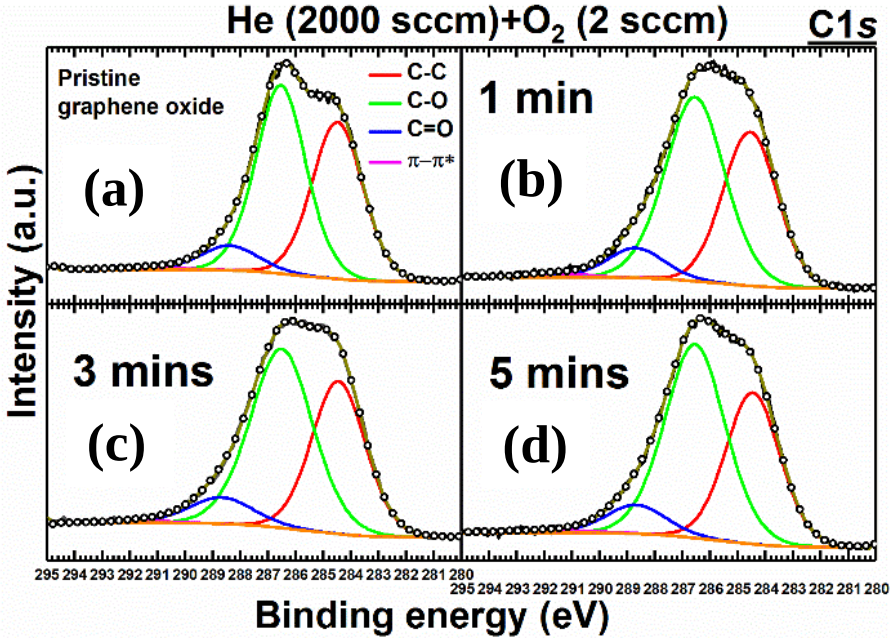

Figure 5.23 Fitted C1*s* core level photoelectron spectra of (a) pristine and (b – d) 1, 3 and 5 mins oxygen (2 sccm) plasma functionalized GO.

O1*s*: O1*s* spectra of He + O_2 (2 sccm) plasma-functionalized samples show an additional contribution from C_a-O at ~ 533.3 ± 0.1 eV (Figure 5.24 b-d) compared to pristine graphene oxide (Figure 5.24 a). The concentration of C-O and C_a-O components increase steadily with a reduction in intensity of C_a=O peak. This trend suggest the formation of phenolic groups due to the proximity of C-O-C and C-OH at the basal plane of graphene oxide [319].

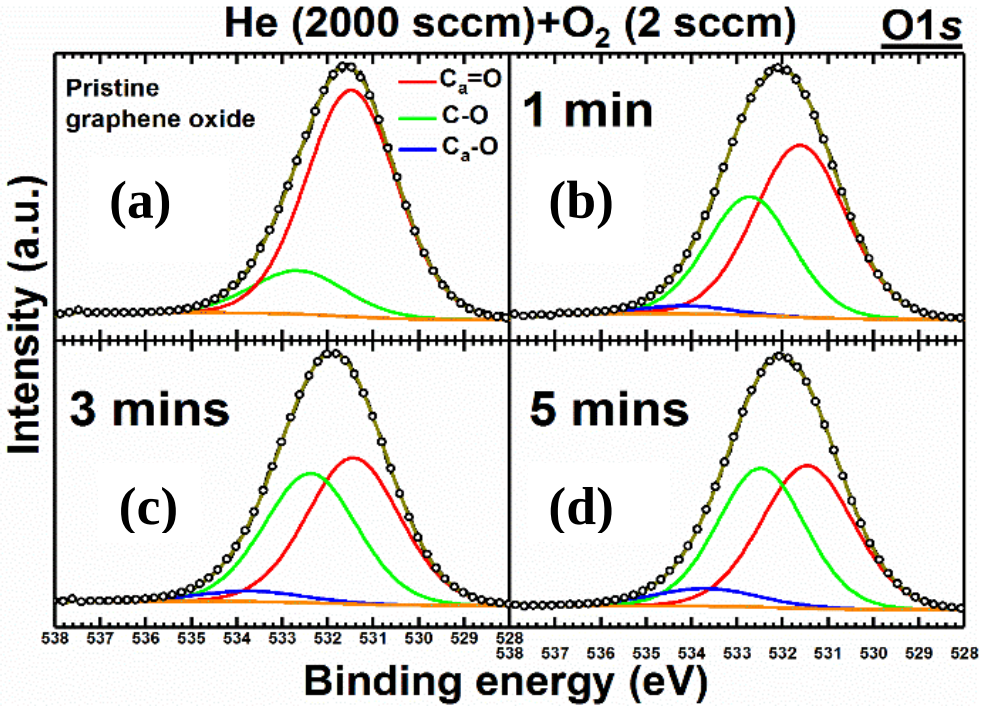

Figure 5.24 Fitted O1*s* core level photoelectron spectra of (a) pristine and (b-d) 1, 3 and 5 mins oxygen (2 sccm) plasma functionalized GO.

(b) Helium (2000 sccm) + oxygen (20 sccm)

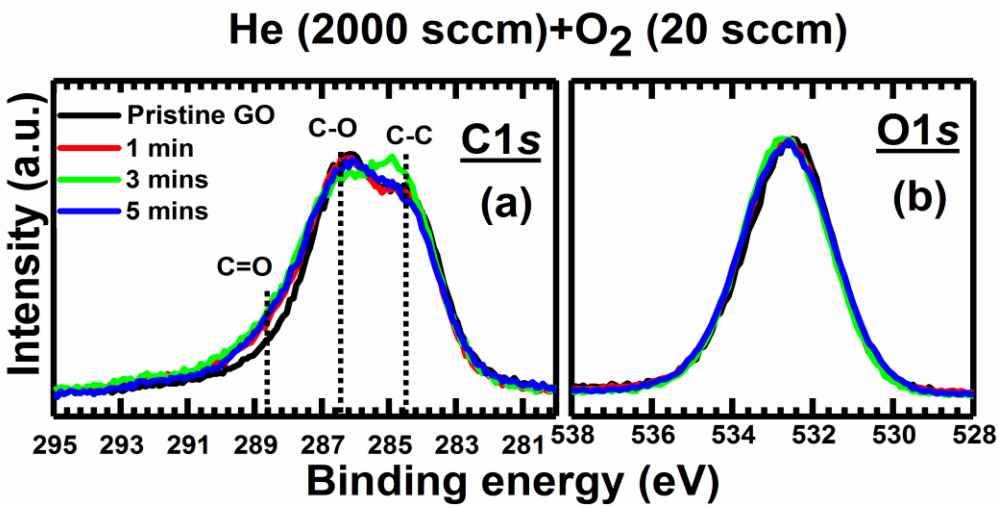

Figure 5.25 Comparison core level spectra of (a) carbon (C1*s*) and (b) oxygen (O1*s*) of pristine and helium-oxygen (20 sccm) functionalized GO.

C1*s*: Figure 5.25 (a) shows the comparison spectra of pristine and plasma functionalized GO with 20 sccm oxygen. The FWHM of C1*s* increased by 0.5 eV after plasma

treatment. This was due to an increase in the oxygen functionalities in GO as a result of excited species present in oxygen plasma. The sp^2 carbon component steadily increased upon plasma functionalization. The effect of 20 sccm oxygen in the plasma is not much pronounced in the O1*s* spectra with the spectra reporting only slight increase in the FWHM (~0.1 eV) after 5 minutes of exposure as shown in Figure 5.25 (b).

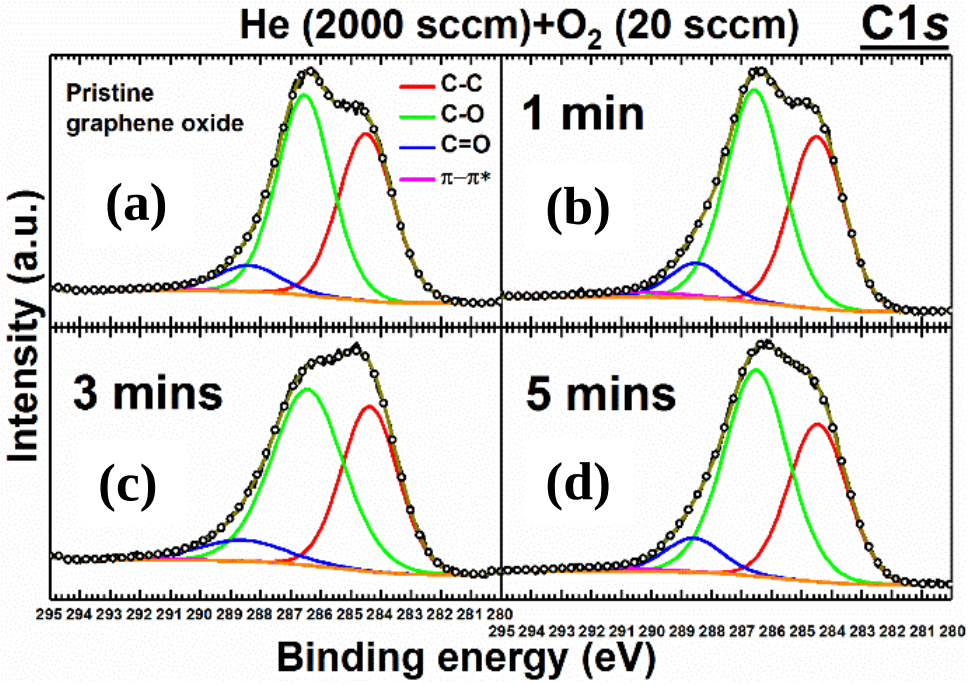

Figure 5.26 Fitted C1*s* core level photoelectron spectra of (a) pristine and (b-d) 1, 3 and 5 mins oxygen (20 sccm) plasma functionalized GO.

The contribution from nearest neighbour interaction of carbon is deconvoluted using peak fitting as shown in Figure 5.26. Intensity of peak corresponding to C-C signature decreases (42 to 40.6% after 5 minutes exposure) whilst C-O intensity remains almost same. A 0.6 eV increase in >C=O concentration in GO films is also observed as a result of carbonyl bond formation at the defect sites in the GO films. The π-π* feature at 291.5 eV doubles in intensity after 5 minutes of plasma treatment (from 0.7 to 1.54%) which suggests healing of some defect sites by bonding of oxygen groups.

O1s: Untreated GO samples showed the contribution from C_a=O and C-O components (Figure 5.27 (a)), whereas He + O_2 (20 sccm) plasma functionalized samples showed an additional feature at ~533.3 ± 0.1 eV due to C_a-O (Figure 5.27 (b-d)). The concentration of C-O and C_a-O components progressive increase with time from 34% (1 min) to 40% (5 mins) and 5.3% (1 min) to 6.1% (5mins), respectively, whereas the C_a=O concentration reduces from 60.6 to 53.7% after 5 minutes. This possibly results from the conversion of C-O-C into phenolic groups or oxidation of C=C [319,334].

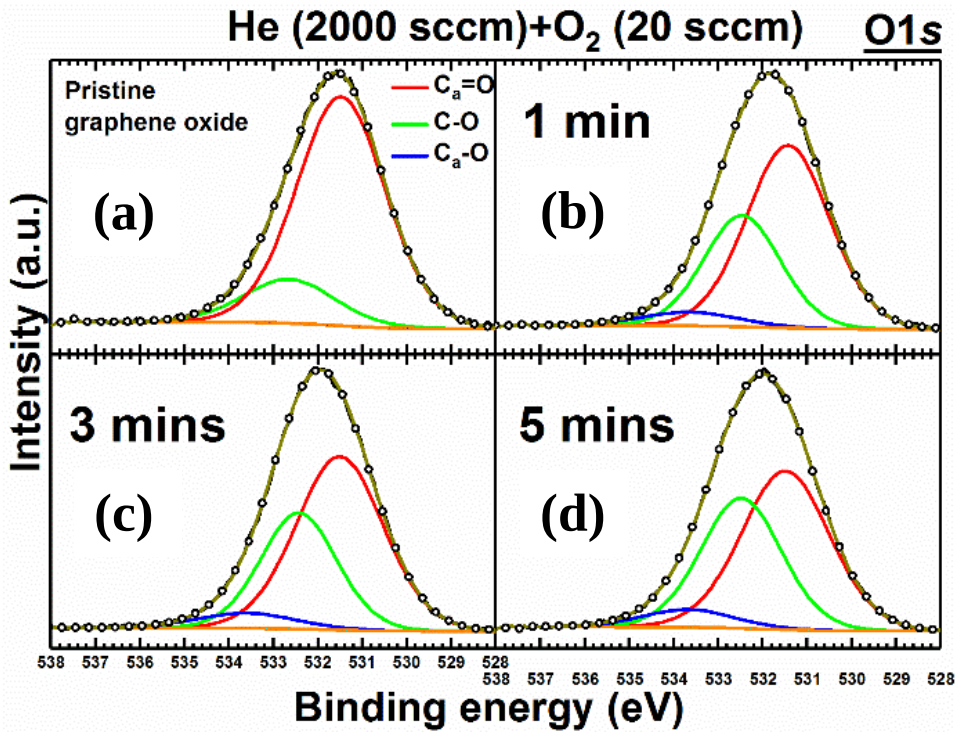

Figure 5.27 Fitted O1*s* core level photoelectron spectra of (a) pristine and (b – d) 1, 3 and 5 mins oxygen (20 sccm) plasma functionalized GO.

Table 5.4 Fitting parameters extracted from XPS spectra of pristine and He + oxygen plasma functionalized graphene oxide.

Sample	Flow rate	Time (min)	Region	Component	% conc. ± 0.2	FWHM ± 0.1 (eV)
Pristine GO			C1*s*	C-C	42.0	2.1
				C-O	50.0	2.1
				C=O	7.48	2.45
				π-π*	0.73	2.5
He + O_2 plasma treated GO	2 sccm	1		C-C	39.0	2.3
				C-O	52.0	2.5
				C=O	8.0	2.4
				π-π*	1.1	2.5
		3		C-C	38.6	2.3
				C-O	53.0	2.6
				C=O	8.0	2.75
				π-π*	0.6	2.4
		5		C-C	37.3	2.3
				C-O	53.7	2.6
				C=O	8.0	2.5
				π-π*	1.0	3.8
	20 sccm	1		C-C	37.2	2.1
				C-O	53.4	2.3
				C=O	8.1	2.2
				π-π*	1.3	2.9
		3		C-C	44.8	2.3
				C-O	45.6	2.5
				C=O	8.6	2.8
				π-π*	1.0	2.7
		5		C-C	40.6	2.4
				C-O	49.1	2.4
				C=O	8.7	2.2
				π-π*	1.5	3.6

Thus, functionalization of graphene oxide with helium and oxygen plasma results in formation of additional oxygen moieties at the graphene oxide surface along with a change in the surface speciation as evident from the C1*s* and O1*s* spectra as shown in Figure 5.28. These oxygen-containing functional groups influence the work function of GO as will be explained in the following section.

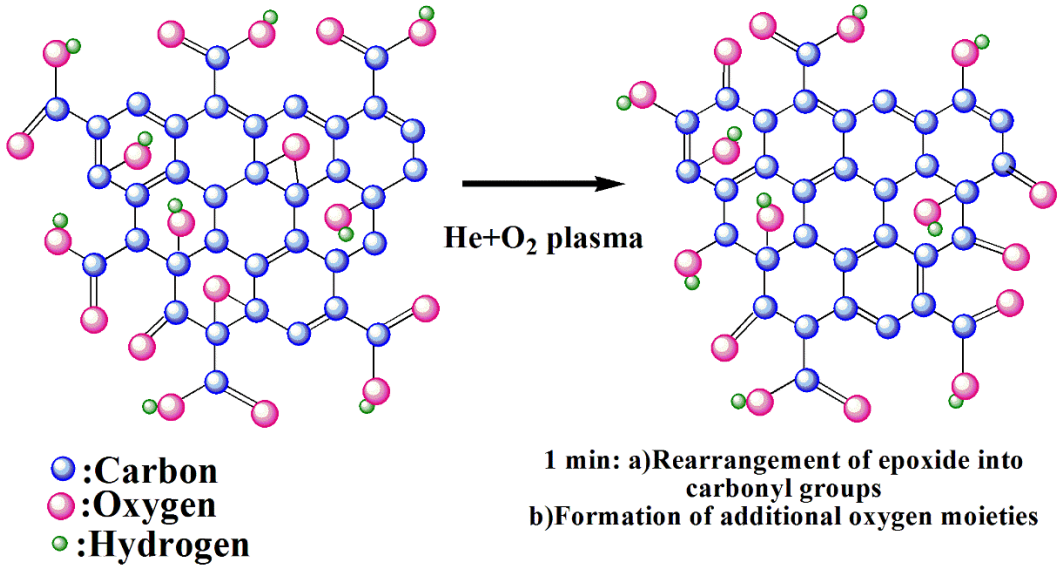

Figure 5.28 Schematic of evolution of graphene oxide after helium + oxygen plasma treatment.

5.3.3 Ultraviolet photoelectron spectroscopy (UPS)

The evolution of valence band electronic structure and properties of graphene oxide upon treatment with nitrogen, hydrogen and oxygen plasma was investigated using UPS. All spectra were calibrated with respect to the UPS spectrum of an Ag foil with Fermi level located at E = 0. As the excitation of UPS sources can bring about excitation of only the valence electrons, information regarding the distribution of electrons in the valence band and hence the density of states (DOS) near the Fermi level can also be extracted. The valence band spectrum for pristine GO consists of component peaks corresponding to 2*p* π (~3.5 eV), 2*p* (π-σ) overlap (~7 eV), 2*p* σ (~9 eV), 2*s*-2*p* mixed states (~11 eV) and 2*s* σ (~14 eV) [335]. The valence band spectra of plasma-functionalized GO are dominated by a broad band centered at ~7 eV, however, they differ with respect to the low energy feature centered at ~3.5 eV, corresponding to DOS due to C2*p* π electrons in various carbon structures [336–338]. Valence band spectra obtained with He I excitation source on pristine and plasma-functionalized GO is as shown in Figure 5.29.

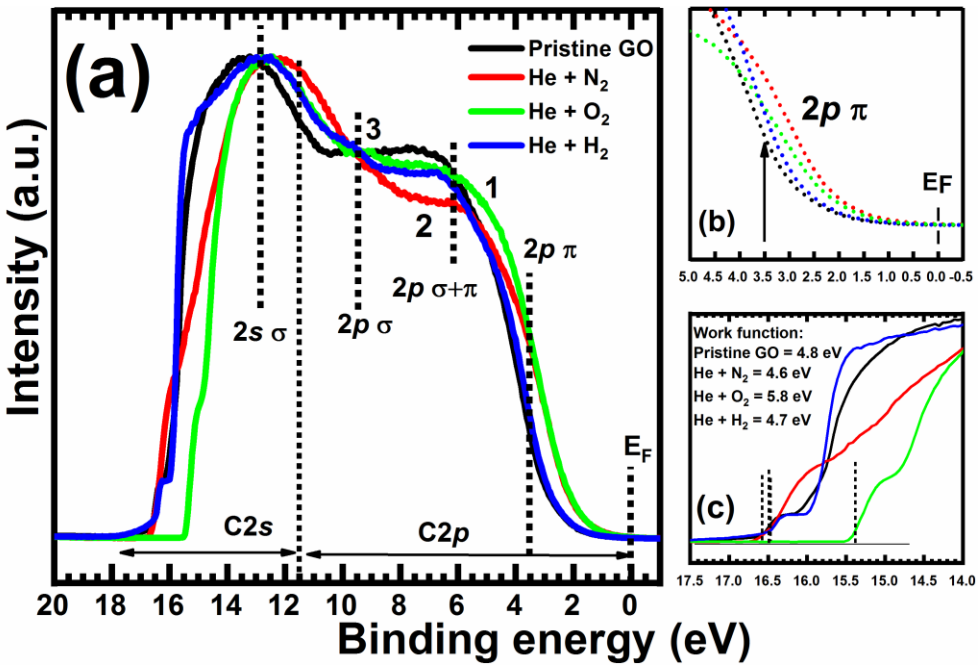

Figure 5.29 UPS spectra of pristine and plasma functionalized GO with different gases: He + N_2 (red), He + O_2 (green) and He + H_2 (blue) corresponding to (a) the entire spectrum inclusive of the secondary cut-off and HOMO regions, (b) HOMO region showing an increase in density of states and (c) work function of the samples calculated from the cut-off region for secondary electrons.

Functionalization with He and N_2 plasma jet results in N doping, which enhances the DOS near the Fermi level [339,340] as can be observed from Figure 5.29 (b). The delocalized 2*p* π states (~3.5 eV) become pronounced upon treatment with He + N_2 plasma jet. The substitution of electron-rich N into the aromatic network in the form of graphitic N would contribute two electrons to the π electron system when compared to one π electron from each carbon atom [339,340]. On the other hand, when pyridinic N atom is bonded to two neighbouring C, the two electrons on the N atom contribute to the localized lone pair. Thus, incorporation of pyridinic N would enhance the C-N 2*p*π states at the expense of C-C 2*p* π electron state density. Souto *et al*. have reported that the top of the valence band for diamond-like films undergo significant changes upon nitrogen incorporation [339]. Using He II (40.8 eV) as the excitation source, Luo *et al*. have shown

that the UPS spectra obtained demonstrate the presence of three new bands at ~4.5 eV, 7 eV and ~9.5 eV corresponding to the lone pair of electrons localized on N atom, C2*p* and N2*p* electrons associated with π orbitals of C-N bond and C2*p* and N2*p* electrons shared in σ bonds, respectively [340]. Since, in the present study, He I (21.22 eV) has been used as the excitation source, the aforementioned features cannot be distinctly identified as separate peaks (positions marked as 1, 2 and 3 in Figure 5.29). Nevertheless, a slight increase in DOS around 5 eV and 9 eV have been observed which can be attributed to the increase in density of lone pair on the N atom and the σ electrons of the C-N bonds, respectively. Furthermore, the decrease in intensity around 7 eV might be as a result of reduction in π orbitals of C-C bonds due to the substitution of C by N atom. This also reflects the substitution of C-C bonds by C-N bonds. Thus, UPS spectra proved that in the present study the major bonding configuration after 5 minutes of N doping of GO is graphitic in nature. This result can be corroborated by the N1*s* XPS spectra. The inclusion of nitrogen into the graphitic network would result in the formation of donor levels near the conduction band edge which raises the Fermi level [341], thus lowering the work function and has been explained later.

As compared to pristine GO, the UPS spectra of samples treated with He and H_2 plasma jet demonstrate an increase in intensity around 3.5 eV, which is suggestive of an enhancement in C2*p* π electrons, either due to increase in graphitic carbon content or decrease in surface functional groups [342]. Similar studies on effect of oxidation on the electronic properties of carbon nanotubes have revealed a decrease in C2*p* π electrons attributable to an increase in surface functional groups [343,344]. This result can be corroborated by the C1*s* XPS spectra of He + H_2 plasma treated GO films which shows a significant drop in intensity of the doublet feature corresponding to C-O component (~286.5 eV) upon hydrogen plasma functionalization, thus implying deoxygenation of GO.

Upon treatment with He and O_2 plasma, an increase in DOS near the Fermi level is observed which might be due to the formation of additional states near the conduction band of graphene oxide as a result of incorporation of electron-rich oxygen atom in the graphitic lattice. An enhancement of the C2p π states at ~3.5 eV is observed from Figure 5.29 (b). Increase in density of localized lone pairs over the oxygen atom possibly results in enhancement in the feature at ~5 eV.

The work function of GO and plasma-functionalized GO can be calculated from the secondary electron energy threshold as [345–347]

$$WF\ (\varphi) = h\nu - E_F + E_{cut-off} \quad \text{.....5.2}$$

Where $h\nu$ is the He (I) excitation energy is equal to 21.22 eV, E_F is the Fermi level, and $E_{cut-off}$ is the high binding energy cut-off.

The work function of pristine graphene oxide films was calculated as 4.8 eV, while those for He + N_2, He +H_2 and He + O_2 plasma-treated GO samples were 4.6 eV, 4.7 eV and 5.8 eV, respectively. Nitrogen and hydrogen plasma treatment is observed to have reduced the work function whereas oxygen plasma brings about an increase in work function. The bonding configuration of nitrogen in graphene oxide was shown to influence the work function of GO [255]. Hence, the 0.2 eV decrease in work function in the present study can be attributed to the n-type doping effect of graphitic N which is the predominant species as observed from XPS. The higher work function as observed in case of oxygen plasma functionalized GO samples, possibly results from the presence of surface dipole moments attributable to the oxygen functional groups which disrupt π conjugation [342,343]. Thus, in this chapter it has been shown how the work function of graphene oxide can be tuned by functionalization with different gases in an atmospheric pressure plasma jet.

5.3.4 Electrical properties

Sheet resistivity measurements were undertaken to quantify the variation in film conductivity. The conductivity of functionalized GO films improved by ~10^3 after 3 minutes of treatment with 2 sccm He+H_2 plasma jet. This improved film conductivity suggests recovering of the sp^2 framework upon deoxygenation of graphene oxide with He + H_2 plasma jet. With He + N_2 and He + O_2 plasma treatment, the GO sheet resistivity exceeded the testing limit of our experimental setup, which was 200 MΩ sq^{-1}.

Table 5.5 Variation of sheet resistivity of graphene oxide with plasma functionalization.

Sample Id	**Gas flowrate**		**Time of treatment**	**Sheet resistivity (MΩ sq^{-1})**
Pristine graphene oxide	No plasma		0	138.5
Plasma-treated graphene oxide	He (2000 sccm) +	N_2 (2 sccm)	1, 3, 5 minutes	Out of range
		N_2 (20 sccm)		
	He (2000 sccm) +	O_2 (2 sccm)	1, 3, 5 minutes	Out of range
		O_2 (20 sccm)		
	He (2000 sccm) +	H_2 (2 sccm)	1 min	12.0
			3 mins	0.24
			5 mins	0.098
		H_2 (20 sccm)	1 min	96.5
			3 mins	2.5
			5 mins	0.15

5.4 Conclusions

Tuning the work function of hole conductor molecules is of paramount importance for band alignment in heterojunction devices. The ability to modulate the work function of graphene oxide makes it a low-cost HTM for PSCs. But the conventional chemical techniques lack precision in controlling the oxygen functionalities of GO and are not environment-friendly. This chapter demonstrates that APPJ is a promising candidate for surface functionalization of GO. A low power (3 W) and flow rates as low as 2 sccm can sustain a stable plasma discharge. A systematic investigation of GO functionalization was undertaken using He+N_2, He+H_2 and He+O_2 plasma jets. Detailed

X-ray spectroscopic studies revealed that the active species in plasma are instrumental in varying the surface chemistry and electronic properties of GO. XPS analysis shows that functionalization of graphene oxide with helium and nitrogen results in increase in >C=O concentration due to the formation of carbonyl groups at the defect sites. Increase in phenolic groups occurs due to the rearrangement of epoxide groups to relieve the strain in the GO lattice. N1*s* spectra shows the formation of graphitic nitrogen as a function of increased plasma treatment time because of substitution of C with N in the lattice. Functionalization with helium and hydrogen plasma results in deoxygenation of graphene oxide as evident from the transformation of the C1*s* doublet into singlet feature. Treatment with helium and oxygen plasma results in formation of additional oxygen moieties at the graphene oxide surface along with a variation in the surface speciation as evident from the C1*s* and O1*s* spectra. These oxygen-containing functional groups induces variation in the work function of GO. Valence band spectra acquired using UPS shows the increase in C2*p* π states due to functionalization of GO. Finally, work function variation from 4.8 eV for pristine GO to 4.6, 4.7 and 5.8 eV with nitrogen, hydrogen and oxygen plasma, respectively, is observed. These can be correlated with the variation in bonding configuration after nitrogen doping, deoxygenation of GO and changes in oxygen moieties. This study shows that APPJ is a facile technique for tuning the work function of GO. APPJ-functionalized GO shows promise for hole conductor applications in PSCs.

Chapter 6

In situ functionalization and deposition of dopant-free spiro-OMeTAD hole transport material with atmospheric pressure plasma jet

This chapter describes the deposition of dopant-free spiro-OMeTAD films using an aerosol-assisted atmospheric pressure plasma jet deposition technique. The results suggest that helium and helium + oxygen plasma deposited spiro-OMeTAD films have x3.2 and x4.5 higher conductivities, respectively, compared to aerosolized spiro-OMeTAD. Spectroscopic investigation using XPS show oxidation of plasma-deposited samples and variation in nitrogen chemistry. The valence band was probed using UPS and additional density of states at the top of valence band are observed indicating the change in conductivity related to plasma jet deposition. The work function of the plasma deposited spiro-OMeTAD increased from 4.76 eV for aerosolized samples to 5.1 eV and 4.9 eV after deposition with He plasma and He + O_2 plasma, respectively, signifying an oxidation of the films during deposition. Raman spectroscopy was used to probe the variations in the chemical and structural features of spiro-OMeTAD upon plasma jet deposition. Hence, the plasma jet printing technique can be used for in situ functionalization and tuning of properties while deposition of spiro-OMeTAD hole transport material without the requirement of chemical dopants.

6.1 Introduction and motivation

Recently, immense research is being focussed on flexible electronics for applications in wearable technology, sensors, batteries, supercapacitors, displays and solar cells. Printing of nanostructured materials from solutions using different techniques such as inkjet printing (IJP) [348–350], screen printing [351–354], slot-die coating [355,356], spray coating [357–360] and aerosol jet printing [361] with promise of scaling up to roll-to-roll deposition, has been of primary interest [362–364]. The nature of thin film perovskite material for solar cells has great perspective in the world of flexible electronics [365] including textiles, robotics, and self-powered sensors. Conventional industrial-scale methods of blade-coating, screen printing and slot-die coating have successfully fabricated large-area PSC modules, demonstrating sizes of up to 100 cm^2. [352,366,367]

But the aforementioned techniques suffer from certain disadvantages in terms of scaling up and resolution. IJP is disadvantageous in terms of having low resolution, dependence on the properties of the ink and the variation of the tension in the screen, organic contaminants and the need for post-print thermal treatment. The formation of defect-free uniform films in planar devices remain challenging. Ink development is essential for expanding the use of IJP in PSCs. Also, the current IJP techniques are heavily dependent on post-processing and the nature of substrate which limit their application in flexible devices. Spray coating on the other hand is limited by the composition of the precursor solution, especially the nature of the solvents used. For example, low-boiling point solvents such as chloroform dry too quickly before the droplets reach the substrate, thus leaving the film with pinholes and inhomogeneity in thickness. On the contrary, high-boiling solvents such as DMSO, require additional annealing/drying process post-spraying which lead to shrinkage of film and hence non-uniformity. Moreover, all these printing techniques are primarily focussed on the perovskite ink but not on the HTL. Further optimisation of the techniques are desirable for scaling up and commercialization [368]. The solution-based processes face major challenges such as

(i) drying/post (treatment for obtaining high quality films with desired morphology,

(ii) difficulty in fabricating stoichiometric films,

(iii) limitations of drying temperature, atmosphere, vapour pressure, precursor and solvents,

(iv) incompatibility with *in situ* reduction and tuning the properties.

Hence, a new, advanced printing and *in situ* deposition technique is required to tune the desirable properties that is compatible with any substrate such as semiconductor wafers,

textile, paper, plastic and other flexible materials. Atmospheric pressure plasma jet-based deposition technique presented in this chapter is unique in terms of depositing metals, alloys and organic materials with tailored physical and chemical characteristics. Plasmas are largely favoured in pre- and post-treatment processes. Substrates are pre-treated with plasma to improve their wettability and film adhesion while plasma treatment as an alternative to high temperature sintering has also been explored [369–371]. Plasmas have also been used for improving interfacial contact and charge transport in PSCs [114,116]. Penache *et al.* were the first to report atmospheric pressure based micro-patterning technique and referred to it as 'plasma printing' [372]. Michael Thomas published a review article on the plasma printing technique [373].

APPJs have been extensively used for deposition of coatings, films and nanoparticles. Connor *et al*. demonstrated a highly efficient and high-throughput aerosol-assisted atmospheric pressure plasma based room temperature deposition and patterning technique of metal nanostructures on polymer and silicon substrates using gold precursors [374]. Gandhiraman *et al*. reported an aerosol-assisted, atmospheric pressure plasma based, room temperature deposition, of materials on flexible substrates [107]. Deposition of silver nanowires and silicon dioxide dielectric coatings for encapsulation was demonstrated. This technique showed promise to combine plasma printing with 3D printing technology and for printing electronic components on nonconformal 3D objects. The same group also reported an atmospheric pressure plasma-based printing process using dielectric barrier discharge for deposition of nanoparticles on flexible substrates [108]. Multiwalled carbon nanotubes were deposited on paper to show site-selective deposition process and direct printing without the need for patterning for application as biosensor and chemical sensor. The plasma-printed nanotubes showed enhanced density and conductivity compared with ones without plasma. Dey *et al*. reported plasma-based deposition and *in situ* reduction of highly

acidic graphene oxide using He and H_2 plasma showing promise for printing large-scale conducting patterns of GO with improved conductivity [109]. Copper coatings on polyamide substrates were reported with DBD APPJ by Zhao *et al* [375]. Plasma generated with admixture of Ar and H_2 circumvented the oxidation issue with Cu and resulted in high purity films. More recently, Dey *et al*. have reported a novel atmospheric pressure plasma jet based printing technique for depositing copper films using nano-colloidal ink of copper [376].

Thus, the benefit of plasma jet deposition can be summarised as *in situ* modifications of electrical and optical properties along with the deposition of thin films, high compatibility with flexible and nonconformal platforms due to the lack of necessity of high annealing temperatures or vacuum-based equipment. It is a cost-effective, versatile and high-throughput fabrication technique with great promise in printable, wearable and flexible electronics applications. Plasma deposition offers advantages over competing techniques through its compatibility with flexible substrates with no post-processing requirements. In Chapter 4 of this thesis, a novel APPJ functionalization technique for spiro-OMeTAD was demonstrated for improvement in conductivity of pristine spiro-OMeTAD from 10^{-7} S cm^{-1} to 10^{-5} S cm^{-1} after 5 minutes of plasma treatment. The values are comparable with that of 10-25% Li-TFSI doped molecule. In this chapter, functionalization of spiro-OMeTAD has been extended to the bulk of the film and the findings regarding deposition of spiro-OMeTAD thin films with non-thermal plasmas and the *in situ* modification of the electronic and electrical properties has been reported.

6.2 Experimental details

Schematic experimental set up for plasma jet printing was shown in Figure 2.2 (details of the construction of the equipment provided in Chapter 2). In brief, the plasma

was ignited by applying a potential of about 7 kV between two circular electrodes in the frequency range of 2-4 kHz using He or He + O_2 gases through a Pyrex nozzle. The plasma jet was operated with two gas mixtures, one with only He (3000 sccm) and other comprising He (3000 sccm) + O_2 (30 sccm). The plasma is most intense in the region between the electrodes (active region) followed by an afterglow at the end of the nozzle. The plasma plume is believed to propagate as 'blobs' or 'bullets' [179]. The gases leaving the glass nozzle form a bullet shaped jet that mixes with the ambient air around its surface. In this open plasma boundary, a variety of excited atoms and molecules are formed due to collisional processes between diffused plasma species and neutral molecules from the atmosphere. The size of the jet varies with discharge conditions and experimental parameters, but has a length of ~3 cm and a diameter of a few mm. The spiro-OMeTAD solution was aerosolized using a commercial nebuliser and carried through to the plasma by compressed air. Nozzles with two inlets were used, where the inner capillary was used to inject the aerosolized solution of spiro-OMeTAD while the process gases were introduced through the outer inlet. The aerosolized ink was introduced into the plasma jet and accelerated out of the nozzle to a relatively fine spot (~0.5 x 0.5 sq. cm) which can be tuned by adjusting the diameter of the print head nozzle. The spiro-OMeTAD aerosol is subject to bombardment by electrons, ions and radicals in the plasma once they reach the nozzle head [377] resulting in *in situ* functionalization before deposition of the films onto silicon and glass substrates.

Before the experimental studies were carried out, the plasma jet was tested over a range of conditions to ensure stable operation. Atmospheric pressure plasma deposition and treatment allows surface treatments at low gas temperatures (room temperature), hence the name 'cold plasma'. Plasma deposition of spiro-OMeTAD was studied with two different solvents, chlorobenzene and N, N-dimethyl formamide (DMF). The concentrations of the solutions were varied during optimisation of the deposition to

obtain thin films. Initially 1 mg spiro-OMeTAD was dissolved in 1 mL of chlorobenzene. This resulted in drying of scattered droplets of spiro-OMeTAD aerosol on the silicon substrate instead of formation of any film during plasma deposition. The concentration was doubled (2 mg in 1 mL of chlorobenzene) but there was no substantial improvement in film formation (Figure 6.11). In the next trial, 36 mg of spiro-OMeTAD was dissolved in 1 mL of the solvent and the film formation was improved, though the deposition was not uniform in nature. Finally using 72 mg spiro-OMeTAD in 1 mL chlorobenzene yielded films over sufficiently large areas with the usage of the translational stage (Figure 6.12). Details of the samples studied in this chapter are mentioned in Table 6.1. The plasma deposition experiments were performed inside a fume cupboard to minimise the spreading of aerosol.

Table 6.1 Details of aerosolized and plasma deposited spiro-OMeTAD samples studied in this chapter.

Material	**Solvent**	**Plasma parameters**	**Technique**
Spiro-OMeTAD	Chlorobenzene	No plasma	Aerosolized
		V_{in} = 12 V Frequency = 2 - 3 kHz Helium (3000 sccm) Time = 2 mins	Deposited with He plasma
		V_{in} = 14 V Frequency = 3 - 4 kHz Helium (3000 sccm) + oxygen (30 sccm) Time = 2 mins	Deposited with $He+O_2$ plasma
	N,N-dimethyl formamide (DMF)	No plasma	Aerosolized
		V_{in} = 12V Frequency = 2 - 3 kHz Helium (3000 sccm) Time = 2 mins	Deposited with He plasma
		V_{in} = 14V Frequency = 3 - 4 kHz Helium (3000 sccm) + oxygen (30 sccm) Time = 2 mins	Deposited with $He+O_2$ plasma

6.3 Characterization of plasma-deposited spiro-OMeTAD films

The properties of *in situ* plasma functionalized and deposited spiro-OMeTAD thin films were investigated with the help of various analytical techniques. The electronic properties and changes in surface chemistry of spiro-OMeTAD molecule were studied with the help of XPS. XPS measurements were performed with an in-house load-locked KRATOS XSAM800 instrument using an Mg *K*α (1253.6 eV) excitation source (detailed description in Chapter 2). UPS was used to investigate the variation in valence band during plasma functionalization and deposition using a Thermo Theta Probe spectrometer with a base pressure of $5x10^{\wedge-10}$ mbar using He(I) UV light with photon energy 21.2 eV (described in Chapter 2 in details). Raman spectroscopy studies were undertaken to understand the changes in the vibrational modes of spiro-OMeTAD during plasma functionalization and deposition. A Horiba Jobin-Yvon Labram HR laser Raman microprobe with Ar ion laser (514.5 nm line) as the excitation source was used for the measurements (details in Chapter 2). The laser power was kept <0.5 mW to minimise the heating effect. A Leica optical microscope was used to observe the morphology of the deposited films. The sheet resistivity was measured using a four-point probe equipment with a Keithley SourceMeter (Model 2400), set to measure lower current range in pico Amps (pA) (details in Chapter 2). The current range was set up between 50-100 pA and compliance of 210 V. Care was taken to minimise the noise level due to charging effect in recording the data for each set and the final value was averaged for a range of current values in pA.

6.4 Results and Discussion

6.4.1 X-ray photoelectron spectroscopy (XPS)

XPS was used to probe the electronic properties, and local chemical environment due to plasma-deposition of the spiro-OMeTAD films. C1*s*, N1*s* and O1*s* high resolution

XPS spectra were energy calibrated with respect to the C1*s* of freshly-cleaved HOPG at 284.5 eV (Figure 2.4) and Au 4*f* peak at 84.0 eV as reference.

(a) Chlorobenzene

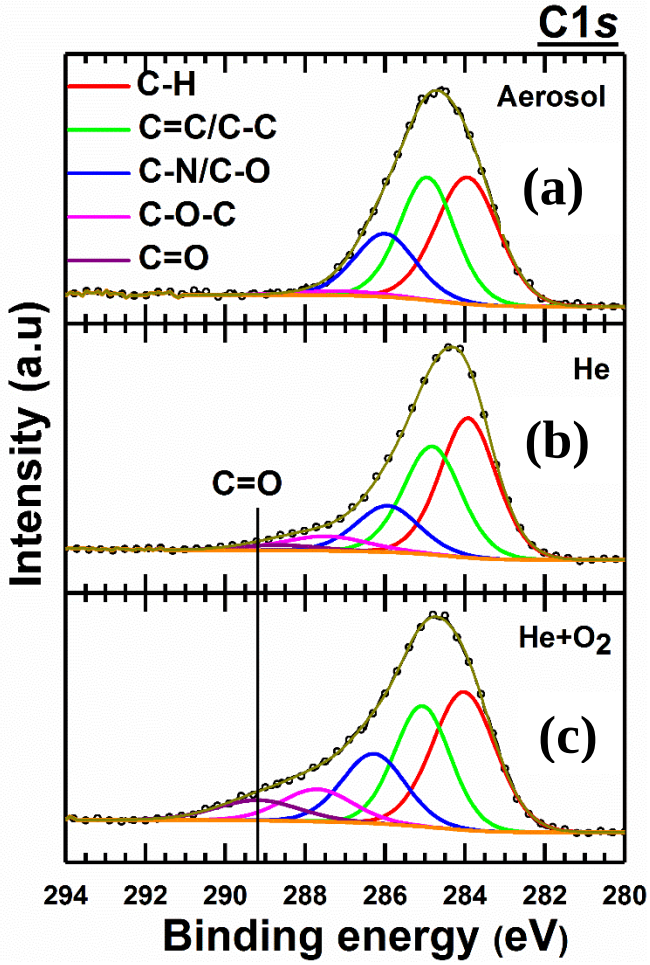

Figure 6.1 C1*s* XPS spectra of (a) aerosolized, (b) helium deposited and (c) helium + oxygen deposited spiro-OMeTAD films using chlorobenzene as solvent.

In Figure 6.1, the C1*s* XPS spectra of (a) aerosolized (without plasma), (b) helium deposited and (c) helium + oxygen deposited spiro-OMeTAD films using chlorobenzene as solvent are shown. The contribution from the different bonding environment around carbon is deconvoluted using a combined Gaussian-Lorentzian lineshape. The C1*s* spectrum of the aerosolized (no plasma) spiro-OMeTAD film has been fitted with C-H, C=C/C-C, C-N/C-O and C_a-O-C components at 283.9 eV, 285.0 eV, 286.0 eV, 287.5

eV, respectively [46,47,55,378] (Figure 6.1 a). The C1*s* spectra of He and He + O_2 plasma deposited films are quite different from the aerosolized films. The plasma deposition process with helium results in broadening of the higher binding energy tail, giving rise to an additional C=O component at 289.1 eV (Figure 6.1 b). The broadening becomes appreciable for the plasma printing process with helium + oxygen with both the C_a-O-C and C=O components increasing in concentration from 6.7 % and 2.3 % to 9.6 and 7.1 %, respectively (Figure 6.1 c). The broadening can be attributed to the functionalization via attachment of OH, atomic and molecular oxygen in the oxygen plasma plume. The interaction of the active species in the plasma jet with the aerosol of spiro-OMeTAD during deposition may result in formation of defect sites which in turn lead to attachment of oxygen moieties. The FWHM of the C-N/C-O component increases steadily from aerosolized to the plasma deposited samples signifying an increase in the carbon bonded to oxygen species. The C=O component may have contribution from carbonyl and carboxylic groups. The formation of carboxylic groups can be associated with an enhancement in conductivity by improving the flexibility of the aromatic backbone or promoting charge carrier along the molecule [379]. In Table 6.2, the FWHM and percentage composition of the components used to fit the C1*s* spectra has been summarized. This demonstrates the efficacy of the He + O_2 plasma jet for oxidation compared to only He plasma. Possibly the active species in He-O_2 plasma jet competes with the species in the He jet and gives rise to the C=O and C_a-O components. These results can be correlated with the oxidation of spiro-OMeTAD using an APPJ as discussed in Chapter 4.

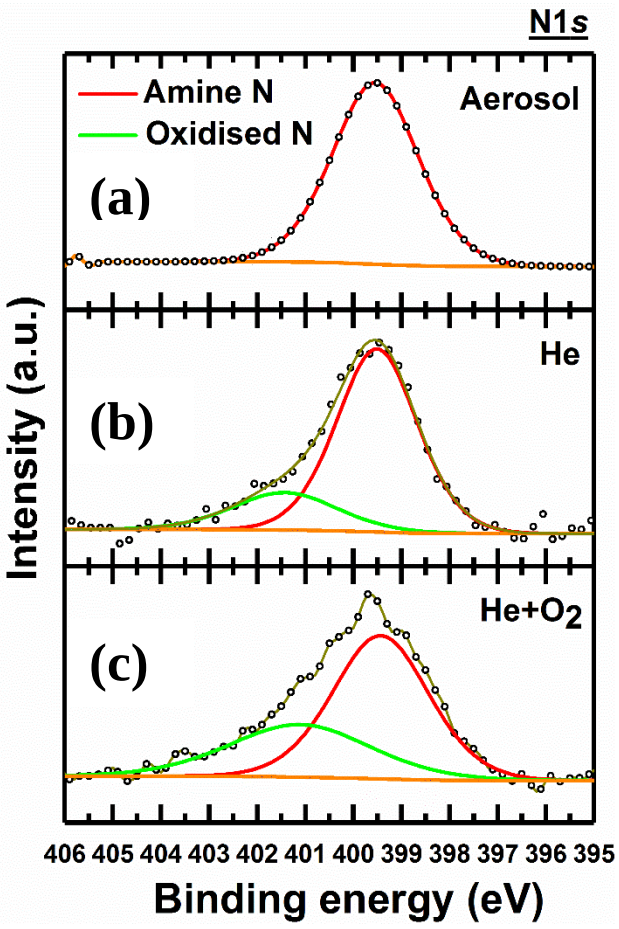

Figure 6.2 N1*s* XPS spectra of (a) aerosolized, (b) helium deposited and (c) helium-oxygen deposited spiro-OMeTAD films using chlorobenzene as solvent.

The deconvoluted N1*s* spectra of aerosolized, He deposited and He + O_2 deposited films are shown in Figure 6.2 (a, b and c, respectively). Scholin *et al.* have reported the N1*s* peak due to amine C-N from spiro-OMeTAD at 400.3 eV from XPS studies on a similar triphenyl amine hole conductor molecule [202,217]. The N1*s* spectrum of the aerosolized sample was fitted with one component at 399.5 corresponding to the amine N peak of the spiro-OMeTAD molecule at 399.5 eV [46,274–277]. The broadening of the N1*s* line shape upon plasma deposition is due to the formation of NO_x species at around 401.3 is clearly visible from Figure 6.2 (b). Due to the formation of oxidised N species, the N1*s* spectrum of He + O_2 plasma deposited film shows a shift towards higher BE. This signifies a variation in the environment around nitrogen in spiro-OMeTAD molecules

due to plasma deposition because of the plasma jet being housed in ambient conditions which brings about addition of oxygen functional groups to nitrogen atoms. This higher binding energy component increases from 21.0 to 35.0 % on using He + O_2 in the plasma deposition process due to the increase in NO_x species Figure 6.2 c). The N1*s* spectra of plasma deposited films can be corroborated with the oxidation of the spiro-OMeTAD as suggested earlier. Modification of the amine N site as a result of plasma processing may influence the conductivity of the films as will be discussed in later sections.

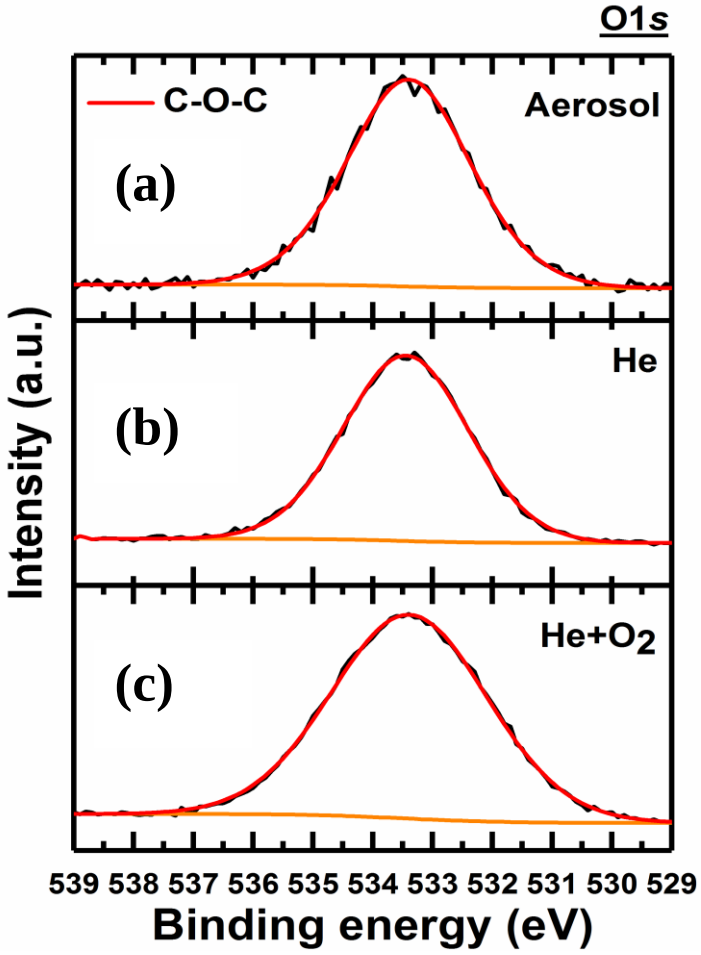

Figure 6.3 O1*s* XPS spectra of (a) aerosolized, (b) helium deposited and (c) helium-oxygen deposited spiro-OMeTAD films in chlorobenzene.

The high resolution O1*s* spectra of (a) aerosolized and (b) Helium plasma and (c) He + O_2 plasma deposited samples, were fitted with a single component at 533.4 ± 0.1

eV corresponding to the C_a-O-C bonding (C_a is aromatic C) in spiro-OMeTAD according to previous reports [46,47] as shown in Figure 6.3. The FWHM of the O1*s* spectrum for He + O_2 plasma deposited film is broadened by 0.6 eV compared to the aerosolized sample due to oxidation of the films (Figure 6.3 c). The introduction of the He plasma jet results in a 0.03 eV enhancement in FWHM of the O1*s* spectra whereas with He + O_2 the FWHM increases by 0.6 eV suggesting an increase in oxygen content in the films. This broadening can be attributed to the C=O component from either the carbonyl or the carboxylic acid groups as is evident from the C1*s* XPS spectra. This demonstrates that using an admixture of helium + oxygen is a more effective *in situ* processing technique compared to only helium plasma.

Table 6.2 Fitting parameters extracted from XPS spectra of aerosolized and plasma deposited spiro-OMeTAD using chlorobenzene as solvent.

Samples	**Core levels**	**Components**	**FWHM ± 0.1 (eV)**	**Atomic % ± 0.2**
Aerosol-CB	C1*s*	C-H	1.8	45.0
		C=C/C-C	1.5	34.8
		C-N/C-O	1.6	16.1
		C_a-O-C	2.8	3.9
		C=O	0	0
	N1*s*	Amine N	2.1	100.0
		Oxidised N	0	0
	O1*s*	C_a-O	2.4	100.0
He deposited-CB	C1*s*	C-H	1.6	42.0
		C=C/C-C	1.7	33.4
		C-N/C-O	1.8	15.5
		C_a-O-C	2.5	6.6
		C=O	2.3	2.3
	N1*s*	Amine N	2.0	79.0
		Oxidised N	2.5	21.0
	O1*s*	C_a-O	2.5	100.0
He+O_2 deposited_ CB	C1*s*	C-H	1.9	36.6
		C=C/C-C	1.6	28.1
		C-N/C-O	1.9	18.4
		C_a-O-C	2.1	9.6
		C=O	2.5	7.1
	N1*s*	Amine N	2.3	64.8
		Oxidised N	3.5	35.1
	O1*s*	C_a-O	3.0	100.0

(b) N, N-Dimethyl formamide (DMF)

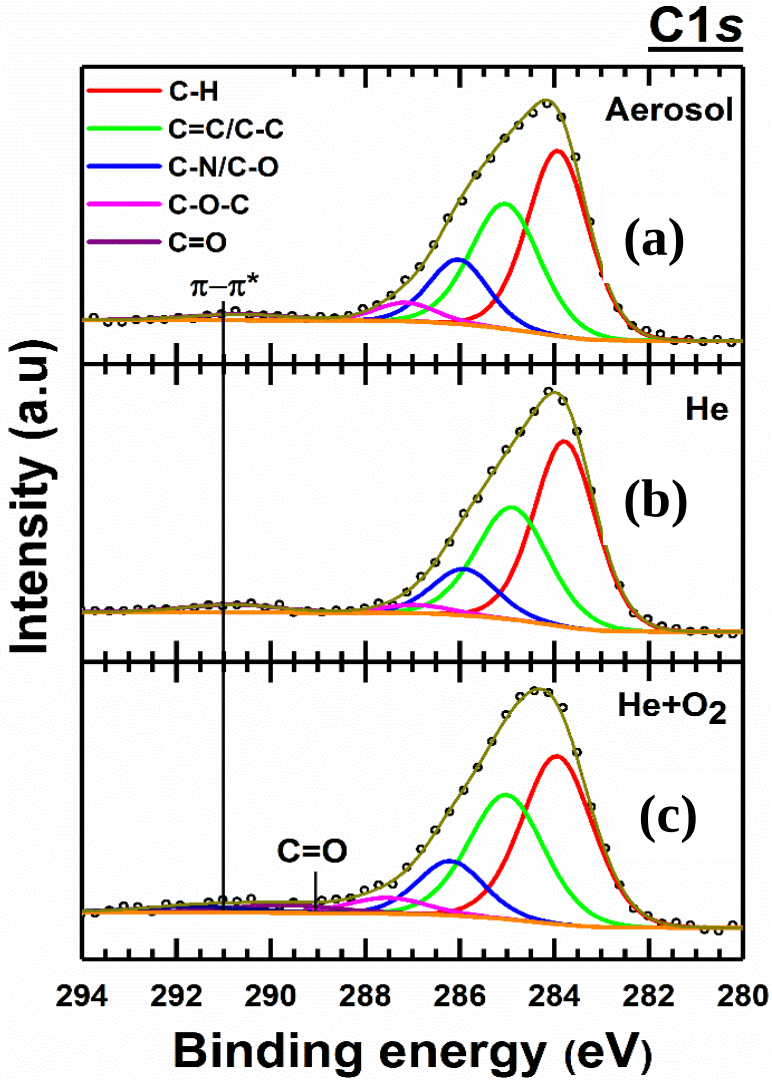

Figure 6.4 C1*s* XPS spectra of (a) aerosolized, (b) helium deposited and (c) helium-oxygen deposited spiro-OMeTAD films with DMF as solvent.

To understand the variation in the bonding environment around carbon atoms before and after plasma jet deposition, the C1*s* spectra were deconvoluted into different components as shown in Figure 6.4 (a–c). The C1*s* spectra for aerosolized spiro-OMeTAD in DMF can be deconvoluted into five components namely, C-H, C=C/C-C, C-N/C-O, C_a-O-C and π-π* at 283.9 eV, 285.0 eV, 285.9 eV, 287.2 eV and 290.7 eV, respectively (Figure 6.4 a). There is no substantial variation in the spectrum when only helium plasma is used for the deposition process (Figure 6.4 b). But with helium +

oxygen plasma, not only does there appear an additional C=O component at 289.2 eV but also the concentration of the C_a-O-C component almost doubles due to the formation of C-OH or C=O as a result of interaction of active species from the oxygen plasma jet (as shown in Figure 6.4 c). Table 6.3 summarises the FWHM and percentage composition of the deconvoluted components which have been used to fit the C1*s*, N1*s* and O1*s* spectra of the aerosolized and plasma deposited spiro-OMeTAD films with DMF as solvent.

The N1*s* spectra of aerosolized, He plasma deposited and He + O_2 plasma-deposited spiro-OMeTAD films with DMF as solvent are as shown in Figure 6.5 (a, b and c, respectively). There is no change in the spectra of aerosolized and He plasma deposited spiro-OMeTAD film (Figure 6.5 (a) and (b), respectively) with both being fitted with a single peak corresponding to amine nitrogen at 399.0 eV. Helium + oxygen plasma deposited samples show an additional component in the higher binding energy region around 401.1 eV due to the formation of the oxidised nitrogen species [278–280].

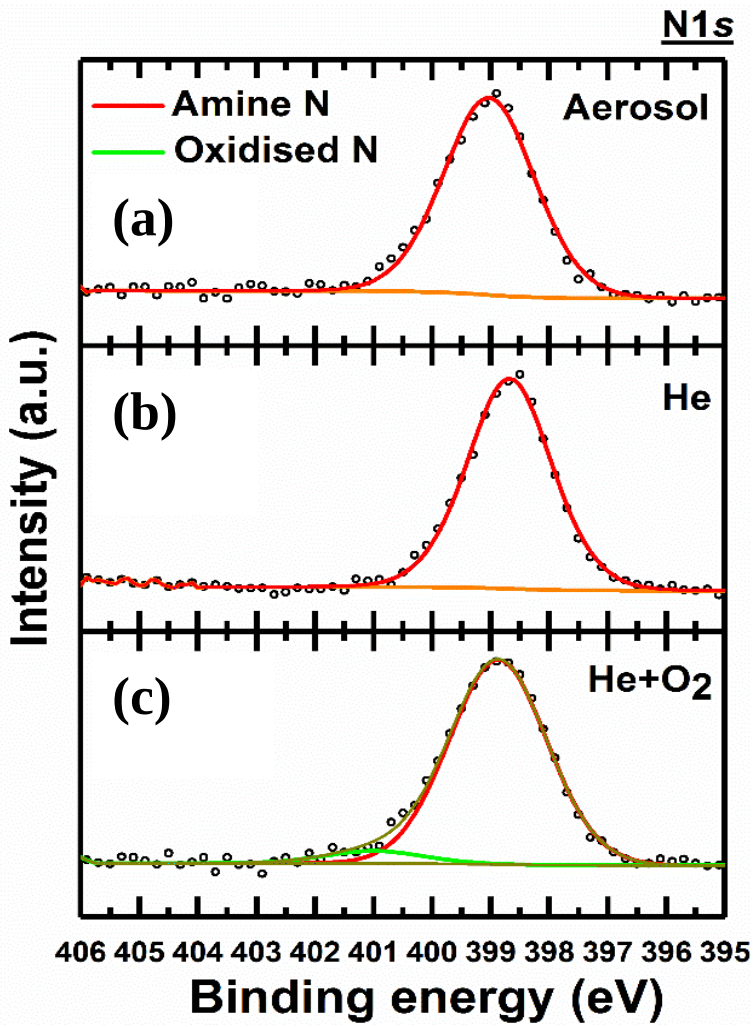

Figure 6.5 N1*s* XPS spectra of (a) aerosolized, (b) helium deposited and (c) helium-oxygen deposited spiro-OMeTAD films using DMF as solvent.

For the O1*s* spectra (Figure 6.6 c), the FWHM decreases by 0.3 eV for the He plasma deposition protocol before increasing again for the He + O_2 plasma jet. The O1*s* spectra of aerosolized, only helium and helium-oxygen deposited spiro-OMeTAD films using DMF as solvent have been fitted with a single component corresponding to the C_a-O-C in spiro-OMeTAD molecule at 533.3 ± 0.1 eV as in Figure 6.6 (a, b and c, respectively). The FWHM is observed to have reduced by 0.3 eV from aerosolized to the He plasma deposited samples before increasing again by 0.4 eV for He + O_2 printed samples. Thus, helium plasma possibly creates a reducing enviroment in spiro-

OMeTAD. This is also evident from the decrease in FWHM of C_a-O-C component of C1*s* spectra from He + O_2 plasma to He plasma deposited sample by 0.3 eV (Figure 6.5). Moreover, the FWHM of the C-N/C-O component increases by 0.2 eV from aerosolized to the He + O_2 plasma deposited sample whereas for He deposited sample, the increase in FWHM is only 0.1 eV.

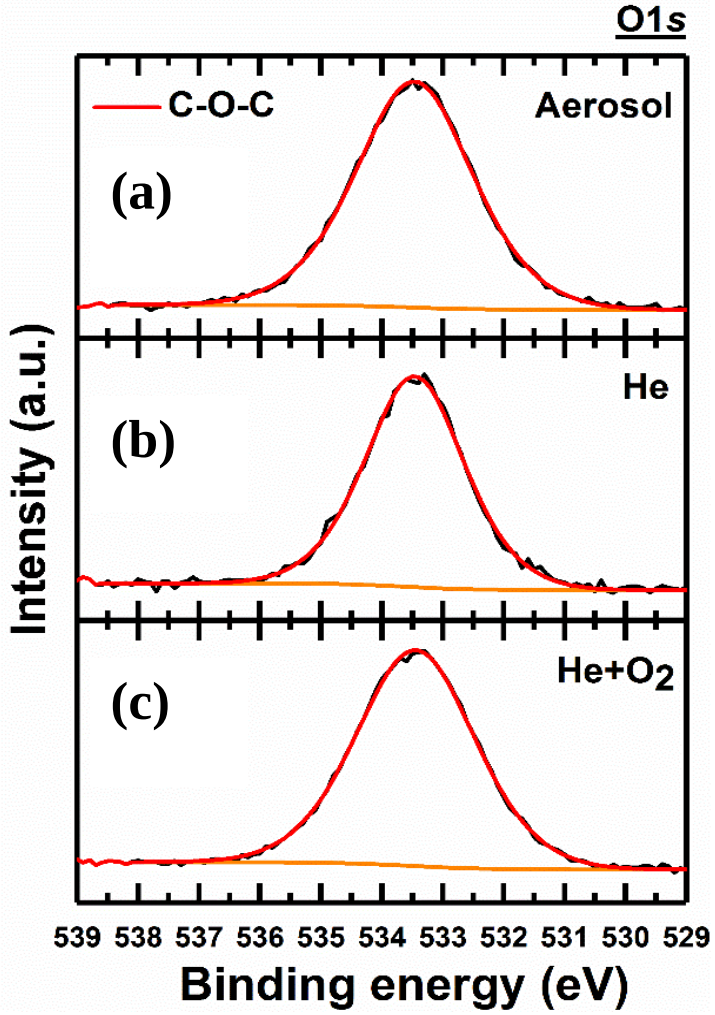

Figure 6.6 O1*s* XPS spectra of (a) aerosolized, (b) helium deposited and (c) helium-oxygen deposited spiro-OMeTAD films using DMF as solvent.

Table 6.3 Fitting parameters extracted from XPS of aerosolized and plasma deposited samples in DMF solvent.

Sample	Core levels	Components	Peak position	FWHM ±0.1 (eV)	Atomic % ± 0.2
Aerosol_DMF	C1*s*	C-H	283.6	1.5	44.4
		C=C/C-C	284.7	1.7	33.6
		C-N/C-O	285.7	1.5	15.0
		C_a-O-C	286.8	1.5	4.4
		C=O	0	0	0
		π-π*	290.3	2.5	2.4
	N1*s*	Amine N	399.0	1.8	100.0
		Oxidised N	0	0	0
	O1*s*	C_a-O-C	532.8	2.2	100.0
He deposited_DMF	C1*s*	C-H	283.3	1.54	48.1
		C=C/C-C	284.4	1.79	33.8
		C-N/C-O	285.4	1.6	12.4
		C_a-O-C	286.4	1.7	2.4
		C=O	0	0	0
		π-π*	290.3	2.38	3.2
	N1*s*	Amine N	398.7	1.69	100.0
		Oxidised N	0	0	0
	O1*s*	C_a-O-C	532.5	1.9	100.0
$He+O_2$ deposited_DMF	C1*s*	C-H	283.4	1.77	43.1
		C=C/C-C	284.5	1.88	33.7
		C-N/C-O	285.7	1.7	13.0
		C_a-O-C	287.0	2.0	4.5
		C=O	289.2	2.7	3.0
		π-π*	291.1	2.8	2.5
	N1*s*	Amine N	398.9	1.97	94.0
		Oxidised N	401.0	1.98	5.9
	O1*s*	C_a-O-C	532.0	2.3	100.0

Thus, it can be concluded that *in situ* modification of the electronic environment in the spiro-OMeTAD molecule occurs due to the plasma deposition process. DMF has low vapour pressure compared to chlorobenzene and hence has less tendency to volatize. Hence, it remains in solution of spiro-OMeTAD and interferes with the spectra [380,381]. The presence of pinholes have also been reported to influence the electronic and electrical properties of spiro-OMeTAD [382]. The presence of trapped bubbles in the films

prepared with DMF (Figure 6.13) has been observed which might subsequently lead to formation of pinholes.

6.4.2 Ultraviolet Photoelectron Spectroscopy (UPS)

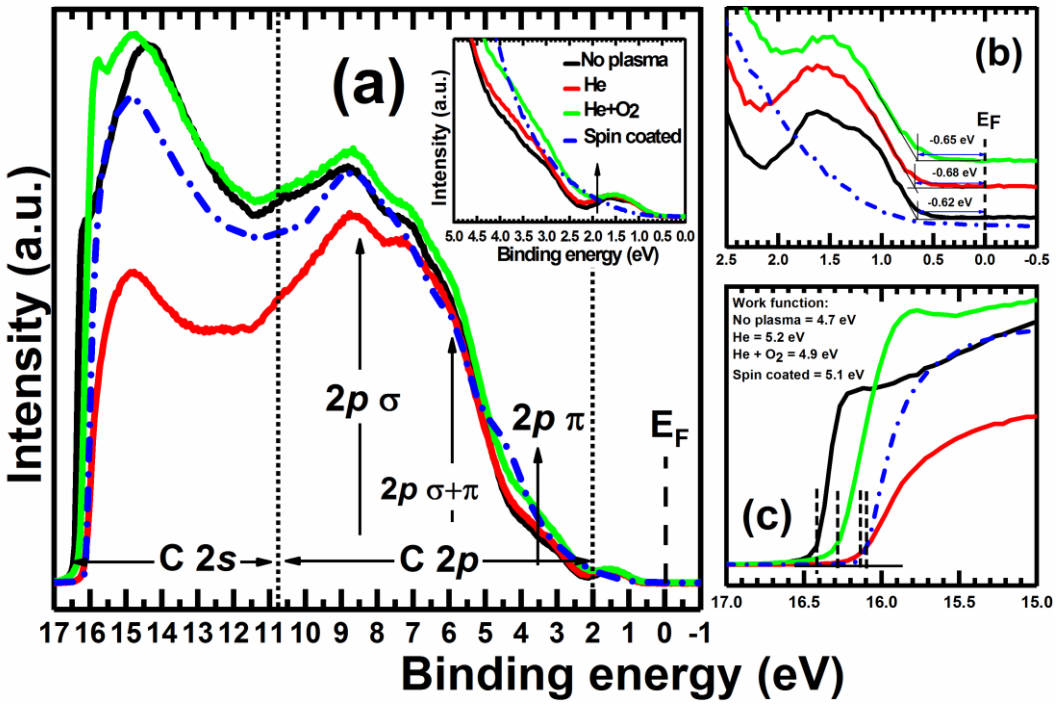

Figure 6.7 UPS spectra (He I = 21.2 eV) of aerosolized and plasma deposited spiro-OMeTAD using chlorobenzene as solvent corresponding to (a) the entire spectrum inclusive of the secondary cut-off and HOMO regions with increase in density of states in the C 2*p* region in the inset, (b) HOMO region showing a shift in the edge away from Fermi level and (c) work function of the samples calculated from the cut-off region for secondary electrons.

Variation in the electronic properties of the aerosolized and plasma deposited spiro-OMeTAD films using chlorobenzene and DMF as solvents were probed using UPS (described in details in section 2.4 of Chapter 2) with He I source (21.2 eV) as shown in Figure 6.7 and Figure 6.8, respectively. The UPS spectra were aligned with respect to the Fermi level of sputter cleaned Ag. Figure 6.7(a) shows the complete UPS spectra, inclusive of photoemission cut-off and HOMO region. Inset shows the increase

in density of states in the C2*p* region of the spin-coated, aerosolized, and plasma deposited spiro-OMeTAD samples. For spiro-OMeTAD, the density of states near Fermi level (0-4 eV) is dominated by the C2*p* π states whereas the feature at ~8 eV corresponds to the C2*p* σ states and they overlap at about 6 eV to form 2*p* σ+π states. Compared to the spin-coated spiro-OMeTAD sample, the aerosolized and plasma-deposited samples showed strong HOMO features (Figure 6.7 (a) inset). A gradual increase in the intensity of the HOMO features was also observed from aerosolized to He and then He + O_2 plasma deposited samples signifying an increase in the DOS which is possibly due to the oxidation taking place during the *in situ* functionalization and deposition process. The edge of the HOMO level with respect to the Fermi edge for the aerosolized spiro-OMeTAD film in chlorobenzene was at -0.62 eV. The comparison of the edge of the HOMO with respect to Fermi level of the aerosolized and plasma deposited samples are shown in Figure 6.7 (b). After deposition with He and He + O_2 plasma, only subtle changes (<0.1 eV) were observed in the position of the HOMO level towards higher binding energy (BE) as shown in Figure 6.7 (b). These results seemed to suggest that p-type doping by He+O_2 plasma is difficult.

The work function (ϕ) values were determined from the secondary electron cut-off (as shown in Figure 6.7 c) in the UPS spectra with the position of this edge shifting towards lower binding energy during plasma deposition. The calculated ϕ values varied from 4.7 eV for aerosolized spiro-OMeTAD to 5.1 eV and 4.9 eV after deposition with He plasma and He + O_2 plasma, respectively. These findings suggest that He+O_2 plasma on spiro-OMeTAD is similar to p-type doping of the hole conductor. For comparison, the work function of spin-coated spiro-OMeTAD was calculated to be 5.1 eV from the secondary cut-off of the UPS spectra. Ono *et al.* have reported the work function value of spiro-OMeTAD to be 3.9 eV whereas Hock *et al*. have calculated the value to be 4.2 eV for both drop-cast and evaporated spiro-OMeTAD films [46,55]. Hawash *et al*. have

reported that the work function values were more or less constant around 4.15 ± 0.03 eV after several hours of air exposure [47]. The work function value of the aerosolized spiro-OMeTAD film is higher than that reported previously on spin coated samples possibly because during the aerosolization (no plasma) process, the solution is agitated with air which makes it inherently oxidized. Formation of additional density of states between valence band and Fermi level is observed which might result in better absorption properties.

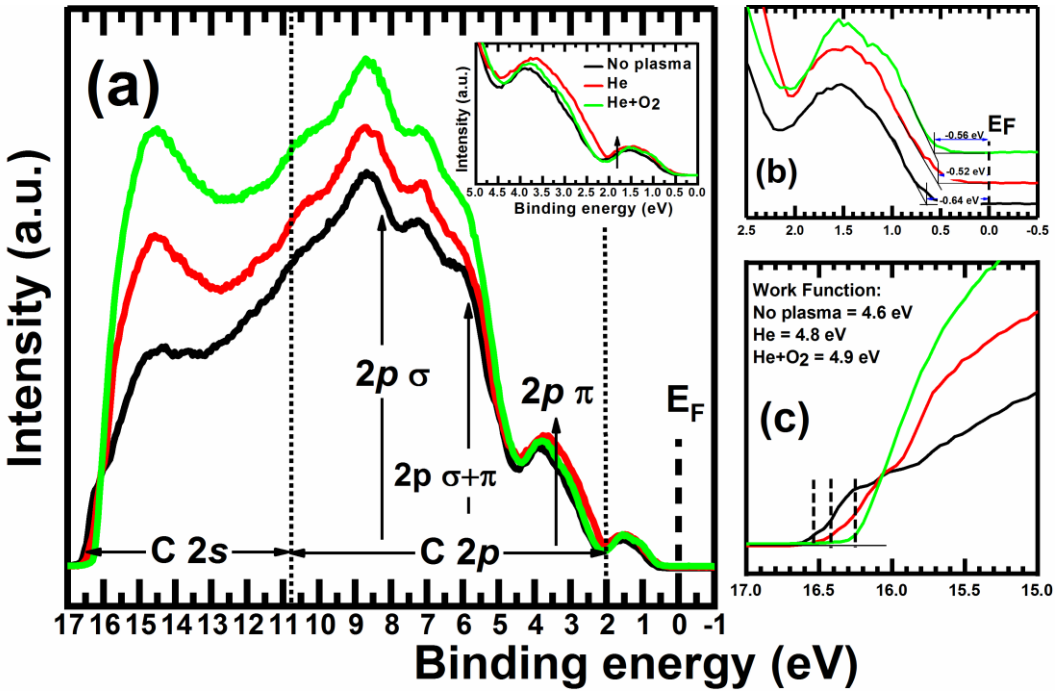

Figure 6.8 UPS spectra (He I = 21.2 eV) of aerosolized and plasma oriented spiro-OMeTAD using DMF as solvent corresponding to (a) the entire spectrum inclusive of the secondary cut-off and HOMO regions with the increment in density of states in the C 2*p* region in inset, (b) HOMO region showing the shift in the edge from Fermi level and (c) work function of the samples calculated from the cut-off region for secondary electrons.

With DMF as solvent, similar DOS features were observed in the range 0-4 eV and 8 eV corresponding to C2*p* π and C2*p* σ hybridisation states as shown in Figure

6.8(a) for aerosolized and plasma-deposited samples. Nevertheless, the 2*p* π states of spiro-OMeTAD with DMF as solvent has stronger features as compared to when chlorobenzene was used (Figure 6.7 a). The edge of the HOMO level for aerosolized spiro-OMeTAD is at -0.64 eV (Figure 6.8 b). On treatment with He plasma jet, the HOMO level showed a shifted towards lower BE settling at -0.52 eV. An additional exposure to the He + O_2 plasma jet resulted in a shift of the edge to -0.56 eV. The work function values gradually increased from 4.6 eV for aerosolized spiro-OMeTAD to 4.8 eV for the He plasma deposited sample and to 4.9 eV for the He+O_2 plasma deposited sample as calculated from the photoemission cut-off shown in Figure 6.8 (c). This proves that the plasma deposition process is dependent on the solvent since different values of ϕ for chlorobenzene and DMF has been calculated, though the trend of increasing work function with plasma print process is maintained. An increasing work function would indicate oxidation and p-type doping of the spiro-OMeTAD films.

Appreciable variation in the lineshape of the UPS spectra of spiro-OMeTAD dissolved in the two solvents, chlorobenzene and DMF was observed. This might be due to the plasma jet interacting differently with these solvents and hence the chemistry of the spiro-OMeTAD molecules is affected during deposition. Detailed optical emission spectroscopy during the plasma deposition process is necessary to understand the changes observed in the emission spectra with plasma and both aerosol and plasma. But the plethora of chemical species formed as a result of the plasma jet and its interaction with the spiro-OMeTAD solution *in situ,* would make the assignment rather complex. Thus, it can be concluded that the plasma jet printing is a versatile process which can be used for deposition as well as *in situ* tuning of the work function of spiro-OMeTAD thin films.

6.4.3 Raman spectroscopy

Raman spectroscopy was undertaken to understand the variation in the structure of spiro-OMeTAD molecules due to *in situ* plasma functionalization and deposition. The excitation wavelength (λ_{exc}) used for Raman spectroscopy was 514.5 nm. The Raman spectra were calibrated with respect to the 520.7 cm^{-1} Raman band of silicon wafers. The spectra were acquired over three different regions of the samples and then averaged for presentation.

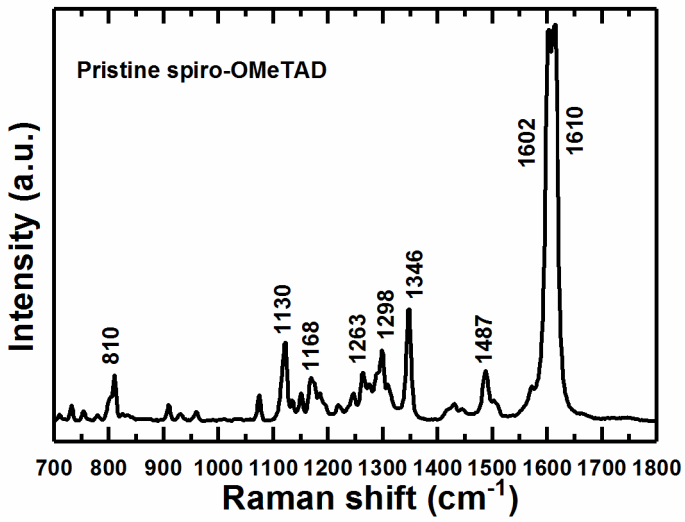

Figure 6.9 Raman spectrum of pristine spiro-OMeTAD in powder form showing the different Raman bands.

The Raman spectra of pristine spiro-OMeTAD (Figure 6.9) displayed many distinct bands with a sharp doublet peak at 1613 and 1602 cm^{-1}. Several other bands at 1487, 1346, 1260-1300, 1100-1170 and 810 cm^{-1} are also observed. Since, there is no available literature on the detailed Raman analysis of spiro-OMeTAD, so the features have been assigned based on spectra of common molecules from available database [383,384]. Polycyclic aromatic hydrocarbons are known to have strong Raman signatures at around 1350 and 1600 cm^{-1} due to aromatic stretching [385].The bands obtained at 1346 and 1610 cm^{-1} for pristine spiro-OMeTAD are characteristic of C=C ring stretching.

According to Lapkowski *et al.* the peaks at 1190 and 1622 cm^{-1} are characteristic of the C-H in-plane bending and C-C stretching deformation in benzenoid rings [386], whereas Zhang *et al.* suggested that presence of a Raman band at 1177 cm^{-1} due to the C-H shear vibration mode [387]. The features around 1168 and 1487 cm^{-1} for the spiro-OMeTAD films can be assigned to the polyconjugated nature of the benzene backbone in spiro-OMeTAD [386,388,389]. Raman spectra of polyconjugated molecules have signature features around 1100-1200 and 1450-1600 cm^{-1} due to the existence of delocalized π electrons. These bands correspond to the stretching vibrations of C-C and C=C, respectively.

Table 6.4 Assignment of Raman peaks for aerosolized and plasma deposited samples.

Assignments	**Band position (cm^{-1}) (from literature)**	**Band position (cm^{-1})**	**Ref**
C=C ring stretching	1622, 1610 and1580	1610 and 1602	386,388–390
C-H in-plane bending or C-H shear vibration mode	1170 or 1190 or 1177	1168	386–390
Asymmetric bending vibration of methoxy group	1460 ± 25 and 1450 ± 15	1487	391
C-O-C stretching + C-H in-plane bending of coronene	800-855	810	392
C-C bond stretching	1130	1121	393
C-O stretching	1320-1210	1297	391
Fingerprint of 2,3-benzofluorene + aromatic C-C stretching of benzo [α]pyrene and pentacene	1368, 1347, 1353	1346	385,394
Fingerprint of 2,3-benzofluorene + aromatic C-C stretching of perylene	1238,1299	1298	385,394
C-H bending in cis RHC=CHR + aromatic C-C stretching of Benzo (α)pyrene	1265, 1270	1263	392
C-H in-plane bending of triphenylene	1062	1073	385

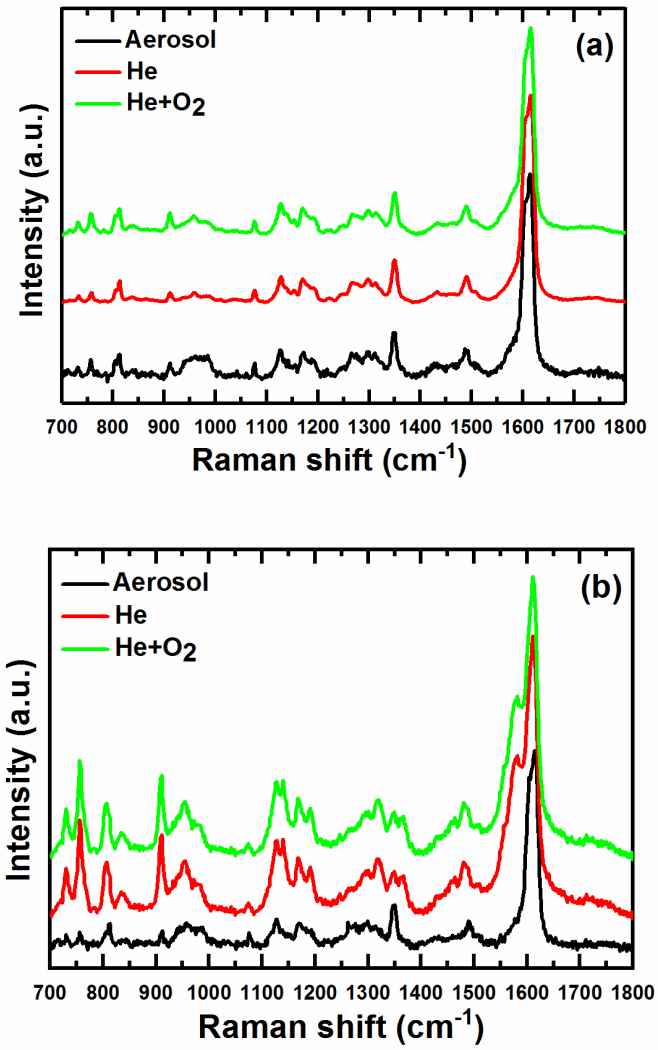

Figure 6.10 Raman spectra of aerosolized, He and He+O_2 deposited spiro-OMeTAD with (a) chlorobenzene and (b) DMF as solvents.

Figure 6.10 (a) shows the Raman spectra of aerosolized, He and He+O_2 deposited spiro-OMeTAD with chlorobenzene as solvent. The major Raman peaks for aerosolized spiro-OMeTAD are centred around 1616, 1488, 1348, 1173, 1128, 1076, 910, 808 and 756 cm^{-1}. The spectra reveal that the molecular vibrations are not influenced by variation in plasma environment. There is no discernible difference in the spectra on comparing between aerosolized, He plasma deposited and He + O_2 plasma deposited spiro-OMeTAD in chlorobenzene which shows that *in situ* plasma functionalization has not resulted in major modification of chemical structure of spiro-OMeTAD.

The plasma-deposited spiro-OMeTAD samples were characterized using FTIR spectroscopy which is complimentary in nature to Raman spectroscopy. However, due to the nature of the thin films deposited on to Silicon there was extensive interference of the spectra from the surface of the film and substrate which resulted in difficulty in interpretations of the spectral features. Hence, the results have not been included in this thesis. Raman signature of >C=O bonding in the spectra was not visible possibly since they are not Raman active.

The Raman spectra of aerosolized, He and He+O_2 plasma deposited spiro-OMeTAD dissolved in DMF is shown in Figure 6.10 (b). The presence of distinct Raman bands at about 1600, 1300-1400, 1100-1200, 900 -950 and 700-800 cm^{-1} is observed. Raman bands at about the same position as pristine spiro-OMeTAD indicates that *in situ* plasma functionalization and deposition does not result in structural modification. The band at 1600 cm^{-1} for the DMF films have been assigned due to C-C stretching of the polycyclic aromatic backbone of spiro-OMeTAD, similar to that reported for pristine and plasma deposited spiro-OMeTAD in chlorobenzene [386,388–390]. The bands between 1250-1000 cm^{-1} are commonly attributed to the C-H in-plane bending observed for polycyclic aromatic hydrocarbons [385]. The exact positions of the bands depend on the number of adjacent hydrogen atoms bonded to the edges of the molecules. In 1-3-di and 1, 2, 3-tri substituted benzenes which have three adjacent H atoms, strong bands are observed at 800-765 cm^{-1} as is the case with perylene. But for 1,4-di, 1,2,4-tri and 1,2,3,4-tetra substituted benzene rings such as benzo[α]pyrene, intense Raman bands are observed at 874 and 909 cm^{-1}, whereas for 1,3-di, 1,2,4-tri-, 1,2,3,5-tetra, 1,2,4,5-tetra and penta substituted benzene molecules, the sharp bands fall in the range 910-835 cm^{-1}. The molecular structure of spiro-OMeTAD consists of the methoxy group which has three adjacent H atoms, the peripheral triphenyl amine group which has two adjacent H atoms whereas the central bifluorene core has both 1 and 2 H atoms in the structure.

Hence, the Raman spectra of spiro-OMeTAD is expected to show the C-H in-plane bending signature of a combination of all these configurations.

There are several visible differences between the spectra of aerosolized and plasma deposited films in DMF. To begin with, the Raman bands have sharper features in case of the plasma deposited samples, be it with He or He + O_2, with the visible splitting of the feature at 1614 cm^{-1} into two features at 1611 and 1581 cm^{-1}. Increased sharpness may be due to better π-π stacking of molecules as has been observed from the C1*s* XPS spectra. On plasma functionalization, the peak at 1349 cm^{-1} has split into two bands but with slightly reduced intensities compared to the aerosolized spectrum. The splitting of the peaks at 1180 and 1133 cm^{-1} has been observed with increase in intensity whereas the features at 910, 808 and 748 cm^{-1} have substantially increased in intensity after *in situ* plasma modification. The Raman bands between 740-900 cm^{-1} are significantly intense as compared to the pristine spiro-OMeTAD sample which might be due to the lesser number of defects in the film due to the deposition process with DMF. The intensity of the Raman bands is affected by the intensity and wavelength of the laser source, concentration of the sample and the scattering properties. Since, for the spiro-OMeTAD films, all the first three factors remain constant, it might be that there is different extent of scattering between the aerosolized and plasma deposited films which bring about a strong change in the intensity. This may corroborate the fact that film formation is improved with the use of plasma as compared to only aerosolized spiro-OMeTAD as has been shown in the optical microscopy of the films (explained in section 6.4.4).

The doublet feature at 1600 cm^{-1} is due to C-C ring stretching effect. On comparison with the pristine spiro-OMeTAD film, the doublet feature at 1602 cm^{-1} is observed to have shifted towards lower wavenumber 1580 cm^{-1} which might be due to

the variation in bond length for C-C ring stretching due to *in situ* plasma functionalization. The Raman band at 1130 cm^{-1} for pristine spiro-OMeTAD film is shifted to 1127 cm^{-1} for aerosolized film in DMF. On exposure to plasma (both He and $He+O_2$), there a splitting of the peaks into two components at 1127 and 1133 cm^{-1}. The spectral shifts may be as a result of the strain in the spiro-OMeTAD molecule while it is exposed to the agitation process and the plasma jet during deposition. Hence, it can be concluded that plasma deposition does not result in significant structural variation of spiro-OMeTAD. But the sharper Raman bands in case of spiro-OMeTAD dissolved in DMF may suggest better π stacking.

6.4.4 Morphology – Optical microscopy

Different concentrations and solvents, chlorobenzene and DMF were used for the deposition process. Initially with low concentration (when 2 mg spiro-OMeTAD was dissolved in 1 mL of chlorobenzene) there was no visible formation of film as can be observed from Figure 6.11. For aerosolized (Figure 6.11 a), Helium deposited film (Figure 6.11 b) and He + O_2 plasma deposited (Figure 6.11 c), random droplets of mist from the aerosolized solution was observed which lacked the uniformity and continuity to form a film.

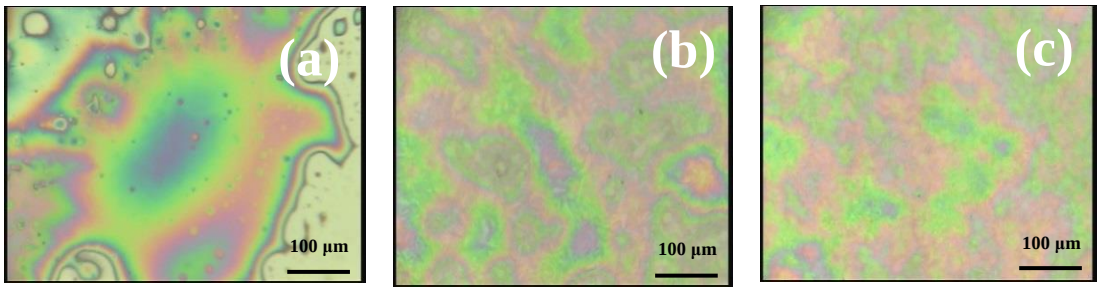

Figure 6.11 Optical images of (a) Aerosolized, (b) helium and (c) helium + oxygen deposited spiro-OMeTAD films in chlorobenzene.

The concentration of the spiro-OMeTAD solution was optimised and a higher concentration of 72 mg spiro-OMeTAD in 1 mL chlorobenzene resulted in uniform film formation as shown in Figure 6.12. The inclusion of plasma jet resulted in improved adhesion of the film to the substrate resulting in uniform film formation (Figure 6.12 (b) and (c)).

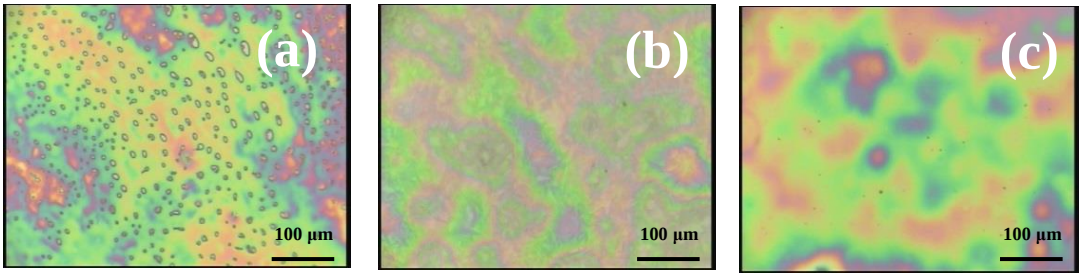

Figure 6.12 (a) Aerosolized, (b) helium and (c) helium + oxygen deposited spiro-OMeTAD films in chlorobenzene.

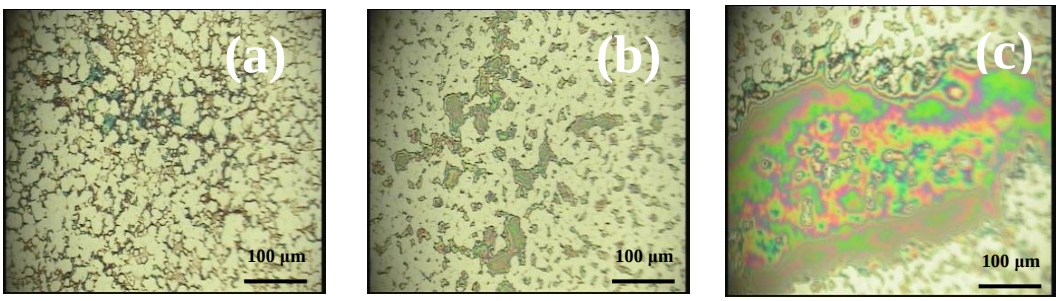

Figure 6.13 (a) Aerosolized, (b) helium and (c) helium + oxygen deposited spiro-OMeTAD films in DMF.

The concentration of spiro-OMeTAD solution in DMF was also optimised at 10 mg in 1 mL and the formation of uniform films was observed as shown in Figure 6.13. The aerosolized film (Figure 6.13 (a)) shows the presence of bubbles due to the trapped gas in the films which are absent in the plasma deposited films (Figure 6.13 (b) and (c)) possibly due to the faster drying and film adhesion with plasma.

6.4.5 Electrical properties – Four-point probe sheet resistivity measurements

Oxygen plasma is known to functionalize the surface of thin films by incorporation of polar functional groups such as C-O, C-OH [395] which may lead to enhancement of the conductivity of the films as is evident from the sheet resistivity values. The average sheet resistance of pristine spiro-OMeTAD film was calculated as 327.70 G Ω sq^{-1} and it decreased to 101.43 G Ω sq^{-1} after using helium plasma in chlorobenzene. The sheet resistance decreased further to 73.52 G Ω sq^{-1} on using helium and oxygen plasma. The results suggest that helium and helium + oxygen plasma deposited spiro-OMeTAD films have x3.2 and x4.5 higher conductivities, respectively, compared to aerosolized spiro-OMeTAD films. But when DMF was used as the solvent, the sheet resistivity decreased only from 64.19 to 55.95 to 46.70 G Ω sq^{-1} for aerosolized, helium plasma and admixture of helium and oxygen, respectively. The sheet resistivity values are summarized in Table 6.5. The trend of decreasing sheet resistivity of spiro-OMeTAD dissolved in both solvents is presented in Figure 6.14. The reduction in sheet resistivity might be due to the increased density of charge carriers as a result of the *in situ* plasma modification of spiro-OMeTAD films. Plasma may promote enhancement of π-π interactions in the molecules which may improve conductivity of plasma-deposited films.

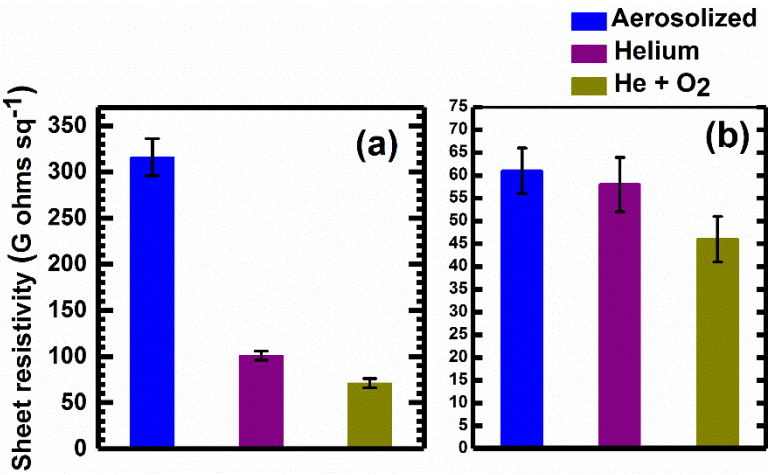

Figure 6.14 Variation of sheet resistivity of spiro-OMeTAD films using (a) chlorobenzene and (b) DMF as solvents.

Table 6.5 Sheet resistivity values of plasma deposited samples.

	Sample ID			Sheet resistance ($G\,\Omega\,sq^{-1}$)
1	Plasma deposited Spiro-OMeTAD	Chlorobenzene	Aerosol	327.70
2			He	101.43
3			$He + O_2$	73.52
4		N,N-dimethyl formamide (DMF)	Aerosol	64.19
5			He	55.95
6			$He + O_2$	46.70

6.5 Comparison between atmospheric pressure plasma-functionalized and plasma-deposited spiro-OMeTAD

6.5.1 Variation in electronic properties

This section briefly compares the variation in electronic and electrical properties of plasma functionalized and *in situ* plasma treated and deposited spiro-OMeTAD. The effect of plasma functionalization of spiro-OMeTAD is explained in detail in Chapter 4. In Figure 6.15, the optical emission spectra of the effluent from He and oxygen APPJ from microjet (red) and DBD plasma (blue) have been compared.

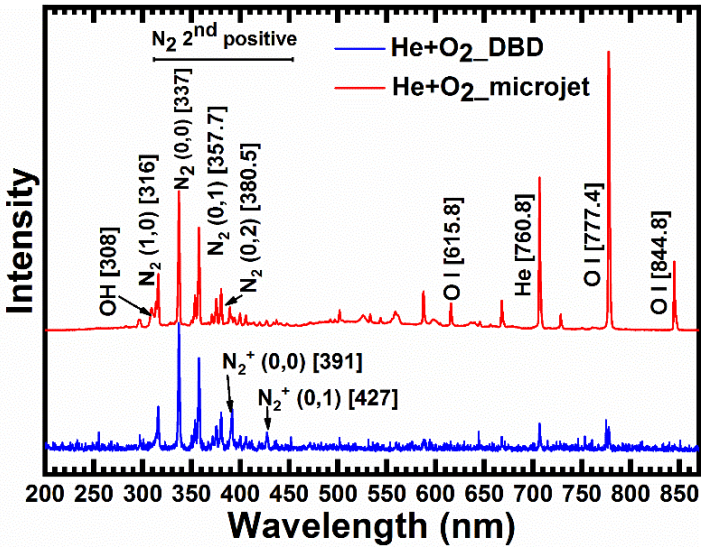

Figure 6.15 Optical emission spectra comparing the effluent from He and oxygen APPJ from microjet (red) and DBD plasma (blue).

OES of the microjet is dominated by lines corresponding to OH^- ($A^2\Sigma^+$ (v = 0, 1) → $X^2\prod$ (Δv=0)) at 308.9 nm, N_2(C-B) second positive system with electronic transitions $C^3\prod_u \rightarrow B^3\prod_g$ in the range 300-450 nm, He I transition $3s^3S^1 \rightarrow 2p^3P^0$ at 706.8 nm, O I transitions $3p^5P \rightarrow 3s^5S^0$ at 777.4 nm and $3p^3P \rightarrow 3s^5S^0$ at 844.8 nm [263–265]. On the contrary, emission lines from N_2(C-B) second positive system are primarily observed in the DBD plasma whereas the other lines are very much lower in intensity. This is possibly because of the fact that the microjet is mostly sustained by bombardment of electrons with different molecules thus giving rise to intense emission lines. DBD is generated by dissociation of molecules with high voltage and hence contain lesser excited species.

Figure 6.16 compares the high resolution C1*s* (a–c), N1*s* (d–f) and O1*s* (g–i) spectra of the pristine, plasma functionalized, and plasma deposited spiro-OMeTAD samples. The C1*s* spectra for both plasma-functionalized and deposited spiro-OMeTAD shows tails towards the higher binding energy corresponding to the oxygen groups attached to the carbon atoms in different configurations. The plasma deposited sample

(Figure 6.16 c) shows comparatively higher percentage of C_a-O-C and C=O component than the plasma-functionalized sample (Figure 6.16 (b)). This is possible due to the *in situ* functionalization effect brought about by the charged species in the He + O_2 plasma jet during deposition of the film. A higher binding energy tail corresponding to the oxidised N species is clearly discernible in the N1*s* spectrum of the plasma treated samples with the deposited sample showing greater percentage of oxidised species compared to the functionalized sample. The inherent functionalization during deposition possibly results in pronounced effect compared to functionalizing with atmospheric pressure plasma jet which affects only the surface of the films. From Figure 6.16 (g, h, i) it is clearly observed that the FWHM of the O1*s* spectrum of plasma functionalized and deposited spiro-OMeTAD is significantly broader compared to the pristine sample. Greater NO_x component for plasma deposited spiro-OMeTAD is observed compared to functionalized sample. This suggests incorporation of oxygen in the plasma jet-deposited spiro-OMeTAD films. The reactive energetic species in the plasma jet consisting of ions, radicals, metastables and photons [396] possibly bring about inherent modifications to the electronic structure of spiro-OMeTAD before the deposition of the films. This results in significant changes in the XPS spectra.

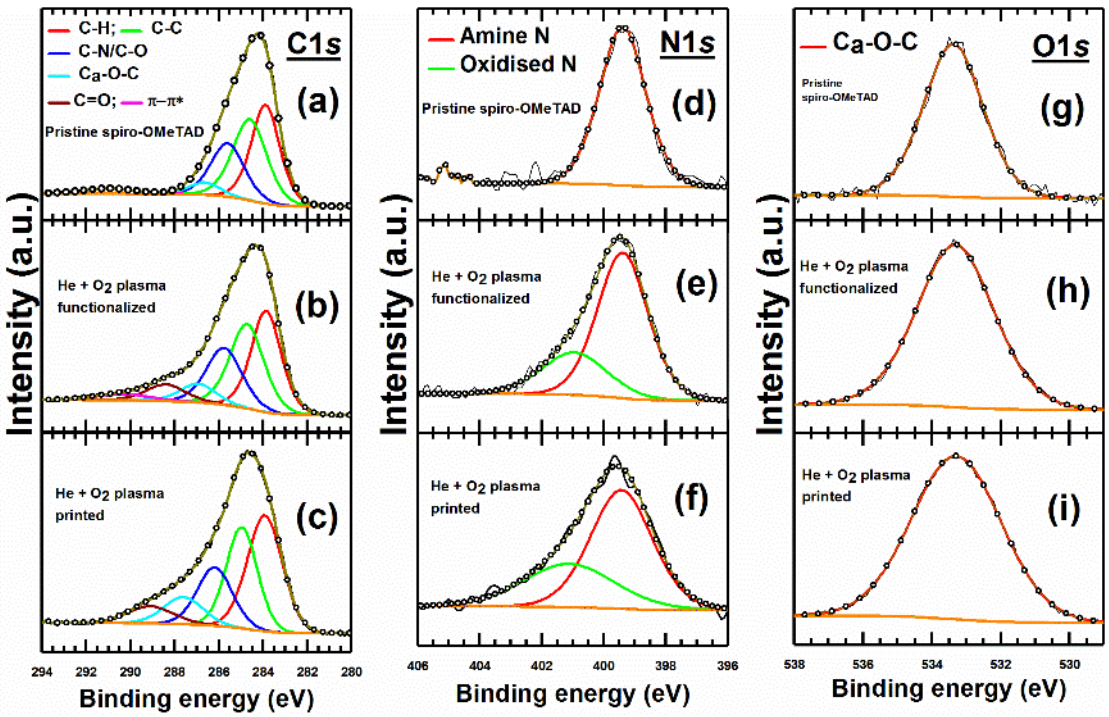

Figure 6.16 Comparison between (a, b, c) C1*s*, (d, e, f) N1*s* and (g, h, i) O1*s* XPS spectra of pristine, plasma-functionalized and plasma deposited spiro-OMeTAD.

6.5.2 Variation in electrical properties

The sheet resistivity values of untreated, plasma functionalized and deposited spiro-OMeTAD are compared in Table 6.6. The sheet resistivity values are observed to decrease both for the functionalized as well as the *in situ* treated and deposited samples. This decrease in resistivity signifies an enhancement in the conductivity and has been explained in chapter 4 in details. In brief, the multitude of energetic ions, radicals and photons in the plasma jet are responsible for increasing the density of charge carriers on the spiro-OMeTAD molecules which results in reduced sheet resistivity.

Table 6.6 Comparison of the sheet resistivity values of plasma functionalized and deposited samples.

Sample ID	Sheet resistivity (G Ω sq^{-1})
Pristine spiro-OMeTAD	80.521
3 minutes He + O_2 plasma functionalized spiro-OMeTAD	11.257
Aerosolized spiro-OMeTAD	327.0
He + O_2 plasma deposited spiro-OMeTAD	73.52

6.6 Conclusion

The major finding presented in this chapter is that atmospheric pressure plasma jet can be used to increase the conductivity *in situ* without the need for elaborate post processes or chemical dopants. The deposition of thin films with *in situ* enhanced conductivity using a plasma jet has been reported for the first time for spiro-OMeTAD. The results suggest that He plasma and He + O_2 plasma deposited spiro-OMeTAD films have x3.2 and x4.5 higher conductivities, respectively, compared to aerosolized spiro-OMeTAD films. XPS confirms that plasma deposition leads to modification of the electronic structure of spiro-OMeTAD resulting in oxidation. The helium + oxygen plasma jet was found to be more effective for the oxidation of spiro-OMeTAD. UPS shows formation of additional density of states on top of the valence band after plasma-deposition. The work function was also observed to vary from 4.7 eV (aerosolized spiro-OMeTAD) to 5.2 eV (He plasma) and 4.9 eV (He+O_2 plasma) when chlorobenzene was used as solvent. With DMF as solvent, the work function varied from 4.6 eV for aerosolized films to 4.8 and 4.9 eV for He only and He+O_2 plasma deposited films, respectively. The increase in work function upon plasma-deposition indicates the p-type doping of spiro-OMeTAD which might be due to the active species in the plasma jet. A difference

in the XPS and UPS spectral line shape depending on the nature of solvent i.e. chlorobenzene and DMF, is observed. This might suggest that the solvents interact differently with spiro-OMeTAD during the inherent plasma functionalization process. Raman spectroscopy of powder and plasma deposited films indicates that there is no fundamental structural damage to spiro-OMeTAD molecules due to the plasma deposition process with either of these solvents. The sharper Raman bands for DMF might indicate better π stacking of the molecules upon using plasma compared to the aerosolized technique. The plasma promotes deposition rates and adhesion on the substrate as can be observed from the optical images. These results show great promise for deposition and *in situ* tailoring the properties of spiro-OMeTAD for hole transport applications in PSCs. Further research is required to understand the mechanism of plasma functionalization during deposition.

Chapter 7

Conclusions and future work

This chapter provides an overview of the contributions made through this thesis and the perspectives of the work carried out for future applications.

7.1 Thesis summary

This thesis focusses on selection of new materials and also the chemical and plasma functionalization and deposition of hole transport materials and a detailed study of their electronic, optical and electrical properties.

In this thesis, different hole transport materials such as spiro-OMeTAD, SFX-OMeTAD, SFX-TAD and graphene oxide have been studied. Spiro-OMeTAD is the most widely explored organic small molecule hole conductor in PSCs. This molecule has been chosen for its suitable HOMO level, high glass transition temperature, amorphous nature and compatibility with solution-processed techniques. Spiro-OMeTAD is commonly doped with Li-TFSI to improve the hole conductivity and mobility. SFX-OMeTAD and SFX-TAD have been introduced as low-cost alternatives to spiro-OMeTAD. These molecules are amorphous in nature, have high solubility, high glass transition temperature and HOMO level alignment identical to spiro-OMeTAD. Graphene oxide has been probed as a cost-effective, alternative HTM to spiro-OMeTAD. Graphene oxide has found applications as charge transport layer and electrode due to the fact that its work function can be tailored to device specification.

There is limited understanding of the variation of electronic properties as a function of Li-TFSI doping using X-ray spectroscopic techniques. Literature survey did not result in any element-specific technique which could provide understanding of the variation in electronic properties of Li-TFSI doped spiro-OMeTAD. Hence, NEXAFS spectroscopy was employed to understand the correlation between structural variation

and electronic properties with different Li-TFSI concentration. A mechanism for the variation of electronic properties as a function of dopant concentration has been proposed. The understanding acquired for spiro-OMeTAD has been extended to the new molecules, SFX-OMeTAD and SFX-TAD.

Functionalization: Improving the conductivity of HTMs without affecting the stability of PSCs is a key challenge. An atmospheric pressure plasma jet technique has been proposed as a novel alternative to chemical doping of spiro-OMeTAD. A low power (10 W) APPJ ignited using admixture of helium and oxygen was used for tuning the properties of spiro-OMeTAD without the need for chemical dopants. A time-dependent systematic investigation yielded an improvement in conductivity from 9.4×10^{-7} S cm^{-1} for the pristine film to 1.15×10^{-5} S cm^{-1} after 5 minutes of plasma treatment. These results were comparable with reports on 10-25% Li-TFSI doped spiro-OMeTAD. Spectroscopic investigation with XPS showed the variation in chemical structure and electronic properties. KPFM measurements demonstrated an increase in work function which is indicative of p-type doping. The increase in conductivity post-plasma functionalization was attributed to either an increase in the charge density in the molecule due to the energetic species in the plasma jet or improvement in π-π stacking of the molecules. This work opens up the possibility of using an APPJ as a facile and effective means of doping and surface functionalization of spiro-OMeTAD films to circumvent the detrimental issues associated with chemicals dopants.

Functionalization with the APPJ was extended to graphene oxide and a low power (3W) jet was used with different admixtures of helium, nitrogen, hydrogen and oxygen gases. XPS revealed the dominance of graphitic nitrogen with varying percentage of pyridinic configuration after treatment with nitrogen plasma. The reduction of GO was observed with only 2 sccm of hydrogen in the plasma jet which in turn resulted in $x10^3$

times enhancement in conductivity of the GO films. The tuning of work function upon functionalization with nitrogen, hydrogen and oxygen plasma indicated both n- and p-type doping as studied using UPS.

Plasma-deposition and *in situ* functionalization: A novel aerosol-based APPJ deposition technique has been developed for *in situ* tuning of the electronic properties of dopant-free spiro-OMeTAD. Plasma-deposited spiro-OMeTAD showed x4.5 higher conductivity compared to aerosolized films. The results were in contrast to traditional printing technologies which are not only dependent on the rheology of the ink but also cannot inherently tune the physical and chemical properties of the deposited ink. Combined spectroscopic techniques of XPS and UPS confirmed that plasma deposition results in oxidation and modification of the electronic properties of spiro-OMeTAD. These results show great promise for deposition and *in situ* tailoring the properties of spiro-OMeTAD for hole transport applications in PSCs.

In summary, this thesis has addressed (i) the understanding of variation in electronic properties due to Li-TFSI doping of spiro-OMeTAD using X-ray spectroscopy (NEXAFS and XPS); (ii) the issue with hygroscopic chemical dopants by proposing a novel functionalization technique using APPJ with conductivity after 5 minutes of treatment being comparable to 10-25% Li-TFSI doping; (iii) APPJ functionalization of graphene oxide with nitrogen, hydrogen and oxygen and tuning the work function for hole transport applications and (iv) a novel aerosol-based APPJ deposition technique for *in situ* tuning of electronic properties of spiro-OMeTAD without the need for post-processing chemical doping.

7.2 Future work

The results presented in this thesis demonstrate the suitability of atmospheric pressure plasmas as environment-friendly, cost-effective, reliable and scalable technique

for functionalization of hole conductor materials. The research undertaken in this thesis has opened up multiple avenues for future investigation as highlighted in the following sections.

Density functional theory (DFT) calculations: DFT calculations are necessary to correlate the NEXAFS transitions to the structural variation of spiro-OMeTAD, SFX-OMeTAD and SFX-TAD hole conductors after doping with Li-TFSI.

Plasma-functionalized spiro-OMeTAD: Spiro-OMeTAD has found applications as buffer layer in PSCs, photodiodes, photodetectors as well as LEDs [397–401]. Plasma-functionalized spiro-OMeTAD with improved conductivity shows promise for hole conductor applications in perovskite solar cells, photodetectors, photodiodes and LEDs as environment-friendly and low-cost alternative to chemically doped spiro-OMeTAD.

APPJ printing: Application of APPJ as a printing technology is a completely new approach for perovskite solar cells and further progress is needed to compete with commercially established traditional printing techniques.

(i) Although the results presented in Chapter 6 demonstrate an efficient, reliable, and reproducible fabrication of spiro-OMeTAD thin films with tailored conductivity and work function, further research is needed to address several interesting questions on plasma diagnostics and electrical characteristics of the aerosol-assisted plasma process setup. Future work will include optimization of nozzle dimensions and process conditions for deposition of various materials of interest in flexible electronics, multiple jets in the form of a showerhead and detailed perovskite performance studies. This aerosol-based APPJ technique opens up the possibility for deposition and *in situ* processing of other layers in perovskite solar cells. Further X-ray spectroscopic investigation and nuclear magnetic resonance (NMR) studies are required to gain deeper understanding of the mechanism of plasma-functionalization.

(ii) ***Fabrication of flexible and wearable electronic devices using APPJ printing:*** Wearable technology is of importance to security, health care, defence and military applications. Photovoltaic cells show immense promise as textile-compatible power sources for wearable devices. Wearable, textile-compatible photovoltaics should not only be environmentally stable but also mechanically robust and sufficiently energy efficient. The APPJ printing technique demonstrated in this thesis was used for deposition of spiro-OMeTAD. It is necessary to optimise several factors such as nozzle dimensions and process parameters for printing thin films of various materials of interest including perovskite absorber layer. Future research would be directed towards wearable fabric-based batteries and photovoltaic devices being fabricated using atmospheric pressure plasma jet deposition techniques.

(iii) ***Plasma annealing:*** High temperature annealing of the perovskite films is crucial for achieving desired device performance. The precise determination of the plasma temperature could not be carried out in the present work. But APPJ shows promise as an alternative to thermal annealing for perovskite absorber such that deposition can be carried on flexible substrates where high temperature is undesirable.

Nanomaterial synthesis using APPJ: Atmospheric pressure plasma-synthesized nanostructures of transition metal oxides following the vapour-liquid-solid growth mechanism have attracted widespread attention due to their extensive applications. Photoactive (i.e. absorb light and generate electron-hole pairs) metal oxides such as TiO_2, CuO, ZnO, Fe_2O_3, and MoO_3 have been exploited for photocatalytic hydrogen generation and water purification. Atmospheric pressure plasma can not only compete with conventional techniques (chemical, thermal and low-pressure plasma), but are also advantageous in terms of being environmentally benign, reliable and cost-effective with promise for large-scale applications.

In situ measurements: Probing the interaction of active species in plasma with the nanomaterials in the active region (between electrodes) and in the afterglow (beyond electrodes) is crucial to develop understanding of the mechanism of improvement in charge conduction. Hard X-rays spectroscopy can be used to probe the nanomaterials both during flight and after film deposition. Understanding the complex chemistries during interaction of plasma jet with the solution during deposition will give more opportunities to tailor the properties. *In situ* X-ray scattering studies of the growth of perovskite crystals, variation in crystallite sizes and number, during the plasma annealing process would be crucial for optimising parameters for obtaining uniform films with promise for better device performance. This technique can even be extended to large-scale roll-to-roll printing technology. Moreover, hard X-rays can be used for probing the perovskite/HTM interface to understand charge transfer dynamics in PSCs and develop more efficient HTMs.

The future of novel functionalized HTMs are bright since their design aims at promoting efficient charge extraction along with encapsulation and trap passivation for enhanced device performance and stability of PSCs.

Bibliography

1. OCDE & International Energy Agency. *Market Report Series: Renewables 2017, Analysis and Forecasts to 2022*. *Executive Summary* (2017).

2. Agency, I. E. International Energy Agency report Technology Roadmap: Solar Photovoltaic Energy. (2014).

3. Green, M. A. The Path to 25% Silicon Solar Cell Efficiency: History of Silicon Cell Evolution. *Prog. Photovoltaics Res. Appl.* **17**, 183–189 (2009).

4. Green, M. A. *et al.* Solar cell efficiency tables (version 51). *Prog. Photovoltaics Res. Appl.* **26**, 3–12 (2018).

5. Shockley, W., Queisser, H. & Queisser, H. J. The Shockley-Queisser limit. *J. Appl. Phys.* **32**, 510–519 (1961).

6. Peng, J., Lu, L. & Yang, H. Review on life cycle assessment of energy payback and greenhouse gas emission of solar photovoltaic systems. *Renew. Sustain. Energy Rev.* **19**, 255–274 (2013).

7. Mohammad Bagher, A. Types of Solar Cells and Application. *Am. J. Opt. Photonics* **3**, 94 (2015).

8. Giorgi, G. & Yamashita, K. Organic–inorganic halide perovskites: an ambipolar class of materials with enhanced photovoltaic performances. *J. Mater. Chem. A* **00**, 1–11 (2015).

9. Stranks, S. D. *et al.* Electron-Hole Diffusion Lengths Exceeding 1 Micrometer in an Organometal Trihalide Perovskite Absorber. *Science (80-.).* **342**, 341–345 (2013).

10. Ryu, S. *et al.* Voltage output of efficient perovskite solar cells with high open-circuit voltage and fill factor. *Energy Environ. Sci.* **7**, 2614 (2014).

11. National Renewable Energy Laboratory. NREL-Best efficiency chart. (2019).

12. Michal Maciejczyk, A. I. and N. R. SFX as low cost 'Spiro' hole-transport material in perovskite solar cells. *J. Mater. Chem. A* **4**, 4855–4863 (2016).

13. Xu, B. *et al.* A low-cost spiro[fluorene-9,9′-xanthene]-based hole transport material for highly efficient solid-state dye-sensitized solar cells and perovskite solar cells. *Energy Environ. Sci.* **9**, 873–877 (2016).

14. Maeno, Y. *et al.* Superconductivity in a layered perovskite without copper. *Nature* **372**, 532–534 (1994).

15. Whatmore, R. W. Pyroelectric devices and materials. *Reports Prog. Phys.* **49**, 1335–1386 (1986).

16. Grätzel, M. Dye-sensitized solar cells. *J. Photochem. Photobiol. C Photochem. Rev.* **4**, 145–153 (2003).

17. Upadhyaya, H. M., Senthilarasu, S., Hsu, M. H. & Kumar, D. K. Recent progress and the status of dye-sensitised solar cell (DSSC) technology with state-of-the-art conversion efficiencies. *Sol. Energy Mater. Sol. Cells* **119**, 291–295 (2013).

18. Kojima, A., Teshima, K., Shirai, Y. & Miyasaka, T. Organometal halide perovskites as visible-light sensitizers for photovoltaic cells. *J. Am. Chem. Soc.* **131**, 6050–6051 (2009).

19. Kim, H.-S. *et al.* Lead iodide perovskite sensitized all-solid-state submicron thin film mesoscopic solar cell with efficiency exceeding 9%. *Sci. Rep.* **2**, 591 (2012).

20. Michael M. Lee, Joël Teuscher, Tsutomu Miyasaka, Takurou N. Murakami, H. J. S.

Efficient Hybrid Solar Cells Based on Meso-Superstructured Organometal Halide Perovskites. *Science (80-.).* **338**, 643–647 (2012).

21. Marchioro, A. *et al.* Unravelling the mechanism of photoinduced charge transfer processes in lead iodide perovskite solar cells. *Nat. Photonics* **8**, 250–255 (2014).

22. Zhu, Z. *et al.* High-performance hole-extraction layer of sol-gel-processed nio nanocrystals for inverted planar perovskite solar cells. *Angew. Chemie - Int. Ed.* **53**, 12571–12575 (2014).

23. Chen, W. *et al.* Efficient and stable large-area perovskite solar cells with inorganic charge extraction layers. *Science (80-.).* **350**, 944–948 (2015).

24. Fang, Y. & Huang, J. Resolving Weak Light of Sub-picowatt per Square Centimeter by Hybrid Perovskite Photodetectors Enabled by Noise Reduction. *Adv. Mater.* **27**, 2804–2810 (2015).

25. Chen, W. *et al.* Hybrid interfacial layer leads to solid performance improvement of inverted perovskite solar cells. *Energy Environ. Sci.* **8**, 629–640 (2015).

26. Park, N.-G. Perovskite Solar Cells: An Emerging Photovoltaic Technology. *Mater. Today* **18**, 1–8 (2014).

27. Rakstys, K. *et al.* Triazatruxene-Based Hole Transporting Materials for Highly Efficient Perovskite Solar Cells. *J. Am. Chem. Soc.* **137**, 16172–16178 (2015).

28. Yaghoobi Nia, N., Matteocci, F., Cina, L. & Di Carlo, A. High Efficiency Perovskite Solar Cell Based on Poly (3-hexylthiophene) (P3HT): The Influence of P3HT Molecular Weight and Mesoscopic Scaffold Layer. *ChemSusChem* **10**, 3854–3860 (2017).

29. Yang, W. S. *et al.* Iodide management in formamidinium-lead-halide–based perovskite layers for efficient solar cells. *Science (80-.).* **356**, 1376–1379 (2017).

30. Heo, J. H. *et al.* Efficient inorganic–organic hybrid heterojunction solar cells containing perovskite compound and polymeric hole conductors. *Nat. Photonics* **7**, 486–491 (2013).

31. Zhang, K. *et al.* Synthetic Metals A thermally and electrochemically stable organic hole-transporting material with an adamantane central core and triarylamine moieties. *Synth. Met.* **162**, 490–496 (2012).

32. Thelakkat, M. Star-shaped, dendrimeric and polymeric triarylamines as photoconductors and hole transport materials for electro-optical applications. *Macromol. Mater. Eng.* **287**, 442–461 (2002).

33. Yin Xiao, C. *et al.* Novel hole transporting materials with a linear π-conjugated structure for highly efficient perovskite solar cells. *Chem. Commun.* **50**, 5799–5928 (2014).

34. Bach, U., De Cloedt, K., Spreitzer, H. & Grätzel, M. Characterization of Hole Transport in a New Class of Spiro-Linked Oligotriphenylamine Compounds. *Adv. Mater.* **12**, 1060–1063 (2000).

35. Poplavskyy, D. & Nelson, J. Nondispersive hole transport in amorphous films of methoxy-spirofluorene-arylamine organic compound. *J. Appl. Phys.* **93**, 341–346 (2003).

36. Naito, K. Quantitative Relations between Glass Transition Temperatures and Thermodynamic Parameters for Various Materials: Molecular Design for Nonpolymeric Organic Dye Glasses with Thermal Stability. *Chem. Mater* **6**, 2343–2350 (1994).

37. Bach, U. *et al.* Solid-state dye-sensitized mesoporous TiO2 solar cells with high photon-to-electron conversion efficiencies. *Nature* **395**, 583–585 (1998).

38. Saragi, T. P. I., Spehr, T., Siebert, A., Fuhrmann-Lieker, T. & Salbeck, J. Spiro Compounds for Organic Optoelectronics. *Chem. Rev.* **107**, 1011–1065 (2007).

39. Shi, D. *et al.* Spiro-OMeTAD single crystals: Remarkably enhanced charge-carrier transport via mesoscale ordering. *Sci. Adv.* **2**, 1–6 (2016).

40. Yavuz, I. & Houk, K. N. Mesoscale Ordering and Charge-Transport of Crystalline Spiro-OMeTAD Organic Semiconductors. *J. Phys. Chem. C* **121**, 993–999 (2017).

41. Snaith, H. J. & Grätzel, M. Enhanced charge mobility in a molecular hole transporter via addition of redox inactive ionic dopant: Implication to dye-sensitized solar cells. *Appl. Phys. Lett* **89**, 262114 (2006).

42. Burschka, J. *et al.* Tris(2-(1H-pyrazol-1-yl)pyridine)cobalt(III) as p-type dopant for organic semiconductors and its application in highly efficient solid-state dye-sensitized solar cells. *J. Am. Chem. Soc.* **133**, 18042–5 (2011).

43. Li, Z. *et al.* Acid Additives Enhancing the Conductivity of Spiro-OMeTAD Toward High-Efficiency and Hysteresis-Less Planar Perovskite Solar Cells. *Adv. Energy Mater.* **1601451**, 1–8 (2016).

44. Liu, Y. *et al.* A dopant-free organic hole transport material for efficient planar heterojunction perovskite solar cells. *J. Mater. Chem. A* **3**, 11940–11947 (2015).

45. Abate, A. *et al.* Lithium salts as 'redox active' p-type dopants for organic semiconductors and their impact in solid-state dye-sensitized solar cells. *Phys. Chem. Chem. Phys.* **15**, 2572–2579 (2013).

46. Ono, L. K. *et al.* Air-Exposure-Induced Gas-Molecule Incorporation into Spiro-MeOTAD Films. *J. Phys. Chem. Lett.* **5**, 1374–1379 (2014).

47. Hawash, Z., Ono, L. K., Raga, S. R., Lee, M. V. & Qi, Y. Air-exposure induced dopant redistribution and energy level shifts in spin-coated Spiro-Meotad films. *Chem. Mater.* **27**, 562–569 (2015).

48. Docampo, P. *et al.* Lessons learned: From dye-sensitized solar cells to all-solid-state hybrid devices. *Adv. Mater.* **26**, 4013–4030 (2014).

49. Pellaroque, A. *et al.* Efficient and Stable Perovskite Solar Cells Using Molybdenum Tris(dithiolene)s as p-Dopants for Spiro-OMeTAD. *ACS Energy Lett.* **2**, 2044–2050 (2017).

50. Walzer, K., Maennig, B., Pfeiffer, M. & Leo, K. Highly Efficient Organic Devices Based on Electrically Doped Transport Layers. *Chem. Rev.* **107**, 1233–1271 (2007).

51. Abate, A., Staff, D. R., Hollman, D. J., Snaith, H. J. & Walker, A. B. Influence of ionizing dopants on charge transport in organic semiconductors. *Phys. Chem. Chem. Phys.* **16**, 1132–1138 (1132).

52. Xu, B. *et al.* AgTFSI as p-type dopant for efficient and stable solid-state dye-sensitized and perovskite solar cells. *ChemSusChem* **7**, 3252–3256 (2014).

53. Bai, Y. *et al.* Low Temperature Solution-Processed Sb:SnO_2 Nanocrystals for Efficient Planar Perovskite Solar Cells. *ChemSusChem* **9**, 2686–2691 (2016).

54. Yang, L. *et al.* Cobalt Salt as Efficient Dopant for Spiro-MeOTAD in Cesium-Containing Planar Perovskite Solar Cells. *J. Nanosci. Nanotechnol.* **18**, 2898–2902 (2018).

55. Hock, R., Mayer, T. & Jaegermann, W. P-type doping of spiro-MeOTAD with WO3 and the spiro-MeOTAD/WO3 interface investigated by synchrotron-induced photoelectron spectroscopy. *J. Phys. Chem. C* **116**, 18146–18154 (2012).

56. Li, M. *et al.* Copper Salts Doped Spiro-OMeTAD for High-Performance Perovskite Solar Cells. *Adv. Energy Mater.* **6**, 1–8 (2016).

57. Chen, C. *et al.* Cu(II) Complexes as p-Type Dopants in Efficient Perovskite Solar Cells.

ACS Energy Lett. **2**, 497–503 (2017).

58. Daems, N., Sheng, X., Vankelecom, I. F. J. & Pescarmona, P. P. Metal-free doped carbon materials as electrocatalysts for the oxygen reduction reaction. *J. Mater. Chem. A* **2**, 4085 (2014).

59. Lindblad, R. Electronic Structures and Energy Level Alignment in Mesoscopic Solar Cells : A Hard and Soft X-ray Photoelectron Spectroscopy Study. (2014).

60. Johansson, E. M. J. *et al.* Spin - Orbit Coupling and Metal - Ligand Interactions in Fe (II), Ru (II), and Os (II) Complexes. *J. Phys. Chem. C* **114**, 10314–10322 (2010).

61. Nguyen, W. H., Bailie, C. D., Unger, E. L. & McGehee, M. D. Enhancing the hole-conductivity of spiro-OMeTAD without oxygen or lithium salts by using spiro(TFSI)2 in perovskite and dye-sensitized solar cells. *J. Am. Chem. Soc.* **136**, 10996–11001 (2014).

62. Fantacci, S., Angelis, F. De, Nazeeruddin, M. K. & Grätzel, M. Electronic and optical properties of the spiro- MeOTAD hole conductor in its neutral and oxidized forms : a DFT / TDDFT investigation. *J. Phys. Chem. C* **115**, 23126–23133 (2011).

63. Krüger, J. *et al.* High efficiency solid-state photovoltaic device due to inhibition of interface charge recombination. *Appl. Phys. Lett.* **79**, 2085–2087 (2001).

64. Enright, B., Redmond, C. & Fitzmaurice, D. Spectroscopic Determination of Flatband Potentials for Polycrystalline Ti02 Electrodes in Mixed Solvent Systems. *J. Phys. Chem* **98**, 6195–6200 (1994).

65. Verónica Ganduglia-Pirovano, M., Hofmann, A. & Sauer, J. Oxygen vacancies in transition metal and rare earth oxides: Current state of understanding and remaining challenges. *Surf. Sci. Rep.* **62**, 219–270 (2007).

66. Juárez-Pérez, E. J. *et al.* Role of the Dopants on the Morphological and Transport Properties of Spiro-MeOTAD Hole Transport Layer. *Chem. Mater.* **28**, 5702–5709 (2016).

67. Wang, S. *et al.* Role of 4-tert-Butylpyridine as a Hole Transport Layer Morphological Controller in Perovskite Solar Cells. *Nano lett* **16**, 5594–5600 (2016).

68. Xie, L.-H. *et al.* Unexpected One-Pot Method to Synthesize Spiro[fluorene-9,9′-xanthene] Building Blocks for Blue-Light-Emitting Materials. *Org. Lett.* **69**, 40 (2004).

69. Gu, J.-F. *et al.* Dumbbell-Shaped Spirocyclic Aromatic Hydrocarbon to Control Intermolecular π-π Stacking Interaction for High-Performance Nondoped Deep-Blue Organic Light-Emitting Devices. *J. Phys. Chem. Lett* **1**, 18 (2010).

70. Chu, Z. *et al.* Synthetic Metals Synthesis of spiro[fluorene-9,9-xanthene] derivatives and their application as hole-transporting materials for organic light-emitting devices. *Synth. Met.* **162**, 614–620 (2012).

71. Sun, M., Xu, R., Xie, L., Wei, Y. & Huang, W. Toward Eco-friendly Green Organic Semiconductors: Recent Advances in Spiro[fluorene-9,9′-xanthene] (SFX)-Based Optoelectronic Materials and Devices. *Chinese J. Chem.* **33**, 815–827 (2015).

72. Cappel, U. B., Daeneke, T. & Bach, U. Oxygen-induced doping of spiro-MeOTAD in solid-state dye-sensitized solar cells and its impact on device performance. *Nano Lett.* **12**, 4925–4931 (2012).

73. Yang, L. *et al.* Initial Light Soaking Treatment Enables Hole Transport Material to Outperform Spiro-OMeTAD in Solid-State Dye-Sensitized Solar Cells. *J. Am. Chem. Soc.* **135**, 7378–7385 (2013).

74. Hawash, Z., Ono, L. K. & Qi, Y. Moisture and Oxygen Enhance Conductivity of LiTFSI-

Doped Spiro-MeOTAD Hole Transport Layer in Perovskite Solar Cells. *Adv. Mater. Interfaces* **3**, 1–6 (2016).

75. Habisreutinger, S. N. *et al.* Carbon Nanotube/Polymer Composites as a Highly Stable Hole Collection Layer in Perovskite Solar Cells. *Nano Lett.* **14**, 5561–5568 (2014).

76. Habisreutinger, S. N. *et al.* Enhanced Hole Extraction in Perovskite Solar Cells Through Carbon Nanotubes. *J. Phys. Chem. Lett.* **5**, 4207–4212 (2014).

77. Habisreutinger, S. N., Noel, N. K., Snaith, H. J. & Nicholas, R. J. Investigating the role of 4-tert butylpyridine in perovskite solar cells. *Adv. Energy Mater.* **7**, 7934 (2017).

78. Burschka, J., Kessler, F., Nazeeruddin, M. K. & Grä, M. Co(III) Complexes as p-Dopants in Solid-State Dye-Sensitized Solar Cells. *Chem. Mater.* **25**, 2986–2990 (2013).

79. Burschka, J. *et al.* Sequential deposition as a route to high-performance perovskite-sensitized solar cells. *Nature* **499**, 316–320 (2013).

80. Hong Noh, J. *et al.* Nanostructured TiO2/CH3NH3PbI3 heterojunction solar cells employing spiro-OMeTAD/Co-complex as hole-transporting material. *J. Mater. Chem. A* **1**, 11842 (2013).

81. Bi, D. *et al.* Efficient luminescent solar cells based on tailored mixed-cation perovskites. *Sci. Adv.* **2**, e1501170–e1501170 (2016).

82. Matsui, T., Seo, J. Y., Saliba, M., Zakeeruddin, S. M. & Grï¿½tzel, M. Room-Temperature Formation of Highly Crystalline Multication Perovskites for Efficient, Low-Cost Solar Cells. *Adv. Mater.* **29**, 2–6 (2017).

83. Luo, J. *et al.* The novel dopant for hole-transporting material opens a new processing route to efficiently reduce hysteresis and improve stability of planar perovskite solar cells. *J. Power Sources* **342**, 886–895 (2017).

84. Burschka, J., Kessler, F., Nazeeruddin, M. K. & Grätzel, M. Co(III) Complexes as p-Dopants in Solid-State Dye-Sensitized Solar Cells. *Chem. Mater.* **25**, 2986–2990 (2013).

85. Gu, X. *et al.* FeCl3 as a low-cost and efficient p-type dopant of Spiro-OMeTAD for high performance perovskite solar cells. *RSC Adv.* **8**, 9409–9413 (2018).

86. Xu, M. *et al.* Improvement in Solid-State Dye Sensitized Solar Cells by p-Type Doping with Lewis Acid SnCl4. *J. Phys. Chem. C* **117**, 22492–22496 (2013).

87. Wang, P. *et al.* Copper iodide as a potential low-cost dopant for spiro-MeOTAD in perovskite solar cells. *J. Mater. Chem. C* **4**, 9003–9008 (2016).

88. Laimer, J. & Störi, H. Recent advances in the research on non-equilibrium atmospheric pressure plasma jets. *Plasma Process. Polym.* **4**, 266–274 (2007).

89. Hayashi, N., Tsutsui, S., Tomari, T. & Guan, W. Sterilization of Medical Equipment Using Oxygen Radicals Produced by Water Vapor RF Plasma. *IEEE Trans. Plasma Sci.* **36**, 1302 (2008).

90. Romero-Mangado, J. *et al.* Efficacy of atmospheric pressure dielectric barrier discharge for inactivating airborne pathogens. *J. Vac. Sci. Technol. A Vacuum, Surfaces, Film.* **35**, 41101–41603 (2017).

91. Sarani, A., Nikiforov, A. Y., De Geyter, N., Morent, R. & Leys, C. Surface modification of polypropylene with an atmospheric pressure plasma jet sustained in argon and an argon/water vapour mixture. *Appl. Surf. Sci.* **257**, 8737–8741 (2011).

92. Sarani, A. *et al.* Surface modification of PTFE using an atmospheric pressure plasma jet in argon and argon+CO2. *Surf. Coatings Technol.* **206**, 2226–2232 (2012).

93. Beams, I., Engineering, P. S. & Kong, H. Guest Editorial Special Issue on Plasma-Based Surface Modification and Treatment Technologies. **37**, 1121–1122 (2009).

94. Machala, Z. *et al.* Emission spectroscopy of atmospheric pressure plasmas for bio-medical and environmental applications. *J. Mol. Spectrosc.* **243**, 194–201 (2007).

95. Morfill, G. E., Kong, M. G. & Zimmermann, J. L. Focus on plasma medicine. *New J. Phys.* **11**, (2009).

96. Dowling, D. P., O'Neill, F. T., Langlais, S. J. & Law, V. J. Influence of dc pulsed atmospheric pressure plasma jet processing conditions on polymer activation. *Plasma Process. Polym.* **8**, 718–727 (2011).

97. Bai, S., Ho, K. K. C., Knox, G. & Bismarck, A. Improving the adhesion between carbon fibres and an elastomer matrix using an acrylonitrile containing atmospheric plasma treatment. *Compos. Interfaces* **20**, 761–782 (2013).

98. Donegan, M., Milosavljević, V. & Dowling, D. P. Activation of PET using an RF atmospheric plasma system. *Plasma Chem. Plasma Process.* **33**, 941–957 (2013).

99. Jin, Y., Ren, C., Yang, L., Zhang, J. & Wang, D. Atmospheric Pressure Plasma Jet in Ar and O2/Ar Mixtures: Properties and High Performance for Surface Cleaning. *Plasma Sci. Technol.* **15**, 1203–1208 (2013).

100. Noh, J. H., Baik, H. K., Noh, I., Park, J.-C. & Lee, I.-S. Surface modification of polytetrafluoroethylene using atmospheric pressure plasma jet for medical application. *Surf. Coatings Technol. Technol.* **201**, 5097–5101 (2007).

101. Ionita, E. R., Ionita, M. D., Stancu, E. C., Teodorescu, M. & Dinescu, G. Small size plasma tools for material processing at atmospheric pressure. *Appl. Surf. Sci.* **255**, 5448–5452 (2009).

102. Fricke, K., Steffen, H., Von Woedtke, T., Schröder, K. & Weltmann, K. D. High rate etching of polymers by means of an atmospheric pressure plasma jet. *Plasma Process. Polym.* **8**, 51–58 (2011).

103. Moritzer, E., Budde, C. & Leister, C. Effect of atmospheric pressure plasma pre-treatment and aging conditions on the surface of thermoplastics. *Weld. World* **59**, 23–32 (2014).

104. Wang, H., Maiyalagan, T. & Wang, X. Review on recent progress in nitrogen-doped graphene: Synthesis, characterization, and its potential applications. *ACS Catal.* **2**, 781–794 (2012).

105. Liepins, R. & Sakaoku, K. Submicron polymer powder in electrodeless radio frequency-induced plasma-initiated polymerization. *J. Appl. Polym. Sci.* **16**, 2633–2645 (1972).

106. Penkov, O. V., Lee, D. H., Kim, H. & Kim, D. E. Frictional behavior of atmospheric plasma jet deposited carbon-ZnO composite coatings. *Compos. Sci. Technol.* **77**, 60–66 (2013).

107. Gandhiraman, R. P. *et al.* Plasma jet printing of electronic materials on flexible and nonconformal objects. *ACS Appl. Mater. Interfaces* **6**, 20860–20867 (2014).

108. Gandhiraman, R. P. *et al.* Plasma jet printing for flexible substrates. *Appl. Phys. Lett* **108**, 123103 (2016).

109. Dey, A. *et al.* Plasma Jet Printing and in situ Reduction of Highly Acidic Graphene Oxide. *ACS Nano* **12**, 5473–5481 (2018).

110. Hashimoto, Y. & Hamagaki, M. Effect of oxygen plasma treatment of indium tin oxide for organic solar cell. *Electr. Eng. Japan (English Transl. Denki Gakkai Ronbunshi)* **154**,

1–7 (2006).

111. Ke, J. C., Wang, Y. H., Chen, K. L. & Huang, C. J. Effect of organic solar cells using various power O2 plasma treatments on the indium tin oxide substrate. *J. Colloid Interface Sci.* **465**, 311–315 (2016).

112. Jesus Id´ígoras, Aparicio, F. J. *et al.* Enhancing Moisture and Water Resistance in Perovskite Solar Cells by Encapsulation with Ultrathin Plasma Polymers. *ACS Appl. Mater. Interfaces* **10**, 11587–11594 (2018).

113. Rolston, N. *et al.* Improved stability and efficiency of perovskite solar cells with submicron flexible barrier films deposited in air. *J. Mater. Chem. A* **5**, 22975–22983 (2017).

114. Xiao, X. *et al.* Argon Plasma Treatment to Tune Perovskite Surface Composition for High Efficiency Solar Cells and Fast Photodetectors. *Adv. Mater.* **30**, 1–7 (2018).

115. Hilt, F. *et al.* Rapid route to efficient, scalable, and robust perovskite photovoltaics in air. *Energy Environ. Sci.* **11**, 2102 (2018).

116. Nishihara, Y., Chikamatsu, M., Kazaoui, S., Miyadera, T. & Yoshida, Y. Influence of O2 plasma treatment on NiOx layer in perovskite solar cells. *Jpn. J. Appl. Phys* **57**, 4–7 (2018).

117. You, P., Liu, Z., Tai, Q., Liu, S. & Yan, F. Efficient Semitransparent Perovskite Solar Cells with Graphene Electrodes. *Adv. Mater.* **27**, 3632–3638 (2015).

118. Wang, J. T., Ball, J. M., Barea, E. M., Abate, A. & Alexander-, J. a. Low-temperature processed electron collection layers of Graphene / TiO2 nanocomposites in thin film perovskite solar cells. *Nano Lett.* **14**, 724–730 (2014).

119. Wu, Z. *et al.* Efficient planar heterojunction perovskite solar cells employing graphene oxide as hole conductor. *Nanoscale* **6**, 10505–10510 (2014).

120. Li, W. *et al.* Graphene oxide as dual functional interface modifier for improving wettability and retarding recombination in hybrid perovskite solar cells. *J. Mater. Chem. A* **2**, 20105–20111 (2014).

121. Li, D. *et al.* Graphene oxide modified hole transport layer for CH 3 NH 3 PbI 3 planar heterojunction solar cells. *Sol. Energy* **131**, 176–182 (2016).

122. Huang, X. *et al.* Moderately reduced graphene oxide/PEDOT:PSS as hole transport layer to fabricate efficient perovskite hybrid solar cells. *Org. Electron.* **39**, 288–295 (2016).

123. Luo, H. *et al.* Efficient and Air-Stable Planar Perovskite Solar Cells Formed on Graphene-Oxide-Modified PEDOT:PSS Hole Transport Layer. *Nano-micro lett.* **39**, 1–11 (2017).

124. Nouri, E. *et al.* Introduction of Graphene Oxide as Buffer Layer in Perovskite Solar Cells and the Promotion of Soluble n-Butyl-substituted Copper Phthalocyanine as Efficient Hole Transporting Material. *Electrochim. Acta* **233**, 36–43 (2017).

125. Yang, Q.-D. *et al.* Graphene oxide as an efficient hole-transporting material for high-performance perovskite solar cells with enhanced stability. *J. Mater. Chem. A* **5**, 9852–9858 (2017).

126. Choul Yu, J. *et al.* Highly efficient and stable inverted perovskite solar cell employing PEDOT:GO composite layer as a hole transport layer. *Sci. Rep.* **8**, 1070 (2018).

127. Yeo, J.-S. *et al.* Highly efficient and stable planar perovskite solar cells with reduced graphene oxide nanosheets as electrode interlayer. *Nano Energy* **12**, 96–104 (2015).

128. Luo, Q. *et al.* Iodide-reduced graphene oxide with dopant-free spiro-OMeTAD for

ambient stable and high-efficiency perovskite solar cells. *J. Mater. Chem. A* **3**, 15996–16004 (2015).

129. Li, Z. *et al.* Laminated Carbon Nanotube Networks for Metal Electrode-Free Efficient perovskite solar cells. *ACS Nano* **8**, 6797–6804 (2014).

130. Wang, X. *et al.* TiO2 nanotube arrays based flexible perovskite solar cells with transparent carbon nanotube electrode. *Nano Energy* **11**, 728–735 (2015).

131. Zhang, H. *et al.* Fluorescent biosensors enabled by graphene and graphene oxide. *Biosens. Bioelectron.* **89**, 96–106 (2017).

132. Xu, Y. & Liu, J. Graphene as Transparent Electrodes: Fabrication and New Emerging Applications. *Small* **12**, 1400–1419 (2016).

133. Liang, X., Fu, Z. & Chou, S. Y. Graphene Transistors Fabricated via Transfer-Printing In Device Active-Areas on Large Wafer. *Nano Lett.* **7**, 3840–3844 (2007).

134. Eda, G., Fanchini, G. & Chhowalla, M. Large-area ultrathin films of reduced graphene oxide as a transparent and flexible electronic material. *Nat. Nanotechnol.* **3**, 270–274 (2008).

135. Gomez, L. *et al.* Continuous, Highly Flexible, and Transparent Graphene Films by Chemical Vapor Deposition for Organic Photovoltaics. *ACS Nano* **4**, 2865–2873 (2010).

136. Hayashi, H. *et al.* Electron Transfer Cascade by Organic/Inorganic Ternary Composites of Porphyrin, Zinc Oxide Nanoparticles, and Reduced Graphene Oxide on a Tin Oxide Electrode that Exhibits Efficient Photocurrent Generation. *J. Am. Chem. Soc* **133**, 7684–7687 (2011).

137. Das, S. K. & Kc, C. B. Studies on the Photocatalytic Electron Pooling of Graphene Oxide Hybrids Decorated with Electron Donor and Electron Acceptor Molecules. *Fullerenes, Nanotub. Carbon Struct.* **22**, 128–137 (2014).

138. William S. Hummers, J. & Offeman, R. E. Preparation of Graphitic Oxide. *J. Am. Chem. Soc* **80**, 1339 (1958).

139. Ramanathan, T. *et al.* Functionalized graphene sheets for polymer nanocomposites. *Nat. Nanotechnol.* **3**, 327–331 (2008).

140. Yin, W.-J., Shi, T. & Yan, Y. Unusual defect physics in $CH_3NH_3PbI_3$ perovskite solar cell absorber. *Appl. Phys. Lett.* **104**, 063903 (2014).

141. Eda, G., Mattevi, C., Yamaguchi, H., Kim, H. & Chhowalla, M. Insulator to Semimetal Transition in Graphene Oxide. *J. Phys. Chem. C* **113**, 15768–15771 (2009).

142. Lee, D.-Y., Na, S.-I. & Kim, S.-S. Graphene oxide/PEDOT:PSS composite hole transport layer for efficient and stable planar heterojunction perovskite solar cells. *Nanoscale* **8**, 1513–1522 (2015).

143. Jung, I., Dikin, D. A., Piner, R. D. & Ruoff, R. S. Tunable Electrical Conductivity of Individual Graphene Oxide Sheets Reduced at 'Low' Temperatures. *NANO Lett.* **8**, 29 (2008).

144. Stratakis, E., Savva, K., Konios, D., Petridis, C. & Kymakis, E. Improving the efficiency of organic photovoltaics by tuning the work function of graphene oxide hole transporting layers. *Nanoscale* **6**, 6925–31 (2014).

145. Misra, A., Kalita, H. & Kottantharayil, A. Work function modulation and thermal stability of reduced graphene oxide gate electrodes in MOS devices. *ACS Appl. Mater. Interfaces* **6**, 786–794 (2014).

146. Martins, T. B., Miwa, R. H., Da Silva, A. J. R. & Fazzio, A. Electronic and transport

properties of boron-doped graphene nanoribbons. *Phys. Rev. Lett.* **98**, 3–6 (2007).

147. Calandra, M. & Mauri, F. Electronic structure of heavily doped graphene: The role of foreign atom states. *Phys. Rev. B* **76**, 1–4 (2007).

148. Tsetseris, L., Wang, B. & Pantelides, S. T. Substitutional doping of graphene: The role of carbon divacancies. *Phys. Rev. B* **89**, 035411-1 (2014).

149. Guo, B. *et al.* Controllable N-Doping of Graphene. *Nano Lett.* **10**, 4975–4980 (2010).

150. Lv, R. *et al.* Nitrogen-doped graphene: Beyond single substitution and enhanced molecular sensing. *Sci. Rep.* **2**, 1–8 (2012).

151. Leela, A. *et al.* Synthesis Of Nitrogen-Doped Graphene Films For Lithium Battery Application. *ACS Nano* **4**, 6337–6342 (2010).

152. Wu, Z. S., Ren, W., Xu, L., Li, F. & Cheng, H. M. Doped graphene sheets as anode materials with superhigh rate and large capacity for lithium ion batteries. *ACS Nano* **5**, 5463–5471 (2011).

153. Yang, W. *et al.* Nitrogen plasma modified CVD grown graphene as counter electrodes for bifacial dye-sensitized solar cells. *Electrochim. Acta* **173**, 715–720 (2015).

154. Jun-Seok Yeo, Jin-Mun Yun, Yen-Sook Jung, Dong-Yu Kim, Yong-Jin Noh, S.-S. K. and S.-I. N. Sulfonic acid-functionalized, reduced graphene oxide as an advanced interfacial material leading to donor polymer-independent high-performance polymer solar cells. *J. Mater. Chem. A* **2**, 292–298 (2014).

155. Chua, C. K. & Pumera, M. Reduction of graphene oxide with substituted borohydrides. *J. Mater. Chem. A* **1**, 1892–1898 (2013).

156. Pei, S. & Cheng, H. M. The reduction of graphene oxide. *Carbon N. Y.* **50**, 3210–3228 (2012).

157. Wei, D. *et al.* Synthesis of n-doped graphene by chemical vapor deposition and its electrical properties. *Nano Lett.* **9**, 1752–1758 (2009).

158. Akada, K., Terasawa, T.-O., Imamura, G., Obata, S. & Saiki, K. Control of work function of graphene by plasma assisted nitrogen doping. *Appl. Phys. Lett.* **104**, 131602–1 (2014).

159. Zeng, J. J. & Lin, Y. J. Tuning the work function of graphene by nitrogen plasma treatment with different radio-frequency powers. *Appl. Phys. Lett.* **104**, (2014).

160. Marcano, D. C. *et al.* Improved Synthesis of Graphene Oxide. *ACS Nano* **4**, 4806–4814 (2010).

161. Hafiz, S. M. *et al.* A practical carbon dioxide gas sensor using room-temperature hydrogen plasma reduced graphene oxide. *Sensors Actuators B* **193**, 692–700 (2014).

162. Li, J., Chen, C., Wei, J., Li, J. & Wang, X. Enhanced Electrochemical Performance of Reduced Graphene Oxides by H_2/Ar Plasma Treatment. *J. Phys. Chem. C* **118**, 28440–28447 (2014).

163. Chandana, L., Ghosal, P. & Challapalli, S. Improved Solar Cell Performance of High Quality Plasma Reduced Graphene Oxide. *Plasma Process. Polym.* **13**, 929–936 (2016).

164. Nourbakhsh, A. *et al.* Bandgap opening in oxygen plasma-treated graphene. *Nanotechnology* **21**, 1–10 (2010).

165. Xie, X. *et al.* An asymmetrically surface-modified graphene film electrochemical actuator. *ACS Nano* **4**, 6050–6054 (2010).

166. Peltekis, N. *et al.* The effect of downstream plasma treatments on graphene surfaces.

Carbon N. Y. **50**, 395–403 (2012).

167. Mao, H., Wang, R., Zhong, J., Zhong, S. & Chen, W. Mildly O2 plasma treated CVD graphene as a promising platform for molecular sensing. *Carbon N. Y.* **76**, 212–219 (2014).

168. Hye Kim, J. *et al.* Large-Scale Plasma Patterning of Transparent Graphene Electrode on Flexible Substrates. *Langmuir* **15**, 11 (2015).

169. Kumar, N. A. *et al.* Plasma-assisted simultaneous reduction and nitrogen doping of graphene oxide nanosheets. *J. Mater. Chem. A* **1**, 4431–4435 (2013).

170. E P Neustroev , E K Burtseva , B D Soloviev, A. R. P. & Timofeev, V. I. P. and V. B. Modification of graphene oxide films by radiofrequency N2 plasma Related content. *Nanotechnology* **29**, 144002–1 (2018).

171. Lee, B.-J., Cho, S.-C. & Jeong, G.-H. Atmospheric pressure plasma treatment on graphene grown by chemical vapor deposition. *Curr. Appl. Phys.* **15**, 563–568 (2015).

172. Lee, S. W., Mattevi, C., Chhowalla, M. & Sankaran, R. M. Plasma-assisted reduction of graphene oxide at low temperature and atmospheric pressure for flexible conductor applications. *J. Phys. Chem. Lett.* **3**, 772–777 (2012).

173. Eng, A. Y. S., Sofer, Z., Šimek, P., Kosina, J. & Pumera, M. Highly hydrogenated graphene through microwave exfoliation of graphite oxide in hydrogen plasma: Towards electrochemical applications. *Chem. - A Eur. J.* **19**, 15583–15592 (2013).

174. Homola, T. *et al.* Atmospheric Dry Hydrogen Plasma Reduction of Inkjet-Printed Flexible Graphene Oxide Electrodes. *ChemSusChem* **11**, 941–947 (2018).

175. Ke, Z. *et al.* Non-thermal hydrogen plasma processing effectively increases the antibacterial activity of graphene oxide. *Appl. Phys. Lett.* **112**, (2018).

176. Yang, S. *et al.* Functionalization of perovskite thin films with moisture-tolerant molecules. *Nat. Energy* **1**, 15016 (2016).

177. Marinov, D. & Braithwaite, N. S. J. Power coupling and electrical characterization of a radio-frequency micro atmospheric pressure plasma jet. *Plasma Sources Sci. Technol.* **23**, 062005 (2014).

178. Kogelschatz, U. Filamentary, patterned, and diffuse barrier discharges. *IEEE Trans. Plasma Sci.* **30**, 1400–1408 (2002).

179. Bahnev, B. Electrical and optical characterisation of an atmosphere pressure plasma jet and its interaction with plasmid DNA. (2011).

180. Briggs, D. & Seah, M. P. *Practical surface analysis*. (Wiley, 1990).

181. Reinert, F. & Hüfner, S. Photoemission spectroscopy—from early days to recent applications. *New J. Phys.* **7**, (2005).

182. Seah, M. P. & Dench, W. A. Quantitative electron spectroscopy of surfaces: A standard data base for electron inelastic mean free paths in solids. *Surf. Interface Anal.* **1**, 2–11 (1979).

183. Brundle, C. R. & Baker, A. D. *Electron spectroscopy : theory, techniques and applications*. (Academic Press, 1981).

184. Attwood, D. T. *Soft x-rays and extreme ultraviolet radiation : principles and applications*. (Cambridge University Press, 2000).

185. Ederer, J. A. R. S. and D. L. *Vacuum Ultraviolet Spectroscopy*. (Cambridge University Press, 1999). doi:10.1017/CBO9781139164429

186. Haehner, G. Near edge X-ray absorption fine structure spectroscopy as a tool to probe electronic and structural properties of thin organic films and liquids. *Chem. Soc. Rev.* **35**, 1244–1255 (2006).

187. Nefedov, A. & Wöll, C. Advanced Applications of NEXAFS Spectroscopy for Functionalized Surfaces. in *Surface science techniques* 277–303 (Springer, Berlin, Heidelberg, 2013).

188. Stöhr, J. *NEXAFS Spectroscopy*. **25**, (Springer Berlin Heidelberg, 1992).

189. Ament, L. J. P., van Veenendaal, M., Devereaux, T. P., Hill, J. P. & Brink, J. van den. Resonant Inelastic X-ray Scattering Studies of Elementary Excitations. **83**, 705–767 (2010).

190. Struve, W. S. *Fundamentals of Molecular Spectroscopy*. (1989).

191. Jorio, A., Saito, R., Dresselhaus, G. & Dresselhaus, M. S. *Raman Spectroscopy in Graphene Related Systems*. *Raman Spectroscopy in Graphene Related Systems* (2011). doi:10.1002/9783527632695

192. Binnig, G., Quate ' ', C. F., Gi, E. L. & Gerber, C. Atomic Force Microscope. *Phys. Rev. Lett.* **56**, 930 (1986).

193. Binnig, G. & Rohrer, H. Scanning tunneling microscopy from birth to adolescence. *Rev. Mod. Phys.* **59**, 369 (1987).

194. Bonnell, D. A. *Scanning probe microscopy and spectroscopy : theory, techniques, and applications*. (Wiley-VCH, 2001).

195. Asylum Research. SPM Applications Guide. 168 (2013).

196. Jeong, H., Lee, K. M., Ahn, Y. H., Lee, S. & Park, J. Y. Non-Contact Local Conductance Mapping of Individual Graphene Oxide Sheets during the Reduction Process. *J. Phys. Chem. Lett.* **6**, 2629–2635 (2015).

197. Yalcin, S. E. S. E. *et al.* Direct Imaging of Charge Transport in Progressively Reduced Graphene Oxide Using Electrostatic Force Microscopy. *ACS Nano* **9**, 2981–8 (2015).

198. Vidyasagar, R., Camargo, B., Pelegova, E., Romanyuk, K. & Kholkin, A. L. Controlling Surface Potential of Graphene Using dc Electric Field. *KnE Mater. Sci.* **1**, 183 (2016).

199. Kazakova, O., Panchal, V. & Burnett, T. Epitaxial Graphene and Graphene–Based Devices Studied by Electrical Scanning Probe Microscopy. *Crystals* **3**, 191–233 (2013).

200. Jeong, H., Ahn, Y. H., Lee, S. & Park, J.-Y. Quantitative non-contact voltage profiling of quasi one-dimensional nanoelectronic devices. *Appl. Phys. Lett.* **104**, 213102–1 (2014).

201. Weaver, J. M. R. & Abraham, D. W. High resolution atomic force microscopy potentiometry High resolution atomic force microscopy potentiometry. *J. Vac. Sci. Technol. B* **9**, 1559–2921 (1991).

202. Schoelin, R. *et al.* Energy level shifts in spiro-OMeTAD molecular thin films when adding Li-TFSI. *J. Phys. Chem. C* **116**, 26300–26305 (2012).

203. Wang, S., Yuan, W. & Meng, Y. S. Spectrum-Dependent Spiro-OMeTAD Oxidization Mechanism in Perovskite Solar Cells. *ACS Appl. Mater. Interfaces* **7**, 24791–24798 (2015).

204. Ehlert, C., Unger, W. E. S. & Saalfrank, P. C K-edge NEXAFS spectra of graphene with physical and chemical defects: a study based on density functional theory. *Phys. Chem. Chem. Phys.* **16**, 14083–14095 (2014).

205. Gerlin, F. *et al.* Stability and extreme ultraviolet photo-reduction of graphene during C-K edge NEXAFS characterization. *Surf. Coatings Technol.* **296**, 211–215 (2016).

206. Gutiérrez, C. *et al.* Imaging chiral symmetry breaking from Kekulé bond order in graphene. *Nat. Phys.* **12**, 1–31 (2015).

207. Solomon, J. L., Madix, R. J. & Stohr, J. Orientation and absolute coverage of benzene, aniline, and phenol on Ag(110) determined by NEXAFS and XPS. *Surface Science* **255**, 12–30 (1991).

208. Turci, C. C., Urquhart, S. G. & Hitchcock, A. P. Inner-shell excitation spectroscopy of aniline, nitrobenzene, and nitroanilines. *Can. J. Chem.* **74**, 851–869 (1996).

209. Dhez, O., Ade, H. & Urquhart, S. G. Calibrated NEXAFS spectra of some common polymers. *J. Electron Spectros. Relat. Phenomena* **128**, 85–96 (2003).

210. Dawit Solomon *et al.* Carbon (1s) NEXAFS Spectroscopy of Biogeochemically Relevant Reference Organic Compounds. *Soil Sci. Soc. Am. J* **73**, 1817–1830 (2008).

211. Bader, M., Haase, J., Frank, K. H., Puschmann, A. & Otto, A. Orientational phase transition in the system pyridine/Ag(111): A near-Edge X-Ray-Absorption fine-Structure study. *Phys. Rev. Lett.* **56**, 1921–1924 (1986).

212. Yannoulis, P., Dudde, R., Frank, K. H. & Koch, E. E. Orientation of aromatic hydrocarbons on metal surfaces as determined by nexafs. *Surf. Sci.* **189**–**190**, 519–528 (1987).

213. Horsley, J. A. *et al.* Resonances in the K shell excitation spectra of benzene and pyridine: Gas phase, solid, and chemisorbed states. *The Journal of Chemical Physics* **83**, 6099 (1985).

214. Huang, S. X., Fischer, D. A. & Gland, J. L. Aniline Adsorption, Hydrogenation, and Hydrogenolysis on the Ni(100) Surface. *J. Phys. Chem.* **100**, 10223–10234 (1996).

215. Mullins, O. C., Mitra-Kirtley, S., Van Elp, J. & Cramer, S. P. Molecular structure of nitrogen in coal from XANES spectroscopy. *Applied Spectroscopy* **47**, 1268–1275 (1993).

216. Solomon, D., Lehmann, J., Kinyangi, J., Liang, B. & Schä, T. Carbon K-Edge NEXAFS and FTIR-ATR Spectroscopic Investigation of Organic Carbon Speciation in Soils. *J. Am. soil Sci. Soc.* **69**, 107–119 (2005).

217. Johansson, E. M. J. *et al.* Interface electronic states and molecular structure of a triarylamine based hole conductor on rutile TiO2(110). *J. Chem. Phys.* **128**, (2008).

218. Latham, K. G., Simone, M. I., Dose, W. M., Allen, J. A. & Donne, S. W. Synchrotron based NEXAFS study on nitrogen doped hydrothermal carbon: Insights into surface functionalities and formation mechanisms. *Carbon N. Y.* **114**, 566–578 (2017).

219. Lee, V. *et al.* Soft X-ray Absorption Spectroscopy Studies of the Electronic Structure Recovery of Graphene Oxide upon Chemical Defunctionalization. *J. Phys. Chem. C* **116**, 20591–20599 (2012).

220. Tirsell, K. G. & Karpenko, V. P. A general purpose sub-keV X-ray facility at the Stanford Synchrotron Radiation Laboratory. *Nucl. Inst. Methods Phys. Res. A* **291**, 511–517 (1990).

221. Wang, H. *et al.* Nickel L-Edge Soft X-ray Spectroscopy of Nickel-Iron Hydrogenases and Model Compounds-Evidence for High-Spin Nickel(II) in the Active Enzyme. *J. Am. Chem. Soc.* **122**, 10544–10522 (2000).

222. Wang, H. *et al.* Integrated X-ray L Absorption Spectra. Counting Holes in Ni Complexes.

J. Phys. Chem. B **102**, 8343–8346 (1998).

223. Heymann, K., Lehmann Johannes, J., Solomon, D., Schmidt, M. W. I. & Regier, T. C 1s K-edge near edge X-ray absorption fine structure (NEXAFS) spectroscopy for characterizing functional group chemistry of black carbon. *Org. Geochem.* **42**, 1055–1064 (2011).

224. Huang, W. & Ptasinska, S. Functionalization of graphene by atmospheric pressure plasma jet in air or H2O2 environments. *Appl. Surf. Sci.* **367**, 160–166 (2016).

225. Keane, M. P., de Brito, A. N., Correia, N., Svensson, S. & Lunell, S. Experimental and theoretical study of the N1s and C1s shake-up satellites in pyridine and aniline. *Chemical Physics* **155**, 379–387 (1991).

226. Baiardi, A. *et al.* Vibrationally resolved NEXAFS at C and N K-edges of pyridine, 2-fluoropyridine and 2,6-difluoropyridine: A combined experimental and theoretical assessment. *J. Chem. Phys.* **143**, (2015).

227. Ganguly, A., Sharma, S., Papakonstantinou, P. & Hamilton, J. Probing the Thermal Deoxygenation of Graphene Oxide using High Resolution In Situ X-Ray based Spectroscopies. *J. Phys. Chem.* **115**, 17009–17019 (2011).

228. Gandhiraman, R. P. *et al.* X-ray Absorption Study of Graphene Oxide and Transition Metal Oxide Nanocomposites. *J. Phys. Chem. C* **118**, 18706–18712 (2014).

229. Aminpirooz, S., Becker, L., Hillert, B. & Haase, J. High resolution NEXAFS studies of aromatic molecules adsorbed and condensed on Ni(111). *Surf. Sci.* **244**, (1991).

230. Boyce, C. K. *et al.* Organic chemical differentiation within fossil plant cell walls detected with X-ray spectromicroscopy. *Geology* **30**, 1039–1042 (2002).

231. Zubavichus, Y., Shaporenko, A., Grunze, M. & Zharnikov, M. Innershell Absorption Spectroscopy of Amino Acids at All Relevant Absorption Edges. *J. Phys. Chem. A* **109**, 6998–7000 (2005).

232. Apen, E., Hitchcock, A. P. & Gland, J. L. Experimental studies of the core excitation of imidazole, 4,5-dicyanoimidazole, and s-triazine. *J. Phys. Chem.* **97**, 6859–6866 (1993).

233. Dennis, R. V. *et al.* Near-edge x-ray absorption fine structure spectroscopy study of nitrogen incorporation in chemically reduced graphene oxide. *J. Vac. Sci. Technol. B* **31**, 041204 (2013).

234. Sainio, S. *et al.* What Does Nitric Acid Really Do to Carbon Nanofibers? *J. Phys. Chem. C* **120**, 22655–22662 (2016).

235. Graf, N. *et al.* XPS and NEXAFS studies of aliphatic and aromatic amine species on functionalized surfaces. *Surf. Sci.* **603**, 2849–2860 (2009).

236. Shard, A. G. *et al.* A NEXAFS examination of unsaturation in plasma polymers of allylamine and propylamine. *J. Phys. Chem. B* **108**, 12472–12480 (2004).

237. W.H.E. Schwarz, T.C. Chang, U. Seeger, K. H. H. Core excitations of symmetrical aromatic molecules-specific correlations in the valence shell and localization in the core shells. *Chem. Phys.* **117**, 73–89 (1987).

238. Banerjee, S. *et al.* Ozonized single-walled carbon nanotubes investigated using NEXAFS spectroscopy. *Chem Commun* 772–773 (2004).

239. Ma, Y., Sette, F., Meigs, G., Modesti, S. & Chen ', C. T. Breaking of Ground-State Symmetry in Core-Excited Ethylene and Benzene. *Phys. Rev. Lett.* **63**, 2044 (1989).

240. Lehmann, J. *et al.* Synchrotron-based near-edge X-ray Spectroscopy of natural organic matter in Soils and sediments. in *Biophysico-Chemical Processes Involving Natural*

Nonliving Organic Matter in Environmental Systems 729–781 (2009).

241. Stohr, J; Gland, J. L.; Kollin, E. B. Desulfurization and structural transformation of thiophene on the Pt(111). *Phys. Rev. Lett.* **53**, 2161–2164 (1984).

242. Nyberg, M. *et al.* The electronic structure and surface chemistry of glycine adsorbed on Cu(110). *J. Chem. Phys.* **112**, 5420–5427 (2000).

243. Dri, C. *et al.* Chemistry of the Methylamine Termination at a Gold Surface: From Autorecognition to Condensation. *J. Phys. Chem. C* **120**, 6104–6115 (2016).

244. Luo, Y. *et al.* In situ hydrolysis of imine derivatives on Au(111) for the formation of aromatic mixed self-assembled monolayers: Multitechnique analysis of this tunable surface modification. *Langmuir* **28**, 358–366 (2012).

245. Oran, U., Swaraj, S., Lippitz, A. & Unger, W. E. S. Surface analysis of plasma deposited polymer films, 7: 'In situ' characterization of plasma deposited allylamine films by ToF-SSIMS, XPS and NEXAFS spectroscopy. *Plasma Process. Polym.* **3**, 288–298 (2006).

246. Chiou, J. W. *et al.* Nitrogen-Functionalized Graphene Nano fl akes (GNFs : N): Tunable Photoluminescence and Electronic Structures. *J. Phys. Chem. C* **116**, 16251–16258 (2012).

247. Ray, S. C. *et al.* X - ray absorption spectroscopy (XAS) study of dip deposited a - C : H (OH) thin films. *J . Phys . Condens . Matter* **16**, 5713–5719 (2004).

248. Yegen, E., Lippitz, A., Treu, D. & Unger, W. E. S. Derivatization of amino groups by pentafluorobenzaldehyde (PFB) as observed by XPS and NEXAFS spectroscopy on spin coated 4,4'-methylenebis(2,6- diethylaniline) films. *Surf. Interface Anal.* **40**, 176–179 (2008).

249. Syugaev, A. V. & Maratkanova, A. N. Polarization-dependent NEXAFS study of adsorption of long-chain surfactants on mechanically milled iron powder. *J. Electron Spectros. Relat. Phenomena* **195**, 71–77 (2014).

250. Ohta, T., Seki, K., Yokoyama, T., Morisada, I. & Edamatsu, K. Polarized XAN ES Studies of Oriented Polyethylene and FI u o r i nated Pol yet hy I enes. *Physica* **41**, 150–153 (1990).

251. Heymann, K., Lehmann, J., Solomon, D., Schmidt, M. W. I. & Regier, T. C 1s K-edge near edge X-ray absorption fine structure (NEXAFS) spectroscopy for characterizing functional group chemistry of black carbon. *Org. Geochem.* **42**, 1055–1064 (2011).

252. Agren, Hans; Carravetta, V. & Vahtras, Olav; Pettersson, La. G. M. Orientational probing of polymeric thin films by NEXAFS: calculations on polytetrafluoroethylene. *Phys. Rev. B* **51**, 848–855 (1995).

253. Schultz, B. J. *et al.* X-ray absorption spectroscopy studies of electronic structure recovery and nitrogen local structure upon thermal reduction of graphene oxide in an ammonia environment. *RSC Adv.* **4**, 634–644 (2014).

254. Marchioro, A. *et al.* Unravelling the mechanism of photoinduced charge transfer processes in lead iodide perovskite solar cells. *Nature Photonics* **8**, 250–255 (2014).

255. Schiros, T. *et al.* Connecting dopant bond type with electronic structure in n-doped graphene. *Nano Lett.* **12**, 4025–4031 (2012).

256. Gao, Y. *et al.* Nitrogen-Doped sp2 -Hybridized Carbon as a Superior Catalyst for Selective Oxidation. *Angew. Chemie Int. Ed.* **52**, 2109–2113 (2013).

257. Bhattacharyya, S., Luebbe, M., Bressler, P. R., Zahn, D. R. T. & Richter, F. Structure of nitrogenated amorphous carbon films from NEXAFS. *Diam. Relat. Mater.* **11**, 8–15

(2002).

258. Djellab, H., Armand, M. & Delabouglise, D. Stabilization of the conductivity of poly(3-methylthiophene) triflimide anions. *Synth. Met.* **74**, 223–226 (1995).

259. Tiep, N. H., Ku, Z. & Fan, H. J. Recent Advances in Improving the Stability of Perovskite Solar Cells. *Adv. Energy Mater.* **6**, 1501420 (2016).

260. Wang, Y.-K. *et al.* Dopant-Free Spiro-Triphenylamine/Fluorene as Hole-Transporting Material for Perovskite Solar Cells with Enhanced Efficiency and Stability. *Adv. Funct. Mater.* **26**, 1375–1381 (2016).

261. Liu, K. *et al.* Spiro[fluorene-9,9 0-xanthene]-based hole transporting materials for efficient perovskite solar cells with enhanced stability. *Mater. Chem. Front.* **1**, 100–110 (2017).

262. Hwang, J. *et al.* Multilayered graphene anode for blue phosphorescent organic light emitting diodes. *Appl. Phys. Lett* **100**, 1 (2012).

263. Krstulovi, N. *et al.* Optical emission spectroscopy characterization of oxygen plasma during treatment of a PET foil. *J. Phys. D Appl. Phys* **39**, 3799–3804 (2006).

264. Milosavljevic, V., Donegan, M., Cullen, P., Dowling, D. & Diagnostics, D. Diagnostics of an O2–He RF Atmospheric Plasma Discharge by Spectral Emission. *J. Phys. Soc. Japan* **83**, 1–8 (2014).

265. Walkup, R. E., Saenger, K. L. & Selwyn, G. S. Studies of atomic oxygen in O2 +CF 4 rf discharges by two-photon laser-induced fluorescence and optical emission spectroscopy. *J. Chem. Phys.* **84**, 2668–2674 (1986).

266. Thiyagarajan, M., Sarani, A. & Nicula, C. Optical emission spectroscopic diagnostics of a non-thermal atmospheric pressure helium-oxygen plasma jet for biomedical applications. *J. Appl. Phys.* **113**, 233302–1 (2013).

267. Kramida, A., Ralchenko, Yu., Reader, J. and N. A. T. NIST: Atomic Spectra Database - Version 5.5.2. (2018). Available at: https://physics.nist.gov/asd. (Accessed: 5th March 2018)

268. Lofthus, Alf; Krupenie, P. H. The spectrum of molecular nitrogen. *J. Phys. chem. Ref. Data* **6**, 113–307 (1977).

269. Singh, M. K. *et al.* Inactivation factors of spore-forming bacteria using low-pressure microwave plasmas in an N2 and O2 gas mixture. *New J. Phys* **11**, 115027 (2009).

270. Gao, W., Alemany, L. B., Ci, L. & Ajayan, P. M. New insights into the structure and reduction of graphite oxide. *Nat. Chem.* **1**, 403–408 (2009).

271. Bagri, A. *et al.* Structural evolution during the reduction of chemically derived graphene oxide. *Nat. Chem.* **2**, 581–587 (2010).

272. Gardella, J., Ferguson, S. A. & Chin, R. L. pi *-pi Shakeup Satellites for the Analysis of Structure and Bonding in Aromatic Polymers by X-Ray Photoelectron Spectroscopy. *Appl. Spectrosc.* **40**, 224–232 (1986).

273. Kelemen, S. R., Rose, K. D. & Kwiatek, P. J. Carbon aromaticity based on XPS II to II*signal intensity. *Appl. Surf. Sci.* **64**, 167–174 (1993).

274. Hulicova-Jurcakova, D. *et al.* Nitrogen-enriched nonporous carbon electrodes with extraordinary supercapacitance. *Adv. Funct. Mater.* **19**, 1800–1809 (2009).

275. Wang, X. *et al.* Nitrogen-enriched ordered mesoporous carbons through direct pyrolysis in ammonia with enhanced capacitive performance. *J. Mater. Chem. A* **1**, 7920 (2013).

276. Wang, X. *et al.* Ammonia-Treated Ordered Mesoporous Carbons as Catalytic Materials for Oxygen Reduction Reaction. *Chem. Mater* **22**, 2178–2180 (2010).

277. Lota, G., Grzyb, B., Machnikowska, H., Machnikowski, J. & Frackowiak, E. Effect of nitrogen in carbon electrode on the supercapacitor performance. *Chem. Phys. Lett.* **404**, 53–58 (2005).

278. Chen, Z., Higgins, D. & Chen, Z. Nitrogen doped carbon nanotubes and their impact on the oxygen reduction reaction in fuel cells. *Carbon N. Y.* **48**, 3057–3065 (2010).

279. Biddinger, E. J. & Ozkan, U. S. Role of Graphitic Edge Plane Exposure in Carbon Nanostructures for Oxygen Reduction Reaction. *J Phys Chem C* **114**, 15306–15314 (2010).

280. Lai, L. *et al.* Exploration of the active center structure of nitrogen-doped graphene-based catalysts for oxygen reduction reaction. *Energy Environ. Sci.* **5**, 7936–7942 (2012).

281. Mattevi, C. *et al.* Evolution of electrical, chemical, and structural properties of transparent and conducting chemically derived graphene thin films. *Adv. Funct. Mater.* **19**, 2577–2583 (2009).

282. Kuwabara, A., Kuroda, S. & Kubota, H. Polymer Surface Treatment by Atmospheric Pressure Low Temperature Surface Discharge Plasma: Its Characteristics and Comparison with Low Pressure Oxygen Plasma Treatment. *Plasma Chem. Plasma Process.* **28**, 263–271 (2008).

283. Reuter, S., Niemi, K., Schulz-Von Der Gathen, V. & Döbele, H. F. Generation of atomic oxygen in the effluent of an atmospheric pressure plasma jet. *Plasma Sources Sci. Technol.* **18**, 1–20 (2009).

284. Qin, P. *et al.* Yttrium-substituted nanocrystalline TiO2 photoanodes for perovskite based heterojunction solar cells. *Nanoscale* **6**, 1508–1514 (2014).

285. Dymshits, A., Henning, A., Segev, G., Rosenwaks, Y. & Etgar, L. The electronic structure of metal oxide/ organo metal halide perovskite junctions in perovskite based solar cells. *Sci. Rep.* **5**, 1–6 (2015).

286. Jiang, C.-S. *et al.* Carrier separation and transport in perovskite solar cells studied by nanometre-scale profiling of electrical potential. *Nat. Commun.* **6**, 1–10 (2015).

287. Solar, P. & With, C. Revealing the Working Mechanisms of Planar Surface Potential Profiling. *IEEE J. Photovoltaics* **8**, 125–131 (2018).

288. Geim, A. K. & Novoselov, K. S. The rise of graphene. *Nat. mater* **6**, 183–191 (2007).

289. Eda, G. & Chhowalla, M. Chemically derived graphene oxide: Towards large-area thin-film electronics and optoelectronics. *Adv. Mater.* **22**, 2392–2415 (2010).

290. Chen, D., Feng, H. & Li, J. Graphene oxide: Preparation, functionalization, and electrochemical applications. *Chem. Rev.* **112**, 6027–6053 (2012).

291. Mishra, M., Joshi, R. K., Ojha, S., Kanjilal, D. & Mohanty, T. Role of oxygen in the work function modification at various stages of chemically synthesized graphene. *J. Phys. Chem. C* **117**, 19746–19750 (2013).

292. Peng, X., Tang, F. & Copple, A. Engineering the work function of armchair graphene nanoribbons using strain and functional species: A first principles study. *J. Phys. Condens. Matter* **24**, (2012).

293. Filleter, T., Emtsev, K. V., Seyller, T. & Bennewitz, R. Local work function measurements of epitaxial graphene. *Appl. Phys. Lett.* **93**, 2012–2015 (2008).

294. Yu, Y.-J. *et al.* Tuning the graphene work function by electric field effect. *Nano Lett.* **9**,

3430–4 (2009).

295. Christians, J. A. *et al.* Tailored interfaces of unencapsulated perovskite solar cells for >1,000 hour operational stability. *Nat. Energy* **3**, 68–74 (2018).

296. Liu, H.-W. *et al.* Rapid atmospheric pressure plasma jet processed reduced graphene oxide counter electrodes for dye-sensitized solar cells. *ACS Appl. Mater. Interfaces* **6**, 15105–12 (2014).

297. Kong, B. S., Geng, J. & Jung, H. T. Layer-by-layer assembly of graphene and gold nanoparticles by vacuum filtration and spontaneous reduction of gold ions. *Chem. Commun.* **16**, 2174–2176 (2009).

298. Yan, L., Punckt, C., Aksay, I. A., Mertin, W. & Bacher, G. Local voltage drop in a single functionalized graphene sheet characterized by Kelvin probe force microscopy. *Nano Lett.* **11**, 3543–3549 (2011).

299. Jiang, J., Krauss, T. D. & Brus, L. E. Electrostatic Force Microscopy Characterization of Trioctylphosphine Oxide Self-assembled Monolayers on Graphite. *J. Phys. Chem. B* **104**, 11936–11941 (2000).

300. Majumdar, B., Sarma, D., Bhattacharya, T. & Sarma, T. K. Graphene Oxide as Metal-Free Catalyst in Oxidative Dehydrogenative C−N Coupling Leading to α-Ketoamides: Importance of Dual Catalytic Activity. *ACS Sustain. Chem. Eng.* **5**, 9286–9294 (2017).

301. Pyun, J. Graphene oxide as catalyst: Application of carbon materials beyond nanotechnology. *Angew. Chemie - Int. Ed.* **50**, 46–48 (2011).

302. Hantel, M. M. Graphite oxide and graphene oxide based electrode materials for electrochemical double layer capacitors. (ETH Zurich, 2013).

303. Channu, V. S., Bobba, R. & Holze, R. Graphite and graphene oxide electrodes for lithium ion batteries. *Colloids Surfaces A Physicochem. Eng. Asp.* **436**, 245–251 (2013).

304. Ogata, C. *et al.* All-Graphene Oxide Flexible Solid-State Supercapacitors with Enhanced Electrochemical Performance. *ACS Appl. Mater. Interfaces* **9**, 26151–26160 (2017).

305. Kim, J., Park, S.-J. & Min, D.-H. Emerging Approaches for Graphene Oxide Biosensor. *Anal. Chem.* **89**, 232–248 (2017).

306. Lee, J., Kim, J., Kim, S. & Min, D.-H. Biosensors based on graphene oxide and its biomedical application. *Adv. Drug Deliv. Rev.* **105**, 275–287 (2016).

307. Sharma, D., Kanchi, S., Sabela, M. I. & Bisetty, K. Insight into the biosensing of graphene oxide: Present and future prospects. *Arab. J. Chem.* **9**, 238–261 (2016).

308. Singh, G. *et al.* Near room temperature reduction of graphene oxide Langmuir-Blodgett monolayers by hydrogen plasma. *Phys. Chem. Chem. Phys.* **16**, 11708–11718 (2014).

309. Jesuraj, P. J. *et al.* Hole injection enhancement in organic light emitting devices using plasma treated graphene oxide. *Appl. Surf. Sci.* **397**, 144–151 (2017).

310. Fantz, U. Basics of plasma spectroscopy. *Plasma Sources Sci. Technol* **15**, S137–S147 (2006).

311. Arkhipenko, V., Kirillov, A., Simonchik, L. & Zgirouski, S. Influence of nitrogen impurities on an electron-excited helium atoms concentration in the self-sustained normal dc glow discharge at atmospheric pressure. *12th Int. Congr. Plasma Phys.* 1–10 (2004).

312. Ono, R. & Oda, T. Dynamics of ozone and OH radicals generated by pulsed corona discharge in humid-air flow reactor measured by laser spectroscopy. *J. Appl. Phys.* **93**, 5876–5882 (2003).

313. Goree, J., Liu, B. & Drake, D. Gas flow dependence for plasma-needle disinfection of S. mutans bacteria. *J. Phys. D Appl. Phys* **39**, 3479–3486 (2006).

314. Meulenbroeks, R. F. G., Van Beek, A. J., Van Helvoort, A. J. G., Van De Sanden, M. C. M. & Schram, D. C. Argon-hydrogen plasma jet investigated by active and passive spectroscopic means. *Phys. Rev. E* **49**, 4397–4406 (1994).

315. Chauvet, L., Thérèse, L., Caillier, B. & Guillot, P. Characterization of an asymmetric DBD plasma jet source at atmospheric pressure. *J. Anal. At. Spectrom.* **29**, 2050–2057 (2014).

316. Shao, Y. *et al.* Nitrogen-doped graphene and its electrochemical applications. *J. Mater. Chem.* **20**, 7491–7496 (2010).

317. Sheng, Z. H. *et al.* Catalyst-free synthesis of nitrogen-doped graphene via thermal annealing graphite oxide with melamine and its excellent electrocatalysis. *ACS Nano* **5**, 4350–4358 (2011).

318. Rani, J. R. *et al.* Epoxy to Carbonyl Group Conversion in Graphene Oxide Thin Films : Effect on Structural and Luminescent Characteristics. *J. Phys. Chem. C* **116**, 19010–19017 (2012).

319. Lerf, A., He, H., Forster, M. & Klinowski, J. Structure of Graphite Oxide Revisited. *J. Phys. Chem. B* **102**, 4477–4482 (1998).

320. Fuente, E., Menéndez, J. A., Díez, M. A., Suárez, D. & Montes-Morán, M. A. Infrared Spectroscopy of Carbon Materials: A Quantum Chemical Study of Model Compounds. *J. Phys. Chem. B* **107**, 6350–6359 (2003).

321. Doniach, S., Sunjic, M. & Sunjic, S. D. and M. Many-electron singularity in X-ray photoemission and X-ray line spectra from metals. *IOP Sci.* **3**, 285 (1970).

322. Bagri, A., Grantab, R., Medhekar, N. V & Shenoy, V. B. Stability and formation mechanisms of carbonyl-and hydroxyl-decorated holes in graphene oxide. *J. Phys. Chem. C* **114**, 12053–12061 (2010).

323. Fan, X. *et al.* Deoxygenation of exfoliated graphite oxide under alkaline conditions: a green route to graphene preparation. *Adv. Mater.* **20**, 4490–4493 (2008).

324. Xu, B. *et al.* What is the choice for supercapacitors: graphene or graphene oxide? *Energy Environ. Sci.* **4**, 2826 (2011).

325. Hu, C. *et al.* One-step preparation of nitrogen-doped graphene quantum dots from oxidized debris of graphene oxide. *J. Mater. Chem. B* **1**, 39 (2013).

326. Permatasari, F. A., Aimon, A. H., Iskandar, F., Ogi, T. & Okuyama, K. Role of C-N Configurations in the Photoluminescence of Graphene Quantum Dots Synthesized by a Hydrothermal Route. *Sci. Rep.* **6**, 21042 (2016).

327. Szabó, T., Berkesi, O. & Dékány, I. DRIFT study of deuterium-exchanged graphite oxide. *Carbon N. Y.* **43**, 3186–3189 (2005).

328. Cecilia Mattevi, B. *et al.* Evolution of Electrical, Chemical, and Structural Properties of Transparent and Conducting Chemically Derived Graphene Thin Films. *Adv. Funct. Mater.* **19**, 2577–2583 (2009).

329. Abbas, G., Papakonstantinou, P., Iyer, G. R. S., Kirkman, I. W. & Chen, L. C. Substitutional nitrogen incorporation through rf glow discharge treatment and subsequent oxygen uptake on vertically aligned carbon nanotubes. *Phys. Rev. B - Condens. Matter Mater. Phys.* **75**, 195429–1 (2007).

330. Usachov, D. *et al.* Nitrogen-Doped Graphene: Efficient Growth, Structure, and

Electronic Properties. *Nano Lett.* **11**, 5401–5407 (2011).

331. Moon, J. *et al.* One-Step Synthesis of N-doped Graphene Quantum Sheets from Monolayer Graphene by Nitrogen Plasma. *Adv. Mater.* **26**, 3501–3505 (2014).

332. Schulze, M., Yanguas-Gil, A., Von Keudell, A. & Awakowicz, P. A robust method to measure metastable and resonant state densities from emission spectra in argon and argon-diluted low pressure plasmas. *J. Phys. D. Appl. Phys.* **41**, (2008).

333. Jin, D.-Z., Yang, Z.-H., Tang, P.-Y., Xiao, K.-X. & Dai, J.-Y. Hydrogen plasma diagnosis in penning ion source by optical emission spectroscopy. *Vacuum* **83**, 451–453 (2009).

334. Szabó, T. *et al.* Evolution of Surface Functional Groups in a Series of Progressively Oxidized Graphite Oxides. *Chem. Mater.* **18**, 2740–2749 (2006).

335. Luo, Z. *et al.* Modulating the electronic structures of graphene by controllable hydrogenation. *Appl. Phys. Lett.* **97**, 1–4 (2010).

336. Mcfeely, F. R. *et al.* X-ray photoemission studies of diamond, graphite, and glassy carbon valence bands. *Phys. Rev. B* **9**, 5268–5278 (1974).

337. Dí, J., Paolicelli, G., Ferrer, S. & Comin, F. Separation of the sp3 and sp2 components in the C 1s photoemission spectra of amorphous carbon films. *Phys. Rev. B* **54**, 8064–8069 (1996).

338. Chen, P. *et al.* Electronic Structure and Optical Limiting Behavior of Carbon Nanotubes. *Phys. Rev. Lett.* **82**, 2548–2551 (1999).

339. Souto, S., Pickholz, M., dos Santos, M. & Alvarez, F. Electronic structure of nitrogen-carbon alloys determined by photoelectron spectroscopy. *Phys. Rev. B - Condens. Matter Mater. Phys.* **57**, 2536–2540 (1998).

340. Luo, Z. *et al.* Pyridinic N doped graphene: synthesis, electronic structure, and electrocatalytic property. *J. Mater. Chem.* **21**, 8038–8044 (2011).

341. Jung, R. & Cheong, J.-K. Investigation of the dependence of the chemical states of the graphene surface on N2 plasma treatment. *J. Korean Phys. Soc.* **60**, 933–936 (2012).

342. Sutar, D. S., Singh, G. & Divakar Botcha, V. Electronic structure of graphene oxide and reduced graphene oxide monolayers. *Appl. Phys. Lett.* **101**, 103103 (2012).

343. Ago, H. *et al.* Work Functions and Surface Functional Groups of Multiwall Carbon Nanotubes. *J. Phys. Chem. B* **103**, 8116–8121 (1999).

344. Hoon Yang, J. *et al.* Effect of Oxidation on Electronic and Geometric Properties of Carbon Nanotubes. *Jpn. J. Appl. Phys.* **41**, 5635 (2002).

345. Park, Y., Choong, V., Gao, Y., Hsieh, B. R. & Tang, C. W. Work function of indium tin oxide transparent conductor measured by photoelectron spectroscopy. *Appl. Phys. Lett.* **68**, 2699–2701 (1996).

346. Kakavelakis, G., Konios, D., Stratakis, E. & Kymakis, E. Enhancement of the efficiency and stability of organic photovoltaic devices via the addition of a lithium-neutralized graphene oxide electron-transporting layer. *Chem. Mater.* **26**, 5988–5993 (2014).

347. Kim, J., Ganorkar, S., Kim, Y.-H. & Kim, S.-I. Graphene oxide hole injection layer for high-efficiency polymer light-emitting diodes by using electrophoretic deposition and electrical reduction. *Carbon N. Y.* **94**, 633–640 (2015).

348. Singh, M., Haverinen, H. M., Dhagat, P. & Jabbour, G. E. Inkjet printing-process and its applications. *Adv. Mater.* **22**, 673–685 (2010).

349. Wei, Zhanhua, Chen, Haining, Keyou, Yan and Yang, S. Inkjet Printing and Instant Chemical Transformation of aCH3 NH3 PbI3 / Nanocarbon Electrode and Interface for Planar Perovskite Solar Cells. *Angew. Chemie - Int. Ed.* **53**, 1–6 (2014).

350. Peng, X. *et al.* Perovskite and Organic Solar Cells Fabricated by Inkjet Printing: Progress and Prospects. *Adv. Funct. Mater.* **27**, 1–27 (2017).

351. Mei, A. *et al.* A hole-conductor-free, fully printable mesoscopic perovskite solar cell with high stability. *Science (80-.).* **345**, 295–298 (2014).

352. Hu, Y. *et al.* Stable Large-Area (10 × 10 cm2) Printable Mesoscopic Perovskite Module Exceeding 10% Efficiency. *Sol. RRL* **1**, 1600019 (2017).

353. Meroni, S. M. P. *et al.* Homogeneous and highly controlled deposition of low viscosity inks and application on fully printable perovskite solar cells. *Sci. Technol. Adv. Mater.* **19**, 1–9 (2018).

354. Raminafshar, C., Dracopoulos, V., Mohammadi, M. R. & Lianos, P. Carbon based perovskite solar cells constructed by screen-printed components. *Electrochim. Acta* **276**, 261–267 (2018).

355. Vak, D. *et al.* 3D printer based slot-die coater as a lab-to-fab translation tool for solution-processed solar cells. *Adv. Energy Mater.* **5**, 1–8 (2015).

356. Hwang, K. *et al.* Toward Large Scale Roll-to-Roll Production of Fully Printed Perovskite Solar Cells. *Adv. Mater.* **27**, 1241–1247 (2015).

357. Boopathi, K. M. *et al.* Preparation of metal halide perovskite solar cells through a liquid droplet assisted method. *J. Mater. Chem. A* **00**, 1–7 (2015).

358. Jung, Y. S. *et al.* Differentially pumped spray deposition as a rapid screening tool for organic and perovskite solar cells. *Sci. Rep.* **6**, 1–9 (2016).

359. Barrows, A. *et al.* Efficient planar heterojunction mixed-halide perovskite solar cells deposited via spray-deposition. *Energy Environ. Sci.* **7**, 1–7 (2014).

360. Hyuck Heo, J., Ho Lee, M., Hyeok Jang, M. & Hyuk Im, S. Highly efficient CH3NH3PbI3ÀxClx mixed halide perovskite solar cells prepared by re-dissolution and crystal grain growth via spray coating. *J. Mater. Chem. A* **4**, 17636–17642 (2016).

361. Bag, S., Deneault, J. R. & Durstock, M. F. Aerosol-Jet-Assisted Thin-Film Growth of CH3NH3PbI3 Perovskites—A Means to Achieve High Quality, Defect-Free Films for Efficient Solar Cells. *Adv. Energy Mater.* **7**, 1–11 (2017).

362. Razza, S., Castro-Hermosa, S., Carlo, A. Di & Brown, T. M. Research Update: Large-area deposition, coating, printing, and processing techniques for the upscaling of perovskite solar cell technology. *APL Mater.* **4**, 091508-1 (2016).

363. Rong, Y. *et al.* Toward Industrial-Scale Production of Perovskite Solar Cells: Screen Printing, Slot-Die Coating, and Emerging Techniques. *J. Phys. Chem. Lett.* **9**, 2707–2713 (2018).

364. Schmidt. T.M, Larsen-Olsen T.T, C. J. Upscaling of perovskite solar cells-fully ambient roll processing of flexible perovksite solar cells with printed back electrodes. *Adv. Energy Mater.* **5**, (2015).

365. Li, Y. *et al.* High-efficiency robust perovskite solar cells on ultrathin flexible substrates. *Nat. Commun.* **7**, 1–10 (2016).

366. Razza, S. *et al.* Perovskite solar cells and large area modules (100 cm2) based on an air flow-assisted PbI2 blade coating deposition process. *J. Power Sources* **277**, 286–291 (2015).

367. Priyadarshi, A. *et al.* A large area (70 cm2) monolithic perovskite solar module with a high efficiency and stability. *Energy Environ. Sci* **9**, 3687 (2016).

368. Kim, J. *et al.* Overcoming the Challenges of Large-Area High-Efficiency Perovskite Solar Cells. *ACS Energy Lett.* **2**, 1978–1984 (2017).

369. Lisco, F., Shaw, A., Wright, A., Walls, J. M. & Iza, F. Atmospheric-pressure plasma surface activation for solution processed photovoltaic devices. *Sol. Energy* **146**, 287–297 (2017).

370. Jui-Hsuan & Tsai. DC-pulse atmospheric-pressure plasma jet and dielectric barrier discharge surface treatments on fluorine-doped tin oxide for perovskite solar cell application. *J. Phys. D Appl. Phys* **51**, 1 (2017).

371. Scott, S. M. *et al.* The thermal stability and consolidation of perovskite variant Cs2SnCl6 using spark plasma sintering. *J Am Ceram Soc* **101**, 2060–2065 (2018).

372. Penache, C. *et al.* Plasma printing: patterned surface functionalisation and coating at atmospheric pressure. *IEE Proc. - Nanobiotechnology* **151**, 139 (2004).

373. Thomas, M. *et al.* Plasma printing and related techniques - Patterning of surfaces using microplasmas at atmospheric pressure. *Plasma Process. Polym.* **9**, 1086–1103 (2012).

374. Niall O. Connor, Ram Prasad Gandhiraman, Colin Doyle, Bryony James, D. E. W. and S. D. Supplementary information for Room temperature deposition of tunable plasmonic nanostructures by atmospheric pressure jet plasma. *J. Mater. Chem.* **22**, 9485 (2012).

375. Zhao, P., Zheng, W., Meng, Y. D. & Nagatsu, M. Characteristics of high-purity Cu thin films deposited on polyimide by radio-frequency Ar/H2 atmospheric-pressure plasma jet. *J. Appl. Phys.* **113**, 123301 (2013).

376. Dey, A. Applications of Atmospheric Pressure Plasma in Surface Engineering. (The Open University, UK, 2017).

377. Mariotti, D. & Sankaran, R. M. Perspectives on atmospheric-pressure plasmas for nanofabrication. *J. Phys. SAppl. Phys.* **44**, 174023–1 (2011).

378. Schölin, R. *et al.* Energy Level Shifts in Spiro-OMeTAD Caused by Adding Li-TFSI Studied by X-ray Photoelectron Spectroscopy. *Appl. Phys. Lett.* 2–3 (2010).

379. Barkoula, N. M., Alcock, B., Cabrera, N. O. & Peijs, T. The Effect of Carboxylic Acid Group on Conductivity of the Aromatic Polyazomethines and Char Composites. *Polym. Polym. Compos.* **16**, 101–113 (2008).

380. Williams, A. E. *et al.* Perovskite processing for photovoltaics: A spectro-thermal evaluation. *J. Mater. Chem. A* **2**, 19338–19346 (2014).

381. Holliman, P. J. *et al.* Solvent issues during processing and device lifetime for perovskite solar cells. *Mater. Res. Innov.* **19**, (2016).

382. Hawash, Z., Ono, L. K. & Qi, Y. Recent Advances in Spiro-MeOTAD Hole Transport Material and Its Applications in Organic–Inorganic Halide Perovskite Solar Cells. *Adv. Mater. Interfaces* **5**, 1–22 (2018).

383. Ginting, R. T. *et al.* Plasmonic Effect of Gold Nanostars in Highly Efficient Organic and Perovskite Solar Cells. *ACS Appl. Mater. Interfaces* **9**, 36111–36118 (2017).

384. Hooper, K. E. A. *et al.* Probing the degradation and homogeneity of embedded perovskite semiconducting layers in photovoltaic devices by Raman spectroscopy. *Phys. Chem. Chem. Phys.* **5246**, 5246–5253 (2017).

385. Strazulla, G. C. L. M. V. B. G. A. B. E. Raman and infrared spectra of polycyclic aromatic hrdrocarbon molecules of possible astrophysical interest. *Astrophys. J.* **396**,

369–377 (1992).

386. Lapkowski, M. *et al.* Electrochemical Oxidation of Polyaniline in Nonaqueous Electrolytes: ‘ In Situ’ Raman Spectroscopic Studies. *Macromolecules* **28**, 1233–1238 (1995).

387. Zhang, X., Zhou, Q., Huang, Y., Li, Z. & Zhang, Z. Contrastive analysis of the Raman spectra of polychlorinated benzene: Hexachlorobenzene and benzene. *Sensors* **11**, 11510–11515 (2011).

388. Quillard, S. *et al.* Spectroelectrochemical measurements of the conducting form of polyaniline and related oligomers. *Synth. Met.* **10**, 768–77 (1999).

389. Kvarnstro, C. *et al.* Raman and FTIR spectroscopic characterization of electrochemically synthesized poly(triphenylamine), PTPA. *J Solid State Electrochem* **6**, 505–512 (2002).

390. Shimanouchi & Takehiko. *Tables of molecular vibrational frequencies, consolidated volume I*. (1976).

391. Raj, A. *et al.* IR, Raman and SERS Spectra of 2 -(Methoxycarbonylmethylsulfanyl)-3,5-dinitrobenzene Carboxylic Acid. *J. Braz. Chem. Soc* **20**, 549–559 (2009).

392. Boyaci, I. H. *et al.* Dispersive and FT-Raman spectroscopic methods in food analysis. *RSC Adv.* **5**, 56606–56624 (2015).

393. Karampelas, S. *et al.* Determination by Raman scattering of the nature of pigments in cultured freshwater pearls from the mollusk Hyriopsis cumingi. *J. Raman Spectrosc.* **38**, 217–230 (2007).

394. Michaelian, K. H. *et al.* Raman and photoacoustic infrared spectra of fluorene derivatives: Experiment and calculations. *Vib. Spectrosc.* **74**, 33–46 (2014).

395. Peng, Y. & Huang, D. Fabrication of patterned reduced graphene oxide nanosheet field-emission cathodic film at room-temperature. *Appl. Surf. Sci.* **283**, 81–86 (2013).

396. Massines, F., Messaoudi, R. & Mayoux, C. Comparison Between Air Filamentary and Helium Glow Dielectric Barrier Discharges for the Polypropylene Surface Treatment. *Plasmas Polym.* **3**, (1998).

397. Schulz, P. *et al.* High-Work-Function Molybdenum Oxide Hole Extraction Contacts in Hybrid Organic−Inorganic Perovskite Solar Cells. *ACS Appl. Mater. Interfaces* **8**, 31491–31499 (2016).

398. Shen, Y. *et al.* Improved Photoresponse Performance of Self-Powered ZnO/Spiro-MeOTAD Heterojunction Ultraviolet Photodetector by Piezo-Phototronic Effect. *ACS Appl. Mater. Interfaces* **8**, 6137–6143 (2016).

399. Bera, A., Das Mahapatra, A., Mondal, S. & Basak, D. Sb2S3/Spiro-OMeTAD Inorganic−Organic Hybrid p−n Junction Diode for High Performance Self-Powered Photodetector. *ACS Appl. Mater. Interfaces* **8**, 34506–34512 (2016).

400. Jaramillo-Quintero, O. A., Sánchez, R. S., Rincón, M. & Mora-Sero, I. Bright Visible-Infrared Light Emitting Diodes Based on Hybrid Halide Perovskite with Spiro-OMeTAD as a Hole Injecting Layer. *J. Phys. Chem. Lett.* **6**, 1883–1890 (2015).

401. Wang, M. *et al.* Electroluminescence from perovskite LEDs with the structure of Ag/Spiro-OMeTAD/CH3NH3PbI3/TiO2/FTO. *Chem. Phys. Lett.* **662**, 176–181 (2016).